Enhanced Heterogeneous Nucleation on Oxides in Al Alloys by Intensive Melt Shearing

A thesis submitted for the degree of

Doctor of Philosophy

by

Hu-Tian Li

BCAST

Brunel University

Uxbridge, UB8 3PH

United Kingdom

February 2011

Dedicated to

my father,

my wife and my daughter,

for their love, endless support and encouragement.

Excellence is the result of

Caring more than others think is wise,

Risking more than others think is safe,

Dreaming more than others think is practical and

Expecting more than others think is possible.

Abstract

Aluminium alloys, including both foundry and wrought alloys, have been extensively used for light-weight structural and functional applications. A grain refined as-cast microstructure is generally highly desirable for either subsequent processing ability or mechanical properties of the finished components. In this thesis, the grain refined microstructures in Al alloys have been achieved by intensive melt shearing using the melt conditioning by advanced shearing technology (MCAST) without deliberate grain refiner additions. Such grain refinement has been attributed to the enhanced heterogeneous nucleation on the dispersed oxide particles. It has been established that the naturally occurring oxides in molten Al alloys normally have a good crystallographic match with the α-Al phase, indicating the high potency of oxide particles as the nucleation sites of the α-Al phase. The governing factors for these oxide particles to be effective grain refiners in Al alloys have been proposed, including the achievement of good wetting between oxide particles and liquid aluminium, a sufficient number density and uniform spatial distribution of the dispersed oxide particles, and near equilibrium kinetic conditions in liquid alloys. In the present study, near equilibrium kinetic conditions can be achieved by intensive melt shearing using a twin screw mechanism, which has been confirmed by the observed equilibrium α-AlFeSi phase in a cast Al alloy and the transformation from γ- to α-Al_2O_3 at 740±20^oC under intensive shearing.

For different alloy systems, depending on the alloy system, and melting conditions, due to the particular types of oxide formed and its crystallographic and chemical characteristics, the nucleation site of the nucleated phase is different. Specifically, $MgAl_2O_4$ relative to MgO, and α-Al_2O_3 relative to γ-Al_2O_3, have higher potency as heterogeneous nucleation sites of α-Al phase in Al alloys.

In future, the modification of the crystallographic match, and of the other surface characteristics related to the interfacial energy between the specific oxides and nucleated phase by trace alloying addition through segregation to the interface between oxides and nucleated phases combined with physical melt processing (such as intensive shearing in the present study) should be investigated in more detail.

Acknowledgements

My sincere thanks and appreciation go to my supervisor, Professor Zhongyun Fan for providing the opportunity to pursue my PhD and for his extensive encouragement, support and guidance throughout my research.

I wish to thank my colleagues who have supported me especially: Dr. Y. Wang for his help with advanced electron microscopy, Dr. M. Xia and Dr. Y. Zuo for their help with processing, Dr. Ian Stone, Prof. John Hunt, Prof. Hasse Fredriksson, Prof. Brian Ralph, and Prof. Geoff Scamans, for their technical knowledge, and Mr. Peter Lloyd, Mr. Stephen Cook and Mr. Carmelo Nunez for their technical assistance. I would like to thank Dr. Philippe Jarry from Alcan Engineered Products for conducting thermodynamic calculation.

I would like to show my gratitude to Prof. László Gránásy, Drs. H. Men, Y. Huang, Jayesh Patel, H. Zhang, Y. Zhang; Drs. Brian McKay, Hari Babu Nadendla, Kumar Sundaram, T.Qin, I. Bayandorian, Mrs Pam Eade, Mrs Carla Cummins, Mrs Nikki Elliott, Mr. Phil Enright , Mr. B. Jiang, Mr. L. Cao, Mr. S. Liang, Mr. F. Yan, Miss Magdalena Nowak and Mr. Ritwik Ritwik, Mr. Simon Jones, Mr. Zen Cassinath, Ms. Kawther Al-Helal, Mr. Spyridon Tzamtzis, Mr. Hiren R. Kotadia, Mr. Richard Keyte for their support in conducting the research work, preparing this thesis, and for many inspiring discussions.

I owe my deepest gratitude to, EPSRC and Norton Aluminium Limited, UK, for financial support to conduct this research work and awarding of DHPA, the Brunel Centre for Advanced Solidification Technology (BCAST) for all the infrastructural support, Alcan Engineered Products for providing partial materials, and the Experimental Techniques Centre (ETC Brunel) for providing their facilities and services in advanced analytical and characterisation techniques.

Lastly, I offer my best regards and blessings to those who made this thesis possible. They are my wife and my daughter, my father and my sister and brother, who gave me the moral support I required during the accomplishing of the project.

Publication List

Peer Reviewed Journal Papers

1. H.T. Li, M. Xia, Ph. Jarry, G.M. Scamans, and Z. Fan, Grain refinement in an AlZnMgCuTi alloy by intensive melt shearing: a multi-step nucleation mechanism, **Journal of Crystal Growth**, 2011, Vol. 314, pp. 285-292.
2. Y. Zuo, H. Li, M. Xia, B. Jiang, G.M. Scamans and Z. Fan, Refining grain structure and porosity of an aluminium alloy with intensive melt shearing, **Scripta Mater.,** 2011,Vol. 64, pp 209-212.
3. Z. Fan, Y. Wang, Z.F. Zhang, M. Xia, H.T. Li, J. Xu, L. Gránásy, G.M. Scamans, Shear Enhanced heterogeneous nucleation in some Mg- and Al-alloys, **International Journal of Cast Metals Research**, 2009, Vol.22, pp. 318-322.
4. Z. Fan, M. Xia, H. Zhang, G. Liu, J.B. Patel, Z. Bian, I. Bayandorian, Y. Wang, H.T. Li, and G.M. Scamans, Melt conditioning by advanced shear technology (MCAST) for refining solidification microstructures, **International Journal of Cast Metals Research**, 2009, Vol.22, pp. 103-107
5. H. T. Li, Y. Zuo, M. Xia, Y. Wang, I. Stone, Z. Fan, Dependence of Fe-rich intermetallics formation on kinetics and mechanical properties in an AlSiCuZnFe alloy, to be submitted to **Metall. Mater. Trans. A.**
6. H. T. Li, Y. Wang, Z. Fan, Mechanisms of enhanced heterogeneous nucleation in binary Al-Mg alloys, to be submitted **Acta Mater**.
7. H. T. Li, Y. Wang, Z. Fan, Grain refinement in commercial purity Al by intensive shearing, to be submitted **Acta Mater**.

Peer Reviewed Conference Papers

1. M. Xia, Y. Wang, H. Li, S. Arumuganathar, Y. Zuo, G.M. Scamans, and Z. Fan, Refinement of Solidification Microstructure by MCAST Process, Proc. of Magnesium Technology, TMS 2009, pp. 135-140.
2. Z. Fan, M. Xia, Z. Bian, I. Bayandorian, L. Cao, H. Li, G. M. Scamans, Refinement of solidification microstructures by the MCAST process, Materials Science Forum, The Fifth International Conference on Solidification and Gravity V, Edited by: A.Roosz, V. Mertinger, P. Barkoczy, Cs. Hoo, September 6-9, 2008, pp. 315-323.

Conference presentations

1 H.T. Li, Z. Fan, Enhanced heterogeneous nucleation based on oxides in Al alloys by intensive shearing, to be made, the 3rd International Conference on Advances in Solidification Processes (ICASP3), 7-10, June, 2011, Aachen/Rolduc, Germany.

2 H. T. Li, Z. Fan, Harnessing oxides to enhance nucleation for microstructural refinement, 4th International Conference on Solidification Science and Processing (ICSSP4), 20-23, November, 2009, Chennai, India.

3 H. T. Li, Z. Fan, Grain Refinement of Wrought Al Alloy by Intensive Melt Shearing, Research Student Conference 2009, June, 2009, Brunel University (1st Prize for Extended Abstract).

Nomenclature

Abbreviation or Symbol	Description
2D	Two-dimensional
3D	Three-dimensional
BCC	Body centred cubic
CCP	Cubic close packed
CET	Columnar to equiaxed transition
COCI	Colour orientation contrast imaging
CP Al	Commercial purity aluminum
DC	Direct chill (casting)
EBSD	Electron backscatter diffraction
EDXS	Energy-dispersive X-ray spectroscopy
EMV	Electromagnetic vibration
FCC	Face centred cubic
GRF	Growth restriction factor
HCP	Hexagonal closed-packed
HPDC	High pressure die casting
HRTEM	High resolution transmission electron microscopy
JANAF	Joint army navy air force
JCPDS	Joint committee on powder diffraction standards
MCAST	Melt conditioning by advanced shear technology
MC-DC	Melt conditioned direct chill casting

Nomenclature

(Continued)

Abbreviation or Symbol	Description
MC-HPDC	Melt conditioned high pressure die casting
OM	Optical microscopy
OR	Orientation relationship
RDC	Rheo-die casting
SAD	Selected area electron diffraction
SDAS	Secondary dendrite arm spacing
SEM	Scanning electron microscopy
SSM	Semi-solid material
TEM	Transmission electron microscopy
UTS	Ultimate tensile strength
XRD	X-ray diffraction

Table of Contents

Chapter 1

Introduction

1.1 Background

Aluminium alloys, including both foundry and wrought alloys, have been extensively used for light-weight structural and functional applications. A grain refined as-cast structure is always highly desirable for either subsequent processing ability or mechanical properties of the finished components. Therefore, additions of chemical grain refiners have been the established industrial practice for more than half a century. However, only less than 1% of the added particles successfully nucleate aluminium grains and this low efficiency is undesirable not only for its immediate cost implications, but also because refiner particles may themselves be detrimental in the final microstructures particularly for products intended for extrusion, deep drawing, or high performance structural applications. At the same time, oxides are inevitably present in liquid aluminium alloys in the form of oxide films and/or oxide clusters that can cause severe difficulties during casting, and become inclusions and other related defects resulting in the degradation of the mechanical properties of cast components. Therefore, extensive effort has been made to remove oxides from liquid metal prior to casting using both chemical and physical methods.

From the sustainability point of view, more and more Al alloys are being recycled in the aluminium industry all over the world because of the huge reduction of energy consumption compared to the production of primary metal refined from raw minerals. During recycling,

more oxides and other inclusions or impurities can be accumulated, which presents an increasing challenge for the aluminium industry in terms of increased processing cost and decreased product quality.

By the application of intensive shearing to liquid metal using melt conditioning by advanced shear technology (MCAST), the naturally occurring oxides can be used as heterogeneous nucleation sites and therefore, grain refined as-cast microstructure and dispersed oxides can be achieved simultaneously. Without doubt, the implementation of this processing technology will benefit the Al industry in terms of both cost reduction and sustainable development.

1.2 Objectives of the present study and the methodology adopted

Grain refinement of Mg based alloys by intensive melt shearing has been investigated by several researchers in our group. However, the effect and underlying mechanisms of intensive shearing in Al based alloys remain unclear although some related studies have been performed (Fang, *et al*., 2007; Kotadia, *et al*., 2010).

The objective of this work was to investigate the effect of intensive melt shearing on microstructural evolution in aluminium alloys, especially on the mechanisms underlying the enhanced heterogeneous nucleation of constitutional phases. In parallel, the evolution of oxides formed in Al alloys has been studied by means of a pressure filtration technique (Cao, 2005; Fan, *et al*., 2009), which has been demonstrated to be a very effective way to concentrate the inclusions formed in molten alloys. Using advanced analytical electron microscopy, including X-ray diffraction analysis, scanning electron microscopy (SEM) and transmission electron microscopy (TEM) and high resolution transmission electron microscopy (HRTEM), the refined grains and constituent particles can be correlated to the dispersed oxides.

1.3 Organization of the thesis

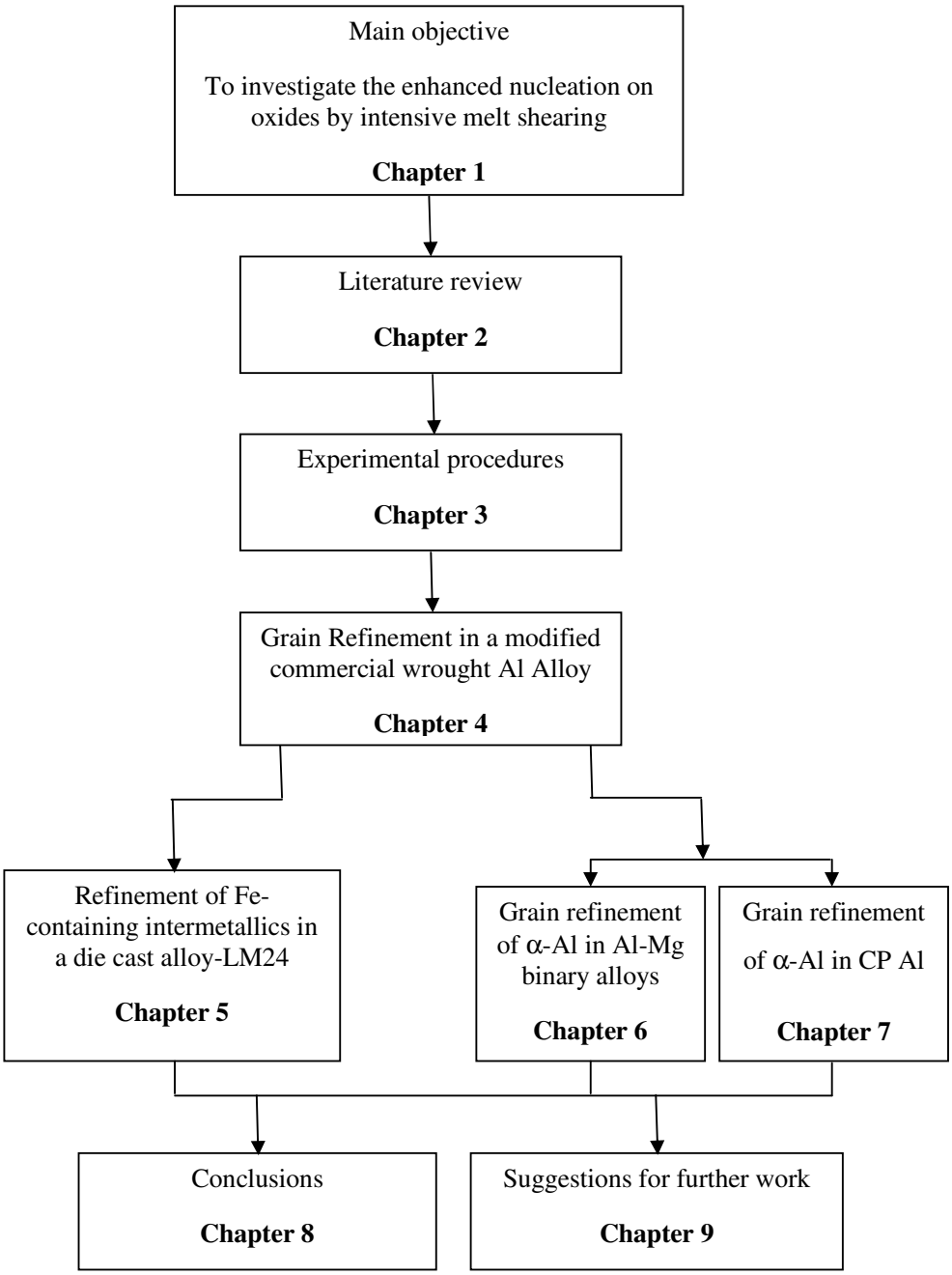

Figure 1.1 *Flow chart showing the organization of the thesis.*

The organisation of this thesis is illustrated in **Figure 1.1**. Following a brief introduction in Chapter 1, the literature survey is presented in Chapter 2, summarising the current understanding of grain refinement, the formation of Fe-containing intermetallic compounds in Al cast alloys and the formation of oxides in liquid Al alloys. Chapter 3 presents the experimental details in the order of the subsequent chapters.

The initial experimental work was focused on the confirmation of the effect of intensive melt shearing on grain refinement of a modified commercial wrought Al alloy, and the results are presented in Chapter 4. It was found that the dispersed $MgAl_2O_4$ particles by intensive melt shearing can act as heterogeneous nucleation sites of Al_3Ti intermetallic particles, which in turn can refine the α-Al phase. This prompted the investigation of the possibility of enhancing heterogeneous nucleation of other intermetallics and α-Al by the dispersed $MgAl_2O_4$ particles. The results on nucleation of Fe-containing intermetallics in LM24 alloy and α-Al in Al-Mg binary alloys are presented in Chapters 5 and 6, respectively. This was followed by an investigation of whether other oxides, such as γ-Al_2O_3 and α-Al_2O_3, nucleate α-Al, and the results on heterogeneous nucleation of α-Al on both γ-Al_2O_3 and α-Al_2O_3 in CP aluminium are presented in Chapter 7. For clarity, the experimental results and discussions are presented in each individual chapter. Chapter 8 presents the overall conclusions from this work. This is followed by suggestions for future research in Chapter 9 and the references are at the end of the thesis.

Chapter 2

Literature review

2.1 Formation of Fe-containing intermetallic compounds in cast Al alloys

LM24 is a pressure die casting alloy which conforms to BS 1490 1988 and is one of the most widely used secondary aluminium casting alloys due to its wide range of main constituent elements, the mechanical properties of which are determined mainly by (a) the degree of supersaturation of copper and magnesium in the α-Al matrix, (b) the constituent phase particles, namely, the iron-intermetallics and copper phases that occur upon solidification, (c) the size of porosity and its distribution, as well as (d) the shape and distribution of the eutectic silicon particles in the matrix (Samuel & Samuel, 1996). This alloy has excellent die casting ability and good mechanical properties that make it ideal for the manufacture of thin walled die castings. As a secondary Al alloy, inclusions and impurities are always present that may degrade the mechanical properties of resultant die castings. Of these microstructural constituents, oxide films, porosity and iron-containing intermetallic compounds are of the most concern.

2.1.1 Formation of Fe-containing intermetallic compounds

Iron is a common impurity in aluminium alloys that arises from a number of possible sources and, at least for Al-Si based casting alloys, is usually considered detrimental in one or more ways. It should be noted that iron does not always exert a negative influence; in certain wrought aluminium alloys (that is, alloys used in forged, extruded or rolled forms), iron can

be a deliberate alloying addition that is made to improve the processing capabilities of the alloy and/or the strength of the final wrought product. However, these wrought alloys are not of normal interest to the foundry industry that is based mainly on the Al-Si alloy family (Taylor, 2004).

Iron is a natural impurity that arises during the manufacture of primary aluminium via the Bayer Process that converts bauxite (the ore) into alumina and the Hall-Héroult electrolytic reduction process that converts alumina into molten aluminium (>900ºC) with the consumption of both electricity and carbon. Depending on the quality of the incoming ore and the control of the processing parameters, molten primary aluminium typically contains between 0.03- 0.15 wt.% iron, with ~ 0.07- 0.10 % being typical for high quality primary metal (Taylor, 2004).

Presently, there is no economically method to remove iron from aluminium so these primary values are the typical baseline and all further melting activities usually increase the iron level. Iron can enter the melt during further downstream melt activities through two basic mechanisms (Taylor, 2004): (1) Liquid aluminium is capable of dissolving iron from unprotected steel tools and furnace equipment, and with long exposure times, Fe levels can reach 2 wt% at normal melt temperatures of ~700ºC (an Al-Fe eutectic exists at 1.7 wt.% Fe, 655ºC - see **Figure 2.1**). For a melt held at 800ºC, the Fe level can reach up to 5%; (2) Iron can also enter an aluminium melt via the addition of low-purity alloying materials, e.g. Si, or via the addition of scrap that contains higher background iron content than the primary metal. These are the reasons why iron levels in aluminium alloys continue to increase with each remelt cycle, and why secondary alloys, particularly those Al-Si alloys destined for high pressure die casting (HPDC) operations, can end up containing iron levels of up to 1.5 wt. %. In the case of HPDC, this is not always an issue as high iron levels assist in minimising the costly problem of die soldering. However, typical secondary Al-Si alloys for non-HPDC

operations usually contain much lower Fe levels ranging from ~ 0.25 to 0.8 wt%, with values around 0.4-0.7 being most common (Taylor, 2004). The reason these moderate iron level alloys find such wide use arises from the necessary commercial balance between the benefits of a reduced metal cost and the acceptable loss of some processing capability and/or final mechanical properties.

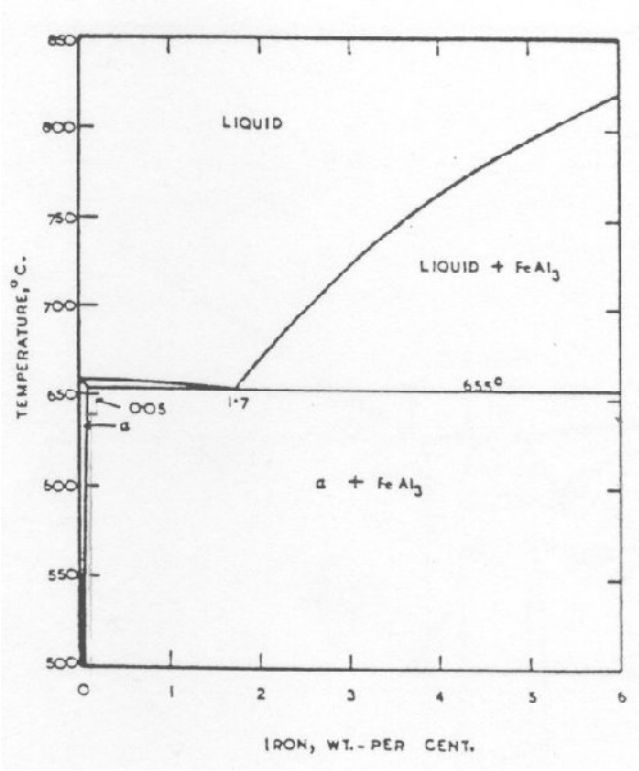

Figure 2.1 *Al rich corner of Al-Fe binary phase diagram (Taylor, 2004).*

In the absence of silicon, the dominant phases that form are Al_3Fe and Al_6Fe, but when silicon is present, the dominant phases are Al_8Fe_2Si (known as α-AlFeSi phase) and Al_5FeSi (known as β-AlFeSi phase). If Mg is also present with silicon, an alternative phase called π-phase can form, $Al_8FeMg_3Si_6$. Another common phase that forms when manganese is present

with silicon is $Al_{15}(Fe, Mn)_3Si_2$, which is sometimes presented as $Al_{17}(Fe_{3.2}Mn_{0.8})Si_2$ (Eivani *et al.*, 2009; JCPDS, 2005), also confusingly known as α-AlFeSi phase in literature.

The β-AlFeSi precipitate with an approximate formula of Al_5FeSi is an important constituent in the Al-Fe-Si or Al-Fe-Mn-Si system. The precipitates are often observed in Al alloys and have long been considered to be detrimental to the mechanical properties of Al alloys. Their crystal structure has been studied by X-ray diffraction since 1950 and by (convergent beam) electron diffraction since 1970, but it still remains a challenge. A monoclinic unit cell with parameters a =6.12 Å, b=6.12 Å, c=41.5 Å and β =91° (Phragmen, 1950) and a tetragonal cell with a = 6.18 Å and *c* = 42.5 Å (Black, 1955) were proposed on the basis of X-ray diffraction data. The former was most frequently used to interpret experimental data. The tetragonal phase, as suggested by Zheng *et al.* (Zheng *et al.*, 2000), however, is not likely to represent such a variant, a tetragonal variant would mean an increase in the symmetry of the β phase. So they proposed that the precipitates are composed of at least two phases with orthorhombic and tetragonal unit cells respectively.

Taylor et al. systematically investigated the correlation between the formation of Fe-containing intermetallic compound and silicon content in Al-Si alloys (Taylor *et al.*, 1999a, b and c). By adopting the methodology developed by Backerud et al., the ternary Al-Fe-Si phase diagram and a set of segregation lines derived from Scheil equation were used to represent the solidification paths for the investigated iron-containing hypoeutectic Al-Si alloys, as shown in **Figure 2.2**, regardless of the copper and magnesium contents (Backerud *et al.*, 1990; Taylor *et al.*, 1999b). It was found that increasing the iron content changes the precipitation sequence of the β-AlFeSi phase, leading to the precipitation of coarse binary β-AlFeSi platelets at a higher temperature. The critical iron level is directly related to the silicon concentration of the alloy. As the silicon content of the alloy increases, the amount of iron that can be tolerated before the β-AlFeSi phase starts to form prior to the Al-Si eutectic

increases. At 5% silicon, the critical iron content is ~0.35%, at 7%Si it rises to ~0.5, at 9% it is ~0.6 and by 11% it reaches ~0.75%. Also for a given iron content, the temperature (and therefore time) at which β-AlFeSi phase can form prior to the Al-Si eutectic decreases with increasing silicon content.

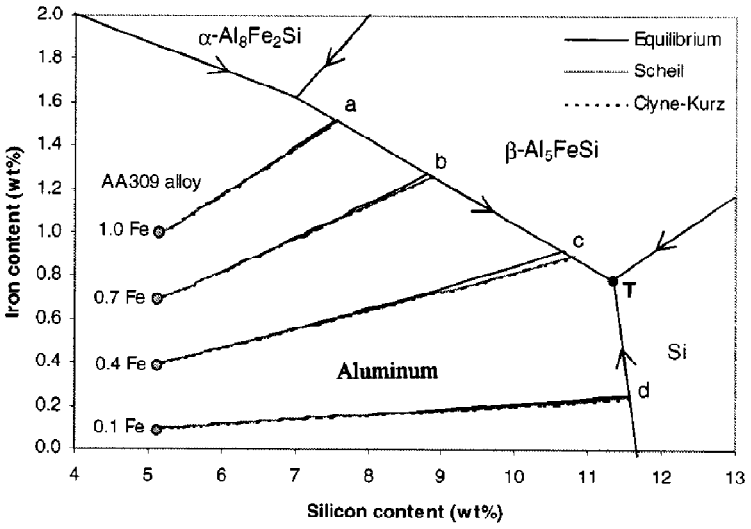

Figure 2.2 *Fe-containing intermetallic phase formation in relation with the concentrations of Fe and Si in Al-Si alloy without Mn addition* (Taylor *et al.*, 1999b).

In contrast, manganese and strontium appear to suppress the coarse binary β-AlFeSi platelets, and Mn further promotes the formation of a more compact and less harmful α-AlFeSi phase (**Figure 2.3**) (Narayanan *et al.*, 1994). It is therefore expected to reduce the negative effects of the Fe-bearing intermetallic phase. Figure 2.3 shows a simplified phase diagram of the Al-Fe-Mn-Si at a 0.38 pct Mn level based on the methodology developed by Backerud et al. (Backerud *et al.*, 1990; Narayanan *et al.*, 1994). From **Figure 2.3**, the solidification process can be analyzed as follows: starting with the formation of α-Al dendrites (line 1), with the interdendritic liquid becoming successively enriched in iron and manganese and silicon. On further solidification, the segregation line penetrates the $Al_{15}(Fe, Mn)_3Si_2$ surface and the

crystallization of the α-AlFeSi phase begins (line 2). The α-AlFeSi phase continues to crystallize along with α-Al until the trough between $Al_{15}(Fe, Mn)_3Si_2$ and Al_5FeSi is reached, whereupon both the α- and β-AlFeSi phases crystallize together (line 3). When the ternary eutectic valley is reached, aluminium, silicon, and β-AlFeSi phases crystallize together in the main eutectic reaction.

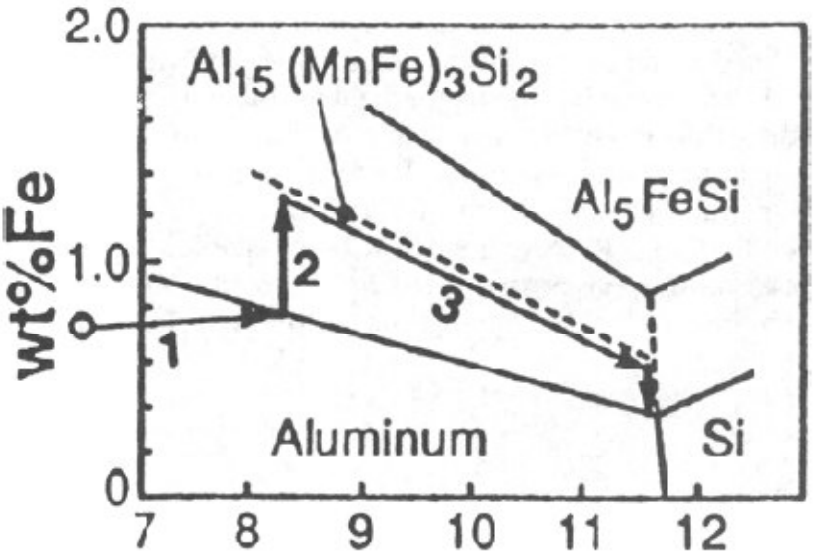

Figure 2.3 *The simplified phase diagram of the Al-Fe-Mn-Si at 0.38wt.% Mn level (Narayanan et al., 1994).*

Formation mechanisms of Fe-containing intermetallic particles in Al-Si cast alloys summarized by Cao and Campbell are in three reactions as follows: (1) pre-dendritic (primary), (2) eutectic reactions, and (3) peritectic reactions (Cao and Campbell, 2004b).

2.1.2 Morphology of Fe-containing intermetallic compounds

The iron-containing intermetallic phases listed above are quite obvious within the microstructures of Al-Si alloys, and can usually be distinguished under the microscope by

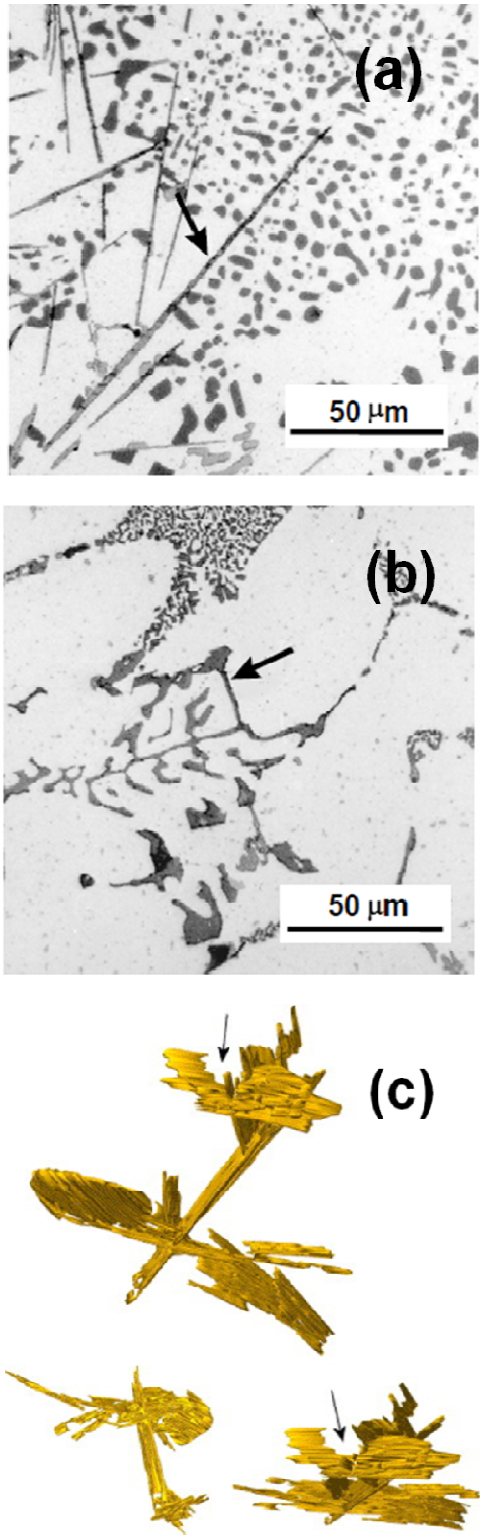

Figure 2.4 *Photomicrographs showing typical morphologies of Fe-containing intermetallics: (a) β-Al_5FeSi platelets; (b) script-like α-Al_8Fe_2Si in an Al-5%Si-1%Cu-0.5%Mg-(Fe) alloy; and (c) three-dimensional reconstruction of β-Al_5FeSi platelets in an Al-9%Si-1%Fe alloy (Taylor, 2004; Dinnis, et al., 2005).*

Table 2.1 *Summary of Fe-containing intermetallic phases formed in Al alloys.*

	α-Al_8Fe_2Si (α-AlFeSi)	β-Al_5FeSi (β-AlFeSi)	$Al_8FeMg_3Si_6$ (π-phase)	References
Variants	α-$Al_{15}(Fe, Mn, Cr)_3Si_2$, $Al_{17}(Fe_{3.2},Mn_{0.8})Si_2$, α-$Al_{19}Fe_4MnSi_2$*	Al_5FeSi, $Al_9Fe_2Si_2$	$Al_9FeMg_3Si_5$	(Cao and Campbell, 2003)(JCPDS, 2005)(Taylor, 2004)
Morphology	Polyhedral or Chinese script-like	Needle (2D)/platelet(3D)	Chinese script-like	(Dinnis *et al.*, 2005)
Crystal system	Hexagonal /bcc (with Mn)	Monoclinic	Hexagonal	(Cao and Campbell, 2003)
Space group	*Im3*	*$P6_3$*	*$P\bar{6}2m$*	(Cao and Campbell, 2003)
Formation conditions	Mn:Fe ratio larger than 0.5	Mn:Fe ratio less than 0.5	Mg present with Si	(Taylor, 2004)
Formation mechanisms	Primary or eutectic reactions	Primary or eutectic reactions	Eutectic reactions	(Cao and Campbell, 2004b)

* (Cooper, 1967)

their dominant shape (morphology) and colour. The β-AlFeSi phases usually exhibit a platelet like shape (arrowed in **Figure 2.4a**). The so-called α-AlFeSi phases form in either a

dendritic or script-like morphology (see **Figure 2.4b**), or more compact, sometimes even as polyhedral crystals.

Dinnis et al. investigated the three-dimensional (3D) as-cast morphology of β-AlFeSi intermetallics in an Al-9%Si-1%Fe alloy via serial sectioning methodology (Dinnis *et al*., 2005). The platelets form a complex and interconnected network (**Figure 2.4c**). Note that although the β-AlFeSi phase has a platelet form in three-dimensions, when observed in a two-dimensional image or photograph, the platelets appear to be "needles". The differing shapes of these iron intermetallics are in part responsible for the impact of iron on castability and mechanical properties. **Table 2.1** summarizes the features and formation mechanisms of different Fe-containing intermetallic phases formed in aluminium alloys.

2.1.3 The effect of Fe-containing intermetallics on the mechanical properties of Al alloys

The detrimental effect of iron begins at quite low primary iron levels but becomes far more serious once a critical iron level (dependant on alloy composition) is exceeded. The detrimental effect of iron on ductility is due to two main reasons: (1) the size and number density of iron-containing intermetallics (particularly the β-AlFeSi phase) increases with iron content, and therefore since these particles participate directly in the fracture mechanism, the more intermetallics there are, the lower the ductility; (2) as the iron level increases, porosity increases, and this defect also has an impact on ductility.

In view of the negative influence of Fe-containing intermetallic phases on the mechanical properties, the Fe-containing intermetallics generally work synergistically with other microstructural constituents (e.g. Si particles and porosities) in initiating cracks and accumulating damage. The morphology of the Fe-containing intermetallics plays a deciding role in the alloy's mechanical properties. The needle/platelet β-AlFeSi phase is considered to be the most detrimental to mechanical properties. This is not because of its edges or tips, but

because of its higher aspect ratio than in the other Fe-containing intermetallic phases. The higher stress concentrations on the β-AlFeSi particles are ascribed to increased dislocation pile-up on the particles because their ability to block the movement of dislocations is increased by the higher aspect ratio. Vorren et al. also observed that bonding between the β-Al_5FeSi phases and the Al matrix is very weak and concluded that the poor bonding strength would cause decohesion to occur and the particles would, in essence, behave as two-dimensional defects (Vorren *et al.*, 1984). The effect of Fe-containing intermetallics becomes even more pronounced when the Si phase is modified because they can be up to twice as large as the Si phase and more elongated. Elongated phases have a stronger interaction with the plastic strain and thus lead to higher particle stresses whereas larger particles are more prone to cracking than smaller ones (Wang *et al*., 1998).

The Fe-containing intermetallic phases are essentially insoluble and may be responsible for an improvement in strength, particularly at elevated temperatures. Wang et al. noted that the addition of iron and nickel makes it possible to reduce the copper content without reducing Al-Si alloy's high temperature strength (Wang *et al*., 1995). However, this is beyond the scope in the present study and will not be stated in detail.

2.1.4 Modification of Fe-containing intermetallic compounds

Chemical methodology-Effect of iron correcting elements

This method is to control the deleterious effects of iron by alloying addition of a suitable neutralizer such as Mn, Cr, Be, Sr, or the rare earth elements such as Y, Nd, La, and Ce reported in comprehensive studies. Among these elements, the most common addition has been Mn, and to a less extent, Cr, Be, Sr, or a rare earth element (Kral *et al*., 2004; Kral *et al*., 2006; Narayanan *et al*.,1994).

Effect of Mn alloying addition

The addition of Mn basically expands the α-AlFeSi phase region, and thus, formation of the α-AlFeSi phase is possible even at high iron contents. This process is called iron neutralization, or iron correction. The manganese is often added at a Mn: Fe ratio of at least 0.5. However, detailed microstructural observations of a range of Al-Si-Cu-Mg alloys have shown that even when manganese is added at these levels it is not always possible to completely eliminate the β-AlFeSi platelets. Furthermore, the addition of manganese actually results in a higher volume fraction of Fe-containing intermetallic particles that can counter some of the ductility gains to be made. This can also lead to machining difficulties, especially when the hard α-AlFeSi phase forms in very large, colonies within the alloy. Moreover, the addition of manganese may be accompanied with other problems such as hot tearing or doing damage to furnace walls due to the formation of a coarse Al(Fe,Mn)Si compound, usually known as "sludge" or "fallout", especially in the die-casting industry, where the melt holding temperatures are generally kept low. The other problem related to the manganese addition is, α-AlFeSi phase is favoured at low cooling rates, whereas both α-AlFeSi and β-AlFeSi phases appear at high cooling rates (Narayanan *et al*.,1994).

Effect of Cr alloying addition

Gustafsson et al. carried out an investigation of the influence of Cr additions on the formation of Fe-containing intermetallics in an A356 aluminium alloy (Gustafsson *et al*.,1986). In their case, 0.2 and 0.37wt.% Cr additions were made to A356 Alloys, corresponding Fe content being 0.2 and 0.5 wt.% respectively. It was found that the coarse β-AlFeSi phase platelets, which form during solidification of alloys containing Fe, are replaced by Chinese script α-$Al_{13}Fe(Cr,Fe)_4Si_4$ particles.

Effect of Sr alloying addition

Cao and Campbell carried out an investigation of the effect of Sr on the sedimentation of primary α-AlFeSi phase at superheating temperatures of 760 and 900°C (Cao *et al.*, 2004a). A convection free experimental technique was used to help quantify the primary α-AlFeSi particles sedimented at 600°C for 4 h. Sr marginally decreases the particle weight formed at a normal melting temperature (760°C), but greatly increases the particle weight at the superheating temperature of 900°C. Sr refines primary α-AlFeSi particles at both temperatures, causing an increase of the number of primary α-AlFeSi particles, especially when superheated at 900°C. In addition, Sr causes a decrease in the particle volume fraction but an increase in the number of the sedimented particles, and a great increase in the depth of the sediment in the mould at higher superheating temperatures. These observations are interpreted in terms of the precipitation of Fe-containing particles on suspended oxide films, and the rigidisation of suspended films at higher temperatures, possibly as a result of their change in chemistry, but especially as a result of inflation of their doubled-over form by hydrogen, and the effect this has on the multiplication of growing Fe-containing intermetallic compounds as a result of their mechanically unstable substrate.

Effect of Be alloying addition

Wang performed investigations on the effects of beryllium (Be) and solution temperature on the morphologies of iron intermetallics, silicon particles and copper intermetallics that relates to the mechanical properties of A319.0 alloys (Wang, 2000). The experimental results indicate that adding Be to the alloy can raise the Al-Al_2Cu eutectic melting temperature, change some platelet-like shape (β-Al_5FeSi) of iron intermetallics to comparatively less harmful Chinese-script morphologies (α-Al_8Fe_2Si), and reduce the amount and average length of β-Al_5FeSi platelets. The fracture behaviour of A319 alloy is affected by the morphologies of the iron intermetallics, silicon particles and copper intermetallics. Fractographic analysis of tested compact tension specimens reveals that the fracture processes are mainly initiated

by void nucleation at β-Al_5FeSi platelets as a result of their cracking and decohesion from the matrix. Adding Be to the A319.0 alloy and optimizing the solution temperature can significantly decrease the number of fracture-initiation sites of β-Al_5FeSi platelets and improve the tensile properties and fracture toughness. Wang and Xiong investigated the effects of beryllium in an Al-7Si-0.4Mg-0.2Ti cast alloy (Wang and Xiong, 2000). Their results showed that a beryllium addition changes the shape of Fe-containing intermetallic compound (named Be-Fe phase) from needle or plate shapes to Chinese scripts or polygons. It was also found that Be-Fe is formed during a peritectic reaction on titanium-rich particles located inside the α-Al. These lead to the higher mechanical properties of the alloy with a Be addition. In addition, an investigation in a similar alloy system by Murali et al. indicates that a Be addition also resulted in some grain refinement (Murali *et al*., 1995). They proposed that the Be-Fe phase particles may act as nuclei for aluminium thus leading to grain refinement. However, Be is considered as a most toxic metal element (Metals Handbook, 1990). Be-oxide and other compounds during melt and machining are harmful to people. Even at the low levels usually specified for A357.0 alloy, Be still leads to health hazards and thus requires use of costly and inconvenient protective measures. For this reason, the elimination of Be from alloys is highly desirable (Mbuya *et al*., 2003).

Other iron neutralizing/correcting elements

Other iron neutralizing/correcting elements have been identified and proposed, such as Co, Mo, Ni, and K, all of which change the iron intermetallic phase that forms, but none of these find any widespread use, partly because of cost and also because of health and safety issues (Ashtari *et al*., 2005; Taylor, 2004).

Physical methodology

Melt superheating treatment

The use of a high temperature melt heat treatment before casting favours the formation of the α-AlFeSi phase over the β-AlFeSi phase. Narayanan et al. investigated the crystallization behaviour of iron-containing intermetallic compounds in an industrial grade 319 aluminium alloy (Narayanan *et al.*,1994). In the absence of manganese, the iron compound crystallizes in the β-AlFeSi phase, at all cooling rates ranging from 0.1 Ks^{-1} to 20 Ks^{-1} under normal casting temperatures (750°C). However, when the melt is superheated to a high temperature (about 200 to 300°C above the liquidus temperature), the Fe-containing compound crystallizes in the α-AlFeSi phase at high cooling rates. This is due to the fact that γ-alumina, which forms at low melt temperatures (≤750°C), acts as a nucleus for crystallization of the β-AlFeSi phase. When the melt is superheated to a high temperature (≥850°C), the γ-alumina transforms to α-alumina. This is a poor nucleus for the crystallization of the β-AlFeSi phase, and as a result, the α-AlFeSi phase forms. Wang et al. performed microstructural observations on hypoeutectic Al-Si alloys with an iron content at 0.75wt% by mixing of a superheated melt at 840°C with a melt holding at 600°C. After this melt heat treatment, some Fe-containing intermetallic phases became globular and were identified as the β-AlFeSi phase (Al_9Fe_2Si) (Wang *et al.*, 2002).

Awano and Shimizu also studied the non-equilibrium crystallization of AlFeSi-type compounds in Al-Si casting alloys made from superheated melts. They reported that the morphology of the Fe containing phase changed from needles to Chinese script when the melt was superheated without using any iron correctors (Awano and Shimizu, 1990).

Effect of solid solution heat treatment

Some researchers carried out a solid solution treatment that causes to some extent either partial dissolution of the Fe-containing intermetallic phases or their transformation from one deleterious form to one which is less detrimental to mechanical properties. However,

previous studies also indicate that the changes in the dissolution of Fe-containing intermetallic compounds in Al-Si-Mg alloys may not be significant parameters that should influence the choice of solution times as far as mechanical properties are concerned. Therefore, the dissolution of the Fe-containing intermetallics as a result of longer solution times may not be an economically and commercially desirable approach (Mbuya *et al.*, 2003).

2.1.5 Kinetic aspects of the formation of Fe-containing intermetallics

In real solidification processes, kinetic factors are of extreme importance, on which both nucleation and growth of various phases precipitated are strongly dependent. Generally speaking, metallic phase, α-Al, grows more easily in its non-faceted manner than most intermetallic phases, which grow by stepwise nucleation on specific crystallographic planes (Backerud *et al.*, 1990). But there are also differences in growth rate between intermetallic crystals. The cubic α-AlFeSi phase grows more easily than the monoclinic β-AlFeSi phase. Therefore it is generally accepted that α-AlFeSi dominates at high cooling rates, provided the chemical composition of the alloy permits the formation of the former phase (Backerud *et al.*, 1990). Experimentally, depending on the cooling rates experienced, Backerud et al. have observed different morphologies of α-AlFeSi in the same alloy system, ranging from polyhedron, dendrites as primary phases to a Chinese-script form as in eutectics corresponding to the variations of cooling rate from $<0.1\ Ks^{-1}$ to $>0.5\ Ks^{-1}$ (Backerud *et al.*, 1990).

Miller et al. investigated the influence of oxides on the formation of Fe-containing intermetallics in an Al-11.6Si-0.37Mg alloy with 1.5wt.% Fe and 0.3wt.% Mn (Miller *et al.*, 2006). While calculation by Thermo-calc predicts the formation of primary α-AlFeSi prior to β-AlFeSi phase (equilibrium formation temperature around 630^{o}C, indicated by a black line in **Figure 2.5**), this event was not observed in their thermal analysis or in their

microstructural observations. The cooling rate for the thermal analysis was 1 Ks^{-1} just prior to the nucleation of the first solid. All these investigations demonstrate the strong dependence of the formation of Fe-containing intermetallics on kinetic factors of liquid alloys in given conditions.

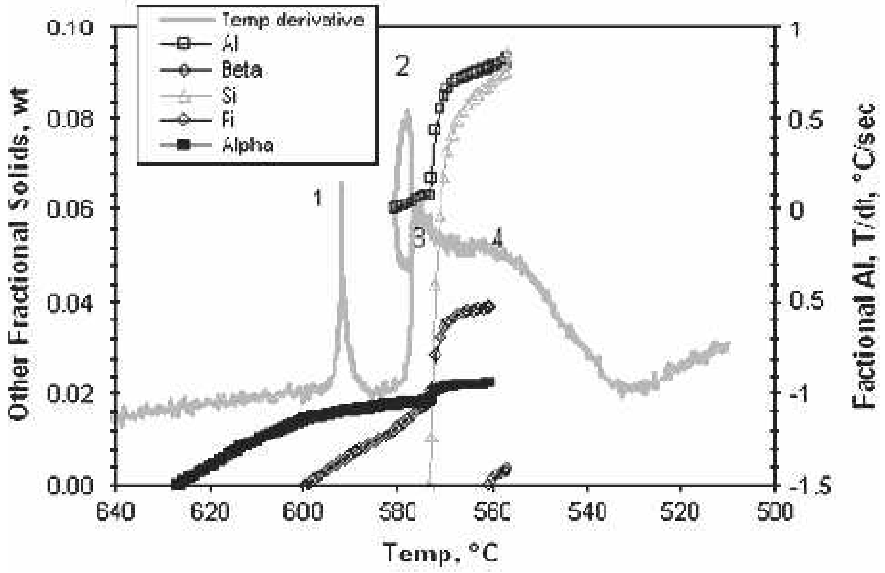

Figure 2.5 *Fractional solids in Al-11.6Si-0.37Mg-1.5Fe-0.3Mn Al alloy indicated by grey line (first derivative of the measured cooling curve): 1: β-AlFeSi; 2. Al+β-AlFeSi; 3. Ternary eutectic reaction: Al + Si + β-AlFeSi (α-AlFeSi); 4. Multi-phase eutectic reaction; and black line (calculated by Thermo-calc), indicating the thermodynamically favourable formation of the α-AlFeSi phase in the case of a lower level of Mn content (Miller et al., 2006).*

Rheo-die casting (RDC) is effective in modifying the morphology of the cubic α-AlFeMnSi compound and monoclinic β-AlFeSi, where the Melt conditioning by advanced shearing technology (MCAST) technique was adopted. Hence, intensive melt shearing improves the Fe tolerance of Al-Si based cast alloys (Fang *et al.*, 2007). However, the mechanism behind this transition from β- to α-AlFeSi phases is not clearly understood.

2.1.6 Effects of Fe-containing intermetallics on the castability

The concept of castability includes fluidity, feedability, volumetric shrinkage, casting porosity, hot tearing and die soldering (Seifeddine, 2007). Here, we focus on feedability, and the related volumetric shrinkage and casting porosity.

It has been suggested that the β-Al_5FeSi intermetallic phase is the primary cause of porosity formation as a result of an increased Fe content in Al-Si alloys. Two theories have been proposed to explain how this phase contributes to porosity formation. The "restricted feeding theory" suggests that β-AlFeSi platelets interfere with liquid feeding and significantly blocks the interdendritic path and hinders liquid flow (Dash and Makhlouf, 2001; Iwahori *et al*., 1988). The "pore nucleation theory" suggests that the β-AlFeSi platelets are active sites for pore nucleation (Roy *et al*., 1996). Both of these theories imply that porosity should increase monotonically with iron content. Taylor et al. investigated the correlation between iron content in the alloy composition and the formation of porosity in Al-Si-Cu based casting aluminium alloys (Taylor *et al*., 1999a, b and c). They identified that the formation of the β-AlFeSi phase actively participates in the nucleation of eutectic silicon. The iron and silicon content of the alloy determines at which point during the solidification sequence the β-AlFeSi precipitates and therefore, when it can participate in the silicon nucleation event. It is therefore, proposed that, at iron critical compositions where the maximum possible amount of ternary eutectic forms, the alloy solidifies with the most open and permeable dendritic network and possibly, with the most mobile interdendritic feeding ability. As a result, feeding is optimized at these compositions and the lowest contents of porosity achieved (Taylor *et al*., 1999c).

2.2 Oxides in the melt of Al alloys

Due to the high affinity of aluminium for oxygen, oxides readily form on the surface of liquid/solid aluminium when it is exposed to an atmosphere containing oxygen (Impey *et al*., 1988). Oxide inclusions can appear at the beginning of melting since they arrive as oxide skins on the surface of the charged material. When remelted in a furnace, surface oxides therefore become suspended in the melt. Also oxide inclusions can be present in the casting if they were formed during preparation of the melt, transferring, or mould filling. Finally oxides are found as massive, film-like, or dross-like inclusions in finished castings (Campbell, 2003). In a real situation, it becomes much more complex due to the nature of multicomponent compositions in an actual Al alloy system. Occurrence of oxides in the melt of aluminium alloys not only results in the metal loss during the melting process prior to solidification, for example, for aluminium alloys, a metal loss of 2% is typical, whereas for certain Al-Mg alloys values may be higher than 10% (Impey *et al*., 1988), but also degrades the quality of melt cleanness and hence deteriorates the properties as a consequence of the formation of inclusions in final products (Green and Campbell, 1993). Therefore, understanding and controlling the formation of oxides in the melt of aluminium alloys are crucial to the development of Al-based alloys and solidification processing. In the current study, it is more important to explore the feasibility of enhanced heterogeneous nucleation by controlling and harnessing oxides.

2.2.1 Principle oxides formed in Al alloys

γ-Al_2O_3 and other metastable transition aluminas

When aluminium is melted, a thin protective amorphous film forms on all surfaces exposed to an atmosphere containing oxygen and/or water moisture through the following reactions (Impey *et al*., 1988):

$$2Al+3/2O_2=Al_2O_3 \quad (2.1)$$

$$2Al+3H_2O=Al_2O_3+3H_2 \quad (2.2)$$

This thin film is fairly impermeable to the diffusion of the metal and oxygen, so can prevent the occurrence of further oxidation. The reason why this film can protect the liquid metal from further oxidation is ascribed to its amorphous nature where it is difficult for diffusing species to find the preferred diffusion paths such as grain boundaries (Cao and Campbell, 2005). However, this amorphous film is thermodynamically unstable when compared to its crystalline counterpart and will transform by means of nucleation and growth if given time and opportunity (Men and Fan, 2010). This crystalline form may be γ-Al_2O_3 or η-Al_2O_3 or others depending on both alloying elements in the melt and the given dynamic conditions which will be discussed in the following sections. The γ-Al_2O_3 forms in a relatively low temperature regime where diffusion rates are quite slow. So the transformation of amorphous to crystalline alumina occurs readily at the melt/oxide interface (Wefers and Misra, 1987). And continuous supplies of metal arriving at this interface is not through diffusion, which is slow, but by the flow of the liquid along capillary channels, which is, much faster (Campbell, 2003).

After an incubation time of 5-10 minutes at 750^{o}C, the amorphous film may transform to a crystalline form of γ-Al_2O_3 or η-Al_2O_3 film (Haginoya and Fukusako, 1983; Impey *et al.*, 1991). The transformation of amorphous to crystalline alumina nucleates and grows rapidly at the melt/oxide surface. It was reported that, after a crystalline γ-Al_2O_3 or η-Al_2O_3 film were formed, they would be subjected to further transformation to an α-Al_2O_3 crystalline form (also termed corundum) with time and temperature. The crystallization to α-Al_2O_3, however, has been reported to be achieved at a temperature of 750^{o}C after an incubation time of about 5 h in commercial purity aluminium (Al-0.15Fe-0.08Si, wt-%) (Impey *et al.*, 1988). With an

extension of holding time or increasing the melt temperature, prior to transformation to α-Al_2O_3, a series of metastable, highly porous oxide phases could be formed (**Table 2.2**) (Levin and Brandon, 1998).

Table 2.2 *Variants of metastable Al_2O_3 structures based on fcc packing of oxygen anions and orientation relationship with γ-Al_2O_3 (Levin and Brandon, 1998).*

Phase	Crystal structure	Lattice parameters	Space group	Cations/unit cell	Orientation relationship with respect to γ-Al_2O_3
γ-Al_2O_3	Cubic	$a_\gamma \approx 7.9$Å	$Fd\bar{3}$m	64/3	-
η-Al_2O_3	Cubic				N/A
δ-Al_2O_3	Tetragonal/orthorhombic	$a \approx a_\gamma$, $b \approx 2a_\gamma$, $c \approx 1.5a_\gamma$	$P2_12_12_1$	64	$(100)_\delta // (100)_\gamma$ $[100]_\delta // [001]_\gamma$
θ-Al_2O_3	Monoclinic	$a \approx 1.5a_\gamma$, $b = a_\gamma\sqrt{2}/4$, $c = a_\gamma\sqrt{2}/2$, $\beta = 104^o$	$C2/m$	8	$(100)_\theta // (001)_\gamma$ $[010]_\theta // [110]_\gamma$

<u>α-Al_2O_3</u>

The thermodynamically stable α-Al_2O_3 structure possesses trigonal symmetry with rhombohedral centring (space group R$\bar{3}$c). The unit cell of α-Al_2O_3 contains 10 ions (6 O^{2-} and 4 Al^{3+}) per unit cell. The oxygen anions in this structure are approximately in hcp packing and the Al cations are located in octahedrally coordinated interstitial sites in the anion sublattice (Yang *et al*., 1998; Wefers and Misra, 1987).

The transformation from γ-Al_2O_3 to α-Al_2O_3 was thought to be quite sluggish in nature (Wefers and Misra, 1987; Narayanan *et al*., 1994). The reported time and temperature for the occurrence of this transformation in published works are quite different due to their different

alloy systems and oxidation conditions. Total conversion from γ-Al_2O_3 to α-Al_2O_3 occurs on heating above 1200^oC for more than one hour (Wefers and Misra, 1987). However, in an industrial grade 319 (Al-6Si-3Cu) alloy, the crystallisation of α-Al_2O_3 was reported to occur at 850^oC and was proposed to be related to the higher content of impurity elements in their alloy (Narayanan *et al*., 1994). Bergsmark et al. investigated the oxidation behaviour of commercial purity aluminum in oxygen at different partial pressures in the temperature range of 800-950^oC and demonstrated that α-Al_2O_3 formed above 850^oC. In their study, specimens prepared at temperatures above 850^oC only revealed diffraction lines from the α-Al_2O_3 phase when powdered scales were subjected to X-ray diffraction analysis (Bergsmark *et al*., 1989). In Impey et al.'s study, a trace of α-Al_2O_3 was identified even at the early stages of melting in commercial purity aluminium at 750^oC (Impey *et al*., 1988). In fact, the exact temperature, extent and transforamation rate depend on a variety of factors such as holding time, environmental atomosphere (including oxygen partial pressure, moisture content, etc.), stirring and melt composition especially the content of active elements in alloys. For example, Narayanan et al. suggest that the presence of magnesium in Al-Si-Cu alloys strongly stabilises the γ-Al_2O_3 oxide, since γ-Al_2O_3 is isomorphous with $MgAl_2O_4$ spinel, and thus increases the transformation temperature from γ-Al_2O_3 to α-Al_2O_3 (Narayanan *et al*., 1994).

Transformation from transition aluminas to stable α-alumina

It is widely accepted that the transformation from γ-→α-Al_2O_3 is very sluggish and several transition aluminas form prior to the transformation to stable α-Al_2O_3 (Wefers and Misra, 1987; Levin and Brandon, 1998). A number of investigations have been focused on the influence of alloying elements on the oxidation dynamics in aluminium alloy melts as will be reviewed later. It is generally accepted that the transformation of γ-→α-Al_2O_3 is a nucleation and growth process (Dynys and Halloran, 1982). However, there are very limited reports

concerning the direct transformation from γ-→α-Al_2O_3 except the one by Chou and Nieh (Chou and Nieh, 1991). Chou and Nieh have reported the nucleation of polycrystalline α-Al_2O_3 from a highly textured γ-Al_2O_3 matrix in reactive, radio-frequency sputter-deposited, nanocrystalline Al_2O_3 thin films. In the films annealed at 1200^{o}C for 2 h, nucleation and concurrent anomalous grain growth of α-Al_2O_3 are observed in the fine-grained, polycrystalline alumina γ-Al_2O_3 matrix (Chou and Nieh, 1991). However, this has been doubted by Levin and Brandon based on the experimental observation of the electron diffraction patterns that the authors have ascribed to polycrystalline γ-Al_2O_3 in a <001> orientation clearly showing the superlattice diffraction spots characteristic of a tripled spinel unit cell, so the layered structure observed by Chou and Nieh most likely results from either θ or δ phases (Levin and Brandon, 1998). Although there are reports for the direct γ-→α-Al_2O_3 transformation during sintering under a high pressure, no specific experimental evidence has been presented to support the direct transformation of γ-→α-Al_2O_3 at atmospheric pressure (Levin and Brandon, 1998). Moreover, it remains unclear whether γ- transforms directly to α-Al_2O_3 on heating at atmospheric pressure or whether there are intermediate phases in a transformation sequence (Levin and Brandon, 1998).

All studies have reported an α-Al_2O_3 grain size at least an order of magnitude larger than that of the parent transition Al_2O_3 and no α-Al_2O_3 nuclei have been noted, suggesting that the growth of α-Al_2O_3 into a transition Al_2O_3 matrix is “explosive”. This means α-Al_2O_3 would grow quickly once a critical nucleus size is formed (Levin and Brandon, 1998). And this implies that the transformation from transition aluminas to α-Al_2O_3 is a nucleation-controlled process (Yang *et al.*, 1998).

From a crystallographic point-of-view, the transition of η- or γ- to θ-alumina is not a reconstructive recrystallization process, but a displacive one in which the ordering of the tetrahedral Al sublattice mainly causes the spinel symmetry to collapse so that the structure,

which exhibits a tetragonal characteristic at the early stage of the transition, settles into a monoclinic θ-alumina at a later stage (Zhou and Snyder, 1991). Although there is no published experimental evidence to support the direct transformation from fcc-based transition aluminas to α-Al_2O_3, it is widely accepted to be a nucleation and growth process, and some attempts have been made to investigate the influence of kinetic conditions on the transformation from transition aluminas to the stable α-Al_2O_3. It was reported that mechanical treatments of γ- alumina markedly increase the density of nuclei and hence the transformation rate (Dynys and Halloran, 1982). Shelleman and Messing studied the effect of enhancing diffusion in the γ- to α- alumina transformation by adding V_2O_5 to both seeded and unseeded γ-alumina. The solubility of alumina in V_2O_5, which melts at 673^{o}C, allowed the rapid transport of aluminium and oxygen ions. The V_2O_5 lowered the α-alumina transformation temperature, as measured by DTA, of the unseeded gel by 25^{o}C. Seeding reduced the transformation temperature by 83^{o}C. The combined effect of enhanced nucleation and diffusion lowered the transformation temperature by 205^{o}C. The transformation to 100% α-alumina occurred in ~30 minutes at 875^{o}C (Shelleman and Messing, 1988; Bagwell and Messing, 1999). Seeding of a transition alumina with α-Al_2O_3 particles also accelerates the transformation kinetics and it has been claimed that both seed concentration and seed size are critical for the successful control of the transformation (Kumagai and Messing, 1985). All the results mentioned above demonstrate the possibility of an accelerated γ- to α-alumina transformation by various enhanced nucleation and diffusion mechanisms.

MgO (Magnesia) and MgO. Al_2O_3 (Spinel)

Magnesium is an important alloying element in aluminium alloys, such as in AA5000 and AA7000 wrought aluminium alloys, where the magnesium content can be up to 7wt.% (Eskin, 2008). When Al alloys contain magnesium, the oxidizing tendency of the liquid aluminium increases sharply with magnesium content because magnesium is surface active in

liquid aluminium (Impey *et al*., 1988). When the magnesium content exceeds approximately 2%, the melt oxidizes rapidly to form magnesium oxide (termed magnesia, MgO). At intermediate magnesium levels which lie between 0.005 and 2%, a mixed oxide $MgO.Al_2O_3$ (spinel) is formed. As the majority of aluminium alloys have some magnesium in the intermediate compositional range (between 0.005 and 2%), a spinel film is usually to be expected. Depending on the magnesium content in aluminium alloys, the oxidation reaction path possibly starts with the formation of amorphous MgO, or $MgAl_2O_4$, or Al_2O_3, which then transforms to crystalline MgO, or $MgAl_2O_4$, or γ-Al_2O_3 films, respectively. As a result of the volume change, the oxide film is subject to the build-up of considerable local stress and is, therefore, inclined to deform or crack. The Pilling-Bedworth ratio (PBR) was developed to describe the volume change caused by the formation of oxides during oxidation of metals (Pilling and Bedworth, 1923), which is the ratio of oxide volume produced to metal volume consumed, (Xu and Gao, 2000; Ha and Kim, 2006). MgO with a PBR of 0.73 does not form a continuous protective layer on the surface of a liquid aluminium alloy, and hence both out-diffusion of magnesium to the top and in-diffusion of oxygen to the inner of the liquid alloy persist (Ha and Kim, 2006; Murthy and Rao, 1995). Therefore the presence of magnesium in Al alloy melts always results in breakaway oxidation.

Due to breakaway oxidation, the main oxides formed on the melt surface may be quite different when other kinetic factors are taken into account such as the melt temperature, holding time and turbulence on the melt surface. Haginoya and Fukusako studied the oxidation behaviour of molten Al-Mg (2-12%) alloys at varying temperatures ranging from 650^{o}C (923K) to 900^{o}C (1173K) for 3h in dry air (Haginoya and Fukusako, 1983). It was identified by quantitative X-ray diffraction analysis that MgO was produced in an early stage of oxidation, and its amount increased temporarily and then decreased gradually. $MgAl_2O_4$ increased gradually in amount with the decreasing amount of MgO. The oxidation reactions

can be described by two consecutive equations, $Mg + 1/2O_2 \rightarrow MgO$ followed by $MgO + 2Al + 3/2O_2 \rightarrow MgAl_2O_4$ (Haginoya and Fukusako, 1983). This reaction mechanism agrees with the formation free energy tabulated in **Table 2.3**.

Table 2.3 *Reactions and the Gibbs' energies for the formation of MgO and $MgAl_2O_4$ (Haginoya and Fukusako, 1983).*

Reaction	ΔG (kJ)		
	923 K	1023 K	1123 K
(1) $Mg + ½ O_2 = MgO$	-28.9	-28.3	-27.7
(2) $Mg + 2Al + 2O_2 = MgAl_2O_4$	-108.6	-106.1	-106.0
(3) $MgO + 2Al + 3/2 O_2 = MgAl_2O_4$	-79.7	-77.7	-76.0
(4) $MgO + Al_2O_3 = MgAl_2O_4$	-0.574 (at 803 K)		

McLeod and Gabryel investigated the growth of a spinel in Al-Mg alloys containing alumina particulate reinforcement (McLeod and Gabryel, 1992). On Al_2O_3, MgO and $MgAl_2O_4$ form according to the following reactions:

$$3Mg + Al_2O_3 = 2Al + 3MgO \quad (2.3)$$

$$3Mg + 4\ Al_2O_3 = 2Al + 3\ MgAl_2O_4 \quad (2.4)$$

Using free energy of formation data from the JANAF tables (3rd edition) and activity coefficient data for the Al/Mg binary (Murray, 1982), the magnesium concentration in equilibrium with the above reactions for liquid alloys can be calculated. The result is shown as a stability diagram in **Figure 2.6**.

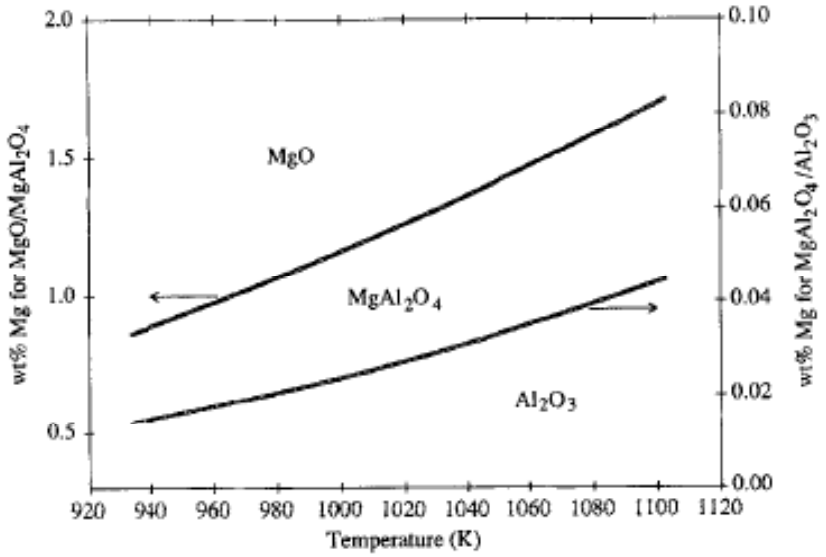

Figure 2.6 *Thermodynamic stability of Al-Mg oxides in Al-Mg alloys containing alumina particulates (McLeod and Gabryel, 1992).*

It is not surprising to find that Al_2O_3 is not stable in aluminium alloys that contain certain levels of magnesium (McLeod and Gabryel, 1992). According to **Figure 2.6**, a low concentration of 0.02 wt.% magnesium in the melt can destabilize the Al_2O_3 to form the $MgAl_2O_4$ spinel, and a higher magnesium content (>1.2 wt.%) give MgO at 1000K. However, due to the following reaction (Pai *et al.*,1995),

$$MgO+Al_2O_3 \rightarrow MgAl_2O_4 \ (\Delta G_{1000K}=-47 kJmol^{-1}) \qquad (2.5)$$

$MgAl_2O_4$ is thermodynamically more stable than MgO and therefore, $MgAl_2O_4$ would be the resultant oxide product if given enough oxidation time.

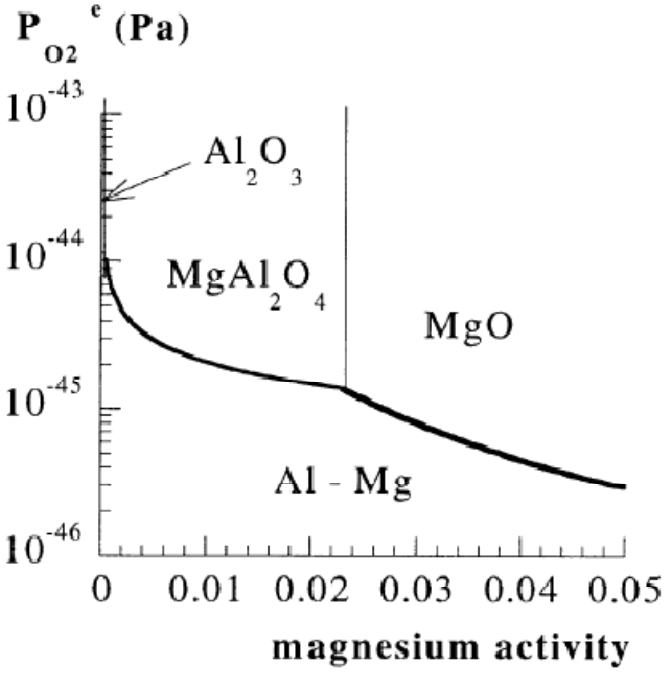

Figure 2.7 *Thermodynamic stability of MgO, $MgAl_2O_4$ and Al_2O_3 phases: Oxygen pressure at equilibrium versus magnesium activity at 700°C (Surla et al., 2001).*

This study on the thermodynamic stability of Al-Mg oxides in Al-Mg alloys containing alumina particulates has been referenced in comprehensive aluminium alloy systems containing magnesium (Murthy and Rao, 1995; Contreras *et al.*, 2004; LIoyd, 1994; Shen *et al.*, 2010). However, it is worth noting the calculation performed by McLeod and Gabryel is based on Al-Mg alloys containing alumina reinforcement. In contrast, Surla et al. carried out a thermodynamical calculation based on the Al-Mg-O_2 system at 700°C (Surla *et al.*, 2001). In this system, three reactions can occur:

$$2Mg + O_2 = 2MgO \quad (2.6)$$

$$Mg + 2Al + 2O_2 = MgAl_2O_4 \quad (2.7)$$

$$2Al + 3/2O_2 = Al_2O_3 \quad (2.8)$$

The calculated results are presented in **Figure 2.7**, with the oxygen pressure versus magnesium activity. **Figure 2.7** indicates that MgO is thermodynamically stable as long as the residual magnesium activity in the alloy is higher than 0.023. This corresponds to a magnesium content of 2.43wt.% in the alloy. Below this limit, $MgAl_2O_4$ appears.

Other oxides in aluminium alloys

CaO, SrO_2, Li_2O_3 could be found in aluminium alloys under some circumstances, which comply with the Ellingham diagram for several oxides, as shown in **Figure 2.8** (Gaskell, 1996). Raiszadeh and Griffiths developed a method to study the history of a double oxide film defect in liquid aluminium alloys (Raiszadeh and Griffiths, 2006). Individually added 0.05wt% Ca and Sr to pure aluminium produced CaO and SrO_2 in the resulted surface oxide layer detected by EDX analysis.

2.2.2 Factors influencing the formation of oxides in Al alloys

Alloying effect

Different alloying elements have different effects on the strength and the oxidation reaction rate of oxide films, depending on their contribution to the density of the oxide film layer, or their influence on the mobility of ionic transport in the oxide (Thiele, 1962). Moore et al. studied the oxidation behaviour in 5182 alloy (about 5% magnesium with other minor alloying constituents including manganese and iron) using X-ray diffraction technique that was heated to 750^{o}C and oxidized with pure O_2 (Moore *et al*.,). The predominant oxide phase was identified as MgO in their case. It was pointed out that during oxidation, the magnesium was drawn to the surface as a result of the chemical potential, forming an oxide such as MgO or the $MgAl_2O_4$ spinel. These oxides can change composition during further oxide growth, depending on the other alloying components and the oxidizing conditions. As growth continued to the micrometre scale, the phases became well defined and less prone to further

change, as the solid-state diffusion in the existing oxide layer became slow relative to the transport of the oxidizing gas (O_2 or H_2O) and cation transport from the bulk.

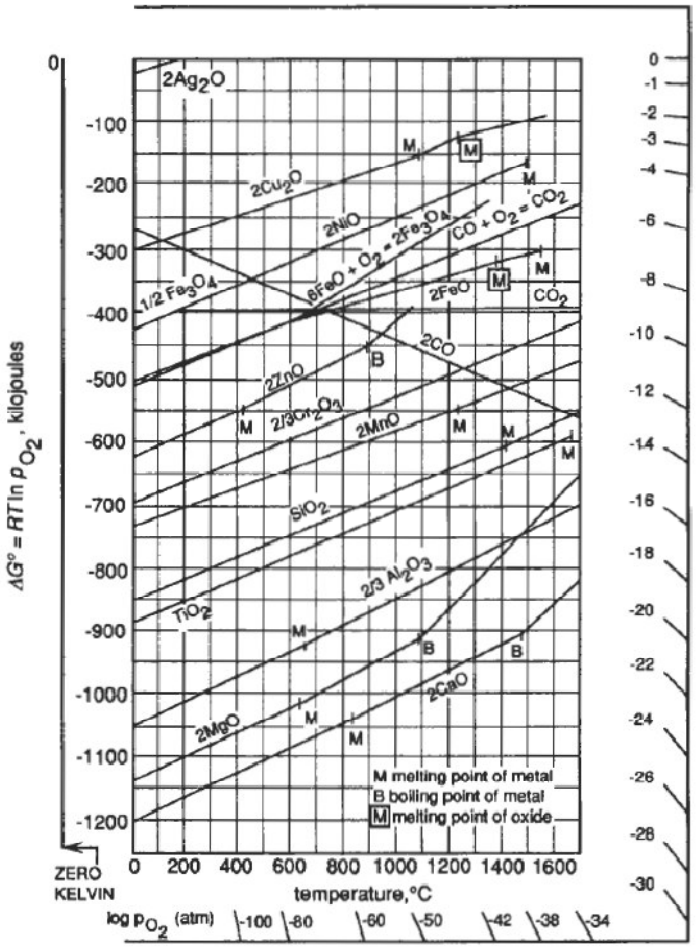

Figure 2.8 *The Ellingham diagram for several oxides* (Gaskell, 1996).

Interestingly, the presence of inclusions (as determined by sample origin and microscopy) had a more dramatic effect on the onset of oxidation and the ultimate oxide growth rate than did the composition of the alloy or the oxidizing atmosphere, although each of these factors had a significant influence.

Under normal melting conditions, the oxidation of pure aluminium at a usual melting temperature such as ~100°C above its melting point is a sluggish process, in particular, in the absence of any turbulence on the melt surface. With the presence of magnesium in alloy composition, the oxidation kinetics will be accelerated significantly because of the formation of MgO and/or $MgAl_2O_4$ (Thiele, 1962; Cochran *et al*., 1977), both of which promote the occurrence of breakaway oxidation. With an increase of the magnesium content in Al-Mg binary alloys, oxidation kinetics can be accelerated further, as presented in **Figure 2.9** (Contreras *et al*., 2004), where oxidation occurred at 900°C in Al-Mg alloys with a magnesium concentration in the range of 1-20wt.%.

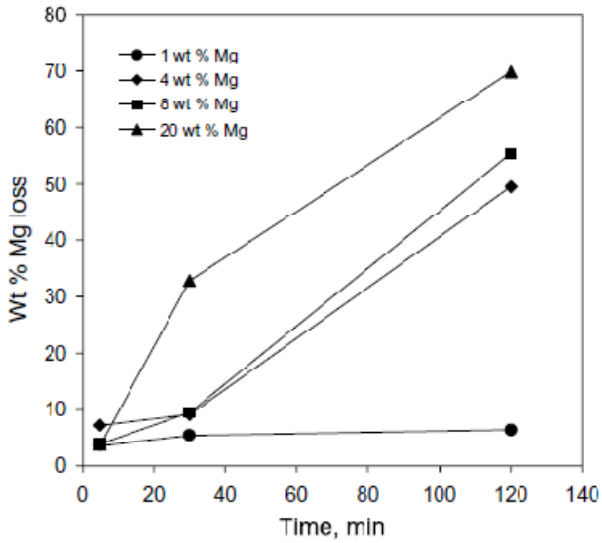

Figure 2.9 *Magnesium loss vs. time for different Al-Mg alloys oxidized at 900°C (Contreras et al., 2004).*

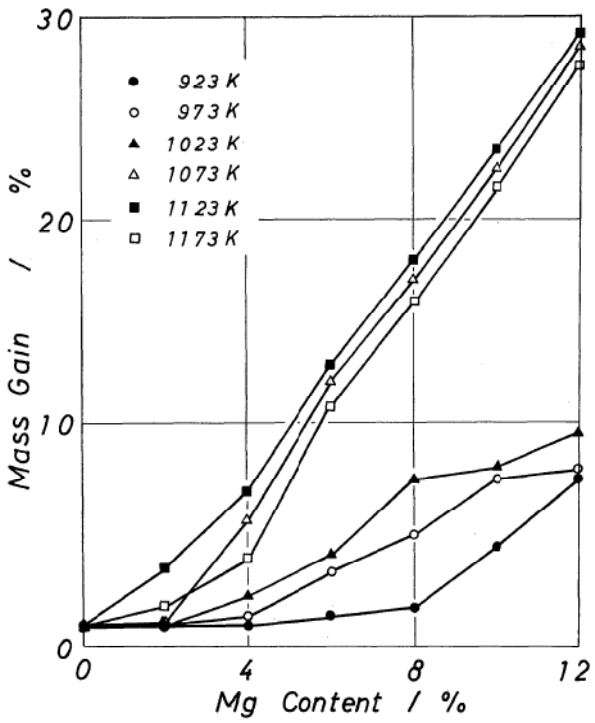

Figure 2.10 *Mass gain of Al-Mg alloys oxidized in air for 3h at various temperatures, related to the magnesium content (Haginoya and Fukusako, 1983).*

Haginoya and Fukusako's work demonstrate the dependence of oxidation dynamics on the temperature of the Al-Mg alloys in air for 3 h (**Figure 2.10**) (Haginoya and Fukusako, 1983). When the alloys were oxidised at temperatures lower than 1023 K, the mass gain of the alloys with Mg content are moderately increased. However, when the alloys were oxidised at temperatures higher than 1023 K, the curves are straightly increased with steep gradients. This implies there may be a transition of oxidation mechanisms. With an extension of the oxidation time (holding at the melting temperature) or an increase in the magnesium content in Al-Mg alloys, more MgO will be transformed to $MgAl_2O_4$, which is thermodynamically favourable (Haginoya and Fukusako, 1983).

$$MgO+2Al+3/2O_2 \rightarrow MgAl_2O_4 \ (\Delta G_{700^oC}=-78.7kJ) \qquad (2.9)$$

So the higher the magnesium content in Al-Mg alloys, the more $MgAl_2O_4$ can be expected to form in an alloy melt.

In addition to the influence of magnesium alloying additions on the formation of oxide scale on aluminium alloys, Si, Fe, Mn, Zn, Cu, Li, Na, Sr, Ca, P, and Be etc., are also very common alloying elements in aluminium alloys and to some extent, have an effect on the formation of oxides.

Basically, the Ellingham diagram (**Figure 2.8**) provides an essential approach to compare the stability of the oxides formed by alloying additions. The influence of alloying additions on the formation of oxides in an aluminium alloy melt can operate by means of both thermodynamic and kinetic aspects, i.e. the types of oxide formed and the wetting between the liquid aluminium alloy and the oxide formed and therefore the rate of breakaway oxidation. Cu, Fe, Si, Mn have a minimal effect on the oxidation of molten aluminium, whereas Mg, Li, Na, and Ca enhance the rate of oxidation (Thiele, 1962; Bergsmark *et al*., 1989; Agema and Fray, 1989).

Zn is one of the very important alloying elements in AA7000 series Al alloys. Zn is also surface active to form oxides with oxygen when the aluminium alloy melts are exposed to air. The well known oxides of Zn include ZnO and $ZnAl_2O_4$ in Al alloys. The latter one has the same crystalline structure as that of the $MgAl_2O_4$ spinel.

Ca is one of surface active elements although it is not a commonly added alloying element in Al alloys. Based on the data of the formation free energy, it is possible to form CaO in an Al alloy melt. Enrichment of calcium has also been detected at the outer oxide scale surface and it is believed that calcium can influence the oxidation kinetics through promotion of breakaway oxidation similar to magnesium (Bergsmark *et al*., 1989).

Small additions of Be were found especially effective in reducing the oxidation of Mg-containing Al alloys by forming a protective BeO film on the surface of the alloy melt (Cochran *et al*., 1977). Due to its toxic nature, however, considerable effort has been made to find an alternative. Strontium (Sr) is a well-known trace alloying element and widely used as a modifier for cast Al-Si alloys to change the morphology of eutectic silicon from acicular to fibrous. In a more recent investigation, ppm levels of Sr additions to Al-Mg (magnesium content in a range from 0.5 to 5%), have resulted in a very significant decrease (98%) of total mass gain in the low magnesium containing Al-Mg alloys. This change in oxidation behaviour was linked to the presence of Sr enrichment of the liquid beneath the initial MgO layer suppressing the formation of the spinel phase (Ozdemir *et al*., 2009).

2.2.3 Kinetics of oxidation occurring at the surface of liquid aluminium

Initial slow oxidation

Oxidation naturally occurring in a molten aluminium alloy includes the following stages: chemically active species react with oxygen, transformation between different variants of oxides and growth of oxides. It has been established that the initially formed oxides are in the form of an amorphous phase. After a time-induction period, transformation from the amorphous to a crystalline oxide occurs. Under some circumstances, the transformation between some transition oxides (e.g. η-, γ-, δ-,θ-Al_2O_3) takes place during this induction period, for instance, in the case without a significant magnesium addition in the alloy of interest. The duration of the induction period depends on kinetic conditions in the alloy melt. In effect, this period is related to the occurrence of breakaway oxidation. It has been established that a high melting temperature, the seeding of crystalline oxide and melt stirring etc., all have a significant influence on the induction period. The complexity of this induction period has been indicated by different shapes on the plot of oxidation mass gain against oxidation time which cannot be described in terms of simple rate equations (linear, parabolic,

etc.) (Cochran *et al*., 1977; Bergsmark *et al*., 1989). The slow growth of the thin, initially formed alumina is in all probability governed by diffusional transport. By assuming that the initial oxidation follows approximate parabolic kinetics, the experimentally observed values of the parabolic rate constants are of the order of 10^{-11} to 10^{-12} cm^2s^{-1}. By extrapolating the value of self-diffusion of oxygen and aluminium in α-alumina above 1200°C (which are the only available data), the self-diffusion coefficients of aluminium and oxygen at the oxidation temperatures (800-950°C) have values of 10^{-22} to 10^{-19} cm^2s^{-1} and 10^{-19} to 10^{-18} cm^2s^{-1}, respectively. Thus the experimental oxidation rate constants are about 10^7-10^{10} times larger than the self-diffusion coefficients of aluminium and oxygen in α-alumina. This large difference suggests that the diffusional transport takes place by grain boundary diffusion or other easy diffusion paths (Bergsmark *et al*., 1989).

Breakaway oxidation

Generally speaking, pure aluminium and commercial aluminium alloys, nominally free of magnesium, oxidize slowly at normal melt processing temperatures, if undisturbed, because a protective aluminium oxide film forms. In contrast, Al-Mg melts under the same conditions can oxidize much more rapidly with the formation of magnesium oxide and magnesium aluminate films (Cochran *et al*., 1977). In order to decrease the oxidation rate occurring on the surface of a liquid aluminium alloy, attempts should be made to delay the occurrence of breakaway oxidation, in other words, extend the induction period because of an accompanied sudden increase in oxidation rate. Cochran et al. systematically investigated the effects of melt temperature, alloy composition (with a focus on the magnesium content), seeding conditions (with the addition of oxides to the alloy melt) and atmospheric composition on the oxidation kinetics (Cochran *et al*., 1977). It has been demonstrated that the induction period is shortened by (1) increasing the melt temperature or Mg content; (2) adding crystalline magnesium oxide or magnesium aluminate seeds from previous oxidation products if these

oxides can be well wetted by liquid alloys. In addition, trace additions of Na, Be to Al-Mg alloys can significantly decrease the oxidation rate. As little as 0.001 wt. % Be inhibited the oxidation of Al-3.5wt.%Mg alloy for at least 46 h at 800^{o}C, whereas without the Be breakaway oxidation started shortly after melting. Similarly, in a Al-0.7wt.%Mg alloy at 725^{o}C, the time for oxidation to completely exhaust the magnesium increased from 8-12 h at 0.0002 wt.% Na to 24 h at 0.0006 wt.% Na to 42 h at 0.009 wt.% Na and 72 h at 0.003 wt.% Na (Cochran *et al*., 1977). Dusting powdered B onto the surface of the melts containing 4.5wt. % Mg also decreased the oxidation. It is proposed that the atomic size may be an important factor governing the inhibiting action because B, Be and Na, all are among the smallest solid elements in the periodic table. This small atomic size may facilitate the diffusion of the additive throughout the surface during oxidation, so its oxide will be finely dispersed to inhibit crystallization of the magnesium aluminate. However, unlike Na or Be, B does not preferentially oxidize from the alloy to concentrate in the surface film. Thus, B would be effective only when added to the melt surface (Cochran *et al*., 1977).

2.2.4 Thermal history and the formation of different morphological types of oxides in Al alloys-young film, old film and bifilm

The surface oxide film on an aluminium alloy melt acts as a protector from either further oxidation or diffusion of gas into the underlying metal. The problem concerning the mechanical properties in a finished component related to a surface oxide film mainly occurs when it becomes a submerged film.

Oxide films exhibit a variety of appearances because of their different chemical compositions, thicknesses, strengths and interactions with the melts. Campbell describes the morphology of oxide films as young and old oxide films to differentiate the behaviours of oxide films according to their different thicknesses (Campbell, 2003). Young films are characterized by their very thin thickness, some hundreds of nanometres in thickness. Young

oxide films are formed during pouring or mould filling since this process normally takes several seconds to tens of seconds (Campbell, 2003). Given time, young oxide films will thicken and turn into old oxide films. The thickness of old oxide films varies greatly, and has been estimated to be from several micrometres to a millimetre (Campbell, 2003).

During pouring or stirring of the melt, the surface film may be broken or folded over with a dry side lying against the other dry side. These folded films will trap gas between them and then entrain this into the bulk of the melt. Clearly, the side of the film which grew on the liquid surface is wetted by the melt, whereas the opposite side is presented to air. After solidification, these folded oxide films will act as cracks in the final casting known as a double oxide film defects (Cao and Campbell, 2000). It is commonly the case that cast aluminium alloys readily contain oxide films. The entrainment of surface oxide films into the bulk of the melt occurs for a number of reasons as follows: surface turbulence, pouring, surface flooding and bubble trail (Campbell, 2003).

According to Cao and Campbell, oxides display different SEM energy dispersive X-ray spectral characteristics. Young oxide films, usually form during pouring and exhibit a low oxygen peak because of the short period of formation and extreme thinness, while old thick oxides form prior to pouring display significantly higher oxygen peaks (Cao and Campbell, 2005). The studies by Green and Campbell suggest that observation of fracture surfaces containing oxide films is one of the feasible methods to study the features of oxides. And they suggest that two types of oxide films, young and old ones, can be identified by the different dimensions of the wrinkles and folds which, in turn, are controlled by the thickness of the films indicating their formation at different stages (Green and Campbell, 1994).

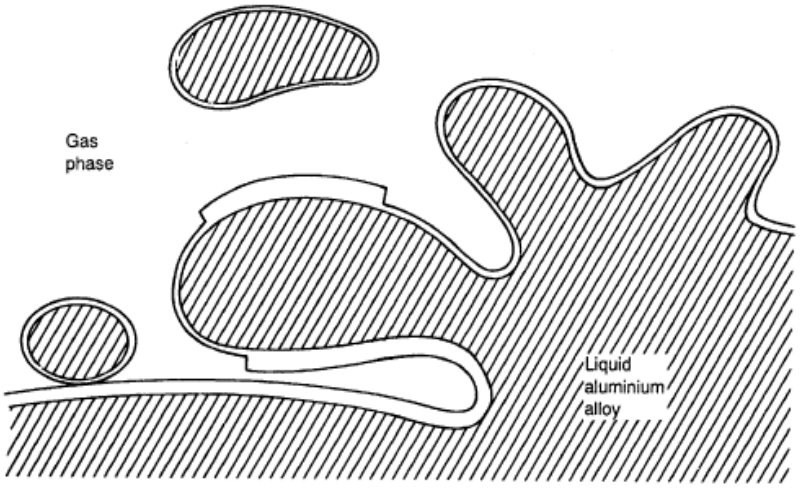

Figure 2.11 *Formation of folded double oxide films (Campbell, 2003).*

Based on the SEM observation in fracture surfaces of Al-11.29Si-0.38Mg-0.70Fe-0.59Mn sand castings, the thickness of a young oxide film was estimated to be less than one micrometre (Cao and Campbell, 2005). In another independent study, the thickness of an oxide film formed in an Al-Mg alloy melt during the initial stage (10 s) of oxidation is known to be approximately 20nm (Green and Campbell, 1993). These young oxide films are often entrained due to the surface turbulence created during pouring (Campbell, 2003). Compared to young oxide films, old oxide films have a varied thickness, ranging from several micrometres up to millimetres. It was reported that the thickness of an oxide film formed on an Al melt held for approximately 60 minutes is of the order of tens of micrometres (Thiele, 1962). Although usually extremely thin, oxide films present in Al melts often have an extensive area, varying in linear size from several micrometres to centimetres (Cao and Campbell, 2005). The doubled over oxide film (bifilm) reflects the nature of the entrained surface oxides as cracks in a liquid metal (**Figure 2.11**).

The entrainment action is a simple folding action and necessarily brings the two upper dry surfaces of the oxide into contact thus creating an unbonded inner interface. The dry sides of bifilm naturally become very effective barriers for metal elements to diffuse in the melt as a result of the air gap entrained between the layers of the oxide. The outer surfaces of the folded film are fully wetted by the melt. The term "wetted" here refers to the perfect atomic contact between the oxide and the liquid from which it has grown. The gaseous gap between the two dry sides of the doubled over film constitutes a crack in the liquid and may be frozen into castings which constitutes a crack defect in the final casting component. On a 2-D metallurgical section, a bifilm appears to be either a linear or entangled network of cracks (Cao and Campbell, 2005).

2.2.5 Deformation ability of oxides formed in the melt of Al alloys

Under the compressive or deformational strains which occur naturally during the disturbance of the surface of the melt, wrinkles or folds are formed on the oxide film. Most of the deformation in oxide films is found to take place in the regions with a relatively fresh oxide film which has some deformability due to its thinness and consequent flexibility (Agema and Fray, 1989). It was reported that although the strength of the film increased with increasing oxidation time and temperature, the film became extremely brittle. Therefore, cracks and ruptures are readily observed in the old oxide films indicating their poor strength. This may be one of the reasons why, on a microscale, the surfaces of oxide films appear to be porous and have some degree of roughness (Cao and Campbell, 2005).

The porous feature of α-Al_2O_3 films can also be related to the development of stresses inside the films due to a change of volume. For example, the transformation from γ-Al_2O_3 to α-Al_2O_3 crystals is accompanied by a 24% decrease in volume causing considerable tensile stresses which result in the fracture of the oxides (Impey *et al.*, 1988). The development of a tensile stress within the oxide scale would also result in subsequent localised failure of the

scale, through which liquid metal may exude, as a consequence of the wetting of alumina by liquid aluminium, resulting in the formation of oxide nodules (Impey *et al*., 1988). Narayanan et al. also observed a percent weight change occurred at the temperature corresponding to the transformation from γ-Al_2O_3 to α-Al_2O_3. They concluded that this is due to the rupturing of surface oxide films (volumetric shrinkage due to density changes during the transformation from γ-Al_2O_3 to α-Al_2O_3) caused by ordering and growth of the α-Al_2O_3, which leads to creation of channels to the base melt surface and hence acceleration of the further oxidation process (Narayanan *et al*., 1994).

2.2.6 The interface between an oxide and liquid aluminium and related wetting behaviour

The interface between an oxide and liquid aluminium alloy plays a key role in determining the resultant microstructural constituents, such as heterogeneous nucleation on oxide particles, formation of porosity and preparation of particulate reinforced Al based composites.

General characteristics

According to Weyl (Weyl, 1953; Delannay *et al*., 1987), the larger size and higher polarizability of the oxygen anions as compared to the cations cause a reconstruction of the oxide surface with a displacement of the cations from the surface to the interior, as shown in **Figure 2.12**. A double layer is created of which the extreme outer layer contains only anions. On the basis of this widely accepted model, it is generally assumed that adhesion with oxides is essentially governed by the interactions of the metal atoms with the oxygen anions only (Delannay *et al*., 1987).

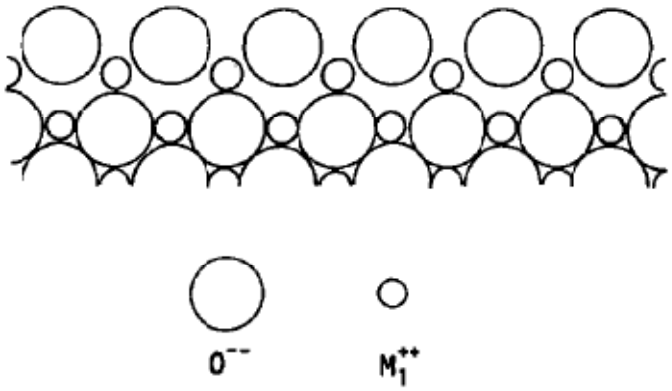

Figure 2.12 *The Weyl model of the reconstruction of the surface of an ionic compound (Delannay et al., 1987).*

Based on this model, Livey and Murray (Livey and Murray, 1956) state that the low wetability of oxides by liquid metals is due to the repulsion of the negative electron gas of the metal by the negative anion monolayer (Delannay *et al*.,1987). This qualitative argument has never been evaluated in quantitative terms. On the contrary, it has been argued that the electrostatic attraction between cations in the liquid metal and the negative anions of the oxide should favour wetting (Cabrera and Mott, 1948; Delannay *et al*., 1987).

It was early recognized by Humenik and Kingery that the work of adhesion of liquid metals on oxide surfaces increases with increasing affinity of the metal for oxygen, i.e. with increasing standard free energy of oxide formation (Humenik and Kingery, 1954). A more comprehensive model is proposed by Naidich (Naidich, 1981). Naidich attributes a major role to oxygen in solution in the liquid metal (Delannay *et al*., 1987). According to this model, the oxygen in a liquid metal creates, with a metal in its vicinity, a Me^{2+} -O^{2-} complex. Such a complex strongly adsorbs at the interface as a result of the electrostatic attraction between the Me^{2+} cation so formed and the anionic layer at the oxide surface. The higher the affinity of the metal for oxygen, the lower the solubility of the Me^{2+} -O^{2-} complex and the higher its

interfacial activity. Naidich suggests that, when enough oxygen is present in the melt, a layer of (liquid) metal oxide is formed in contact with the surface of the solid oxide, as displayed in **Figure 2.13**. As neutral atoms cannot bind with the oxygen anions of the solid oxide surface, the presence of oxygen in the bulk is essential (Naidich, 1981; Delannay *et al*., 1987).

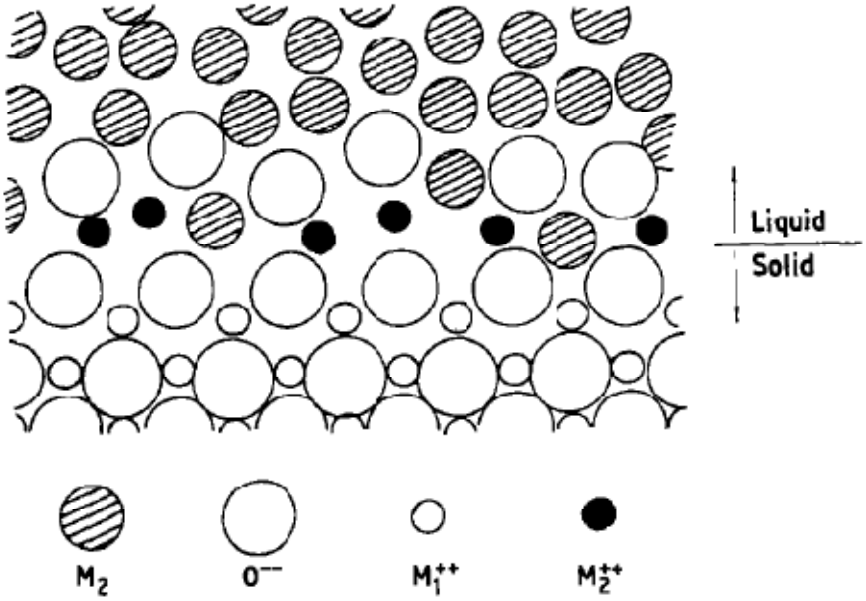

Figure 2.13 *The interface of liquid metal-oxide according to the model of Naidich (Naidich, 1981).*

Gas bridge model and the effect of magnesium

A model concerning the interfacial structure of suspended ceramic dispersoids in a molten metal has been developed by Ramani et al (Ramani *et al*., 1991). It is well known that all ceramic dispersoids in suspension in the melt are surrounded by physically or chemically absorbed gas, as shown in **Figure 2.14**, where particles are represented as spheres. To initiate the wetting of the particle surface by a molten metal, the molten metal has to overcome this gas layer. Under a particular condition, the gas layer is ruptured by either the turbulence created in the melt or the reaction with the melt (e.g. the scavenging effect of magnesium in

Al alloy, as stated below), causing the wetting of the surface of the particles with the molten metal (Sreekumar *et al.*, 2008).

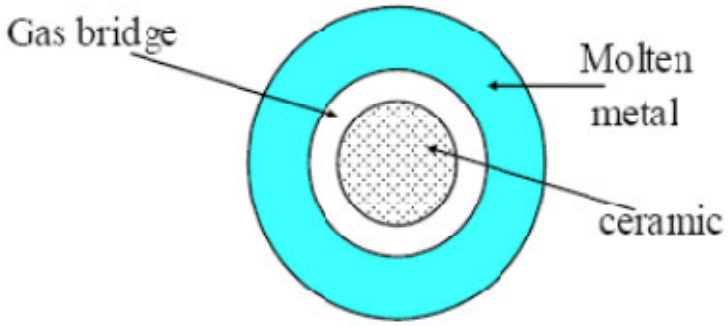

Figure 2.14 Schematic of gas bridge model of ceramic (oxides) in a molten metal (Ramani *et al.*, 1991).

Magnesium is one of the important alloying elements in aluminium alloys, including both Al-Si based casting alloys and wrought aluminium alloys for alloy strengthening. On the other hand, magnesium can also act as a powerful surfactant in aluminium alloys (Delannay *et al.*, 1987). This is due to the fact that magnesium moves to the free surface and can be readily oxidized to form MgO or $MgAl_2O_4$, depending on the thermodynamic and kinetics conditions. So if an oxygen-containing surface comes into contact with magnesium, there is a likely chance of oxygen becoming scavenged (Pai *et al.*, 1995). In such a case, magnesium can reduce the surface tension and the viscosity of aluminium alloys (Contreras *et al.*, 2004). In a similar way, in an aluminium alloy containing large amount of dispersoids, magnesium can also scavenge the oxygen from the surface of the dispersoids, leading to an increase in the surface energy of the dispersoids (Pai *et al.*, 1995). In addition, magnesium can reduce the

solid-liquid interfacial energy by aiding the reaction at the surface of the dispersoids by forming new compounds (Pai *et al*., 1995).

2.3 Grain refinement mechanisms

2.3.1 Historical development of grain refinement by chemical additives

A grain refined as-cast microstructure is always desired concerning both castability and mechanical properties for aluminium alloy products. For wrought Al alloys, it also facilitates the downstream processing due to the fact that the finer grain size reduces the size of defects such as microporosity and second-phase particles, and eliminates the occurrence of hot tearing because of the improved permeability in the mushy zone. As a result, a grain refinement operation has been a very common practice in the aluminium alloy foundry industry for more than half a century since Cibula clearly identified the effectiveness of Ti and Ti+B in grain refining (Flemings, 1974). At first the elements Ti and B were added to the melt in salt form but it soon became apparent that an aluminium based master alloys containing typically 3-10 wt.% Ti and 0-3 wt.% B offered significant advantages in terms of metal cleanness and high product quality. Currently, master alloys are widely produced in waffle form, for addition to holding furnaces, or in 9.55 mm diameter rod form, which is continuously fed into the molten metal stream in a transfer launder. Overall addition levels vary considerably depending on the base alloy composition and casting route but it is not uncommon for an Al-5Ti-1B master alloy to be added at a rate of 1 kg/1000kg giving the concentration of Ti and B of 0.005 and 0.001wt.%, respectively (McCartney, 1989). However, this operation is of low efficiency and only about less than 1% of the added particles successfully nucleate α-aluminium grains. This low efficiency is undesirable not only for its immediate cost implications, but also because refiner particles may themselves be

detrimental in the final microstructures (Greer, 2003). This may well be undesirable particularly in ingots for products intended for extrusion, deep drawing, or high performance structural applications (McCartney, 1989). Comprehensive and tremendous efforts have been made to understand the grain refinement mechanism, including both stages of nucleation and growth, since the beginning of use of grain refiners.

2.3.2 Understanding the grain refinement mechanism-Nucleation paradigm

In principle, the mechanisms of grain refinement are very simple. First, large amounts of potent heterogeneous nucleating sites must be introduced into the melt and second, compositional and heat and fluid flow conditions must be such that a large number of these sites actually become active and then nucleate the desired solid phases (McCartney, 1989). However, due to the limitation of the time interval and very low volume fraction of nucleating particles, the nucleation mechanisms based on inoculants are still not well understood (McCartney, 1989; Quested, 2004; Easton and StJohn, 1999; Murty *et al.*, 2002).

Nucleant-particle theories

This theory was first postulated by Cibula (Cibula, 1949-1950). Cibula proposed that nucleation occurred on the borides or carbides, when they were present in the melt. This theory attributes the effects of nominally binary Al-Ti master alloys to the presence of TiC nuclei even where no deliberate carbon addition is made; residual carbon levels of several hundred ppm being sufficient, it was argued, to promote the formation of TiC. Although careful processing has permitted the production of effective Al-Ti-C master alloys (Banerji and Reif, 1985 and 1986), and Al-Sc, Al-Zr, grain refining systems have also been developed for some Al alloys (Quested, 2004), the Al-Ti-B system is still one of the most common grain refiners. When comparisons are made between boride and aluminide particles, it was suggested that the Al_3Ti aluminide is better nucleant than TiB_2 boride. Mohanty et al. have confirmed that borides are pushed to the grain boundaries and that no grain refinement is

obtained when there is no solute Ti present, which suggests that the lattice disregistry between Al and borides is large, indicating that borides are a poor nucleant (Mohanty and Gruzleski, 1995; Easton and StJohn, 1999). Another evidence to support the above argument is that there were no orientation relationships found between borides and α-Al phases, while multiple orientation relationship are known between Al_3Ti and α-Al matrix (Davies *et al.*, 1970; Arnberg *et al.*,1982).

Phase diagram theories

In order to explain the grain refinement that occurred by grain refiners with a lower Ti content and a B addition, it has been suggested that a shift of the peritectic point to low Ti concentrations (for instance, 0.05 wt.% Ti) is caused by the addition of B, and this is the reason for grain refinement (Easton and StJohn, 1999). So this theory is also called the "Peritectic theory" (McCartney, 1989). Hence, it was commonly assumed that there was a ternary Al-Ti-B peritectic, and speculations and theories were based on this assumption (Cornish, 1975; Maxwell and Hellawell, 1975). Although this theory, that a B addition changes the phase diagram markedly, so that Al_3Ti is stable even at low concentrations of Ti, explains many of the phenomena observed, it disagrees with phase-diagram calculations (Jones and Pearson, 1976; Easton and StJohn, 1999). Jones and Pearson, and Sigworth have carried out theoretical thermodynamic analyses and drawn the conclusion that changes in the phase diagram due to B additions cannot be used to explain the grain refinement mechanism of Al-Ti-B additions (Jones and Pearson, 1976; Sigworth, 1984 and 1986). In other words, their thermodynamic calculations didn't support the suggestion by Marcantonio and Mondolfo that there is a ternary eutectic at 0.05wt%Ti and 0.01%B (Marcantonio and Mondolfo, 1971).

$$L \rightarrow \alpha\text{-}Al + Al_3Ti + (Al,Ti)B_2 \qquad (2.10)$$

The peritectic hulk theory

This theory is also based on the understanding that Al_3Ti is a more powerful nucleant than TiB_2. This theory suggests that the borides form a shell around the aluminide particles, and hence, slow the dissolution of the aluminides, as diffusion needs to proceed through the boride shell (Easton and StJohn, 1999). However, borides are very stable in Al melts compared to Al_3Ti, at hypoperitectic Ti compositions. This does not seem possible. Even with B in the master alloy, the Al_3Ti still dissolves within minutes at high temperatures.

The hypernucleation theory

Jones developed a theory to explain hypernucleation based on Ti segregation to TiB_2 particles, thus forming pre-existing solid α-aluminium with a high Ti content from which solid α-Al grows. It was proposed that the melt solutes segregate stably to the melt-substrate interface to enhance the potency of the substrate, and in the right conditions stable pseudo-crystals can be created above the principal liquidus of the alloy, and immediately below the alloy liquidus these pseudo-crystals allow α-Al to grow without undercooling (Jones, 1985 and 1988). Solutes of similar ionic size to Al lead to hypernucleation, whereas solutes of grossly mismatching size will destroy the hypernucleation process. The atomic size of Ti is very similar to Al and hence promotes hypernucleation. Jones suggested that there is an activity gradient produced by the addition of TiB_2 particles into the melt, which is thermodynamically unsound, since, at equilibrium, the chemical potential and activity gradients must be constant (Sigworth, 1996). The other problem with this theory is that there is no experimental evidence to support this mechanism.

The duplex nucleation theory

The duplex nucleation theory is one of the most recent and attractive theories so far. It was first proposed by Mohanty and Gruzleski (Mohanty and Gruzleski, 1995) and then

experimentally evidenced by Schumacher and Greer (Schumacher and Greer, 1994a, 1994b and 1997; Schumacher, *et al*., 1998).

Mohanty and Gruzleski's work

In fact, the development of the duplex nucleation theory stemmed from Backerud's work in 1971, in which Al_3Ti was observed on boride particles (Backerud, 1971). In Mohandy and Gruzleski's work, large synthetic TiB_2 particles at a size of 5μm in diameter were added to Al melts. When there was no excess Ti, no grain refinement was observed and the added TiB_2 particles were observed at grain boundaries. However, when excess Ti was added, significant grain refinement was achieved and meanwhile, the added boride particles were found at the grain centres. At hyperperitectic concentrations of Ti, an Al_3Ti layer was formed on the surface of TiB_2 particles, around which was an α-Al layer. So the nucleation sequence was proposed as follows: in the presence of dissolved Ti even below the peritectic level, an interfacial $A1_3Ti$ layer is formed at the TiB_2/melt interface which in turn nucleates the α-Al grains. In order to explain this duplex nucleation mechanism, it is proposed that the formation of the $A1_3Ti$ layer is caused by a concentration gradient of Ti towards the boride particles. Due to local equilibrium near the borides, the $A1_3Ti$ layer would be stable and hence then nucleate α-Al (Mohanty and Gruzleski, 1995).To experimentally confirm the segregation behaviour of Ti associated with boride particles, a liquid metal cleanness analyser was used for on-line sampling of Al melts treated with grain refiners. Chemical analysis of samples drawn from the bottom and top of the melt after prolonged holding, indicate a higher residual Ti in the sludge than that near the melt surface (Mohanty *et al*., 1995).

Schumacher and Greer's work

In the 1990s, Greer and Schumacher et al. developed a type of experimental technique in which microstructural investigations of nucleation events became possible by embedding

grain refining particles in an Al based glassy matrix (Schumacher and Greer, 1994a, 1994b and 1997; Schumacher, *et al.*, 1998). Through microstructural studies of refining particles in an Al-rich metallic glass matrix, evidence has been provided to support the duplex nucleation theory that in the presence of excess Ti, thin Al_3Ti layers can be present on the surface of the TiB_2 particles, even at low overall Ti levels where Al_3Ti would not otherwise be stable.

Although the duplex nucleation theory has been the most attractive theory regarding the enhanced heterogeneous nucleation behaviour by grain refiner additions of the Al-Ti-B system so far, there are still some questions to be answered. It is recognised that Ti could segregate to the surface of boride particles. However, it was argued that Al_3Ti would not become stable due to a monolayer of Ti at the interface between the boride and α-Al (Sigworth, 1996).

Other nucleation theory-adsorption models

In parallel to the development of an understanding of the nucleation mechanism in the aluminium alloys with a grain refiner added, as mentioned above, the argument of the importance of physical and chemical features of the nucleant surface have been investigated by different investigators (Zhang and Cantor, 1992; Glicksman and Childs, 1962). Glicksman and Childs carried out an investigation of nucleation catalysis of bulk liquid tin when in contact with a variety of gross catalytic substrates. Some evidence of a crystallographic misfit influencing nucleation catalysis was observed; however, it shows also the misfit effects of the substrates of different chemical species tend to be masked by other factors (Glicksman and Childs, 1962). Zhang and Cantor et al. developed an adsorption model for the case when the undercooling for nucleation of a solid phase by inoculants is very small, where the classical spherical cap model appears to break down and it is thermodynamically favourable to have an adsorbed layer of a new crystalline phase which is then the basis for growth (Zhang and

Cantor, 1992; Greer *et al*., 2000). This adsorption model would be consistent with the high resolution transmission electron microscopy observations, showing a layer of Al_3Ti as thin as three monolayers on TiB_2 particles in glassy matrix studies (Schumacher, *et al*., 1998; Greer *et al*., 2000).

2.3.3 Understanding of grain refinement mechanism-solute paradigm

In parallel to the development of grain refiners based on the Al-Ti-B system, considerable efforts have also been made to achieve grain refined microstructures in different Al alloy systems, including both cast and wrought Al alloys (Spittle and Sadli, 1995; Kearns and Cooper, 1997). One of the most important findings is that the grain refinement effect of the Al-Ti-B system grain refiners are not so effective in casting Al alloys as that in wrought Al alloys, especially in the cases where Al-Ti-B grain refiners with excess Ti were added (Mohanty and Gruzleski, 1996). In fact, as early as in the middle 1970s, Hellawell and Maxwell developed a model to predict the grain refinement effect by consideration of the nucleant potency, cooling rate and the segregation tendency of solute elements (Maxwell and Hellawell, 1975). However, it is Easton and StJohn who systematically develop the solute paradigm to understand the grain refinement effect (Easton and StJohn, 1999, 2001, 2005 and 2008).

2.3.4 Columnar to equiaxed transition and grain refinement

In a review paper by McCartney, it is pointed out that the role of a grain refiner is, in essence, to promote the columnar to equiaxed transition (CET) and obtain a fully equiaxed grain structure (McCartney, 1989). Therefore it is critical to have a complete picture of the CET for achievement of grain refinement. CET has been widely investigated in the field of alloy solidification theoretically (Hunt, 1985; Gaumann *et al*., 1997) and experimentally (Gandin and Rappaz, 1994; Vandyoussefi and Greer, 2002; Spittle, 2006). The analytical model developed by Hunt, is based on equiaxed grains nucleated in the constitutionally undercooled

region ahead of a columnar front blocking the advance of that front if the volume fraction of equiaxed grains is sufficient. The identified key parameters in deciding whether growth is columnar or equiaxed are as follows: (1) solidification front velocity; (2) temperature gradient in the liquid; (3) the number of potential nucleation sites and (4) the nucleation undercooling at which those sites become active (Vandyoussefi and Greer, 2002).

An experimental combined with modelling investigation of grain refinement of directionally solidified Al-4.15wt.% Mg alloys was carried out by Vandyoussefi and Greer using a cellular automaton-finite element model (Vandyoussefi and Greer, 2002). In their study, the assumption of a spatially isothermal melt was removed; instead the influence of both the release of latent heat and the temperature gradient in the liquid *G* was included by adopting an enthalpy-based finite element algorithm. Their simulations show that the latent heat released gives a quasi-isothermal zone interrupting the temperature gradient. This zone is important in limiting the degree of grain refinement which can be achieved, but also facilitates growth of equiaxed rather than elongated grains. And their results also confirmed the basic analysis of the CET offered by Hunt, i.e., there is a competition between continued growth of existing grains and the appearance of new grains in the constitutionally undercooled region ahead of the main growth front (Hunt, 1984).

2.3.5 Understanding of grain refinement mechanism-Free growth model

Based on the commercial application of grain refiner additions, Greer and co-workers developed the free growth model so as to enhance the understanding of the grain refinement mechanism and further improve the efficiency of existing grain refiners in practice. In their model, based on the understanding that high potency of inoculant particles such as TiB_2 with excess Ti in Al-Ti-B grain refiners and the corresponding very small undercooling for nucleation of α-Al, as little as 0.01K (Greer *et al.*, 2000;Vandyoussefi and Greer, 2002; Quested and Greer, 2004 and 2006), it was assumed that the nucleation stage itself is not the

controlling factor for the achievement of grain refinement, whereas the grain refinement achieved is determined by a free growth condition in which the required undercooling for free growth, ΔT_{fg}, is inversely proportional to the particle diameter of inoculants:

$$\Delta T_{fg} = 4\sigma/\Delta S_v d \qquad (2.11)$$

where σ is the solid-liquid interfacial energy and ΔSv is the entropy of fusion per unit volume. More importantly, in their modelling, based on the understanding of recalescence limiting the number of active nucleation particles and therefore the number of grains, the size distribution of grain refiner particles rather than the size as a single fixed value was treated as the input. To achieve this, spatially-homogenised grain refiner particles throughout the bulk melt was assumed and neither settling nor agglomeration behaviours of grain refiner particles were taken into account in their model. The reported result by Günther et al. demonstrated that grain refinement of gravity die-cast Mg-alloys can be achieved via the addition of a SiC master alloy (Gunther *et al*., 2006). And a simulation method for heterogeneous nucleation was developed based on the free growth model and examined experimentally by a study of grain refinement in AZ31 alloy by the addition of SiC particles. The model makes quantitatively correct predictions for the grain size and its variation with cooling rate, indicating the applicability of the free growth model in the field of grain refinement of other alloy systems by the addition of grain refiners (Gunther *et al*., 2006).

2.3.6 Grain refinement by a physical approach

Investigations of the grain refinement induced by melt agitation have been explored for a long time. These physical approaches involve mechanical stirring, electromagnetic stirring (Campbell, 1981;Griffiths, 1997), electromagnetic vibration (EMV) (Radjai and Miwa, 2000), and ultrasonic stirring (Atamanenko *et al*., 2010) etc. To a certain extent grain refinement has been achieved by means of these physical approaches. However, the

mechanism underlying is basically based on dendrite fragmentation due to the limited shearing force imposed.

2.4 Oxides acting as nucleation sites of phase constituents in Al alloys

2.4.1 Potential of oxides acting as nucleation agent in Al alloys

In practice, oxides are always inevitably present in liquid metals and alloys in forms of oxide clusters and/or oxide films causing severe difficulties during solidification processing, and become inclusions and related defects inducing degradation of mechanical properties in the final cast components. Over the last decades, tremendous and comprehensive efforts have been made to remove oxides from liquid metals prior to solidification processing through both chemical and physical approaches (Davis, 1993; Sigworth *et al*., 1989; Cao and Campbell, 2003), which have proven to be useful but not at all efficient and economical. Recently, a novel solidification processing technology named Melt Conditioning by Advanced Shear Technology (MCAST) (Fan *et al*., 2009; Fang *et al*., 2007; Xia, *et al*., 2009), has been developed in BCAST at Brunel University, for conditioning liquid metal under intensive forced convection before solidification in order to produce grain refined and uniform as-cast microstructures. It has recently been demonstrated that naturally occurring oxides in liquid Mg alloys can be harnessed to enhance heterogeneous nucleation for microstructural refinement in commercial Mg-Al alloys. It was established that both oxide clusters and films are composites, where nano-scale oxide particles are embedded in a liquid metal matrix. Such oxide particles can be effectively dispersed by intensive forced convection and such dispersed oxide particles can be potent sites for heterogeneous nucleation since they often have a good crystallographic match with the nucleated solid crystalline phases (Fan *et al*., 2009).

2.4.2 Nucleation of Fe-containing intermetallics on oxides in Al alloys

It is well established that both oxides and Fe-containing intermetallics are two critical microstructural constituents determining the properties of Al alloys. In an effort to remove the oxide films from Al melts, precipitation and sedimentation of primary Fe-containing intermetallic compounds onto the oxide films, causing them to sink under the weight of these Fe-containing intermetallics, were extensively studied by Cao and Campbell (Cao and Campbell, 2003, 2004a, 2004b, 2005 and 2006). After the Fe-containing sediments sink to the bottom of a melt along with the oxide films, by removing this settled layer, the amount of oxide films in the liquid Al can be reduced. Cao and Campbell calculated the planar disregistry between α-AlFeSi and typical oxides in Al-Si alloys such as MgO, $MgAl_2O_4$, γ-Al_2O_3, and α-Al_2O_3. It seems that all these oxides could be good substrates for the nucleation of the α-AlFeSi phase (Cao and Campbell, 2003). They proposed that the wetted surface of the oxide films provides a preferential nucleation site for Fe-containing intermetallics.

Miller et al. also investigated the influence of oxides on the formation of Fe-containing intermetallics in an Al-11.6Si-0.37Mg alloy (Miller *et al.*, 2006). In order to highlight the role of oxides, both high melt agitation to induce more entrained oxide films, and direct additions of oxide particles (α-Al_2O_3 and $MgAl_2O_4$) were made to introduce more oxides into the alloy melt. Their observations are in general agreement with the argument proposed by Cao and Campbell that α-AlFeSi and β-AlFeSi intermetallics can nucleate on the wetted side of double oxide films entrained into the melt during casting (Cao and Campbell, 2003). Fe-containing intermetallics have been observed to be associated with both α-Al_2O_3 and $MgAl_2O_4$ particles externally added, both being likely to be present within oxide films depending on the alloy composition.

Khalifa et al. evaluated the nucleation of Fe-containing intermetallic phases in dilute Al-Si-Fe alloys on different types of oxide particles, which were introduced into the molten alloys

using a gas injection technique (Khalifa *et al.*, 2005). By quantitative evaluation of the number of oxide particles that have a direct physical contact with the nucleated Fe-containing intermetallic phase as observed through an optical microscopy, they concluded that nucleation of the Fe-containing intermetallic phases in the alloys investigated does not seem to be largely affected by the type of the nucleating surface. It is worth noting that the formation of Fe-containing intermetallic phases in their alloys mainly occurred in interdendritic regions due to the dilute Al alloy compositions used, where the primary α-Al phase solidified first and so most oxide particles were subsequently pushed to interdendritic areas. This may partly contribute to the quantified number of oxide particles in physical contact with the Fe-containing particles. Although, their results still suggest that oxide particles can be nucleation sites for Fe-containing intermetallics, if so, it is possible to be utilized to manipulate the formation of Fe-containing intermetallics such as α-AlFeSi and β-AlFeSi phases by the controllable nucleation of Fe-containing phases on some oxides.

2.4.3 Nucleation of the α-Al phase on oxides in Al alloys

The nucleation of the α-Al phase on the externally added oxide particles in Al-Si-Fe alloys was carried out by Khalifa et al. (Khalifa *et al*., 2004) using a gas injection technique (Mohanty and Gruzleski, 1995). Their results showed that in dilute alloys containing less than 1.5 wt.% (Si+Fe), nucleation of the α-Al phase can be promoted by the addition of oxide particles through a quantitative evaluation of the occurrence levels of oxides in the α-Al phase. However, the grain size evolution associated with the oxide additions was not reported in their study.

2.5 Characteristics of the melt with intensive shearing

Recently, the Melt Conditioning by Advanced Shear Technology (MCAST) using a twin-screw machine, has been developed for conditioning liquid metal under intensive forced convection before solidification (Ji *et al*., 2001). The twin-screw machine (named the MCAST unit hereafter) consists of a barrel and a pair of closely intermeshing, self-wiping and co-rotating screws. The screws have a specially designed profile to achieve high shear rate and high intensity of turbulence. Once poured into the twin-screw machine, molten alloy is quickly cooled to a pre-determined shearing temperature and experiences high intensity of turbulence.

2.5.1 Characteristics of the fluid flow with intensive melt shearing

The fluid flow characteristics within the MCAST unit has been thoroughly analysed by Ji et al. (2001). The fluid flow within the MCAST unit is characterized by a high shear rate and a high intensity of turbulence, with a cyclic variation of shear rate. During the intensive melt shearing, there is an enormous amount of changing interfacial area, providing enhanced heat transfer and strong dispersion function. In this continuous flow field, the fluid undergoes cyclic stretching, folding and reorienting processes (Ji *et al*., 2001). This is shown schematically in **Figure 2.15** with respect to the streamlines during the take-over of the materials from one screw to the other.

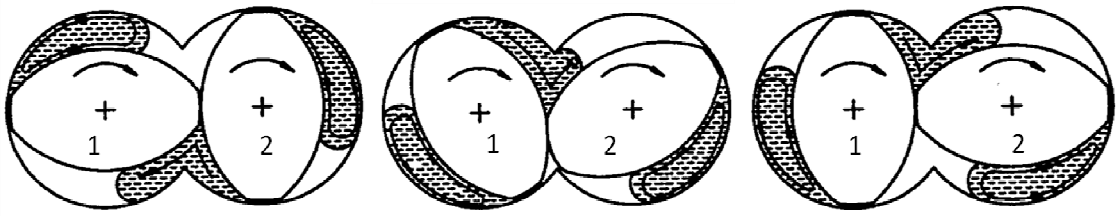

Figure 2.15 *Schematics showing the fluid flow characteristics against shearing time on the cross-section of the twin screws, represented by numbers "1" and "2". The fluid flow experences cyclic stretching, folding and reorienting processes (Ji et al.,2001).*

2.5.2 Characteristics of thermal and compositional field of the melt with intensive shearing

The melt with intensive shearing is extremely uniform in terms of composition fields, thermal conditions and dispersed individual oxide particles. In addition, Ji and Fan (2002) have analysed and experimentally investigated the influence of intensive melt shearing on the thermal and compositional profiles in the vicinity of an advancing solid/liquid interface. Under a stationary condition, the constitutional undercooling is relatively large, as shown schematically in **Figure 2.16a**. Under simple shear flow, the forced convection enhances both mass and thermal transport. As a consequence, the thickness of both the thermal- and solutal-diffusion boundary layers is reduced, which, in turn, increases both the thermal and concentration gradients at the interface although the solute-concentration peak at the solid/liquid interface (C_i) is also reduced. The net effect of simple shear flow is to reduce the constitutional undercooling, **Figure 2.16b**. The introduction of turbulent flow further reduces the constitutional undercooling by reducing the thermal and solutal diffusion-layer thicknesses, as depicted in **Figure 2.16c**. They further argued that at a very high intensity of turbulence, both the thermal- and solutal-diffusion boundary layers will diminish, and convection will be responsible for both thermal and mass-transport processes. Under such conditions, constitutional undercooling does not exist anymore.

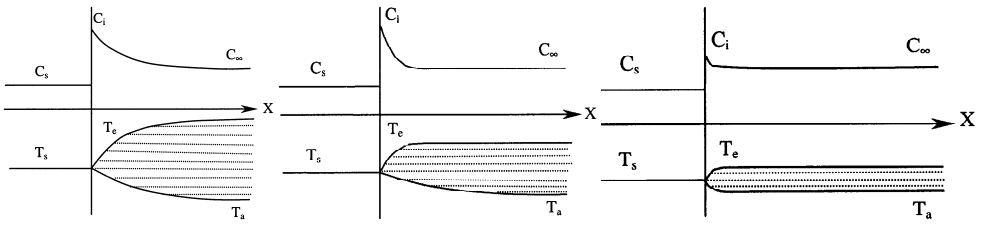

Figure 2.16 *Schematic illustration of the constitutional undercooling (shaded area) at the solidification front obtained under different flow conditions: (a) no convection; (b) pure shear flow; and (c) turbulent flow (Ji and Fan 2002).*

It has been shown that the nature of fluid flow has a very significant influence on the morphology of the solidification structure. A numerical study by Qin and Fan by means of a boundary element method, reveals, that a laminar flow encourages dendritic growth while a turbulent flow favours non-dendritic growth (Qin and Fan, 2000). Das et al. and Das and Fan carried out a Monte-Carlo simulation of the morphological development of solidification structures under forced fluid flow (Das *et al.*, 2002; Das and Fan, 2004). A laminar type flow is shown to destabilize the solid-liquid interface promoting dendritic growth for a solid growing from a fixed substrate. However, a turbulent type fluid flow that penetrates into the interdendritic region supplying solvent atoms (in other words, depleting the interdendritic solutal boundary layer) seems to prevent dendritic growth and stabilizes the solid-liquid interface such that compact solidification morphology develops (Das *et al*., 2002). Consequently, with intensive melt shearing, the following two aspects can be expected. One is increased solid/liquid interface stability; the other is significant decreased constitutional undercooling in front of the advancing solid/liquid interface.

In this thesis, by adopting the MCAST prior to solidification, it is possible to control the morphology, size and size distribution of oxides formed in Al alloy melts, therefore, this is expected to enhance the heterogeneous nucleation on oxide particles and hence achieve grain refined α-Al phase or refined Fe-containing intermetallic compounds.

Chapter 3

Experimental procedures

3.1 Grain refinement of an AlZnMgCuTi wrought alloy by intensive melt shearing

In direct chill (DC) casting of Al alloys, a grain refined microstructure is generally desirable (Nadella *et al.*, 2008; McCartney, 1989). Al-Ti-B master alloys as grain refiner additions are commonly added to melts for DC ingot production of wrought Al alloys, as presented in **Figure 3.1**.

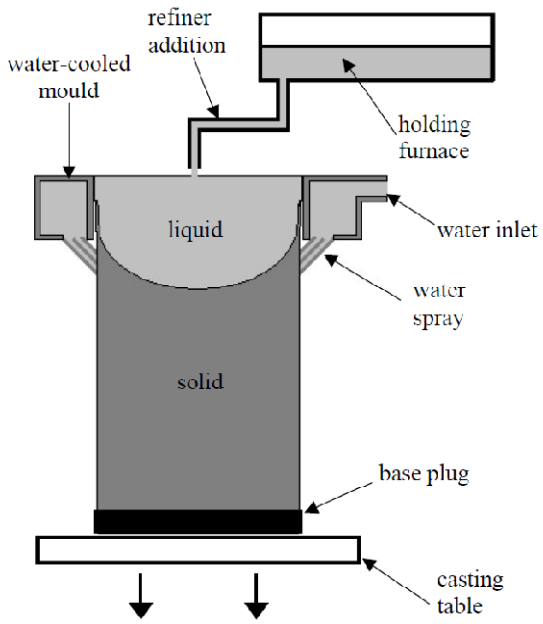

Figure 3.1 *Schematic of direct chill casting process of wrought Al alloys (Quested, 2004).*

However, only less than 1% of the added particles successfully nucleate aluminium grains and this low efficiency is undesirable not only for its immediate cost implications, but also because refiner particles may themselves be detrimental in the final microstructures particularly for products intended for extrusion, deep drawing, or high performance structural applications (McCartney, 1989; Greer, 2003). In this chapter, the grain refinement of intensive shearing with the MCAST process on an experimental wrought Al alloy has been investigated.

3.1.1 Experimental AlZnMgCuTi wrought alloy

The alloy chemistry of the experimental wrought alloy is summarized in **Table 3.1**. The liquidus temperature of α-Al was determined as 628^{o}C by computer-aided thermal analysis.

Table 3.1 *Chemical composition of the experimental wrought Al alloy.*

Element	Zn	Mg	Cu	Ti	Si	Fe	Al
(wt.%)	10.5	2	1.6	0.2	0.15	0.35	Balance

3.1.2 Processing procedures adopted

Melt conditioned direct chill casting

A schematic of melt conditioned direct chilling casting (MC-DC) is shown in **Figure 3.2,** by which the oxide films in liquid alloys can be effectively dispersed by intensive shearing. In line with the procedure of grain refiner addition in industrial practice, which the grain refiner is added to the melt at temperatures greater than the liquidus temperature (**Figure 3.1**), the melt shearing temperature with the MCAST process should be also well above 628^{o}C of the liquidus temperature of the experimental alloy and was set at 650^{o}C. The temperature inside the MCAST unit is controlled by the barrel temperature which is accomplished by an

electrical element and corresponding electrical control system. The temperature control accuracy is within ±2°C. Other parameters were as follows: Melting temperature: 750°C; Shearing time: 60 s; Rotation speed of the MCAST unit: 500rpm.

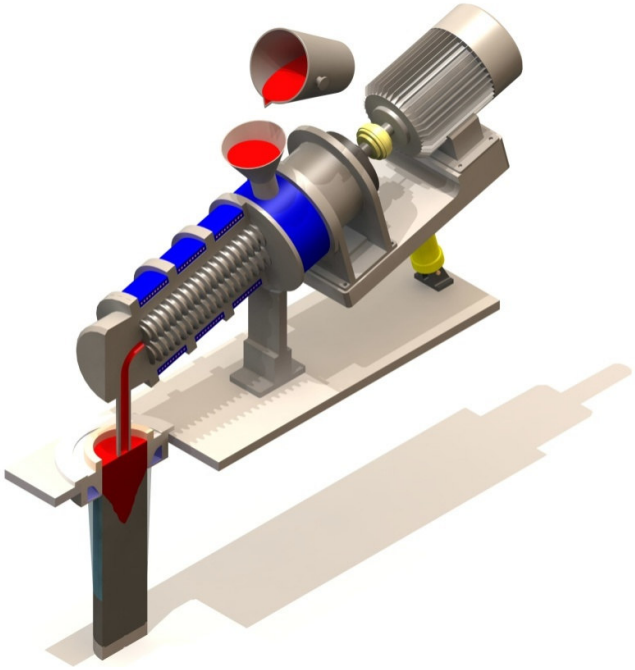

Figure 3. 2 *Schematic illustration of MC-DC setup using a twin screw MCAST unit.*

Specially designed solidification procedure to demonstrate the grain refining effect of intensive shearing

In order to eliminate the influence of the melt pouring operation on the nucleation events, such as a catalytic mechanism of the mould walls, grain multiplication through a dendrite fragment mechanism, a specially designed solidification experiment was carried out, as shown in **Figure 3.3**.

This experimental design was also based on previous results that showed the effect of intensive melt shearing was retained for at least 10 minutes after melt shearing (Fan *et al*.,

2009). After shearing, although the dispersed oxide particles have a tendency to agglomerate to minimize interfacial energy, this process is driven by the Brownian motion and it takes a long time before any observable agglomerates form in the melt, since the rate of agglomeration is usually several orders of magnitude slower than that of de-agglomeration (Fan *et al*., 2009).

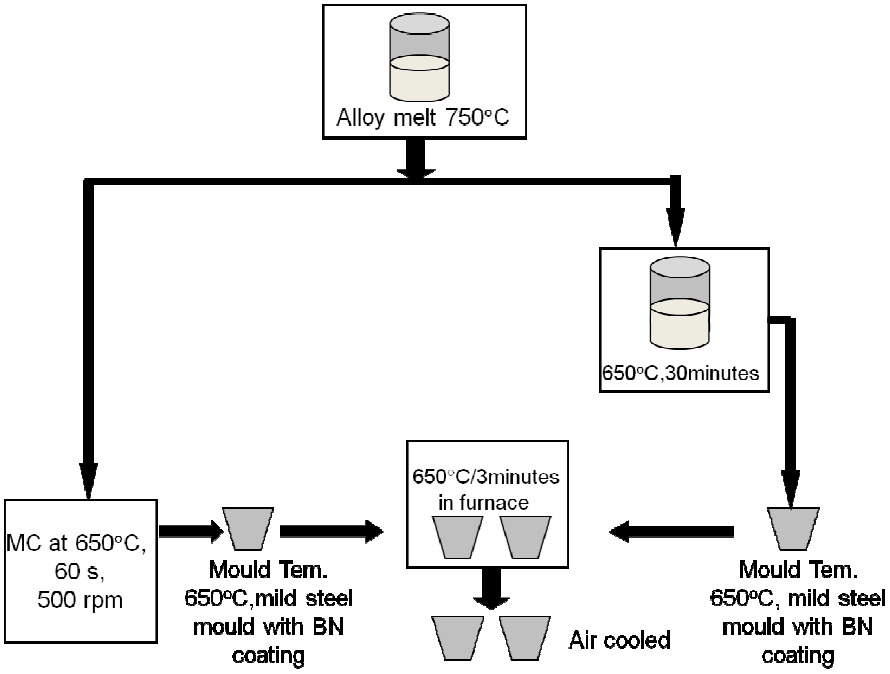

Figure 3.3 *Experimental flow chart of a specially designed solidification procedure.*

The temperatures of the mould and melt were monitored and controlled, and the influence of the pouring operation on the grain structure was minimised by isothermally holding in a preheated electrical resistance furnace. A mild steel mould, wrapped with a thermally insulating blanket (2mm in thickness) and coated with boron nitride, was preheated to the same temperature as that used for intensive melt shearing by the MCAST process. The

dimensions of the mild steel mould samples and the corresponding cross section for grain size assessment are schematically shown in **Figure 3.4**.

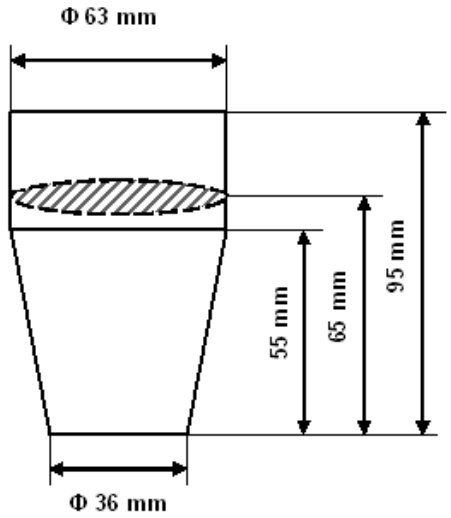

Figure 3.4 *Dimensions of the mild steel mould used.*

For the sample with intensive shearing, the alloy melt was poured into the MCAST unit at 750^{o}C. After intensive melt shearing, the melt was transferred to the preheated mild steel mould. For the alloy melt without intensive melt shearing, the melt was air cooled to 650^{o}C (from 750^{o}C), and was then transferred directly into a preheated mild steel mould. The two mild steel moulds were isothermally held in a holding furnace at 650^{o}C for 3 minutes. During isothermal holding, the temperature of the melt was monitored by a *K* type thermocouple to make sure the temperature of the melt was within 650±2^{o}C. The thermocouple used was calibrated against the melting temperature for pure Al (99.86wt.%). The two mild steel moulds were then taken out of the holding furnace and air cooled to room temperature. The cooling rate of the sample cast in this mould was determined to be 0.6 Ks^{-1} by computer-aided thermal analysis.

TP-1 samples

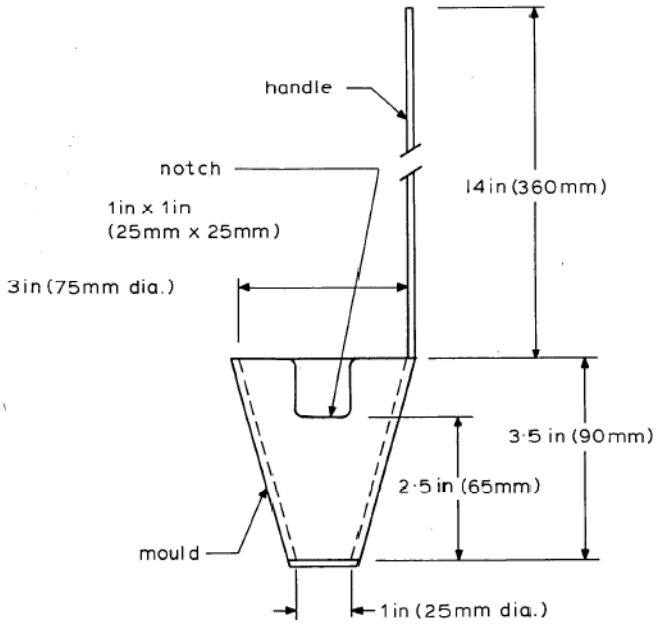

Figure 3.5 *Schematic illustration of TP-1 mould used in the present study (McCartney, 1989).*

In order to assess the effects of intensive melt shearing on the grain size under a fixed cooling rate, a standard grain-refiner test, the TP-1 test, was adopted. This test was established by the Aluminium Association and was initially designed to compare the efficiency of different kinds of grain refiners (TP-1, 1987; McCartney, 1989; Murty *et al*., 2002). The cooling rate at the specific section height (perpendicular to its axis and 38 mm from its base) in the standard TP-1 mould was estimated to be 3.58 Ks^{-1} by direct temperature measurement when the melt superheat is around 720^{o}C (Greer *et al*., 2000). Each conical sample was then sectioned perpendicular to its axis and 38 mm from its base. In the standard TP-1 test procedure, a test sample is removed from the metal bath using a cone-shaped crucible, as shown in **Figure 3.5**. This crucible is then inserted to a fixed depth in a water bath which promotes directional freezing, similar in nature to the solidification process in DC cast aluminium ingots (Spittle and Sadli, 1995; Greer *et al*., 2000). In the current study, the TP-1 mould was put below the

transfer tube of the MCAST unit immediately after the completion of shearing. This is the difference from the standard TP-1 test procedure for both cases with and without shearing in the current study. Here, the TP-1 mould was preheated to 350^{o}C for more than 2 h in a preheated furnace before collecting the alloy melt.

Influence of shearing time on the grain refinement

A wide range of shearing time was used to evaluate the grain refinement by intensive shearing, ranging from 0, 9, 15, 30, 60, 120, 240, up to 480 s. Other parameters were as follows: Melting at 750^{o}C for 2 h prior to being poured into the BCAST unit at the same temperature; Shearing time: 60 s; Rotation speed of the MCAST unit: 500rpm.

Effect of thermal history of alloy melt on the grain refinement

In order to experimentally confirm the grain refining effect of intensive shearing via the enhanced heterogeneous nucleation on oxide particles, the pouring temperature of the alloy melt into the MCAST unit was set at different temperatures. Three different processing schemes were used for TP-1 samples with the same casting temperature all at 650^{o}C, as presented in **Figure 3.6**. For the sample without melt shearing, the melt was air cooled to 650^{o}C from 750^{o}C and then cast into a TP-1 mould (scheme A in **Figure 3.6**); for the samples with melt shearing, two different melt conditioning processes were adopted. One was isothermally sheared at 650^{o}C for 60 s after the melt temperature had been air cooled to 650^{o}C and then poured into the MCAST unit (scheme B in **Figure 3.6**). The other one was sheared immediately after the melt was poured into the MCAST unit from 750^{o}C, including two consecutive stages of 60 s in total: continuous cooling and shearing from 750 to 650^{o}C and subsequent isothermal shearing at 650^{o}C (scheme C in **Figure 3.6**). In **Figure 3.6**, the calculated volume fraction of Al_3Ti against temperature by FactSage software is also included (the same as **Figure 4.1**) to facilitate the understanding of the development of Al_3Ti during different processes.

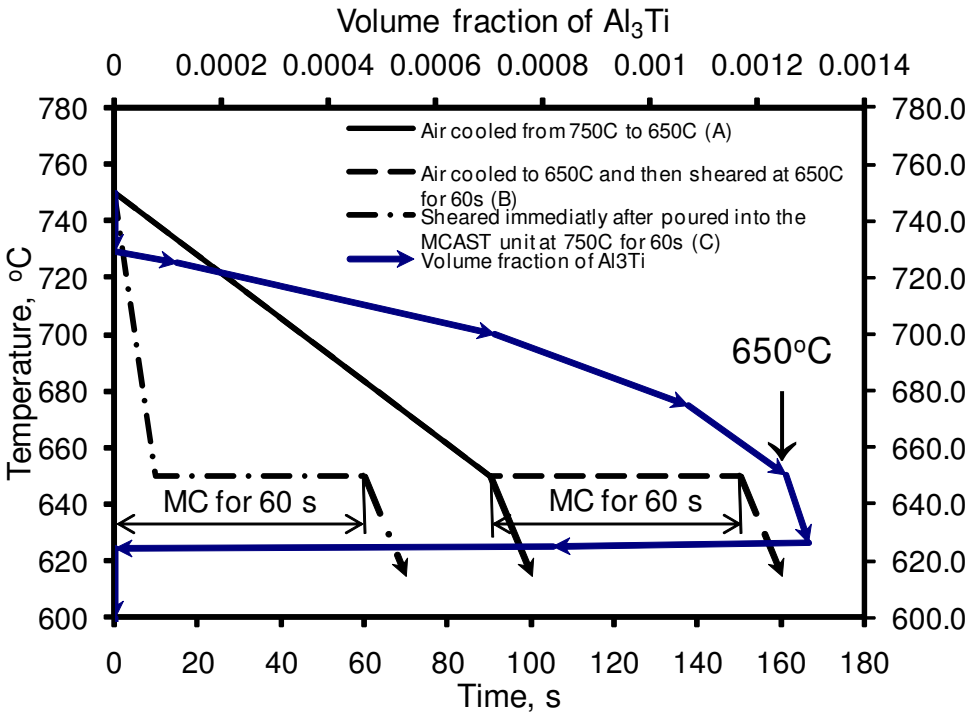

Figure 3.6 *Processing schemes used for TP-1 and wedge-shaped samples overlaid with the thermodynamically calculated volume fraction of Al_3Ti against temperature by FactSage software.*

Effect of cooling rate on the grain refinement

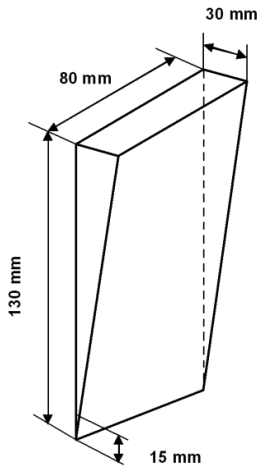

Figure 3.7 *Schematic of the dimensions of the wedge-shaped sample and the location on the cross section is indicated, where grain size was evaluated.*

A wedge-shaped copper mould was used to evaluate the grain refinement by intensive melt shearing under high cooling rates. The tip of the sample has a very high cooling rate of up to 1000 Ks^{-1} (Norman *et al.*, 1998). The geometry of the wedge-shaped sample is shown in **Figure 3.7**. For the wedge-shaped copper mould samples, schemes A and C as in **Figure 3.6** were used for both cases with and without shearing.

Pressure filtration experiment to concentrate the oxides formed in molten alloys

A pressure Filtration Technique (Prefil Footprinter®) was used to provide both real -time representations of melt quality characteristics and concentrate metallurgical samples for further inclusion evaluation if necessary (Cao, 2005). **Figure 3.8** shows schematically the working principle of the Prefil Footprinter (Enright *et al.*, 2003). The equipment pressurizes the melt, forcing it through a fine filter. Examination of the materials trapped in and above the filter can provide extra information of the inclusions in an alloy melt (Cao, 2005).

In the current study, the pressure filtration technique was adopted to concentrate oxides or intermetallic particles formed in the alloy melt. Metallographic samples from cross sections were investigated using different characterisation techniques. A model alloy Al-20Zn-0.05Ti was subjected to pressure filtration to investigate the characteristics of the oxides formed in the alloy melt with intensive shearing. The reason for choosing this alloy chemistry was to decrease the liquidus of the Al-Zn alloy to the same as the experimental wrought alloy with a simplified composition. The filtration crucible, made of a low heat capacity and highly insulating fibrous materials (Cao, 2005), was preheated to ~ 300-350°C to reduce heat loss during transfer of the liquid alloy. The model alloy was prepared with commercial purity Al (99.86wt.%), pure Zn and Al-10Ti (in wt.%) master alloy. Without shearing, the alloy was melted at 750°C and air cooled to 650°C, then transferred into the filtration crucible. With shearing, the alloy melt was melted at 750°C and then poured into the MCAST unit, sheared for 60 s, and then transferred into the filtration crucible. The shearing temperature of the

MCAST unit was set at 650^{o}C. The rotation speed of the MCAST unit was set at 500 rpm. Filtered samples containing the concentrated oxides within the metal (~ 5 mm in thickness) in contact with the filter were sectioned, mounted, and polished for metallographic examination.

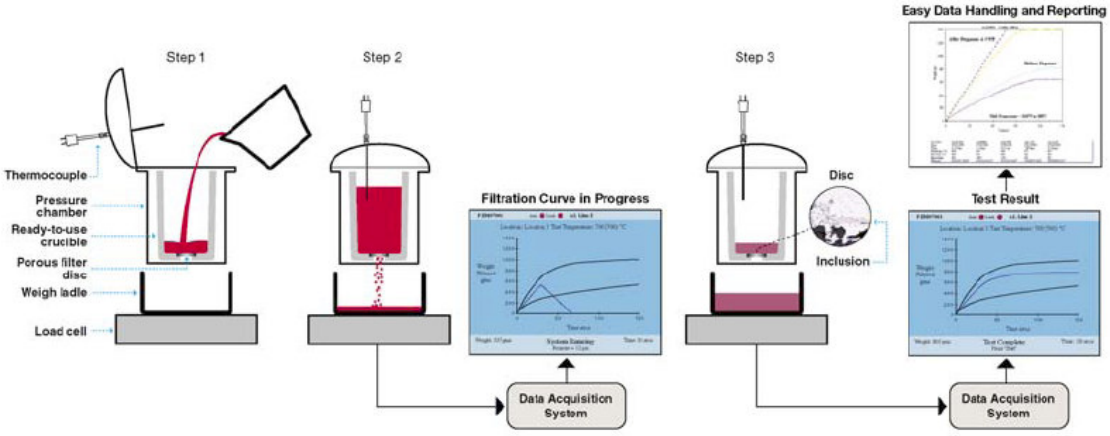

Figure 3.8 *Schematic illustration of working principle of pressure filtration technique (Enright et al., 2003).*

3.1.3 Characterisation techniques

<u>Quantitative evaluation of the grain size of α-Al</u>

There are two approaches to assessing the grain size. The scanning electron microscope (SEM) based techniques of colour orientation contrast imaging (COCI) and automated electron backscatter diffraction (EBSD) patterns were found to be reliable when compared to the conventional optical microscope (OP) based techniques, with less boundaries missed (Day and Quested, 1999; Humphreys, 1999; Gao *et al*., 2005). In fact, both COCI and EBSD techniques are mainly used for nano-sized specimens due to the low speed of data acquisition. In consideration of the efficiency and cost-effectiveness, in the present study,

optical microscopy with an image analysis system was employed to quantitatively analyse the grain size from anodized samples.

The metallographic samples for optical microscopy and scanning electron microscopy (SEM) were prepared using standard metallographic procedures. The samples for grain size measurement were anodized with Barker's reagent (4% HBF_4 in distilled water) and then viewed under polarized light using a Zeiss optical microscope with an Axio Vision 4.3 image analysis system. The mean linear intercept technique was used to measure the grain size and the values of mean linear intercept are quoted throughout this thesis. In each case, at least 300 grains were measured.

Quantitative analysis of the size and size distribution of Al_3Ti intermetallics

Based on the thermodynamically calculated results, formation of Al_3Ti intermetallic particles can be expected in this alloy and quantitative analysis of the size and size distribution of Al_3Ti intermetallic particles were carried out for TP-1 samples. The number of fields of view using a Zeiss optical microscope with an Axio Vision 4.3 image analysis system for quantitative analysis was 50 at 100×.

SEM investigation of oxides formed in a model alloy

The oxides formed in an Al-20Zn-0.05Ti alloy were concentrated by pressure filtration technique and investigated by scanning electron microscopy (SEM) and energy dispersive X-ray spectroscopy (EDX) analysis. SEM was carried out with a field emission gun Zeiss Supera 35 machine, equipped with an EDX facility and operated at an accelerating voltage of 5-20 kV.

3.2 Formation of Fe-containing intermetallics in an AlSiCuFeMg alloy under intensive shearing

In this chapter, convection-free isothermal holding of a liquid alloy of LM24, at a holding temperature above the precipitation temperature of the primary Fe-containing intermetallic phase, combined with subsequent different cooling modes was carried out to investigate the influence of cooling rate on the formation of Fe-containing intermetallics. MCAST was used to investigate the crystallization behaviour of the Fe-containing intermetallic phases under intensive shearing conditions. HPDC and MC-HPDC tensile samples were prepared and mechanically tested to compare their mechanical response to the modification of the Fe-containing intermetallic phase.

3.2.1 Compositions of an AlSiCuFeMg alloy

The specific composition of the LM24 alloy used in this investigation is given in **Table 3.2**. One of the reasons for choosing this alloy with a relatively high level of iron and low level of manganese was to make sure the Fe-containing intermetallic phase formed as a primary phase. The other reason was to investigate the formation of α-AlFeSi in an alloy with a low value of Mn/Fe ratio.

Table 3.2 *Composition of the LM24 alloy used in this investigation (in wt.%).*

Si	Fe	Mn	Mg	Cu	Zn	Ni	Al
7.76	1.08	0.27	0.11	3.21	2.28	0.03	Balance

3.2.2 Processing procedures adopted

Convection-free isothermal holding and solidification experiments

Isothermal holding experiments were carried out using a modified convection-free isothermal holding apparatus, which was developed by Cao (Cao and Campbell, 2003), as shown in **Figure 3.9.**

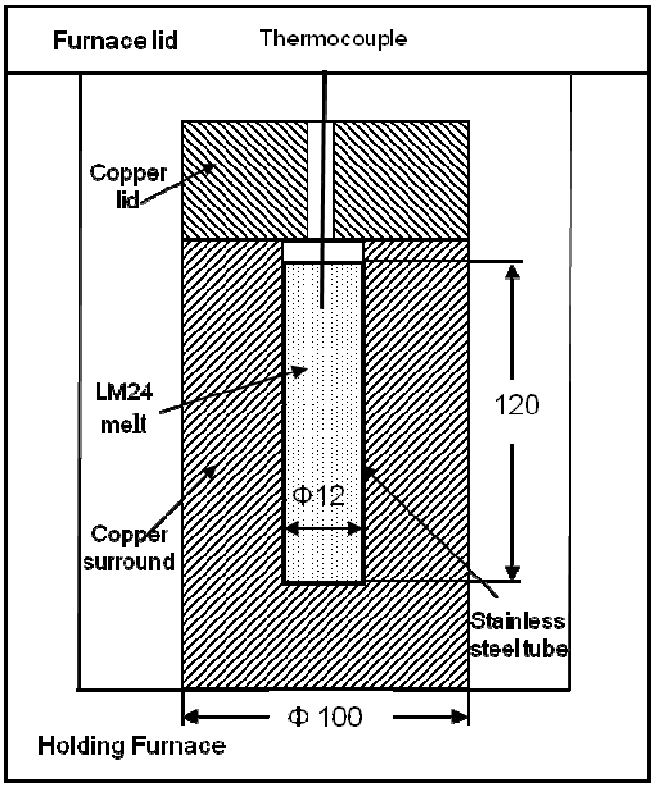

Figure 3.9 *Experimental apparatus used for the convection-free isothermal holding experiments.*

The dimensions of the holding crucible were 12mm in diameter and 120mm in length. It was made of stainless steel and internally coated with boron nitride to avoid contamination of the alloy melt during isothermal holding. The use of a copper surround (made from commercially pure copper) facilitated the rapid homogenisation of the melt temperature to the holding temperature and minimised the natural convection occurring inside the resistance-heated

furnace during isothermal holding. The alloy was melted at 730^{o}C. After being melted, the alloy melt was homogenised for 2 h. The melt at 730°C was poured into the holding crucible, which had been preheated at 730°C and wrapped with thermal insulation, and then the holding crucible was quickly transferred into a massive copper surround (**Figure 3.9**). The copper surround had been held at the holding temperature in the resistance-heated holding furnace. The high preheated temperature for the holding crucible and rapid transfer were needed to effectively quench the liquid to the isothermal holding temperatures. The isothermal holding temperature was monitored by a *K* type thermocouple positioned in the centre of the liquid alloys from a fixed distance from the base of the mould to ensure reproducibility of the measurements (**Figure 3.9**).

There were two points of differences between our work and that of Cao and Campbell. One was the isothermal holding temperature. Two types of isothermal holding temperatures were adopted, either below or above the equilibrium formation temperature of the primary Fe-containing intermetallic phase, to investigate the Fe-containing intermetallic phase evolution, i.e. 643 and 652, 665, 674, 684, 700^{o}C. The other was the cooling modes immediately after isothermal holding.

Different cooling modes immediately after isothermal holding

In order to evaluate the influence of different cooling rate at the formation temperature of Fe-containing intermetallic phases in the LM24 alloy, three types of subsequent cooling modes after isothermal holding, namely, furnace cooling, air cooling and end chilling, were explored. After the isothermal holding apparatus had been taken off the holding furnace, air cooling was carried out with the sample cooled inside the copper surround leaving the whole setup sitting on a refractory brick; End chilling was then performed by utilizing of a copper plate 50mm in thickness immediately after the holding crucible was lifted together with the

liquid alloy from the copper surround. The lowest cooling rate in the current study was obtained by leaving the isothermal holding apparatus in the holding furnace and switching off the power to the furnace. In the following section, the solidification experiments including convection-free isothermal holding and subsequent different cooling modes are simply named convection-free solidification.

Melting and intensive melt shearing by the MCAST

In all cases, the alloy was melted at 730^{o}C. After being melted, the alloy melt was homogenised for 2 h. In the cases of TP-1 and pressure filtered samples, with intensive melt shearing, the alloy melt was directly poured into the MCAST unit at 730^{o}C. The rotation speed of the MCAST unit was set at 500rpm and the shearing temperature was set at 645^{o}C for 60 s. In the case of MC-HPDC sample, three different shearing temperatures were investigated, namely, 645, 620, 580^{o}C. For each shearing process, the alloy melt was poured into the MCAST unit at 730^{o}C. The rotation speed of the MCAST unit was fixed at 500rpm and the shearing time was fixed at 60 s.

TP-1 samples

The standard TP-1 mould was adopted to evaluate the formation of Fe-containing intermetallic phase in the LM24 alloy under a well controlled cooling mode with a medium cooling rate. With shearing, after being sheared for 60 s, the alloy was cast into TP-1 mould. Without shearing, the alloy melt was air cooled to 645^{o}C and then cast into TP-1 mould.

Pressure filtration to concentrate the Fe-containing intermetallic phases

In addition to isothermal holding experiments, pressure filtration was utilized to concentrate the Fe-containing intermetallic phases formed. With shearing, the alloy melt was transferred into the pressure filtration crucible immediately after being sheared at 645^{o}C for 60 s.

Without shearing, the alloy melt was air cooled from 750^{o}C to 645^{o}C, and poured into the pressure filtration crucible, and then the pressure filtration operation was started.

Preparation of HPDC and MC-HPDC tensile testing samples

The alloy was subjected to HPDC with and without intensive melt shearing by MCAST to compare the characteristics of the Fe-containing intermetallic phase and to assess the mechanical properties. After the alloy had been sheared for 60 s, it was directly transferred to a standard cold chamber HPDC machine. A 280-ton cold chamber high pressure die caster (LK® Machinery Co. Ltd., Hong Kong) was used to produce standard tensile test specimens, 6.4mm in gauge diameter and 25mm in gauge length. Specimens for microstructural observation were cut from the middle of the gauge length of the tensile test bars. The parameters used in high pressure die caster for the preparation of MC-HPDC sample are listed in **Table 3.3.**

Table 3.3 *Parameters of high pressure die casting used for the preparation of MC-HPDC samples.*

Die temperature, ^{o}C	Filling pressure	Intensification pressure	Pouring temperature, ^{o}C	Melting temperature, ^{o}C
180	60%	85%	700	750

3.2.3 Characterisation techniques

X-ray diffraction analysis of the sedimented Fe-containing intermetallics

Fe-containing intermetallics precipitated close to the base of the sample isothermally held at 665^{o}C and solidified by air cooling, was analysed by X-ray diffractometry (XRD) using a Bruker D8 Advance X-ray diffractometer with Cu radiation at a voltage of 40 kV and a current of 40 mA.

SEM investigation of the Fe-containing intermetallics in the convection-free solidified sample

Scanning electron microscopy (SEM) was carried out with a field emission gun Zeiss Supera 35 machine, equipped with an energy dispersive X ray spectroscopy (EDX) facility and operated at an accelerating voltage of 5-20 kV. At least five independent EDX measurements, which were calibrated with a pure copper standard sample prior to measurement, were performed to obtain each average value from different areas using a fixed accelerating voltage of 15 kV.

SEM characterisation of the Fe-containing intermetallics in HPDC and MC-HPDC samples

To characterise the microstructural features, with a focus on the Fe-containing intermetallic particles formed, SEM combined with EDX analysis were performed. Scanning electron microscopy (SEM) was carried out with a field emission gun Zeiss Supera 35 machine, equipped with an energy dispersive X-ray spectroscopy (EDX) facility and operated at an accelerating voltage of 3-20 kV. At least five independent EDX measurements, which were calibrated with a pure copper standard sample, were performed to obtain each average value from different areas using a fixed accelerating voltage of 15 kV.

Quantitative analysis of the area fraction of Fe-containing intermetallics

Quantitative analysis of the area fraction of Fe-containing intermetallic phases in HPDC and MC-HPDC samples was performed under optical microscopy using a Zeiss optical microscope with an Axio Vision 4.3 image analysis system for quantitative analysis with about 25 fields at 500× from one edge of the tensile sample to the other edge. The quantitative analysis was carried out along three different lines over the cross section for each sample.

Quantitative characterisation of the porosity content in HPDC and MC-HPDC samples

Quantitative analysis of the area fraction of the porosity formed in HPDC and MC-HPDC samples was performed under optical microscopy using a Zeiss optical microscope with an Axio Vision 4.3 image analysis system with about 7 fields at 100× from one edge of the tensile sample to the other edge. The quantitative analysis was carried out along three different lines over the cross section for each sample.

3.2.4 Mechanical properties of HPDC and MC-HPDC samples

The mechanical properties were measured at room temperature by a universal materials tensile testing machine (Instron® 5569) at a crosshead speed of 1mm/minute (strain rate: 0.66×10^{-3} s^{-1}). In each case, at least 8 samples were tensile tested and averaged to give the values of corresponding properties.

3.3 Grain refinement in Al-Mg binary alloys by intensive shearing

Magnesium is one of important alloying elements in Al alloys. As the majority of Al alloys have some magnesium in the intermediate compositional range (between 0.005 and 7wt.%), a $MgAl_2O_4$ or MgO film is usually to be expected. The influence of intensive melt shearing on the grain refining effect in Al-Mg binary alloys was investigated.

3.3.1 Compositions of Al-Mg binary alloys

A wide range of magnesium containing Al-Mg binary alloys were subjected to intensive melt shearing, ranging from 0, 0.2, 0.7, 1.0, 3.0, 5.0 to 7wt.%Mg. A commercial purity Al (CP Al, **Table 3.4**) and a pure Mg (≥99.95wt.%). ingot were used to prepare the Al-Mg binary alloys.

Table 3.4 *Composition of CP Al used in the present study (in wt. %).*

Al	Mg	Si	Fe	Mn	Ni	Zn	Cr	Cu	Ti
99.86	<0.001	0.03	0.08	0.001	0.0047	0.003	0.001	0.001	0.006

3.3.2 Processing procedures adopted

High temperature melt shearing

A MCAST unit was developed with a higher running temperature of up to 850^{o}C. In all cases, the shearing temperature was set at 700^{o}C, the rotation speed of the MCAST unit was set at 500rpm and the shearing time was 60 s.

TP-1 samples

The standard TP-1 test was adopted to cast samples for grain size assessment. The melting temperature was 750^{o}C. After homogenization for 1h, the alloy melt at 750^{o}C was poured into the MCAST unit for intensive shearing. After being sheared for 60 s, the melt was directly cast into a TP-1 mould, which had been preheated at 350^{o}C for 2 h. For the cases without shearing, alloy melts were air cooled from 750 to 700 ^{o}C then cast into TP-1 mould.

Investigation of the oxides formed in Al-Mg binary alloy melts

In order to investigate the oxides formed on the surface of liquid Al-Mg binary alloys, the oxides were concentrated by means of the pressure filtration technique. Two levels of magnesium containing Al-Mg alloys were investigated, namely, 0.7 wt. % and 5.0 wt. % Mg.

For the cases without shearing, in both Al-0.7 wt. % Mg and Al-5.0 wt. % Mg alloy melts, the oxides were concentrated after isothermal holding at 700^{o}C for 4 h. For the cases with shearing, Al-5.0 wt. %Mg alloy was sheared at 700^{o}C for 60 s with the rotation speed set at 500 rpm and then immediately subjected to pressure filtration.

Identification of the exposed surface of spinel oxide in Al-0.7Mg

In order to identify the exposed surface of naturally occurring surface of spinel in Al-0.7Mg alloy, an Al-0.7Mg alloy was melted and isothermally held at 800^{o}C for 4 h in a resistance furnace for 4 h and then pressure filtered at 700^{o}C. The high melting and holding temperature ensured that sufficient large sized spinel particles formed to facilitate the measurement of the angle between the exposed surfaces with a number of SEM micrographs. 20 SEM micrographs were measured to obtain statistically important data of the angle between two exposed surfaces of spinel. By comparison with the data of the angle between {111} planes in an ideal fcc crystal, namely 70.5^{o} or 109.5^{o}, the exposed surfaces of spinel particles can be identified by whether they are {111} or not. The metallographic sample was prepared by standard metallographic technique and then observed using a Zeiss Supera 35 FEG microscope, equipped with an energy dispersive X-ray spectroscopy (EDX) facility, operated at an accelerating voltage of 5-15 kV.

3.3.3 Characterisation techniques

Grain size assessment

The metallographic samples for optical microscopy and scanning electron microscopy (SEM) were prepared using standard metallographic procedures. The samples for grain size measurement were anodized with Barker's reagent (4% HBF_4 in distilled water) and then viewed under polarized light using a Zeiss optical microscope with an Axio Vision 4.3 image analysis system. The mean linear intercept technique was used to measure the grain size and the values of mean linear intercept are quoted throughout this thesis. In each case, at least 300 grains were measured.

SEM observation of the oxides formed in Al-Mg binary alloys

The collected oxide samples, in both Al-0.7 wt. % Mg and Al-5.0 wt. % Mg alloys, and the one sheared at 700°C of Al-5.0wt.% Mg alloy, were all investigated by scanning electron microscopy using a Zeiss Supera 35 FEG microscope, equipped with an energy dispersive X ray spectroscopy (EDX) facility, operated at an accelerating voltage of 5-15 kV, to investigate the evolution of oxide particles with magnesium content in Al-Mg binary alloys and melt shearing conditions.

TEM investigation of the oxides formed in Al-Mg binary alloys

The oxide samples concentrated from Al-0.7 wt. % Mg alloy by pressure filtration were made into thin foils for TEM investigation. The morphological characteristics and crystallographic orientation relationship with the α-Al phase were investigated to understand the grain refining mechanisms by intensive melt shearing using a JEOL 2000FX analytical TEM.

3.4 Grain refining in a commercial purity Al by intensive shearing

3.4.1 Compositions of a commercial purity Al

The compositions of a commercial purity Al (CP Al) used in this section was the same as the one used in Section 3.3.1, as shown in **Table 3.4**.

3.4.2 Processing procedures adopted

Influence of superheating on the grain size of CP Al

In order to investigate the effect of the oxides naturally occurring in liquid aluminium on the grain size of CP Al, different melting temperatures, ranging from 680, 700, 720, 740, 760, 800, 840, 880 to 920°C, were adopted and the grain structure and grain size of TP-1 sample were evaluated. In consideration of the fact that the reverse transformation from α- to γ-Al_2O_3

does not occur on cooling (Yan *et al.*, 2010), influence of different thermal histories of the alloy melt, i.e. both increasing and decreasing melt temperature, on the microstructures of CP Al were investigated. For the samples cast during decreasing melting temperature, the CP Al melts were superheated to 940^{o}C, homogenised for 1 h, and then air cooed to target cast temperatures and cast into TP-1 mould.

Melting and high temperature intensive melt shearing for CP Al

The high temperature MCAST unit was used to investigate the grain refining effect of intensive shearing on CP Al. A wide range of shearing temperatures from 680, 700, 720, 740, 760, 800, to 840^{o}C were explored to study the influence of the superheat of the shearing temperature on the grain refining effect of CP Al. In each case, CP Al was melted at a temperature 30^{o}C above the corresponding shearing temperature and after being melted, homogenised for 1 h and then poured into the MCAST unit for shearing. For the samples sheared at 680^{o}C, the melting temperature of CP Al was set at 730^{o}C to ensure a complete melting.

TP-1 sample

After the CP Al melt had been sheared at the corresponding temperature for 60 s, the melt was directly cast into a TP-1 mould to facilitate the grain size assessment by subsequent sample preparation and linear intercept counting. In all cases, the TP-1 mould was preheated to 350^{o}C for 2 h.

Oxides collection

In order to investigate the oxides formed on the surface of CP Al melt, two types of collecting methods were explored. One was collected by skimming and collecting the films formed on the melt and then remelting the entrained aluminium as much as possible. The other one was concentration via the pressure filtration technique. The first method was applied to the non-

sheared CP Al melts both at 700°C and 920°C. The second method was applied to both sheared and non-sheared melts at 700°C. The reason for choosing theses two temperatures is to obtain γ-Al_2O_3 and α-Al_2O_3, respectively, according to the understanding of the formation temperature of γ-Al_2O_3 and α-Al_2O_3 in liquid Al alloys (Narayanan, *et al.* 1994).

Isothermal holding and collection of oxides by skimming from the melt surface

In order to understand the morphological features of the oxides formed in CP Al melts at different superheating temperatures, oxides formed on the melt surface were skimmed carefully. For the oxides collected at 700°C, the melt was subjected to extended oxidation by isothermal holding in a graphite crucible for 24 h. For the oxides collected at 920°C, it was oxidized and isothermally held in the same crucible for 3 h. The graphite crucible was internally coated with boron nitride.

Isothermal holding and collection of oxides by the pressure filtration technique

CP Al was melted at 750°C and then homogenised at 700°C for 5 h. During isothermal holding, the melt was stirred using a ceramic bar every 20 minutes to generate more oxides. The pressure filtration experiment was carried out at 700°C immediately after the melt was transferred to the filtration crucible. For the sample held at 920°C for 5 h, the melt was stirred using a ceramic bar every 20 minutes to generate more oxides. The graphite crucible used for the melting and holding of CP Al was internally coated with boron nitride.

Intensive melt shearing and pressure filtration

CP Al was melted at 750°C, homogenised at 700°C for 1 h and then subjected to shearing at 700°C for 60 s. Immediately after being sheared, the sheared melt was directly transferred to the pressure filtration crucible to concentrate the oxides formed.

3.4.3 Characterisation techniques

Assessment of grain structures and grain sizes

Metallographic sample preparation and macro etching

Specimens for grain size assessment were cut from the cross section 38mm from the base of TP-1 samples. The specimens were prepared by the standard metallographic procedure. The longitudinal section of the TP-1 sample was prepared by the standard metallographic procedure and then was macro etched. A modified Keller's reagent was used for macro etching.

Electropolishing

For CP Al, due to the fact that it is low in alloying elements, an electropolishing after normal mechanical polishing was necessary to highlight the grain boundaries. The electropolishing solution was: 5ml $HClO_4$ (perchloric acid), 95ml CH_3COOH. The value of the applied voltage was 30~35V for 120 s.

Anodizing and quantification of grain sizes

After electropolishing, the samples for grain size measurement were anodized at an applied voltage of 20 V for 60-90 s with Barker's reagent (4% HBF4 in distilled water) and then viewed under polarized light using a Zeiss optical microscope with an Axio Vision 4.3 image analysis system. The mean linear intercept technique was used to measure the grain size and the values of mean linear intercept are quoted. In each case, at least 300 grains were measured.

X-ray diffraction to identify the crystal structures of the oxides formed

The collected oxides samples, both at 700^{o}C and 920^{o}C, were analysed by X-ray diffractometry (XRD), which was performed using a Bruker D8 Advance X-ray

diffractometer with Cu radiation at a voltage of 40 kV and a current of 40 mA. The parameters were as follows: 2θ range: from 5-100^{o}, step time: 61.59998s; step size: 0.009172^{o}. For the sample collected at 700^{o}C, due to the thin film feature of the oxide formed at this temperature, a low scanning rate was adopted. The parameters were as follows: 2θ range: from 30-70^{o}, step time: 154.005005s; step size: 0.009172^{o}.

SEM investigation of the evolution of the oxides formed in CP Al melt

The collected oxide samples, both at 700^{o}C and 920^{o}C, and the sample sheared at 700^{o}C and then pressure filtered, were also investigated by scanning electron microscopy using a Zeiss Supera 35 FEG microscope, equipped with an energy dispersive X ray spectroscopy (EDX) facility, operated at an accelerating voltage of 5-15 kV, to investigate the evolution of oxide particles with different melting temperatures and shearing conditions.

TEM and HRTEM investigations of the oxides formed in CP Al melt

The oxides concentrated from CP Al melts by pressure filtration at 700^{o}C and 920^{o}C, were prepared into thin foils to facilitate TEM investigation. The identity of the oxides formed was further confirmed by selected area diffraction pattern and TEM-DEX analysis. The crystallographic features of the oxides were investigated to understand the grain refining mechanisms by intensive melt shearing. HRTEM analysis was conducted on a Tecnai FEG F30 TEM instrument operated at an accelerating voltage of 300 kV.

Chapter 4

Grain refinement in an AlZnMgCuTi wrought alloy by intensive shearing

4.1 Introduction

In direct chill (DC) casting of aluminium alloys, grain refinement has influence on the mechanical properties of the solidified materials, the homogenization treatment kinetics, the formability during thermo-mechanical processing, the occurrence of surface defects during downstream processing, and the anodizing properties (McCartney, 1989; Nadella *et al.*, 2008; Greer, 2003). During casting, grain refinement directly influences the formation of porosity and hot tearing. The macrosegregation features and microsegregation scale, especially when related to transport phenomena, are strongly influenced by the grain refining strategy.

Al-Ti-B master alloys as grain refiner additions are commonly added to melts for the DC ingot production of wrought aluminium alloys. However, only less than 1% of the added particles successfully nucleate aluminium grains and this low efficiency is undesirable not only for its immediate cost implications, but also because refiner particles may themselves be detrimental in the final microstructures (Greer, 2003) particularly for products intended for extrusion, deep drawing, or high performance structural applications (McCartney, 1989).

Recently, the Melt Conditioning by Advanced Shear Technology (MCAST) has been developed for conditioning liquid metal under intensive forced convection before

solidification. It has been demonstrated that naturally occurring oxides can enhance heterogeneous nucleation for microstructural refinement in commercial Mg-Al alloys (Fan *et al.*, 2009).

The aim of this chapter is to investigate the grain refining effect in a modified commercial wrought Al alloy by intensive melt shearing. We have used a specially designed solidification procedure with a scheme to eliminate the influence of pouring operation on the grain structures. A standard TP-1 mould (TP-1, 1987) and a wedge-shaped copper mould were used to assess the grain refinement by intensive melt shearing under varying cooling rates. A pressure filtration technique (Cao, 2005) combined with SEM observation and quantitative metallographic analysis was used to investigate the evolution of oxides and correlate it with the achieved grain refinement. Based on these experimental results, a multi-step nucleation mechanism is proposed.

4.2 Results

4.2.1 Thermodynamic assessment of the equilibrium formation temperature of Al_3Ti in an experimental alloy

The determination of the equilibrium formation temperature of Al_3Ti is critical to the selection of parameters for melt shearing. The thermodynamically calculated equilibrium volume fractions of both the Al_3Ti and α-Al phases are presented in **Figure 4.1**, as a function of temperature for the experimental AlZnMgCuTi alloy using FactSage software. **Figure 4.1** suggests that the equilibrium formation temperature of Al_3Ti in the experimental alloy is 729^oC.

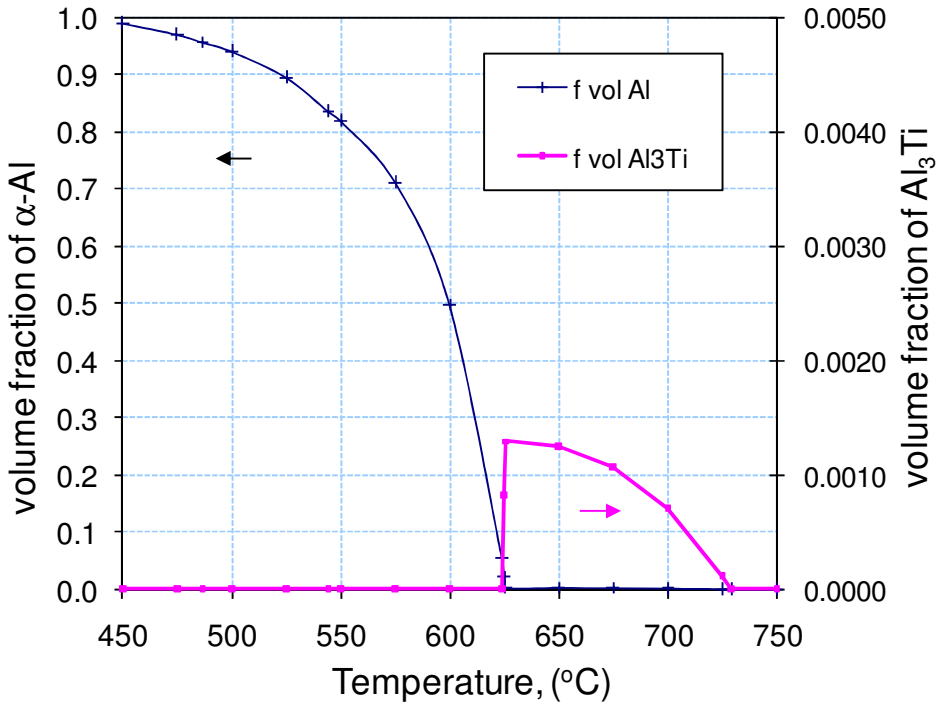

Figure 4.1 *Thermodynamically calculated solid fraction and volume fraction of Al_3Ti in an AlZnMgCuTi alloy using FactSage software.*

4.2.2 Grain refining effect by intensive melt shearing

In order to demonstrate the grain refining effect by intensive melt shearing, a specially designed solidification experiment was carried out, as displayed in **Figure 3.3**, to eliminate the influence of melt pouring operation on the solidification nucleation event, such as catalysis mechanism of mould wall. The grain refinement by intensive melt shearing is shown in **Figure 4.2**. The grain size in the sheared sample was decreased to 260 μm (**Figure 4.2b**) compared to 620μm for the non-sheared sample (**Figure 4.2d**). Chilled grains adjacent to the mould wall and a coarse equiaxed grain structure were observed in the non-sheared sample (Edge: **Figure 4.2a** and Centre: **Figure 4.2b**). For the sheared sample, chilled grains adjacent to the mould wall were not observed and the grain structures both near the edge and in the interior were finer and more uniform (Edge: **Figure 4.2c** and Centre: **Figure 4.2d**).

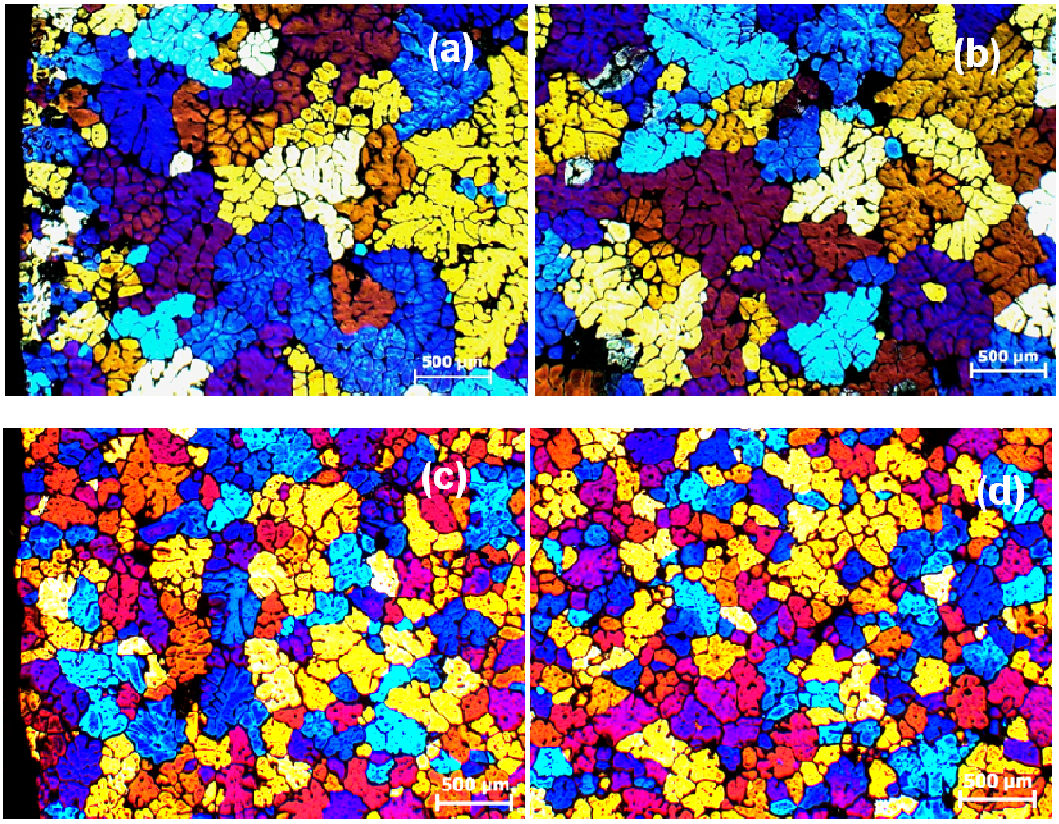

Figure 4.2 *Grain refinement by intensive shearing demonstrated in specially designed solidification procedure. (a) edge zone and (b) central region showing the coarse and non-uniform grain structures in the non-sheared sample; (c) edge zone and (d) central region showing much finer and uniform grain structures in the sheared sample.*

4.2.3 Influence of shearing time on the grain refinement by intensive shearing

A range of shearing time was adopted to investigate the influence of shearing time on the grain refinement effect. The influence of shearing time on the grain size of TP-1 samples is shown in **Figure 4.3**, with the alloy melts directly transferred into the MCAST unit (scheme C in **Figure 3.6**). The plot of grain size against shearing time indicates that the grain size reaches a minimum after 10~20 s.

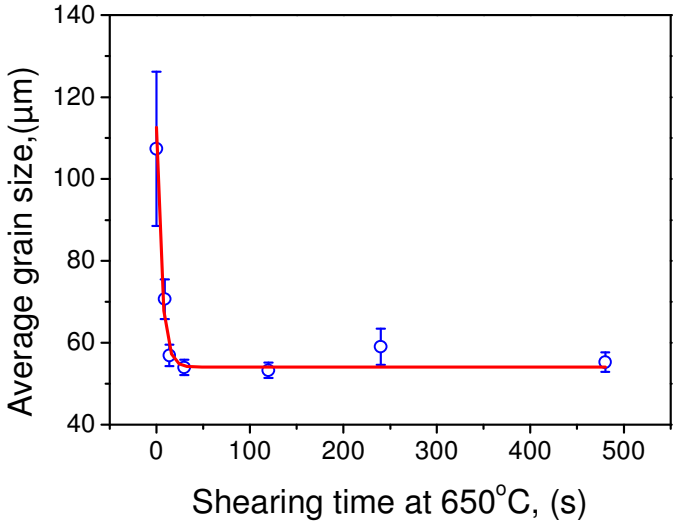

Figure 4.3 *Influence of shearing time on the grain refinement in TP-1 samples, with the alloy melts directly transferred into the MCAST unit (scheme C in Figure 3.6). The solid lines represent the best fit to the experimental data.*

4.2.4 Influence of thermal history on the grain refinement by intensive shearing

In order to experimentally clarify the grain refining effect of intensive shearing via the enhanced heterogeneous nucleation by activating the nucleation sites on oxide particles, the pouring temperature of alloy melt into the MCAST unit was set at different temperatures (**Figure 3.6**). Typical optical micrographs of the TP-1 samples cast at 650°C with different thermal histories are presented in **Figure 4.4**. For the sample without shearing (processing scheme A in **Figure 3.6**), the average grain size was 123±24μm, (**Figure 4.4a**); for the sample in **Figure 4.4b**, after the melt temperature was air cooled to 650°C, then poured into the MCAST unit and sheared (scheme B in **Figure 3.6**), the grain size was 120±21 μm almost the same as in **Figure 4.4a**; however, in the case of the sample sheared with the melt directly transferred into the MCAST unit from 750°C (scheme C in **Figure 3.6**), the grain size was reduced to 48±3.5 μm (**Figure 4.4c**).

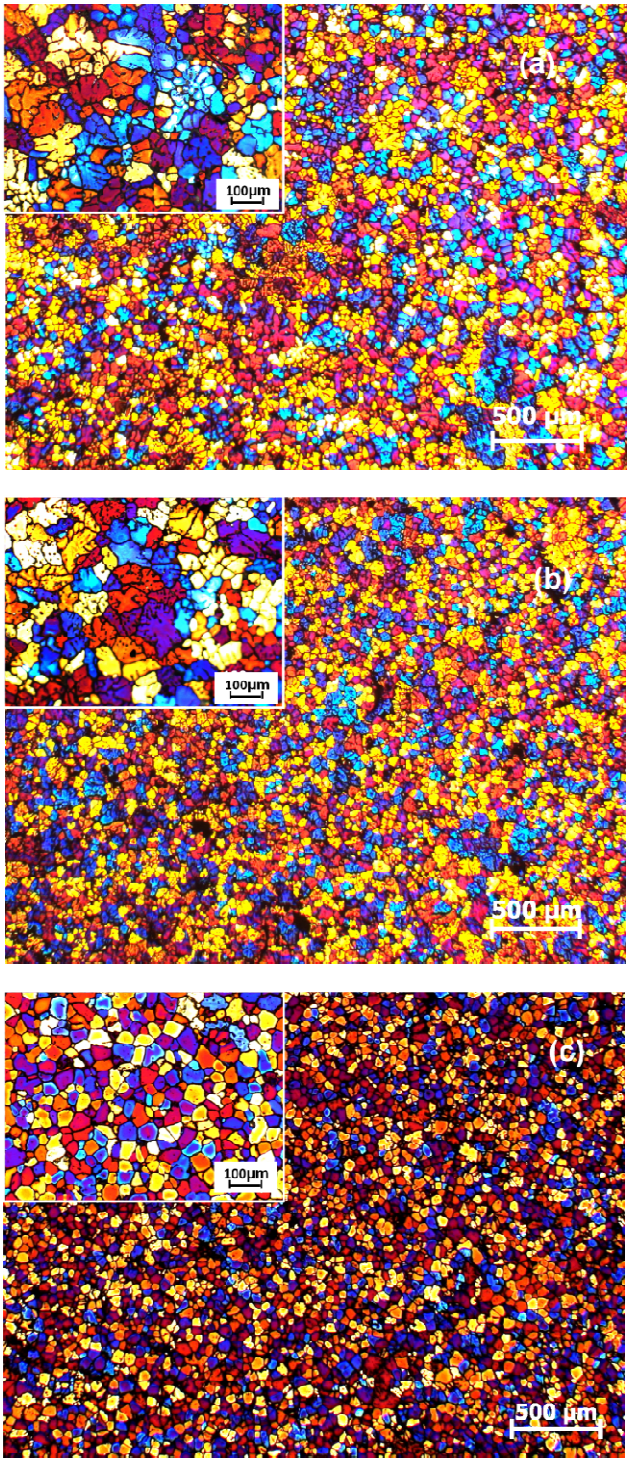

Figure 4.4 *Influence of melt thermal history on the grain structures in TP-1 samples: (a) air cooled to 650 °C from 750°C and cast without shearing (scheme A in Figure 3.6), grain size: 123±24µm; (b) air cooled to 650°C and then sheared (scheme B in Figure 3.6), grain size: 120±21µm; (c) Poured into the MCAST unit at 750°C and then sheared (scheme C in Figure 3.6), grain size: 48±3.5µm. The inserts show high magnification images.*

4.2.5 Effect of cooling rate on the grain refinement with intensive melt shearing

The grain refining effect of intensive shearing in the tip of wedge-shaped samples, where a very high cooling rate of 1000 Ks^{-1} was achieved (Norman, Prangnell, & McEwen, 1998), can be seen in **Figure 4.5**. There was an almost total absence of columnar grains at the edge of the sheared sample (**Figure 4.5b**) in contrast to the readily observed columnar grains at the edge zone of the sample without intensive melt shearing (**Figure 4.5a**).

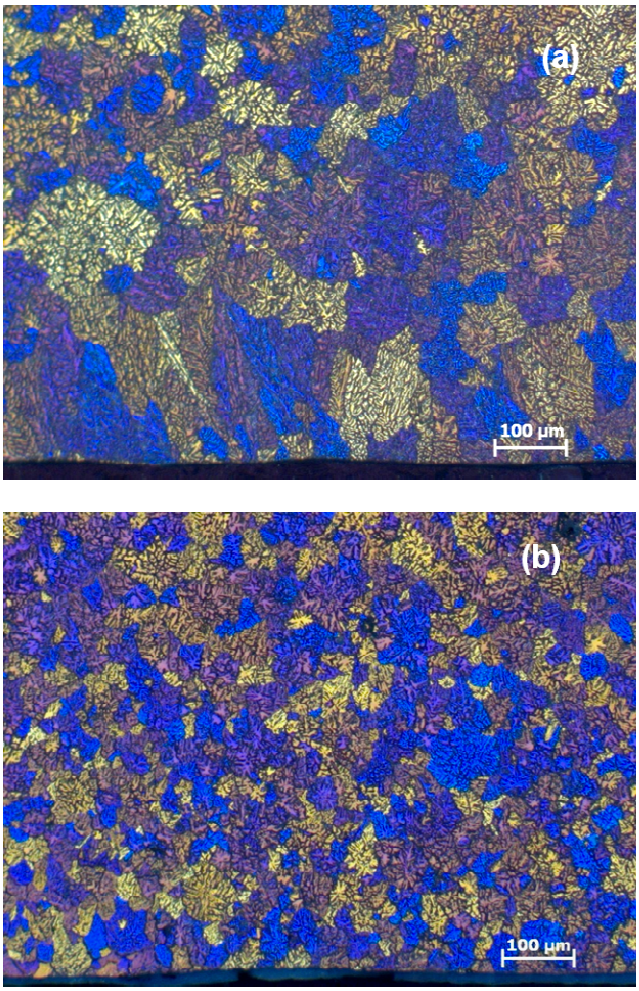

Figure 4.5 *Grain structures in the tip of wedge-shaped samples of experimental alloy: (a) without shearing (scheme A in Figure 3.6), showing columnar dendrites in the location close to the edge of sample; (b) with shearing (scheme C in Figure 3.6), showing much finer equiaxed grains throughout the cross section of sample.*

Figure 4.6 compares the sensitivity of grain size to the variation of cooling rate with and without intensive melt shearing. It can be seen clearly that the grain refinement by intensive melt shearing occurs across the cooling rate range examined and is more pronounced under the conditions of a lower cooling rate during the solidification process.

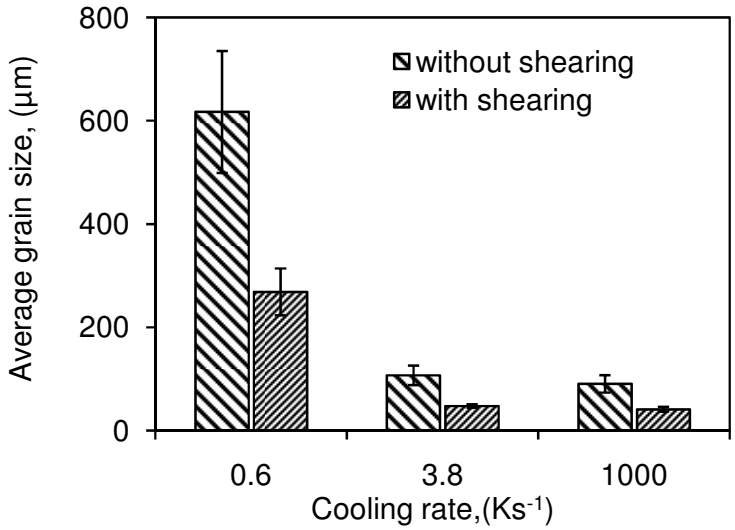

Figure 4.6 *Grain size comparisons under varying cooling rates with and without shearing.*

4.2.6 Characteristics of Al_3Ti intermetallics and oxide particles

Based on the thermodynamically calculated results (**Figure 4.1**), formation of Al_3Ti intermetallic particles can be expected in this alloy. The formation of Al_3Ti in TP-1 samples is compared in **Figure 4.7** and **Figure 4.8**, under conditions with and without shearing. It is seen clearly that Al_3Ti intermetallic particles in the non-sheared TP-1 sample exhibit agglomerates or dendritic morphology, as indicated in **Figures 4.7a**, **4.7c** and **4.8a**. With shearing, Al_3Ti particles show dispersed and almost equiaxed particles, as shown in **Figure 4.7b** and **Figure 4.8b**. Detailed SEM observations were carried out for TP-1 samples with and without shearing, as shown in **Figure 4.9** (scheme C and scheme A in **Figure 3.6**). **Figure 4.9a** shows that Al_3Ti intermetallic particles can be readily observed within the

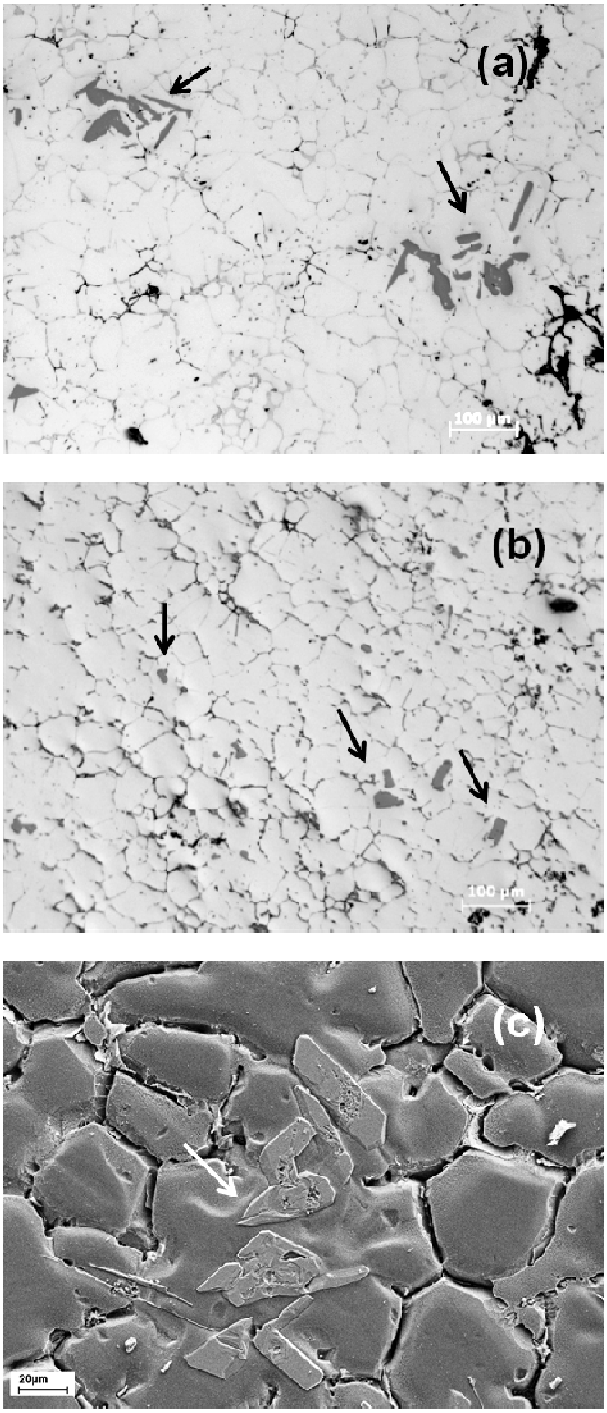

Figure 4.7 *(a) Optical micrograph showing agglomeration of dendritic Al_3Ti particles in a TP-1 sample cast at 650^{o}C without shearing; (b) Optical micrograph of Al_3Ti in a TP-1 sample sheared at 650 ^{o}C, showing dispersed Al_3Ti particles inside grains; and (c) SEM image of Al_3Ti particles showing dendritic morphology in a TP-1 sample cast at 650^{o}C without shearing (after being deep etched).*

interior of refined grains. Comprehensive SEM observations indicated that there is an association between the intermetallic Al_3Ti particles and oxide particles, as shown in **Figures 4.9b** and **4.9c**, where a typical Al_3Ti intermetallic particle is associated with an oxide particle located in the centre of an α-Al grain. The EDX spectrum of the oxide particle shown in the insert of **Figure 4.9c** indicates it possibly to be $MgAl_2O_4$.

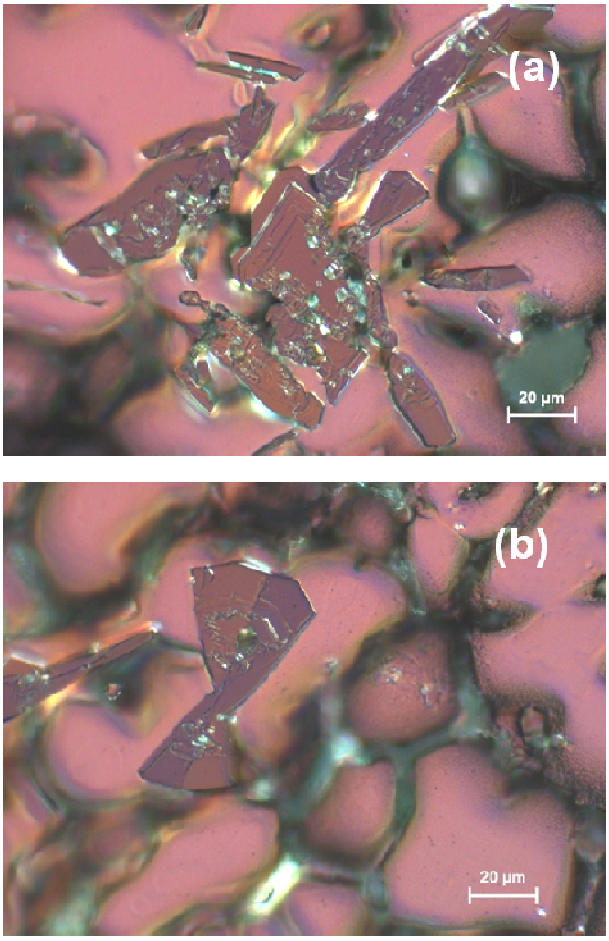

Figure 4.8 *Morphological change of Al_3Ti intermetallic particles by intensive shearing: (a) large dendritic Al_3Ti in a non-sheared TP-1 sample and (b) compact Al_3Ti in a sheared TP-1 sample revealed by deep etching and polarized light observations.*

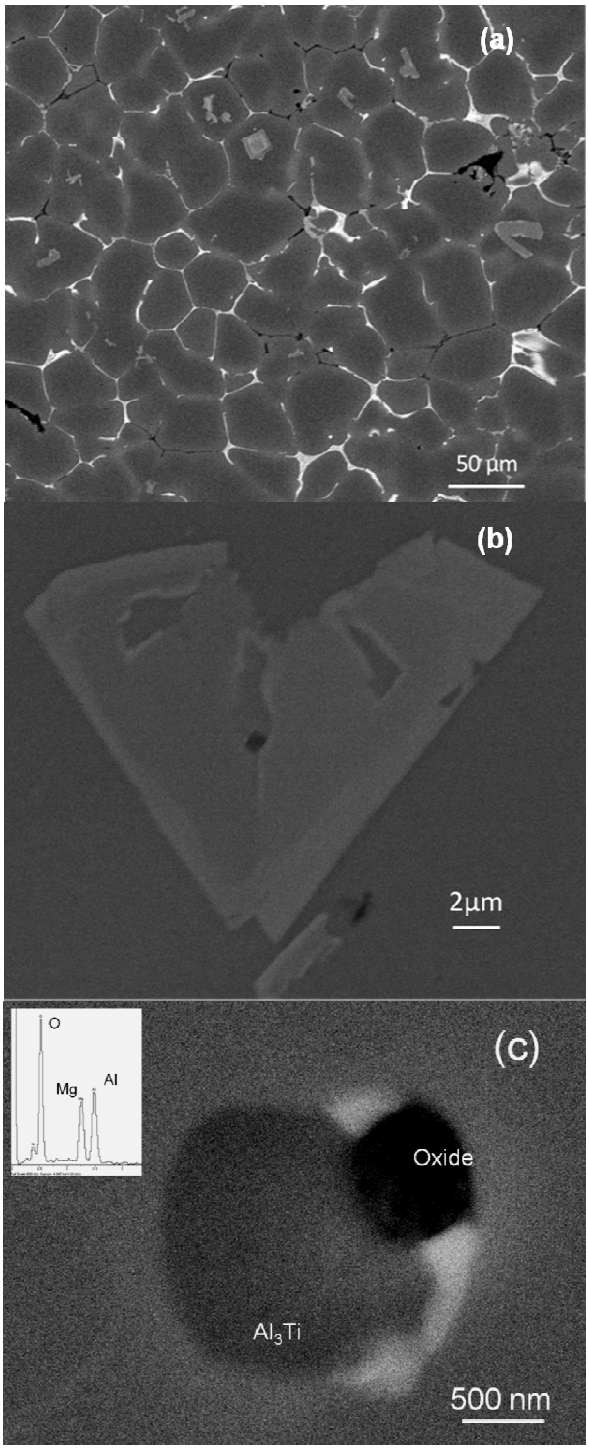

Figure 4.9 *(a) SEM backscattered electron images of grain structure showing frequently observed Al_3Ti intermetallics inside the grain interior in melt conditioned TP-1 sample; (b) SEM image showing the Al_3Ti intermetallic particle associated with oxide particles and (c) high magnification image highlighting an association between Al_3Ti and oxide particles, with insert of the EDX spectrum of the oxide particle indicating it possibly to be $MgAl_2O_4$.*

The size and size distribution of Al_3Ti intermetallic particles in TP-1 samples with (scheme C in **Figure 3.6**) and without shearing (scheme A in **Figure 3.6**) are plotted in **Figure 4.10**, showing that the Al_3Ti particles with intensive shearing have a smaller average size and a narrower size distribution compared to the sample without shearing. For instance, the size frequency of the Al_3Ti particles observed within α-aluminium grains in the sheared TP-1 sample was 78.3% in the range of 6~20μm, compared to the value for the sample without shearing of only 42.7%.

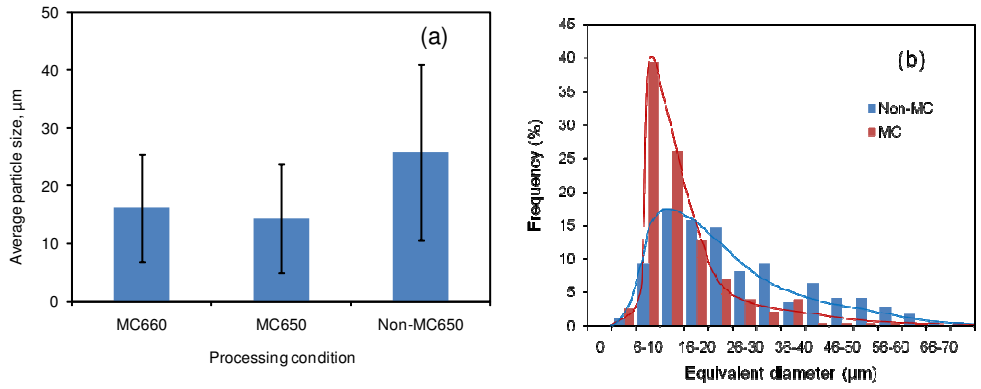

Figure 4.10 *(a) Comparison of average size of Al_3Ti particles and (b) size distributions of Al_3Ti intermetallic particles formed in TP-1 samples with and without shearing (scheme A and C in Figure 3.6).*

4.2.7 Characteristics of oxides formed in a model alloy Al-20Zn-0.05Ti

A model alloy Al-20Zn-0.05Ti was subjected to pressure filtration to investigate the characteristics of oxides formed in the melt with/without intensive shearing. Oxides evolution with intensive shearing is compared in **Figure 4.11** and **Figure 4.12** in the melt of this model alloy. Without shearing, oxides are in the form of oxide films or oxide clusters, as shown in **Figures. 4.11a-c**. Within films or clusters, crystalline oxide particles with sub-micron size are held together by capillary pressure (Fan *et al.*, 2009) and each individual particle is surrounded by other particles rather than the aluminium matrix (**Figure 4.11c**). The SEM-

EDX spectrum shown in **Figure 4.11d** suggests that the oxides formed in the model alloy could be $ZnAl_2O_4$. After intensive shearing, it can be seen from **Figure 4.12** that oxides are in the form of dispersed individual particles, which are embedded in the aluminium alloy matrix.

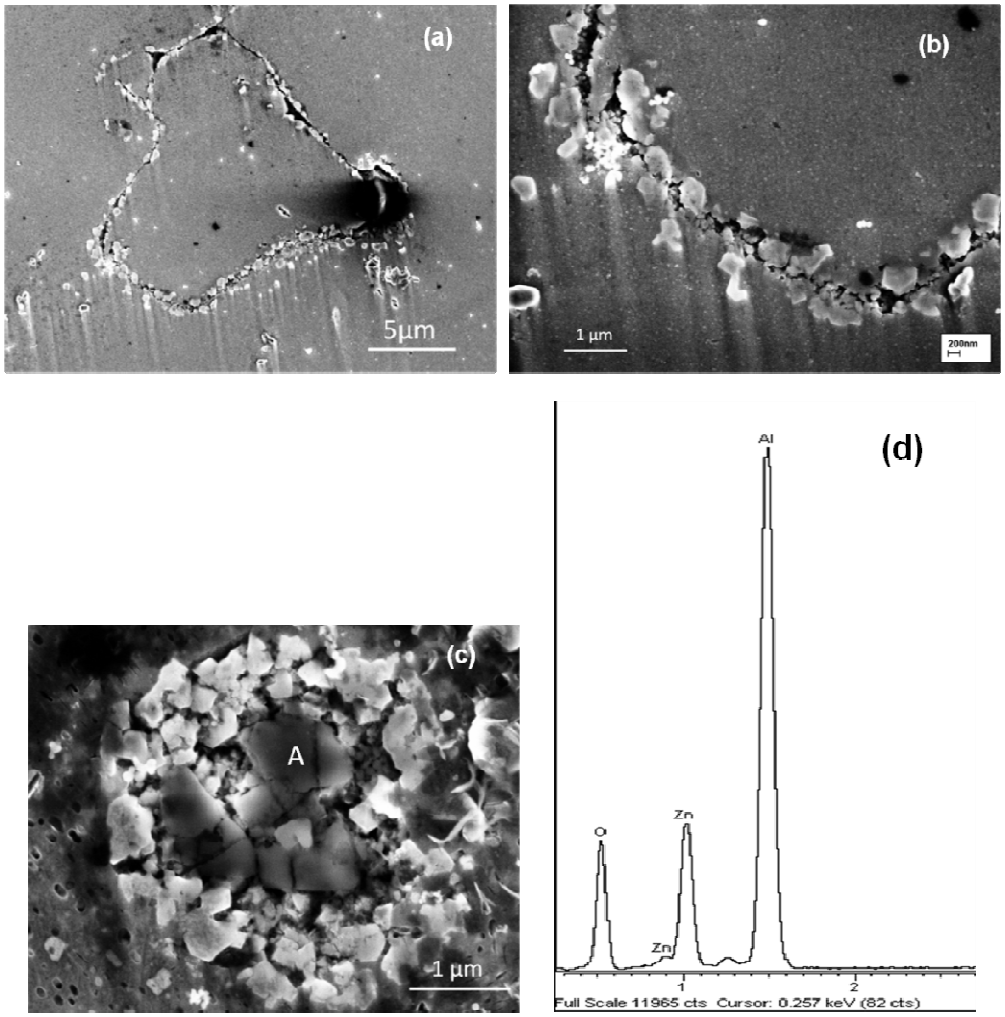

Figure 4.11 *SEM micrographs showing typical morphology of oxides in non-sheared and filtered sample of Al-20Zn-0.05Ti. (a) low and (b) high magnification images of oxide film and (c) of an oxide cluster, both of which consist of oxide particles with sub-micron size in diameter; (d) a typical EDX spectrum of individual oxide particles indicated by "A" in (c), suggesting that it is likely that faceted particles are $ZnAl_2O_4$ phase.*

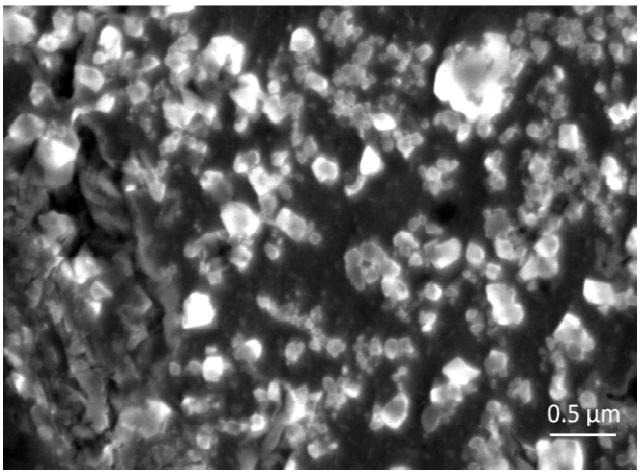

Figure 4.12 *A typical SEM micrograph of dispersed particles of Zn-spinel phase in Al matrix, in the sheared and filtered sample of Al-20Zn-0.05Ti.*

4.3 Discussion

4.3.1 Thermodynamical assessment of equilibrium formation temperature of Al_3Ti

Assessment of the liquidus temperature of the alloy could be done by adding the binary peritectic contribution of Ti to the liquidus of the hypoperitectic multicomponent alloy. However, Fortier et al. mentioned that for a 7046A alloy the formation temperature of Al_3Zr is 20°C higher than that in the Al-Zr binary alloy (Fortier *et al.*, 2008). The same might be true for titanium aluminide in a binary vs. a multicomponent alloy. In the present study, FactSage calculations suggest that the equilibrium formation temperature for Al_3Ti in the experimental alloy is 729°C (**Figure 4.1**), in accordance with the trend published for Al_3Zr (Fortier *et al.*, 2008). Depending on the nucleation conditions, Al_3Ti precipitates may form at a quite variable undercooling or even supercooling temperature (StJohn and Hogan, 1982).

4.3.2 Improved nucleation efficiency of Al_3Ti by intensive shearing

For non-sheared samples, the grain size was coarser and chill zones of finer grain size were found compared to the sheared samples where the grain size was finer and uniform across the

entire sample. This difference in grain structure can be understood as without shearing, nucleation behaviour was triggered by thermal undercooling through the mould wall, whilst after shearing, nucleation occurred throughout the whole volume of the sample by enhanced heterogeneous nucleation and resulted in homogeneous solidification.

Fluid flow during intensive melt shearing has been analysed previously (Ji and Fan, 2002; Ji *et al.,* 2001; Das *et al.*, 2002). The MCAST unit has a pair of screws co-rotating inside a barrel. The screw profiles are fully intermeshing and self-wiping and fluid flow is characterized by a high shear rate and a high intensity of turbulence, with a cyclic variation of shear rate. During shearing, there is an enormous amount of changing interfacial area, providing enhanced heat transfer and strong dispersive mixing. Thus, the melt with intensive shearing is extremely uniform in terms of composition fields, thermal conditions and dispersed individual oxide particles and Al_3Ti particles.

4.3.3 Oxides as nucleation sites of Al_3Ti-a multi step nucleation mechanism

For an oxide particle to act as a nucleus for Al_3Ti there should be good crystallographic matching. Al_3Ti has a tetragonal structure based on an ordered cubic close packed (ccp) structure (Quested, 2004). Each of the oxides possibly formed in the experimental alloy melt, γ-Al_2O_3, MgO, $ZnAl_2O_4$ and $MgAl_2O_4$, has a similar cubic structure (Villars and Calvert, 1991; Surendran *et al.*, 2004). Based on reported lattice parameters and the expression of crystallographic misfit $f=[(d_2-d_1)/d_2]\times100$, where d_2 and d_1 are interatomic spacing of Al_3Ti and each individual oxide phase, respectively, the estimated misfit f along the closely packed directions between Zn-spinel/Mg-spinel and Al_3Ti are only 0.84% and 0.92%, respectively. This means that both Zn-spinel and Mg-spinel could be good substrates for the nucleation of the Al_3Ti phase. In a much more recent investigation on the formation of oxides in Al-6Zn-XMg (X=0 and 2 wt.%) alloys, Zn-spinel and Mg-spinel were detected on the Al-6Zn and Al-6Zn-2Mg alloy samples, respectively (Chen *et al.*, 2010). In the experimental wrought alloy,

the oxide formed is more likely to be Mg-spinel due to the relatively high magnesium content. With melt conditioning, dispersed Mg-spinel particles in the alloy melt may act as active nucleation sites for Al_3Ti particles. When the alloy melt was poured into the MCAST unit from 750^{o}C (scheme C in **Figure 3.6**) in the current study, the existing oxides in the alloy melt were dispersed within a few seconds. Based on the thermodynamic calculation using FactSage software, the formation temperature of Al_3Ti intermetallic phase in the experimental alloy, can be estimated as 729^{o}C (**Figure 4.1**). Hence Al_3Ti would precipitate below this temperature. Due to the good crystallographic match between oxide and Al_3Ti phases as discussed above, Al_3Ti particles would preferably nucleate on oxide particles at relatively low undercooling. This applies for all the sheared samples in the present study except for the case, where the melt temperature was air cooled to 650^{o}C and then poured into the MCAST unit (**Figure 4.4b**, scheme B in **Figure 3.6**). Because of the homogeneous thermal and compositional fields resulting from intensive melt shearing, Al_3Ti particles tend to be equiaxed and with a narrower size distribution, as evidenced by the quantitative metallographic analysis results shown in **Figure 4.10**. Without shearing, the nucleation of Al_3Ti was mainly triggered by thermal undercooling and as a result, Al_3Ti particles exhibited a dendritic morphology and with a wider size distribution, as indicated in **Figure 4.7a** and **Figure 4.8a**.

The respective roles of temperature gradient and nuclei density on the columnar to equiaxed transition (CET) have been well established since Hunt's pioneering work published in 1984 (Hunt, 1984). The role of a grain refining additive is, in essence, to promote the CET (McCartney, 1989). In the modelling work on grain refinement by addition of inoculants (Greer *et al.*, 2000; Quested and Greer, 2004), the isothermal melt model was adopted in which macroscopic temperature gradients were absent, which is a reasonable assumption for air-cooled steel moulds adopted in the specially designed solidification procedure (**Figure**

3.3). At higher gradients such as in the case of wedge-shaped samples a higher nuclei number density is necessary in order to obtain the CET (**Figure 4.5**).

With shearing, dispersed oxide particles and thereby enhanced nucleation of Al_3Ti intermetallic particles with a narrower size distribution will enhance the heterogeneous nucleation of α-aluminium phase. Greer and co-workers developed the free growth model, based on the Al-Ti-B grain refiner system in which TiB_2 particles have high potency of inoculant for α-aluminium (Greer *et al.*, 2000; Quested and Greer, 2004). It was concluded that the grain refinement achieved is determined by a free-growth condition in which the required growth undercooling for free growth, ΔT_{fg}, is inversely proportional to the particle diameter of inoculants, d

$$\Delta T_{fg} = {}^{4\sigma}/_{\Delta S_v}\, d \qquad (4.1)$$

where σ is the solid-liquid interfacial energy and ΔS_v is the entropy of fusion per unit volume. More importantly, in their modelling, based on the understanding of recalescence limiting the number of active nucleation particles and therefore the number of grains, the size distribution of grain refiner particles rather than the size in single fixed value was treated as input. To achieve this, spatially dispersed grain refiner particles throughout the bulk melt are necessary and either settling or agglomeration behaviour of grain refiner particles should be avoided. In other words, the existence of potent nucleating agents may not necessarily lead to grain refinement in the solidified microstructure. For effective grain refinement of a given alloy composition, the potent nucleating particles need to have sufficient numbers, favourable particle size and size distribution.

In the present work, intensive melt shearing was used to disperse the oxide films and clusters into individual oxide particles which promote the nucleation of Al_3Ti particles on these oxide

particles. As a consequence, Al_3Ti particles with a compact and equiaxed morphology and a narrower size distribution were obtained, which in turn enhanced heterogeneous nucleation of α-aluminium grains throughout the entire volume of alloy melt. As a result, significant grain refinement effects can be achieved by intensive melt shearing. This grain refinement mechanism is termed a multi-step nucleation mechanism, as schematically illustrated in **Figure 4.13**. Inside the MCAST unit at 750°C, the oxide films in alloy melt were uniformly dispersed throughout the alloy melt (**Figure 4.13a**). At a temperature below 729°C (the equilibrium formation temperature based on thermodynamic calculation), Al_3Ti nucleated on dispersed oxides particles (**Figure 4.13b**). At a temperature below 625°C (liquidus temperature of α-Al based on thermodynamic calculation), α-Al phase nucleated on Al_3Ti. This consecutive sequence of nucleation is termed a multi-step nucleation mechanism.

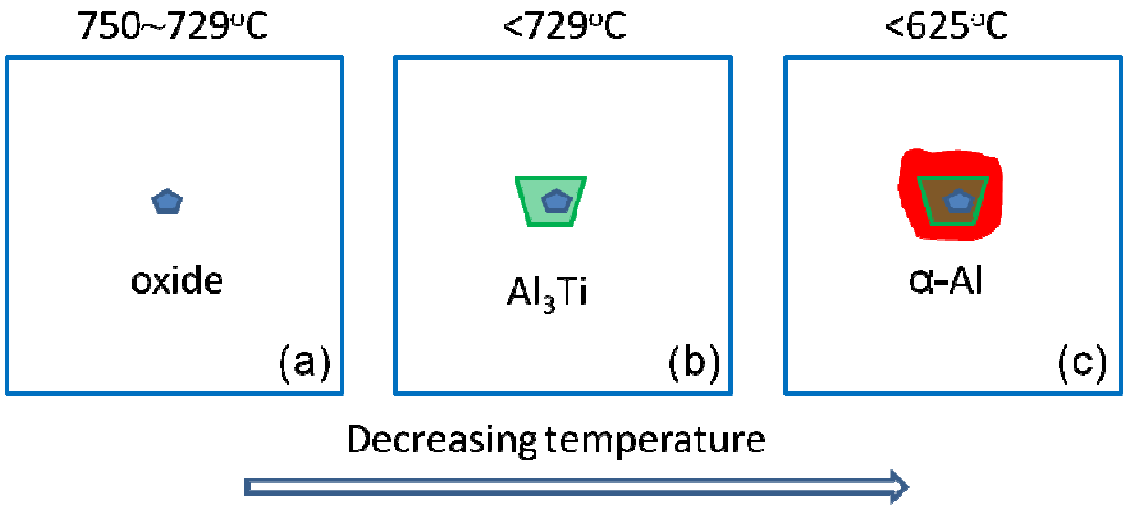

Figure 4.13 *Schematic of a multi-step nucleation mechanism. (a) After poured into the MCAST unit at 750°C, the oxides films in alloy melt were uniformly dispersed throughout the alloy melt; (b) At a temperature below 729°C (the equilibrium formation temperature of Al_3Ti based on thermodynamic calculation), Al_3Ti nucleated on dispersed oxides particles; and (c) At a temperature below 625°C (liquidus temperature of α-Al based on thermodynamic calculation), α-Al phase nucleated on Al_3Ti. This consecutive sequence of the heterogeneous nucleation behaviours is termed a multi-step nucleation mechanism.*

The argument of the enhanced heterogeneous nucleation by Al_3Ti through a multi-step nucleation mechanism is also supported by the result shown in **Figure 4.4b**, where Al_3Ti had formed before the melt was poured into the MCAST unit at 650^{o}C (scheme B in **Figure 3.6**), so that intensive melt shearing (dispersed oxide) had no influence on the formation of Al_3Ti and hence no effect on the grain refinement. In terms of the influence of melt shearing time, when the melt shearing time exceeded a critical value, 10~20 s, a sufficient number of individual dispersed oxide particles has been achieved for the heterogeneous nucleation of Al_3Ti particles. Further increasing the melt shearing time doesn't contribute to an enhanced heterogeneous nucleation of Al_3Ti particles on oxide particles and its size distribution. Therefore the grain size cannot be refined further (**Figure 4.3**).

4.4 Conclusions of Chapter 4

(1) Oxides formed in the liquid experimental wrought AlZnMgCuTi alloy are in the form of films or clusters of $MgAl_2O_4$.

(2) Dispersion of $MgAl_2O_4$ particles can be achieved by intensive melt shearing in the experimental wrought alloy.

(3) Dispersed oxide particles can act as active nucleation sites of Al_3Ti intermetallic particles by intensive shearing, provided shearing occurs during the formation of the Al_3Ti phase.

(4) Following the dispersion of oxide particles by intensive melt shearing, a narrower size distribution of Al_3Ti particles is produced providing many active sites for α-Al nucleation resulting in a finer grain size. This multi-step nucleation process, oxide to Al_3Ti to α-Al, is shown to be significantly enhanced by intensive melt shearing during the formation of the Al_3Ti phase.

(5) Grain refinement has been successfully achieved in an experimental wrought AlZnMgCuTi alloy by intensive melt shearing. The grain refining effect is more pronounced under the conditions of lower cooling rate during solidification.

Chapter 5

Formation of Fe-containing intermetallics in an AlSiCuFeMg alloy under intensive shearing

5.1 Introduction

In a typical Al die casting alloy, due to the low solid solubility of iron in aluminium matrix, formation of iron-containing intermetallic compounds is one of the major concerns due to its negative influence on mechanical properties. It is generally accepted that high manganese content and a high cooling rate are beneficial for the formation of α-AlFeSi. Although, significant inconsistency still exists including both the comprehensively quoted sludge factor for the threshold temperature of the formation of Fe-containing phase and the Fe/Mn ratio influencing the type of the Fe-containing intermetallic phase formed.

Some previous studies have suggested the feasibility of nucleation of Fe-containing intermetallics on oxide particles, including both naturally occurring and externally added oxides (Cao and Campbell, 2003, 2004a, 2004b, 2006, 2005; Miller *et al.,* 2006; Khalifa, *et al.*, 2005). It was proposed that the wetted surface of the oxide films provides a preferential nucleation site for Fe-containing intermetallics. If so, oxides can be utilized to manipulate the formation of Fe-containing intermetallics such as the α-AlFeSi, β-AlFeSi phases by the controllable nucleation of Fe-containing phases on some oxides.

In this chapter, the dependence of the formation of Fe-containing intermetallics on naturally occurring oxides has been investigated in a typical die cast Al alloy. Melt conditioning by advanced shearing technology (MCAST), was used to investigate the formation of Fe-containing intermetallic phases under intensive forced convection. Experimental observations were then compared with the predictions by CALPHAD (**Figure 5.1**) and existing experimental results (Balitchev *et al.*, 2003). In order to assess the mechanical response to the modification of Fe-containing intermetallic phases, HPDC and MC-HPDC tensile samples were tensile tested and microstructural constituents including both Fe-containing intermetallic phases and microporosity characteristics were evaluated and correlated with the mechanical properties.

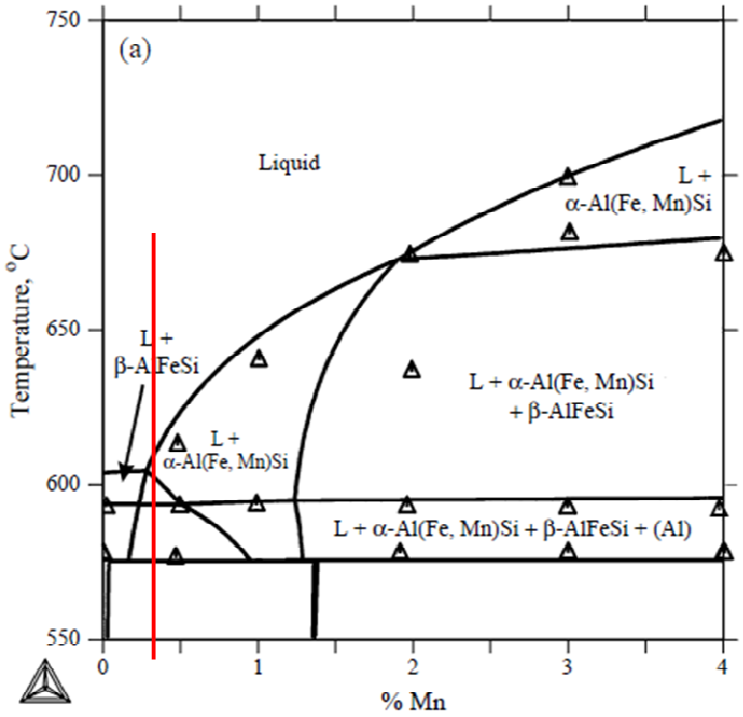

Figure 5.1 *Thermodynamically calculated isopleths at 10.0% Si, 1.0% Fe with experimental data* (Balitchev *et al.*, 2003). *The vertical line indicates the Mn content in the experimental LM24 alloy showing the sequence of the formation of Fe-containing intermetallic phases.*

5.2 Results

5.2.1 Formation of Fe-containing intermetallics in the convection-free solidified samples

In order to investigate the influence of cooling rate on the formation of the Fe-containing intermetallics, especially around the equilibrium formation temperature, solidification experiments including convection-free isothermal holding combined with subsequent different cooling modes were carried out. For simplicity, this solidification experiment is named convection-free solidification hereafter.

Fe-containing intermetallics in the convection-free solidified samples

The Fe-containing intermetallic phases formed during the convection-free solidification with different cooling rates are shown in **Figure 5.2**. With end chilling, needle-shaped Fe-containing intermetallic particles were dominant, as shown in **Figure 5.2a**. However, with air cooling within the copper surround, the Fe-containing intermetallic phases were mainly dendritic particles as shown in **Figure 5.2b**. With furnace cooling, the Fe-containing intermetallic phases display polyhedral morphology, as shown in **Figure 5.2c**. According to their different morphological characteristics, the needle-shaped phases in **Figure 5.2a** are tentatively termed β-AlFeSi phase, while those dendritic and polyhedral ones in **Figure 5.2b** and **Figure 5.2c** are termed α-AlFeSi, respectively. These results demonstrate that the Fe-containing intermetallic phase can form as a primary phase in the present alloy. The comparison made between **Figure 5.2a** and **Figure 5.2b** suggests that the dendritic Fe-containing intermetallic particles (**Figure 5.2b**) were not formed during isothermal holding but during the subsequent cooling stage. Comparison made between **Figure 5.2a** and **Figure 5.2c** also supports this argument. The sedimented α-AlFeSi phases in **Figure 5.2b** and **Figure 5.2c** can be explained in terms of the gravity segregation behaviour of the α-AlFeSi phase during the subsequent solidification due to the fact that the Fe-containing intermetallic phases

have a higher density than liquid aluminium alloys (Shabestari and Gruzleski, 1995). This confirms the holding temperature adopted in **Figure 5.2a** through **Figure 5.2c** was higher than the equilibrium formation temperature of the primary α-AlFeSi phase in this alloy.

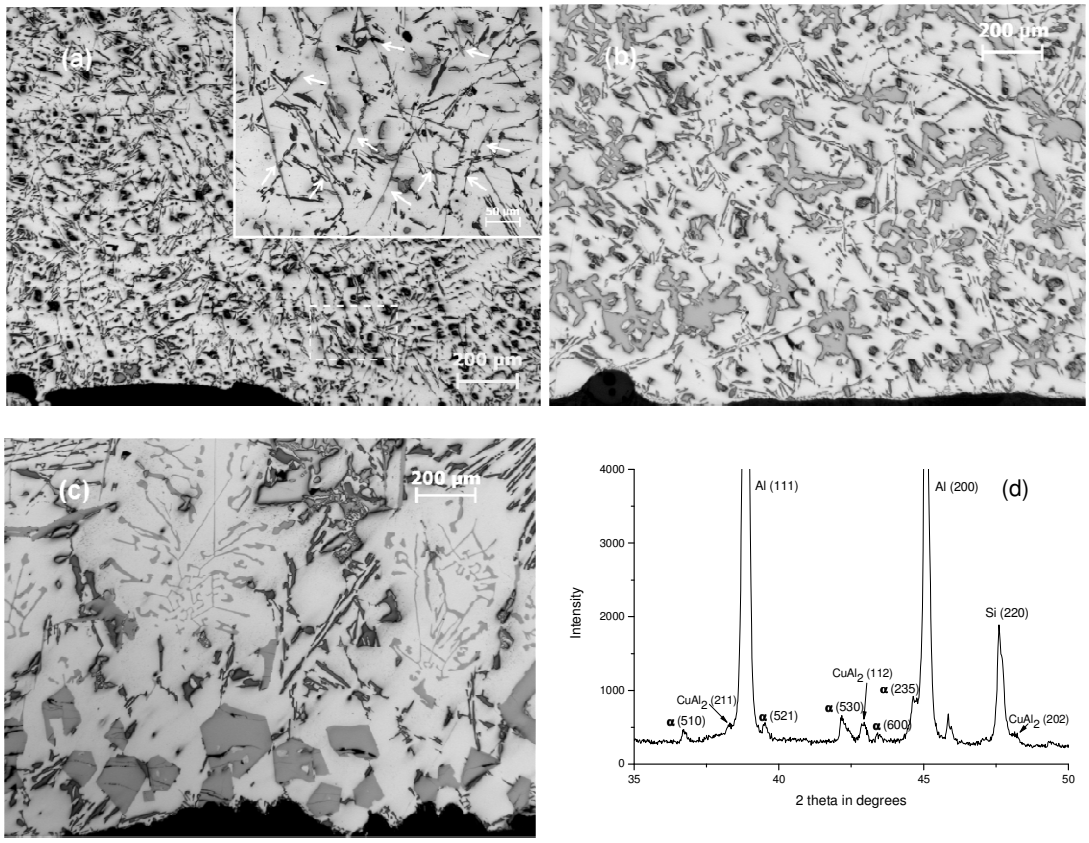

Figure 5.2 *Influence of cooling modes after isothermal holding on the formation of Fe-containing intermetallics. OM images of Fe-containing intermetallic particles precipitated in the location close to the base in isothermally held samples at 665°C with subsequent different cooling rate (longitudinal section): (a) Mainly needle-shaped β-AlFeSi phase (with insert to highlight) and few Chinese script in the sample isothermally held and then end chilled; (b) Dendritic α-AlFeSi phase in the sample isothermally held and then air cooled; (c) Polyhedral α-AlFeSi phase in the sample isothermally held and then furnace cooled; (d) XRD trace of the sample isothermally held at 665°C for 6 h and then air cooled (transverse cross section very close to the base) identifying the α-AlFeSi phase with the formula of* $Al_{17}(Fe_{3.2},Mn_{0.8})Si_2$.

The formation temperature of α-AlFeSi intermetallics as a primary phase in this alloy should be around 650°C (Backerud *et al.*, 1990). As is well known, the β-AlFeSi phase can be a primary phase which forms just at a temperature lower than that of the primary α-AlFeSi phase depending on the local composition (Cao and Campbell, 2003).

Identification of the Fe-containing intermetallics in the convection-free solidified samples

To identify the crystal structure of the Fe-containing intermetallics formed, the specimen sectioned from the location close to the base of the air cooled sample isothermally held at 665°C for 6 h was subjected to X-ray diffraction. The indexed XRD trace shown in **Figure 5.2d** suggests that the dendritic Fe-containing intermetallic particles (shown in **Figure 5.2b**) can be identified as $Al_{17}(Fe_{3.2},Mn_{0.8})Si_2$, which is a type of the α-Al(Fe,Mn)Si phase (**Table 2.1**) (JCPDS, 2005).

Composition of Fe-containing intermetallic phases in the convection-free solidified samples

In order to analyze the phase chemistry of the Fe-containing intermetallics in the convection-free solidified samples, SEM and EDX analysis were carried out for the samples solidified by different cooling modes. **Figure 5.3** displays the SEM back scattered images of needle-shaped and equiaxed Fe-containing intermetallic phases formed in the sample isothermally held at 665°C for 6 h. **Table 5.1** presents the quantification results of the needle-shaped and dendritic Fe-containing intermetallic phases by SEM-EDX analysis. The SEM-EDX analysis results demonstrate that the Fe-containing phases with dendritic morphology (**Figure 5.2b**) or polyhedral morphology (**Figure 5.2c**), have almost the same composition. The SEM-EDX analysis results are consistent with the indexed XRD results, confirming the needle phase and equiaxed phase to be β-$Al_9Fe_2Si_2$ and α-$Al_{17}(Fe_{3.2},Mn_{0.8})Si_2$, respectively. For the α-AlFeSi

phase, it is in good agreement with the indexed result by XRD. It is clear that the Mn content in the α-AlFeSi phase is very low, i.e. 1:4=Mn:Fe in atomic pct.

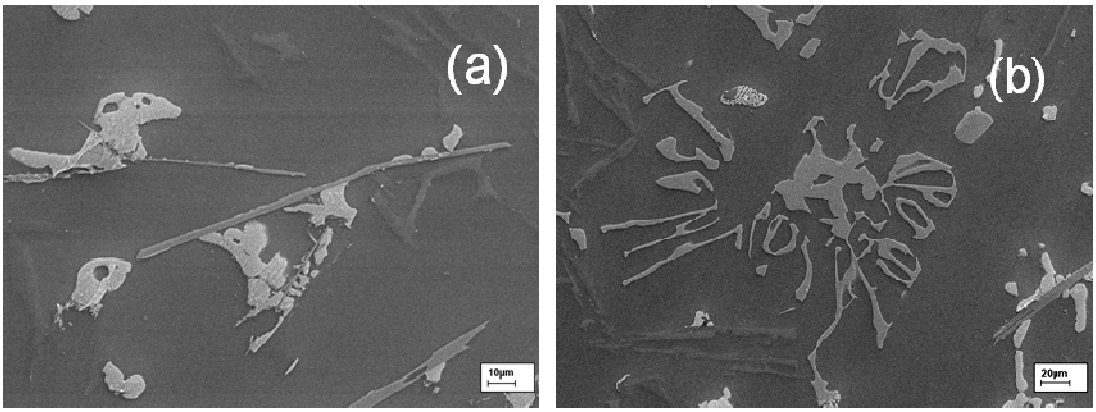

Figure 5.3 *SEM back sacattered images of Fe-containing intermetallic phases in the sample isothermally held at 665°C for 6 h. (a) needle-shaped β-AlFeSi phase in the sample end chilled; and (b) dendritic α-$Al_{17}(Fe_{3.2},Mn_{0.8})Si_2$ phase in the sample air cooled.*

Table 5.1 *EDX semi-quantification results of needle shaped and dendritic Fe-containing intermetallic phases in the convection-free solidified sample isothermally held at 665 °C for 6 h (in at.%).*

Elements	Al	Si	Fe	Mn	Notes
Needle-shaped	66.29±0.51	17.57±0.19	16.00±0.28	-	This work
β-$Al_9Fe_2Si_2$	69.2	15.4	15.4	-	Stoichiometry
β-Al_5FeSi	71.4	14.3	14.3	-	Stoichiometry
Dendritic	72.04 ±0.40	9.99±0.27	13.64±0.23	4.33±0.19	This work
$Al_{17}(Fe_{3.2},Mn_{0.8})Si_2$	73.9	8.7	13.9	3.5	Stoichiometry

Dependence of phase selection of Fe-containing intermetallics on the isothermal holding temperature

The influence of isothermal holding temperature on the formation of Fe-containing intermetallic phase was studied. The holding temperature was chosen to be below or above

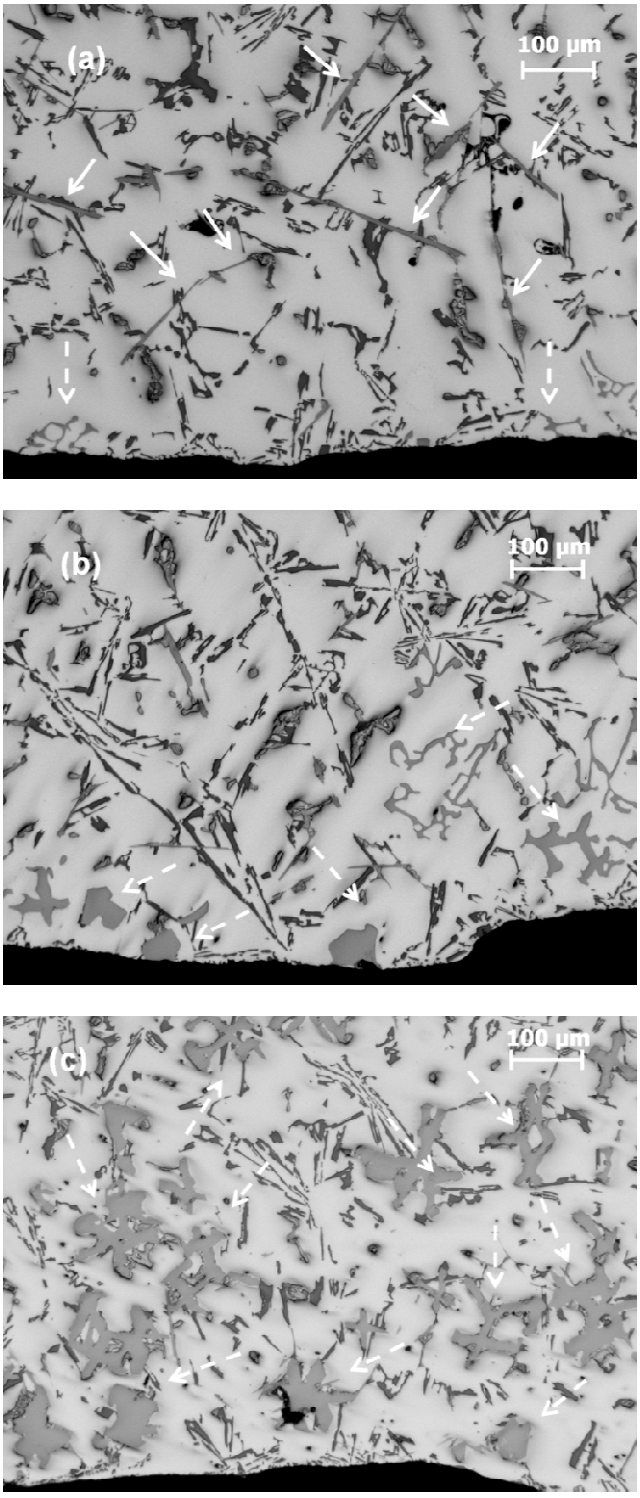

Figure 5.4 *Influence of the isothermal holding temperature on the formation of Fe-containing intermetallic phases in the convection-free solidification after being air cooled. Optical micrographs in longitudinal sections of the samples isothermally held at these temperatures of: (a) 643; (b) 652; (c) 674°C. Dashed arrowed phases: a-AlFeSi intermetallics; solid arrowed phases: β-AlFeSi intermetallics.*

the equilibrium formation temperature of the primary α-AlFeSi phase (650°C). After being isothermally held for 6 h, the alloys were air cooled to room temperature. The selection of the formed Fe-containing intermetallics is compared in **Figure 5.4**.It can be seen clearly that mainly needle-shaped β-AlFeSi phases are formed in the sample isothermally held at 643°C and then air cooled (**Figure 5.4a**). However, for all the samples isothermally held above 650°C, namely, 652, 665 (refer to **Figure 5.2b**) and 674°C, mainly α-AlFeSi phases are formed (**Figure 5.4b** and **Figure 5.4c**). These results suggest the significant dependence of the selection of Fe-containing intermetallic phase on the kinetic conditions at the equilibrium formation temperature of the Fe-containing phase. In other words, the formation of β-AlFeSi is kinetically favourable under normal solidification conditions.

Association between oxides and Fe-containing intermetallic phases

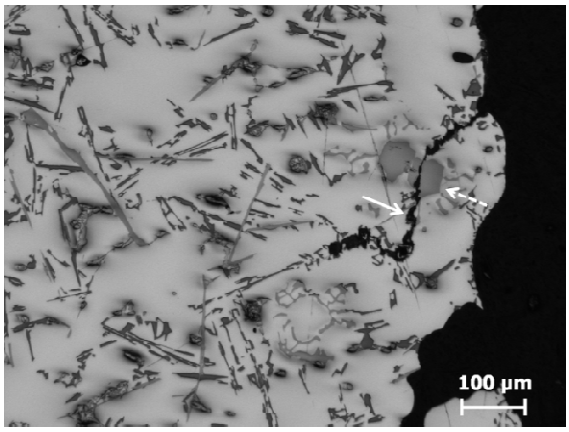

Figure 5.5 *A typical optical micrograph showing the formation of α-AlFeSi phase (dashed arrow) associated with an oxide film (solid arrow) in a sample isothermally held at 643°C and air cooled.*

Nucleation of Fe-containing intermetallic phases on oxides films has been proposed in previous investigations (Cao and Campbell, 2003; Miller *et al.*, 2006). In the present study, close association between oxide films and Fe-containing intermetallic phases was observed in

a sample isothermally held at 643°C for 6 h and subsequently air cooled to room temperature, as indicated in **Figure 5.5**.

Estimation of cooling rate adopted by different cooling modes

In order to determine the cooling rate of the different cooling modes after isothermal holding, the secondary dendrite arm spacing (DAS) was measured in the optical micrographs taken at a location close to the base of the samples isothermally held at 665°C and subsequent end chilled or air cooled, respectively, as shown in **Figure 5.2a** and **Figure 5.2b**. The cooling rate was calculated according to the following formula (Spear and Gardner, 1963).

$$\log\frac{dT}{dt} = -\left(\frac{\log(DAS)-1.66}{0.40}\right) \qquad (5.1)$$

Where *dT/dt* is given in Ks^{-1} and *DAS* in μm. It can be seen from **Table 5.2** that there is a huge difference between these two kinds of cooling modes.

Table 5.2 *Measured secondary dendrite arm spacings (DAS) and calculated cooling rates in some convection-free solidified samples.*

	End chill	Air cooling
DAS (μm)	26.8	85
Cooling rate (*dT/dt*, Ks^{-1})	3.8	0.2

5.2.2 Fe-containing intermetallics formed in TP-1 and MC-TP-1 samples

The TP-1 test can provide a well controlled cooling mode during solidification and was used to assess the formation of Fe-containing intermetallic phases under an intermediate cooling rate in the current study. In the TP-1 sample without melt shearing, needle-shaped Fe-containing intermetallics are mainly observed, as displayed in **Figure 5.6a** and very little Chinese script Fe-containing intermetallic phases appeared as shown in **Figure 5.6b**, while in

the sheared TP-1 samples, compact polyhedral Fe-containing intermetallic particles are mainly observed, as shown in **Figure 5.6c** and very little Chinese script Fe-containing intermetallic phases can be seen, as displayed in **Figure 5.6d**.

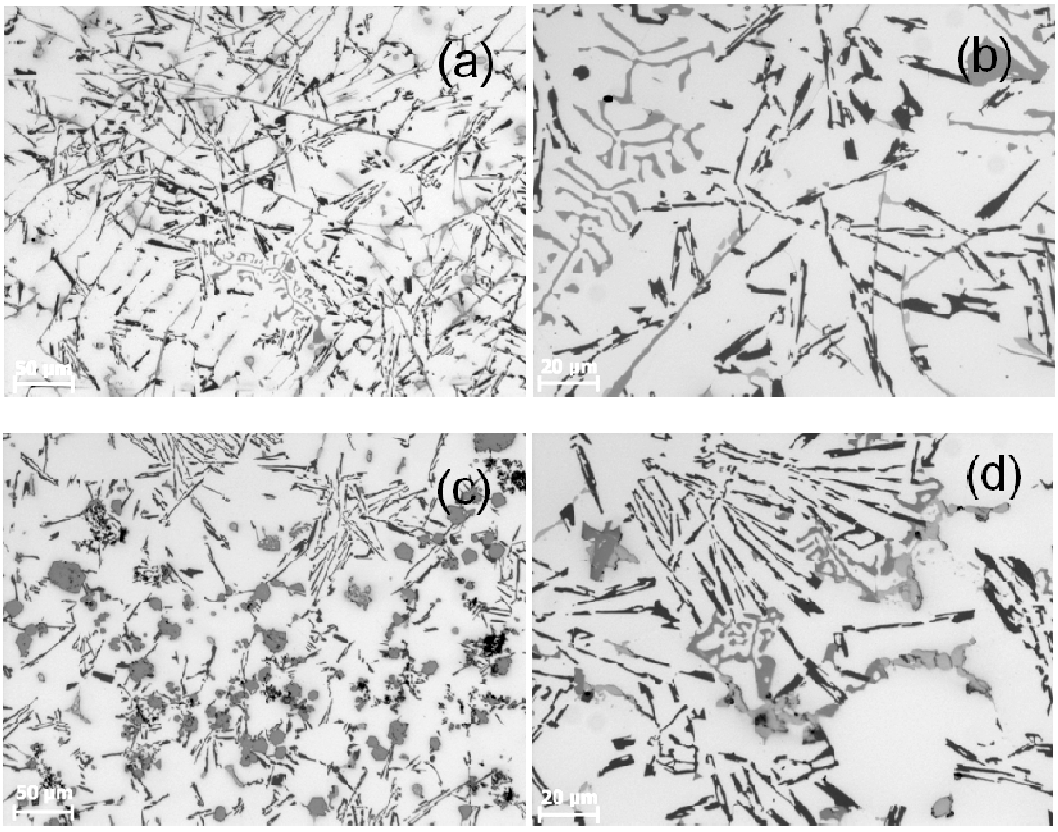

Figure 5.6 *Optical micrographs of LM24 TP-1 samples: (a) Primary β-AlFeSi needles in TP-1 sample; (b) Few Chinese script α-AlFeSi in TP-1sample; (c) Equiaxed α-AlFeSi phase in MC-TP-1 sample cast after being sheared at 645°C and (d) Few Chinese script α-AlFeSi phase in MC-TP-1sample cast after being sheared at 645°C.*

5.2.3 Fe-containing intermetallics formed in pressure filtered samples with/without shearing

To investigate the effect of intensive shearing on the formation of Fe-containing intermetallic phases, the pressure filtration technique was used to concentrate the Fe-containing intermetallics formed. In the pressure filtered sample without shearing, a dendritic α-AlFeSi

phase and very little needle-shaped β-AlFeSi phases are observed, as displayed in **Figure 5.7a**. However, in the sample with shearing, only the polyhedral α-AlFeSi phases are observed, as depicted in **Figure 5.7b**. Another interesting feature shown in **Figure 5.7b** is the significantly refined Fe-containing intermetallic particles after shearing compared with that in **Figure 5.7a** without shearing.

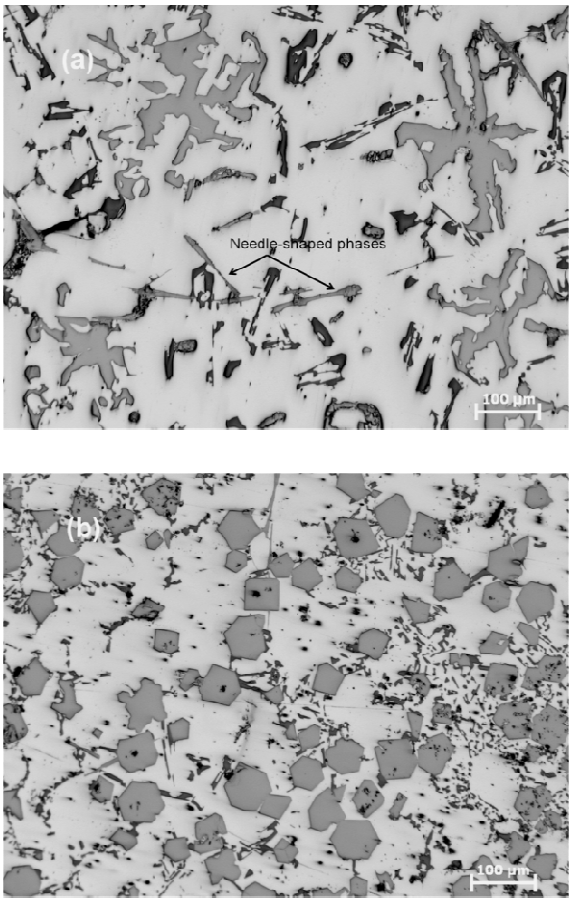

Figure 5.7 *Fe-containing intermetallic particles in the pressure filtered samples: (a) dendritic and needle-shaped Fe-containing intermetallics in the non-sheared sample cast at 645^{o}C; and (b) polyhedral α-AlFeSi intermetallic particles in the sample sheared at 645^{o}C.*

5.2.4 Oxides formed in liquid LM24 alloys

In order to identify the oxides formed in liquid LM24 alloy, a pressure filtered sample was made to concentrate the oxides formed in liquid LM24 alloy. The SEM micrograph in **Figure 5.8a** shows the clusters of oxide particles. The SEM-EDX spectrum in **Figure 5.8b** identifies that the oxide is $MgAl_2O_4$ spinel.

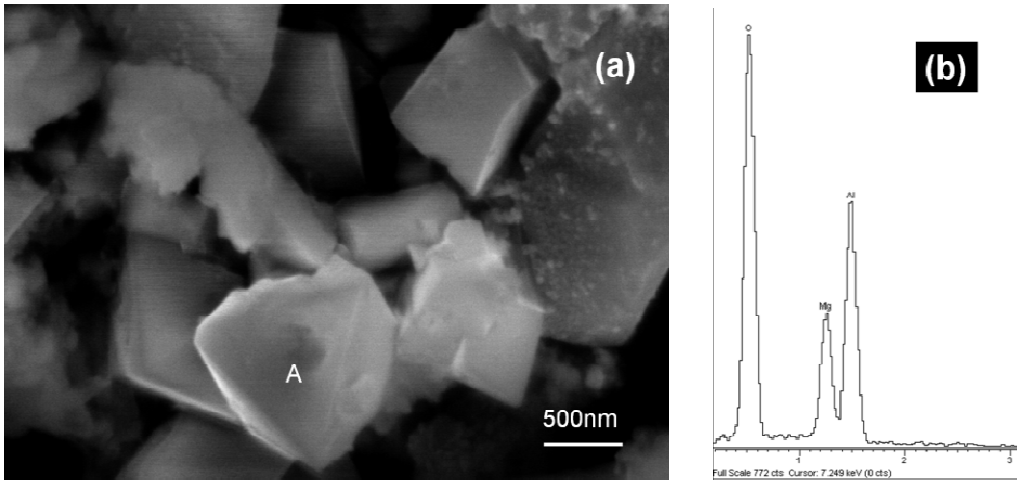

Figure 5.8 *Clusters of $MgAl_2O_4$ spinel particles formed in liquid LM24 alloy. (a) Showing clusters of oxide particles in the sample pressure filtered and deep etched; (b) SEM-EDX spectrum of the particle marked by "A" in (a) identifying it to be $MgAl_2O_4$.*

5.2.5 Fe-containing intermetallics formed in HPDC and MC-HPDC samples

Fe-containing intermetallic phases are one of the important microstructural constituents affecting the mechanical properties in high pressure die castings (HPDC). **Figure 5.9** shows SEM images of Fe-containing intermetallic phases in HPDC and MC-HPDC tensile samples (sheared at 645^{o}C). In the HPDC sample (**Figure 5.9a**), both agglomerates of the polyhedral α-AlFeSi phase and the needle-shaped β-AlFeSi phase are clearly seen, however, in the MC-HPDC sample (**Figure 5.9b**), only dispersed polyhedral α-AlFeSi particles and very little finer needle-shaped β-AlFeSi phase are observed.

Phase identification of Fe-containing intermetallics formed in HPDC and MC-HPDC by SEM-EDX analysis

The above statements concerning the phase identity have been confirmed by comprehensive SEM-EDX analysis, as shown in **Figure 5.9c** and **Figure 5.9d**. **Table 5.3** gives the SEM-EDX analysis results of the Fe-containing intermetallic phases in HPDC and MC-HPDC tensile samples shown in **Figure 5.9a** and **Figure 5.9b**. In the present study, the needle-shaped phases are likely to be β-Al_5(Fe,Mn)Si with a monoclinic unit cell based on the above SEM-EDX analysis result (**Table 5.3**). However, for simplicity and consistency in the use of terminology, it is still named the β-AlFeSi phase.

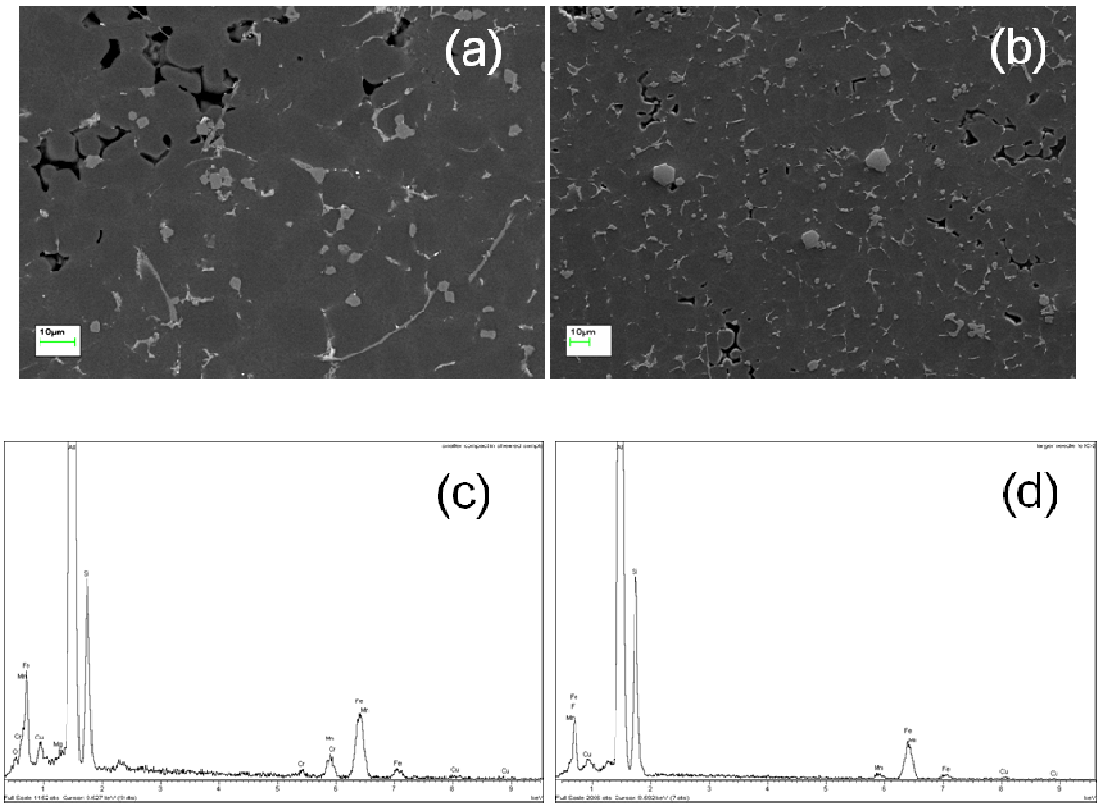

Figure 5.9 *(a) SEM back scattered image showing the agglomerates of α-AlFeSi and needle-shaped Fe-containing intermetallic particles in HPDC sample and (b) SEM back scattered image showing dispersed polyhedral α-AlFeSi intermetallic particles in MC-HPDC sample and SEM-EDX spectra of different intermetallics present in HPDC and MC-HPDC samples, (sheared at 645^{o}C). (c) α-AlFeSi (d) β-AlFeSi intermetallic phase.*

Table 5.3 *SEM-EDX analysis results of Fe-containing intermetallics in HPDC and MC-HPDC tensile test specimens (in wt.%).*

Fe-containing intermetallics	Al	Si	Cr	Mn	Fe	Cu	Notes
Polyhedral phases	58.29	10.04	1.24	6.16	22.53	1.74	Present work
α-Al(Fe,Mn)Si $[Al_{15}(Fe,Mn)_3Si_2]$	60.9	8.2	-	13.5	15.6	1.5	(Narayanan *et al.*, 1994)
Large needle-shaped phases	47.69	25.03	-	1.98	23.77	1.52	Present work
β-Al_5FeSi	46.5	27	-	4.2	20.8	-	(Narayanan *et al.*, 1994)

Effect of shearing temperature on the morphological evolution of the α-AlFeSi intermetallic phase in MC-HPDC samples

Based on the results obtained in the convection-free solidification experiments, the selection of primary Fe-containing intermetallic phase is heavily dependent on the kinetic conditions at the formation temperature of the Fe-containing intermetallic phases. **Figure 5.10** shows the variation of the Fe-containing intermetallic phases in HPDC and MC-HPDC samples with various shearing temperatures. It is seen clearly that the Fe-containing intermetallic phases display agglomerates of α-AlFeSi particles and β-AlFeSi needles in conventional HPDC samples (**Figure 5.10a**). With intensive melt shearing, these were modified to dispersed α-AlFeSi particles in MC-HPDC samples, within a wide range of shearing temperature from 645 to 580^{o}C (**Figures 5.10b** through **5.10d**). With a decrease of the shearing temperature, the morphology of α-AlFeSi was changed from polyhedral (sheared at 645^{o}C, **Figure 5.10b**) to polyhedral and partially irregular shape (sheared at 620^{o}C, **Figure 5.10c**), and then to a star-like particles (sheared at 580^{o}C, **Figure 5.10d**). However, all particles are mainly α-

AlFeSi phases. At the same time, the amount (area fraction) of the large sized β-AlFeSi needles in MC-HPDC samples was decreased from 0.27% sheared at 645°C to 0.06% in the MC-HPDC sample sheared at 580°C. For the sample sheared at 645°C, the large-sized needle-shaped Fe-containing phase were formed in the shot sleeve of the high pressure die caster, while for the sample sheared at 580°C (below the liquidus), almost all the iron in the alloy is consumed to form the α-AlFeSi phase. These results suggest that intensive melt shearing promotes the selection of the α-AlFeSi phase.

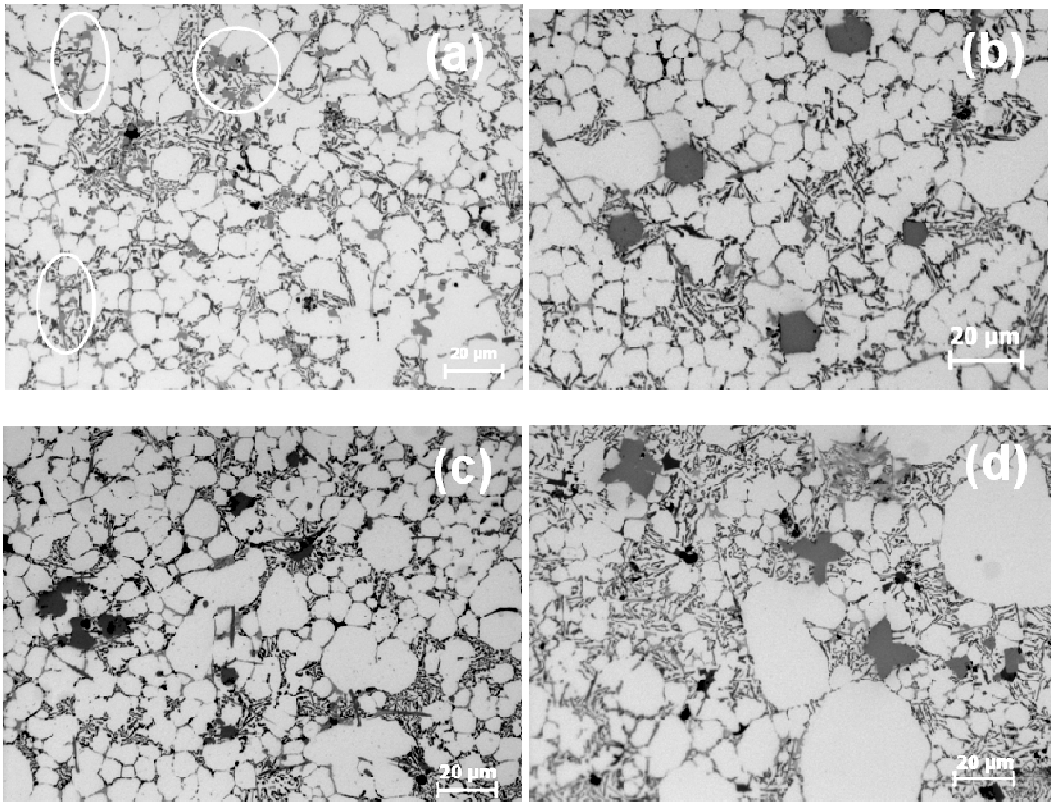

Figure 5.10 *The evolution of the Fe-containing intermetallic phases in HPDC and MC-HPDC samples with shearing temperatures.* (a) *Agglomerates of α-AlFeSi intermetallic particles indicated by white circles and β-AlFeSi needles in an HPDC sample cast at 700°C; (b) Polyhedral α-AlFeSi particles in a MC-HPDC sample, sheared at 645°C; (c) Polyhedral and irregular α-AlFeSi particles in a MC-HPDC sample, sheared at 620°C; and (d) Star-like α-AlFeSi particles in a MC-HPDC sample, sheared at 580°C.*

Spatial distribution of different Fe-containing intermetallic particles

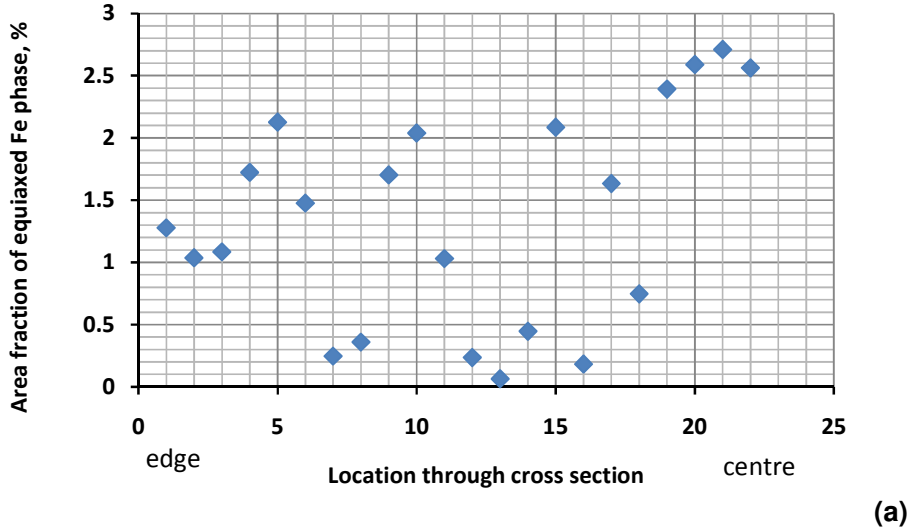

(a)

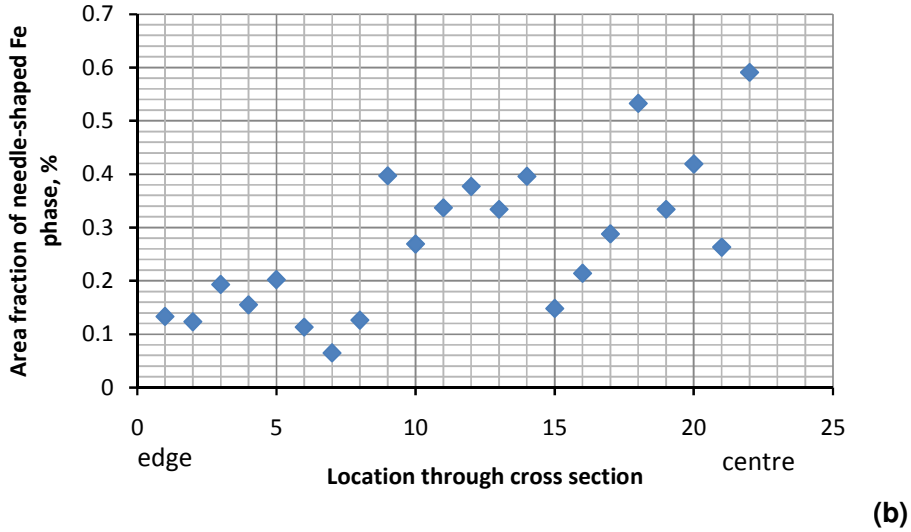

(b)

Figure 5.11 S*patial distributions of (a) α-AlFeSi intermetallic particles in a MC-HPDC tensile sample and (b) β-AlFeSi intermetallic particles in an HPDC sample.*

Spatial distribution of microstructural constituents determines the uniformity of microstructures. The spatial distribution of α-AlFeSi intermetallic particles in a MC-HPDC sample and β-AlFeSi intermetallic particles in a conventional HPDC sample are presented in **Figure 5.11**. It can be seen that the α-AlFeSi intermetallic particles in the MC-HPDC sample

are almost uniformly distributed across the whole section (**Figure 5.11a**, for simplicity, only the distribution on the half section is displayed in **Figure 5.11** due to its symmetry), while more and more β-AlFeSi particles can be observed towards the central region of the cross section in a conventional HPDC sample (**Figure 5.11b**).

Refined eutectic Fe-containing intermetallic phase in MC-HPDC samples

In a Al-Si cast alloy, eutectic structure is one of important microstructural constituents. From **Figure 5.9b**, the refined eutectic α-AlFeSi particles and the β-AlFeSi needles may be seen, in MC-HPDC samples sheared at 645^{o}C. This can be ascribed to the effect of intensive shearing on the enhanced nucleation of α-AlFeSi phase by dispersed oxide particles at eutectic temperature. But further investigation is needed.

Porosity content and distribution in HPDC and MC-HPDC samples

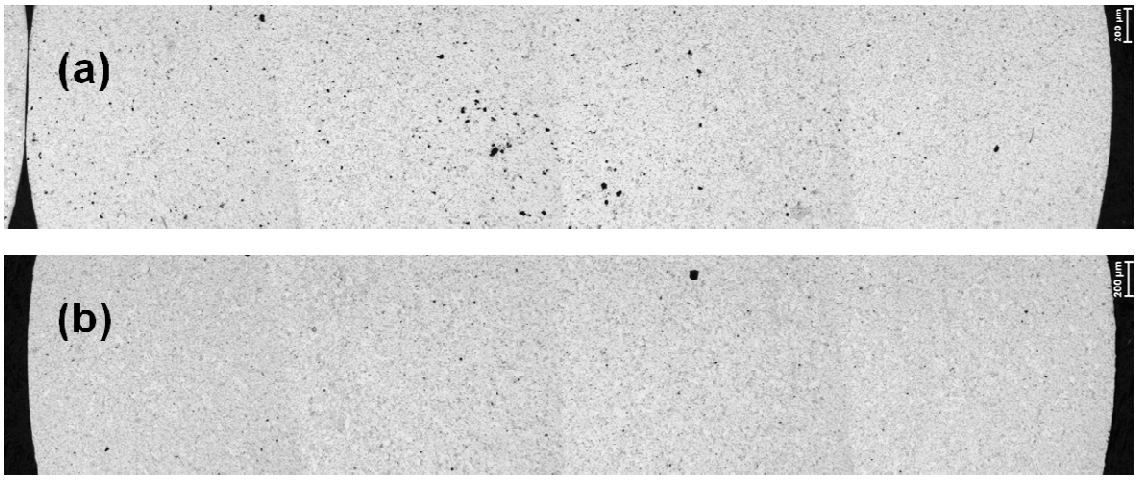

Figure 5.12 *Cross section of HPDC and MC-HPDC tensile sample, showing significantly decreased content of porosity by intensive shearing: (a) HPDC tensile test sample cast at 700^{o}C and (b) MC-HPDC tensile test sample, sheared at 645^{o}C.*

The content of porosity and its distribution have a significant influence on the mechanical properties of HPDC samples. **Figure 5.12** presents the macrographs of the cross sections of

the HPDC and MC-HPDC tensile test samples showing the porosity. A higher area fraction of porosity is clearly seen in the HPDC tensile test sample, especially in the central region of the cross section (**Figure 5.12a**), while the area fraction in the MC-HPDC sample is much lower and more uniform (**Figure 5.12b**).

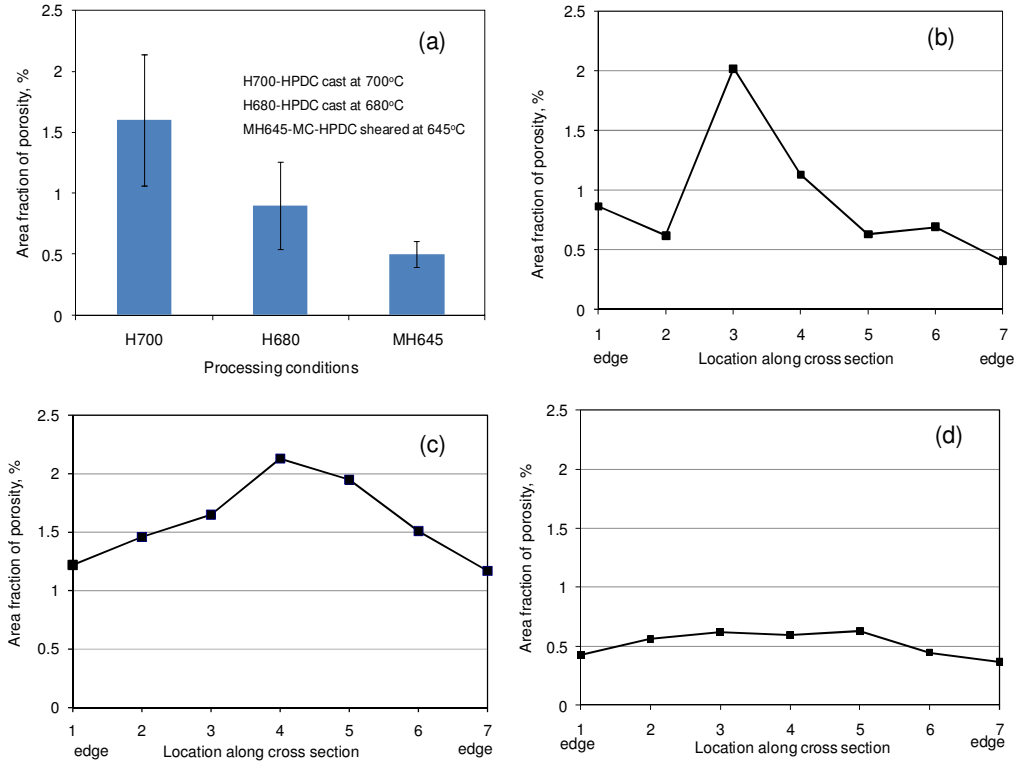

Figure 5.13 *Comparisons of content and spatial distribution of porosity between HPDC and MC-HPDC tensile test samples:* (a) *Comparisons of content of porosity (area fraction).;and porosity spatial distribution in: (b) HPDC tensile test sample cast at 700°C; (c) HPDC tensile test sample cast at 680°C and (d)MC-HPDC tensile test sample sheared at 645°C.*

Figure 5.13 compares the quantitative reuslts of the porosity content and spatial distribution characteristics in HPDC and MC-HPDC samples. With intensive shearing, the amount of porosity (area fraction) decreased significantly from 1.6% in the conventional HPDC samples to 0.5% in the MC-HPDC sample, as displayed in **Figure 5.13a**. More interestingly, the

spatial distribution of porosity on the cross sections of tensile samples exibit different features, as shown in **Figure 5.13b** through **5.13d**. Without shearing prior to die casting, distribution of porosity is not uniform and is mainly concentrated in the central region of the cross section of tensile samples, as indicated in **Figure 5.13b** and **Figure 5.13c**; with intensive shearing, the porosity distribution of the MC-HPDC sample is more uniform as shown in **Figure 5.13d**. The similarity of the spatial distribution features between the β-AlFeSi needles (**Figure 5.11b**) and porosity suggests a direct association in their formation.

Mechanical properties of HPDC and MC-HPDC samples

Figure 5.14 shows the tensile strength and elongation of MC-HPDC and HPDC samples. The MC-HPDC samples were sheared at 645^{o}C prior to high pressure die casting. With intensive melt shearing, an improvement of ductility (elongation) was achieved as shown in **Figure 5.14a**. **Figure 5.14b** shows a typical SEM fractographic image in a HPDC sample after a tensile test, showing the agglomerates of Fe-containing intermetallic phase present in the fracture surface.

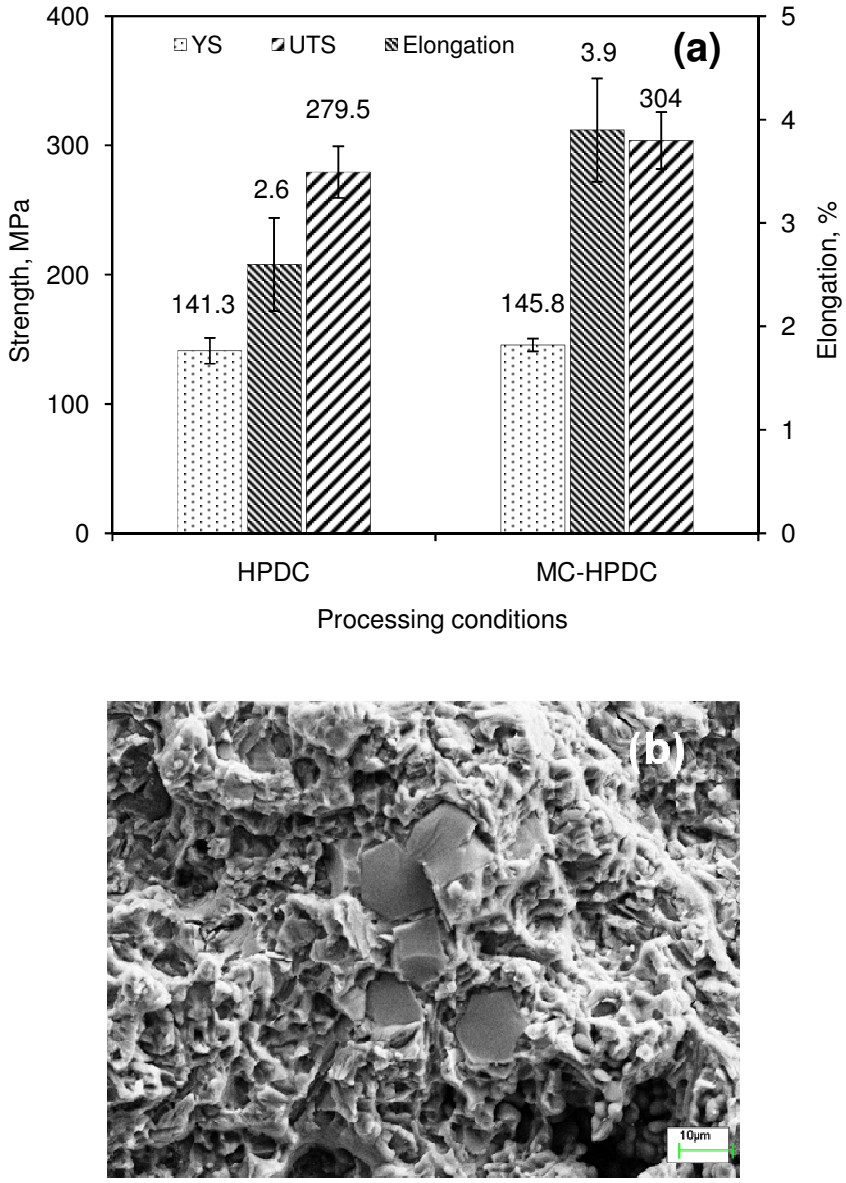

Figure 5.14 *Improved mechanical properties in MC-HPDC samples compared with the conventional HPDC samples. (a) Tensile strength and elongation of MC-HPDC and HPDC samples; (b) SEM fractography image showing the agglomerates of α-AlFeSi phase in a tensile fractured HPDC sample.*

5.3 Discussion

According to the thermodynamic phase diagram calculated results of Al-Fe-Mn-Si quaternary system, as shown in **Figure 5.1**, regardless of the copper or magnesium content, the primary α-Al(Fe,Mn)Si phase is expected to form in the experimental alloy. This is reasonable based

on the report of Glaisher that Cu, Mg, Ni, and Zn had little effect on the formation of the primary Fe-containing intermetallic phases, although there are reports in which Al atoms in α-Al(Fe,Mn)Si phase can be substituted by Cu atoms to certain extent (Narayanan *et al.*, 1994). However, an increase in the Si content appeared to lower the formation temperatures of Fe-containing intermetallic phases (Glaisher, 1951). In fact, the formation temperature of the α-Al(Fe,Mn)Si phase in the experimental alloy should be higher than as indicated in **Figure 5.1**, because of the lower silicon (7.76wt.%) and slightly higher iron (1.08wt.%) contents in the present study. These calculated isopleths indicate the formation sequence of the Fe-containing intermetallic phase should be the α-Al(Fe,Mn)Si phase first and followed by the β-AlFeSi phase.

5.3.1 Formation of α-AlFeSi intermetallic phase under near equilibrium solidification

In comparison with the observation in **Figure 5.2a**, where needle-shaped β-AlFeSi phases are dominant in the location close to the base of the sample although they experienced the same isothermal holding procedure, therefore, it can be concluded that the α-AlFeSi phases (shown in **Figure 5.2b** and **Figure 5.2c**) were not formed during isothermal holding but during the subsequent cooling stage. It has been realised that, the β-AlFeSi phase could be a primary phase which forms at a temperature somewhat lower than that of the primary α-AlFeSi phase (Cao and Campbell, 2004b). As stated above, for the samples in **Figure 5.2a** and **Figure 5.2b**, the cooling rates by end chill or air cooling, were estimated as 3.8 Ks^{-1} or 0.2 Ks^{-1}, respectively. This suggests that there might be a critical cooling rate between 0.2 and 3.8 Ks^{-1} for a selection between the α-AlFeSi phase and the β-AlFeSi phase as a primary phase in the present alloy. The evolution of Fe-containing phases with the isothermal holding temperature (shown in **Figure 5.3**) indicates that the formation of β-AlFeSi is kinetically favourable under normal solidification conditions. From the results discussed above, it can be concluded that

there is a competition between the α-AlFeSi phase and the β-AlFeSi phase related to the kinetic conditions at their formation temperatures.

The measured phase chemistry of the α-AlFeSi phase had lower manganese content in the α-AlFeSi phase compared to the normally suggested value of the Mn/Fe ratio to form an α-AlFeSi phase. This is consistent with the results of a previous study of the α-AlFeSi phase formed under a relatively slow cooling rate (Tibballs *et al.*, 2001). In their study, a cubic α-AlFe(Mn)Si phase resulted in an alloy with 3wt. % Fe and 1.0wt% Mn, where the cooling rate exerted on the alloy melt during solidification was in the range of 7×10^{-4} ~1.4×10^{-3} Ks^{-1}, which was really slow in practice and can be taken to be near equilibrium solidification. The above results suggest that under near equilibrium conditions, α-AlFeSi phases easily form even though the value of the Mn/Fe ratio is far below the normally suggested value of 0.5.

5.3.2 The formation of α-AlFeSi intermetallic phase promoted by intensive shearing

It is widely accepted that the segregation behaviour of Fe and Mn is critical to the formation of Fe-containing intermetallics in Al alloys (Backerud *et al.*, 1990; Fang *et al.*, 2007; Taylor *et al.*, 1999b). Segregation behaviour is essentially a result of kinetic conditions. Jackson et al. developed an analytical model for non-equilibrium segregation during crystallization (Jackson *et al.*, 2004). In their model, a parameter was introduced to characterise to what extent the chemical potential difference transfer occurred between the species A and B during crystallization. When the atoms move around rapidly by diffusion compared to the rate of the advance of the interface, each atom species will behave independently. In the limit, the crystallization process depends on the chemical potentials of the species present. When the diffusion jump rate is very slow compared to the rate at which the interface is advancing, all of the atoms present at the interface are incorporated into the crystal as growth proceeds. In this case, different species will be incorporated into the crystals in a cooperative mode and a

chemical potential difference transfer will occur. The crystallization process depends on the difference between the free energies of the two phases present rather than on the chemical potentials of the individual species (Jackson *et al.*, 2004). This theory can be used to explain the reported comprehensive experimental results that the α-AlFeSi phase has a wide compositional spectrum in terms of the ratio of Mn/Fe in the published literature where different solidification conditions and hence different segregation behaviour of Fe and Mn were explored (Narayanan *et al.*, 1994; Miller *et al.*, 2006; Timelli and Bonollo, 2010). This theory can also be used to understand the formation of the Fe-containing intermetallic phase with and without intensive melt shearing.

In a previous study, it was found that under steady two-dimensional convective flow, the effective diffusion coefficient is one to three orders of magnitude larger than the molecular diffusion coefficient (McCarty and Horsthemke, 1988). With intensive melt shearing by the MCAST process, it might be reasonable to expect the diffusion of atom species in the melt would be enhanced even more significantly, where a much higher shear rate (above 10^3 s^{-1}) can be achieved and the flow characteristics change to be highly turbulent, whereas this value is about 10 s^{-1} for normal stirring (Flemings, 1991). On the other hand, the rate of interfacial migration was relatively slow under an almost isothermal condition. This feature facilitates the species of atom (such as Fe, Mn) to behave independently rather than in a cooperative mode. In other words, the Mn/Fe ratio, in this case, is not strictly defined by a cooperative mode (chemical potential difference transfer). In turn, it facilitates the crystallization of α-AlFeSi phase. This argument is supported by the observation of the nearly perfectly polyhedral α-AlFeSi phase in samples sheared at 645^{o}C shown in **Figure 5.6c** (MC-TP-1 sample), **Figure 5.7b** (the pressure filtered sample) and **Figure 5.8b** (the MC-HPDC sample). These compact polyhedral α-AlFeSi particles are similar to those observed in the

isothermally held and then furnace cooled sample (**Figure 5.2c**). This also suggests that intensive melt shearing can provide near equilibrium kinetic conditions.

The selection of the α-AlFeSi phase promoted by intensive melt shearing can also be explained from the viewpoint of enhanced heterogeneous nucleation of the α-AlFeSi phase on oxide particles dispersed by intensive shearing. Extensive observations have suggested an association between oxides and formation of Fe-containing intermetallics in Al-Si based alloys (Narayanan *et al.*, 1994; Cao and Campbell, 2003; Miller *et al.*, 2006; Khalifa *et al.*, 2005). The association between the formation of the α-AlFeSi phase and oxide films was also observed in our study (**Figure 5.5**). It has been well established that oxides film can be dispersed into individual particles with intensive shearing either in Mg- or Al-alloys (Fan *et al.*, 2009; Li *et al.*, 2011). In the present study, the oxide in liquid LM24 has been identified to be $MgAl_2O_4$ spinel (**Figure 5.8**). The lattice misfit between $MgAl_2O_4$ and α-AlFe(Mn)Si phase at room temperature is calculated and listed in **Table 5.4**, by matching the closest crystal planes and direction. The good lattice match indicate that $MgAl_2O_4$ spinel can be potent nucleation sites for α-AlFe(Mn)Si phase. As a result, sufficient oxide particles are available with shearing that could contribute to the enhanced nucleation of the α-AlFeSi phase. This argument is also supported by the observation of significantly increased number density of α-AlFeSi particles in sheared and pressure filtered sample (**Figure 5.7b**).

To summarise, the selection of α-AlFeSi promoted by intensive melt shearing can be attributed to two factors. One is the achievement of a near equilibrium kinetic condition. The other is the enhanced heterogeneous nucleation of α-AlFeSi phase on dispersed oxide particles by intensive shearing.

Table 5.4 *Estimated lattice misfit between $MgAl_2O_4$ and α-AlFe(Mn)Si phase at room temperature.*

Interface	Crystal structure & lattice parameters, nm	OR: $(hkl)[hkl]_N$// $(uvw)[uvw]_S$	d[hkl], nm	d[uvw], nm	f_0 (%)
$MgAl_2O_4$/ α-AlFe(Mn)Si	fcc, a=0.80831 bcc, a=1.256	(111)[110]// (110)[111]	2×0.57156	1.08773	4.85

5.3.3 Modification of Fe-containing intermetallics and improved integrity of MC-HPDC

The reason why the equiaxed α-AlFeSi phase and needle-shaped β-AlFeSi phase displayed different spatial distribution characteristics should be closely related to their different rheological behaviours. During the filling process of a high pressure die casting, the flow will experience a high shear rate, which is approximately an order of 10^5 s^{-1} within the gate (Murray and Griffiths, 1996). Due to the non-slip boundary condition at the die walls, a velocity gradient is expected across the section of the die cavity (Sannes and Westengen, 1998). On the other hand, the viscosity of semi solid metal is strongly dependent on the solid fraction and the morphology of solid particles. As a consequence, a flow of a low solid fraction or with equiaxed solid particles will then flow close to the die walls, while a flow of a high solid fraction or with dendritic/needle-shaped particles will concentrate to the centre. This explains why equiaxed α-AlFeSi can be uniformly distributed throughout the cross section of MC-HPDC samples (**Figure 5.11a**), while needle-shaped β-AlFeSi was concentrated in the central region of the cross sections of the HPDC samples (**Figure 5.11b**).

Porosity is usually formed during the casting process due to combined effect of both dissolved gases (hydrogen) and volumetric shrinkage (Chaijaruwanich *et al.*, 2007). It has been well established that a decrease in the melt temperature reduces the total amount of porosity primarily via a reduction in the gas porosity, which is closely related to the decreased hydrogen solubility in liquid aluminium alloys. In the present study, a contribution to the decreased total porosity content is possibly related to decreased gas porosity due to the decrease in the melt temperature by intensive shearing.

Another reason for the decreased content of porosity is possibly related to the modification of Fe-containing intermetallic phases. With intensive melt shearing, most of the iron in alloys was consumed to form dispersed polyhedral α-AlFeSi particles, including both primary α-AlFeSi and eutectic α-AlFeSi intermetallic particles, as shown in **Figure 5.9b** and **Figure 5.10b** through **Figure 5.10d**, and hence contributes to the improved permeability of the alloy in the mushy zone and thereby the decreased volumetric shrinkage related porosity content. Without shearing, in addition to agglomerates of α-AlFeSi, the coarse β-AlFeSi platelets (either as a primary phase or through the binary Al + β-AlFeSi eutectic reaction) have been reported to interfere with feeding into interdendritic areas and thereby increase the total porosity content in the finished castings (Taylor *et al.*, 1999a, 1999b and 1999c). This interpretation is consistent with the similar characteristics displayed in the spatial distribution of the area fraction of the β-AlFeSi platelets (**Figure 5.11b**) and porosity content in HPDC samples (**Figure 5.12 a** and **Figures 5.13b** and **5.13c**).

The formation of agglomerates of α-AlFeSi particles and β-AlFeSi needles are harmful to the mechanical properties of Al-Si HPDC samples, which can cause stress concentration and cracks resulting in premature failure. With intensive melt shearing by MCAST, the Fe-containing phase formed mainly in the form of dispersed polyhedral α-AlFeSi particles in

MC-HPDC samples, rather than the agglomerates of α-AlFeSi and needle-shaped β-AlFeSi phase in conventional HPDC samples. In addition, the integrity of MC-HPDC tensile samples is improved in terms of the significantly decreased porosity content. Therefore, the improvement of ductility (tensile elongation) shown in **Figure 5.14a**, can be ascribed to both the modification of Fe-containing intermetallics to dispersed α-AlFeSi particles and a significantly decreased porosity content in MC-HPDC samples, both of which contributed to the avoiding of premature failure induced by stress concentration from the agglomerates of α-AlFeSi, large-sized needle-shaped β-AlFeSi phase and high content of porosity in conventional HPDC samples. **Figure 5.14b** gives an example of the agglomerates of Fe-containing intermetallic phase related fracture morphology in a conventional HPDC tensile sample, suggesting its negative contribution to mechanical performance.

5.4 Conclusions of Chapter 5

(1) Oxide formed in liquid LM24 is $MgAl_2O_4$ existing in the forms of oxide films or clusters.

(2) Intensive melt shearing promotes the nucleation of the α-AlFeSi phase on dispersed $MgAl_2O_4$ particles.

(3) There is a competition between the formation of primary α-AlFeSi and β-AlFeSi intermetallic phases, which is heavily dependent on the kinetic conditions such as cooling rate and intensive melt shearing during the formation of the Fe-containing intermetallic phase.

(4) Due to the significantly decreased amount of the β-AlFeSi phase, the permeability of liquid alloy was improved and in turn the porosity content in MC-HPDC samples was decreased. As a consequence of the combined effect of the modification of the Fe-

containing intermetallic phase and decreased content of porosity, the tensile elongation of MC-HPDC sample was improved.

Chapter 6

Grain refinement in Al-Mg binary alloys by intensive shearing

6.1 Introduction

In practice, oxides are always present in liquid aluminium alloys. They affect casting process and cause degradation of mechanical properties in the final cast components. Magnesium is an important alloying element in aluminium alloys, such as 5××× and 7××× wrought aluminium alloys, where the Mg content added can be as high as 7wt.% (Eskin, 2008). In Mg-containing Al alloys, either $MgAl_2O_4$ or MgO can be present in alloy melts during a normal melting procedure, depending on the Mg content, melting temperature and duration at a melting temperature (Cochran *et al.*, 1977).

In Chapters 4 and 5, we have demonstrated that spinel oxides in Al alloys can be effectively dispersed into individual particles and enhanced heterogeneous nucleation on these particles can be achieved by intensive shearing which resulted in refined Al_3Ti or Fe-containing intermetallic particles in two different Al alloys. In view of the fact that both $MgAl_2O_4$ and α-Al have a face-centered cubic (fcc) crystal structure (Cao and Campbell, 2003), it is expected to enhance the heterogeneous nucleation of α-Al phases on oxide particles and then achieve grain refined α-Al phases via intensive melt shearing. In this chapter, the grain refining effect of intensive shearing in Al-Mg binary alloys has been presented.

A set of binary Al-Mg alloys with varying magnesium content was subjected to intensive melt shearing. Oxides formed in the alloy melts were collected and characterised. The crystallographic match and orientation relationship between the oxides and α-Al phase were characterised by analytical electron microscopy to understand the enhanced heterogeneous nucleation behaviour.

6.2 Results

6.2.1 Effect of magnesium content on the grain size in Al-Mg binary alloys

In order to investigate the influence of naturally occurring oxides on the grain size of Al-Mg alloys without shearing, a set of binary Al-Mg alloys was melted and cast into TP-1 samples under the same conditions. The grain structures of the set of Al-Mg binary alloys are displayed in **Figures 6.1a** through **6.1d** with a low level of magnesium (≤1.0wt.%) and **Figures 6.2a** to **6.2c** with a high level of magnesium (3.0~7.0wt.%), as a function of magnesium content. For comparison, the micrographs (with/without shearing) of commercial purity aluminium (CP Al, <0.001wt.% Mg) melted and cast using the same procedure are included in **Figure 6.1**. Quantified grain size results are plotted in **Figure 6.3** (solid line), as a function of magnesium content. It can be seen that the grain size decreased progressively with an increase in the magnesium content in Al-Mg binary alloys. In particular, the grain size decreased rapidly in the lower magnesium containing alloys (≤1.0 wt.% Mg), from 1100±189 μm of CP Al to 343±73 μm at 1.0 wt% Mg (**Figure 6.1a** through **6.1d**); while for the Al-Mg alloys with magnesium contents ranging from 3.0 to 7.0 wt.%, the grain size decreased very slowly, with the grain size from 343±73 μm at 1.0 wt% Mg to 240±44 μm at 7.0 wt.% Mg (**Figures 6.2a** to **6.2c**). These results suggest that there is a critical magnesium content around 1.0 wt.% Mg, to achieve a significantly grain refined structure in Al-Mg binary alloys.

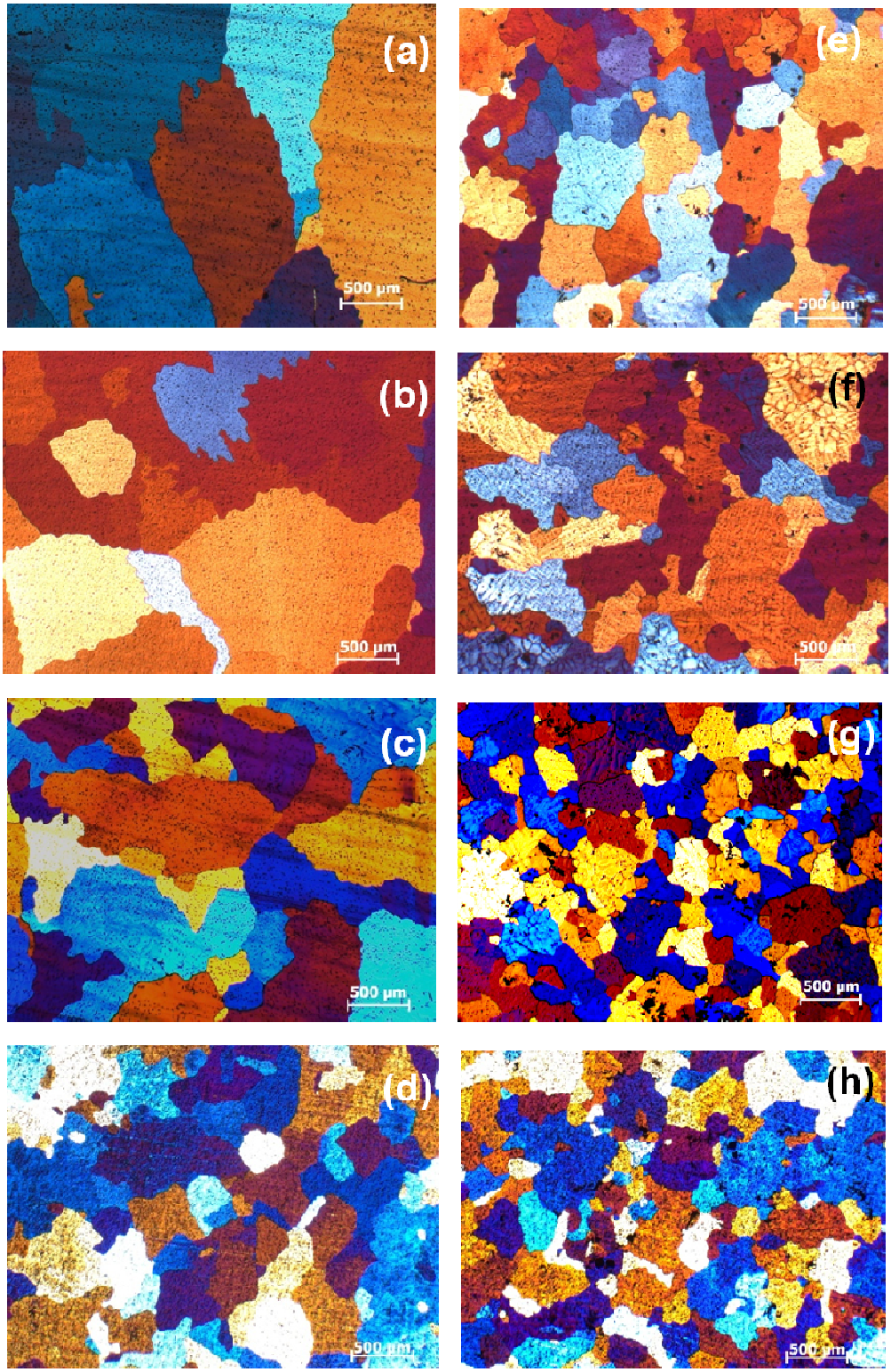

Figure 6.1 *Grain structures in Al-Mg alloys as a function of Mg contents (low levels of magnesium, in wt.%) and shearing:(a) 0Mg (CP Al), non-sheared; (b) 0.2Mg, non-sheared; (c) 0.7Mg, non-sheared; (d) 1.0 Mg, non-sheared; (e) 0Mg, sheared; (f) 0.2Mg, sheared; (g) 0.7Mg, sheared; (h)1.0Mg, sheared.*

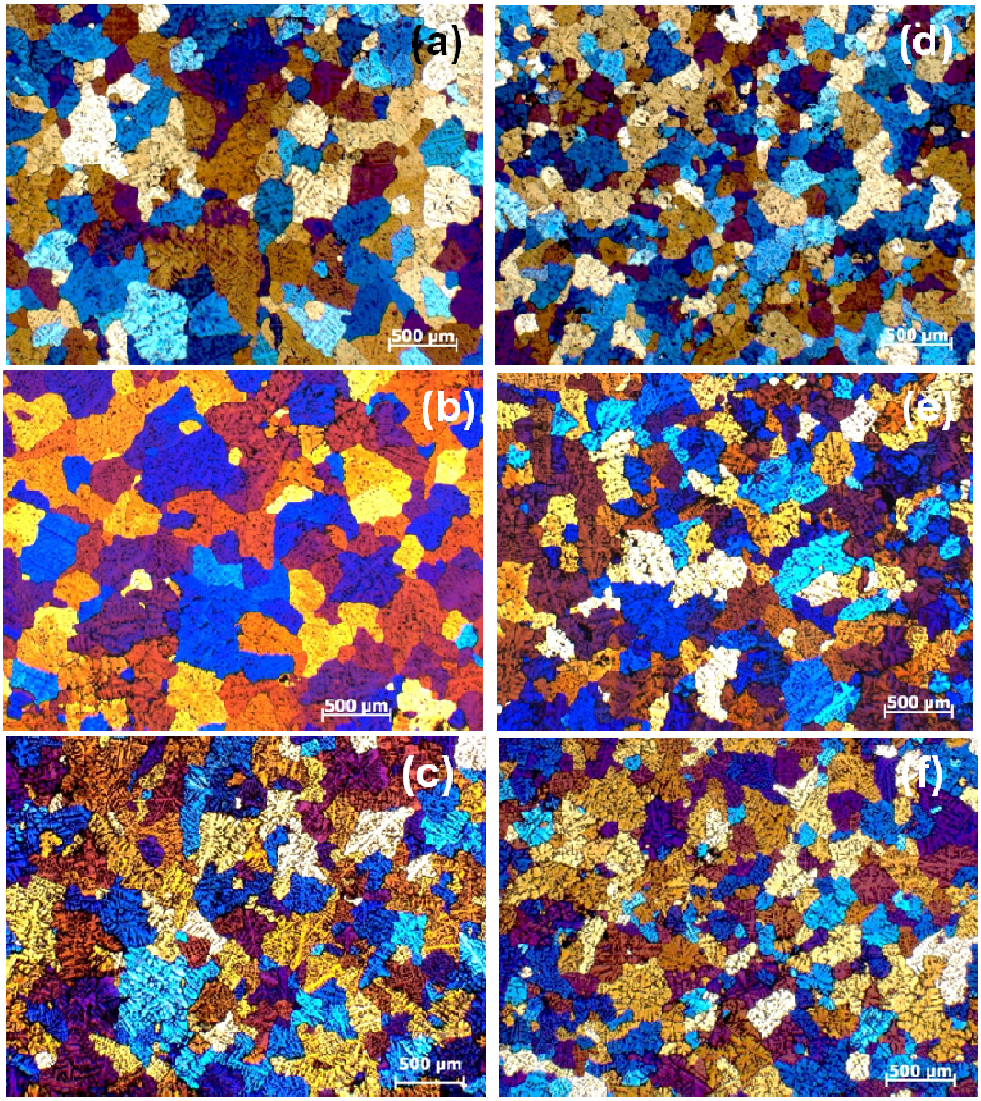

Figure 6.2 *Grain structures in Al-Mg alloys as a function of Mg contents (high levels of magnesium, in wt.%) and shearing:(a) 3.0Mg, non-sheared; (b) 5.0Mg, non-sheared; (c) 7.0Mg, non-sheared; (d) 3.0Mg, sheared; (e)5.0Mg,sheared; (f) 7.0Mg, sheared.*

6.2.2 Effect of intensive shearing on the grain size in Al-Mg binary alloys

To explore the effect of intensive melt shearing on the grain refinement of Al-Mg alloys, the alloy melts were subjected to shearing after the identical melting procedures, and then cast into TP-1 samples. The grain structures of sheared TP-1 samples of Al-Mg binary alloys are

presented in **Figures 6.1e** through **6.1h** and **Figures 6.2d** to **6.2f.** Quantified grain size results are plotted in **Figure 6.3** (dashed line), as a function of magnesium content.

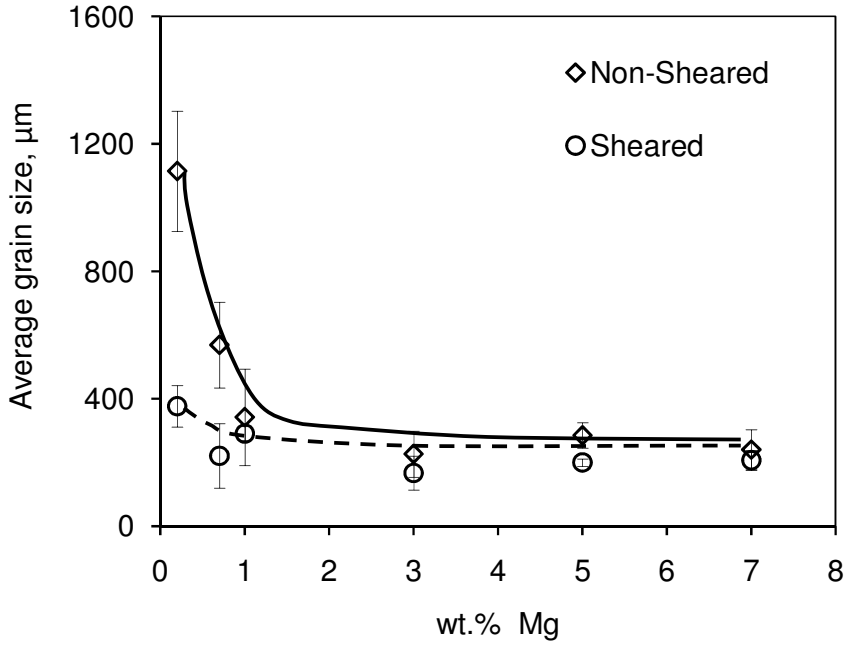

Figure 6.3 *Grain size as a function of magnesium content in Al-Mg alloys with and without shearing. The lines represent the best fit to the experimental data.*

In the range of lower magnesium content, e.g. from 0 to 1.0 wt.%Mg, the grain size decreased sharply to a very small value. For instance, in the case of CP Al, its grain size decreased from 1200±189μm (non-sheared) to 379±65μm (sheared); for the alloy with 0.2wt.%Mg, the grain size decreased from 1115±134μm (non-sheared) to 377±101μm (sheared). However, for the 1.0wt.% magnesium-containing alloy, the grain size decreased only from 343±73μm to 291±53μm; for the alloy with 7.0 wt.%Mg alloy, the grain size decreased only from 240±44μm to 207±30μm. The above comparisons indicate the similarity between CP Al and lower magnesium containing Al-Mg alloys (<1.0 wt.%), and the similarity between 1.0wt.% and 7.0wt.% magnesium containing Al-Mg alloys in terms of the grain refining effect by intensive shearing. To summarise the above results, it seems that intensive shearing has a

more significant grain refining effect on lower magnesium-containing Al-Mg alloys than in higher magnesium-containing Al-Mg alloys.

6.2.3 Columnar to equiaxed transition in Al-Mg binary alloys

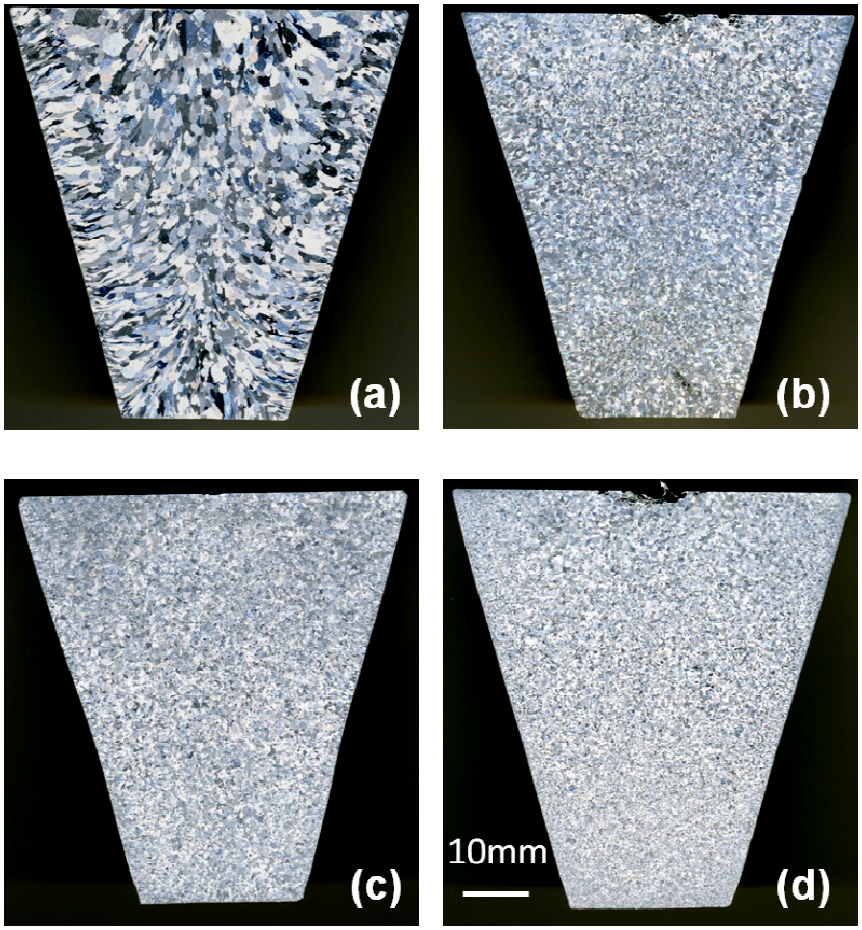

Figure 6.4 *Macrographs of longitudinal sections of TP-1 samples showing the columnar to equiaxed transition achieved by intensive melt shearing. (a) Al-0.7Mg, without shearing, showing the columnar grains; (b) Al-0.7Mg, with shearing, showing equiaxed grains; (c) Al-5Mg, without shearing, showing equiaxed grains; (d) Al-5Mg, with shearing, showing finer equiaxed grains.*

Due to the conic shape of the TP-1 samples, the macro-structural observation on the longitudinal sections can provide more information of the mode of solidification. **Figure 6.4** compares the grain structural transition with intensive melt shearing in Al-0.7Mg and Al-

5Mg alloys, based on the macro-structural observation on the longitudinal sections of the TP-1 samples. In the case of the Al-0.7Mg alloy, without shearing, the grain structure exhibits columnar grains (**Figure 6.4a**); with shearing, the grain structure was changed to equiaxed and much finer grains (**Figure 6.4b**). However, for the Al-5Mg alloy, both samples display equiaxed grains either with shearing or without (**Figure 6.4c** and **Figure 6.4d**); and, with shearing, the grain size becomes only slightly finer (**Figure 6.4d**).

6.2.4 Formation of $MgAl_2O_4$ and MgO in molten Al-Mg alloys

It has been established theoretically and experimentally that the formation of oxides in Al-Mg alloys is dependent on the magnesium concentration in the alloy of interest and melting temperature (Surla *et al.*, 2001; Haginoya and Fukusako, 1983). However, there is very limited information of the microstructural features of the oxides formed in liquid Al-Mg alloys (Haginoya and Fukusako, 1983). In the current study, we collected the oxides formed on the melt surface of two Al-Mg alloys at 700^{o}C containing 0.7wt.% and 5wt.%Mg to investigate the microstructural characteristics of oxides formed in molten Al-Mg alloys.

Figure 6.5 shows the morphological evolution of $MgAl_2O_4$ oxide in the Al-0.7Mg alloy. Because the sample was collected after being isothermally held for 4 h, the thickness or particle size of oxides can provide some information of the evolution of oxides. Initially, oxides existed in the form of thin films as shown in **Figures 6.5a** and **6.5b**. With a longer oxidation time, $MgAl_2O_4$ displays clusters which consist of oxide particles held together by capillary pressure as shown in **Figure 6.5c**.

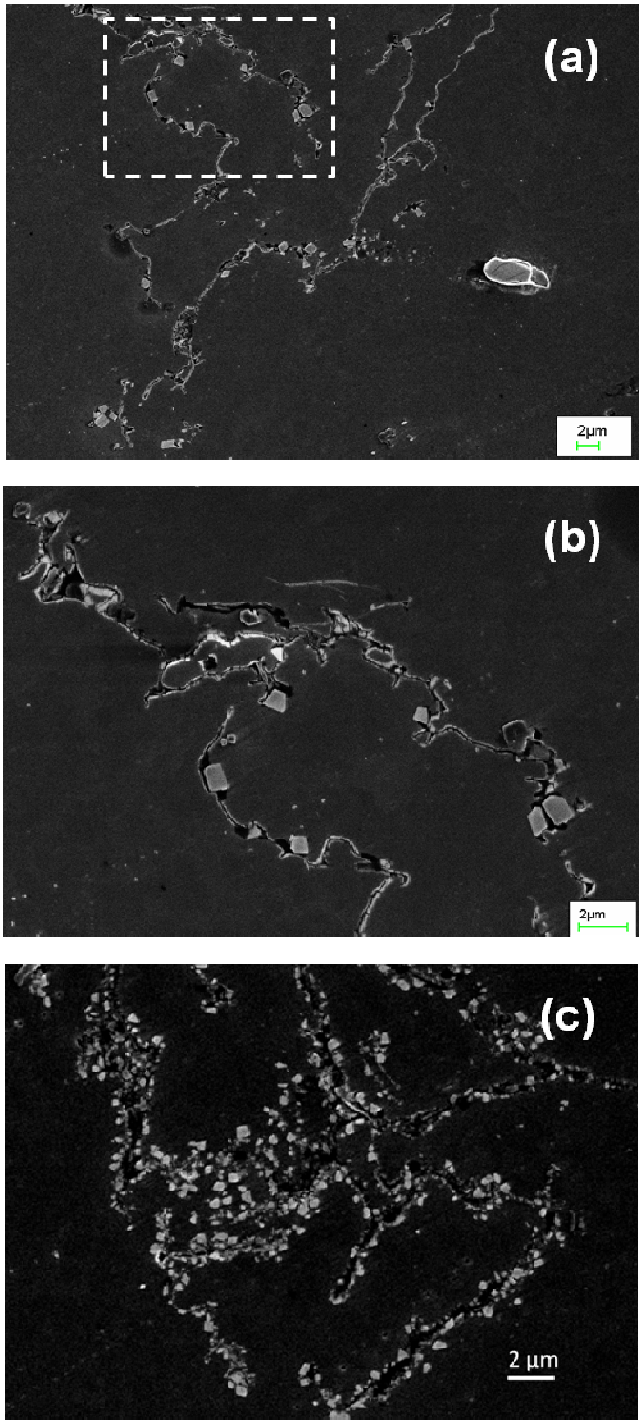

Figure 6.5 *SEM images of $MgAl_2O_4$ in the sample of Al-0.7Mg alloy isothermally held at 700°C for 4 h and then pressure filtered, showing the variation of oxides from thin film, thick film, and individual faceted $MgAl_2O_4$ particle: (a) Low magnification image; (b) enlarged view of the squared area in (a) showing thin films and few individual particles of $MgAl_2O_4$; and (c) showing the clusters of $MgAl_2O_4$ particles.*

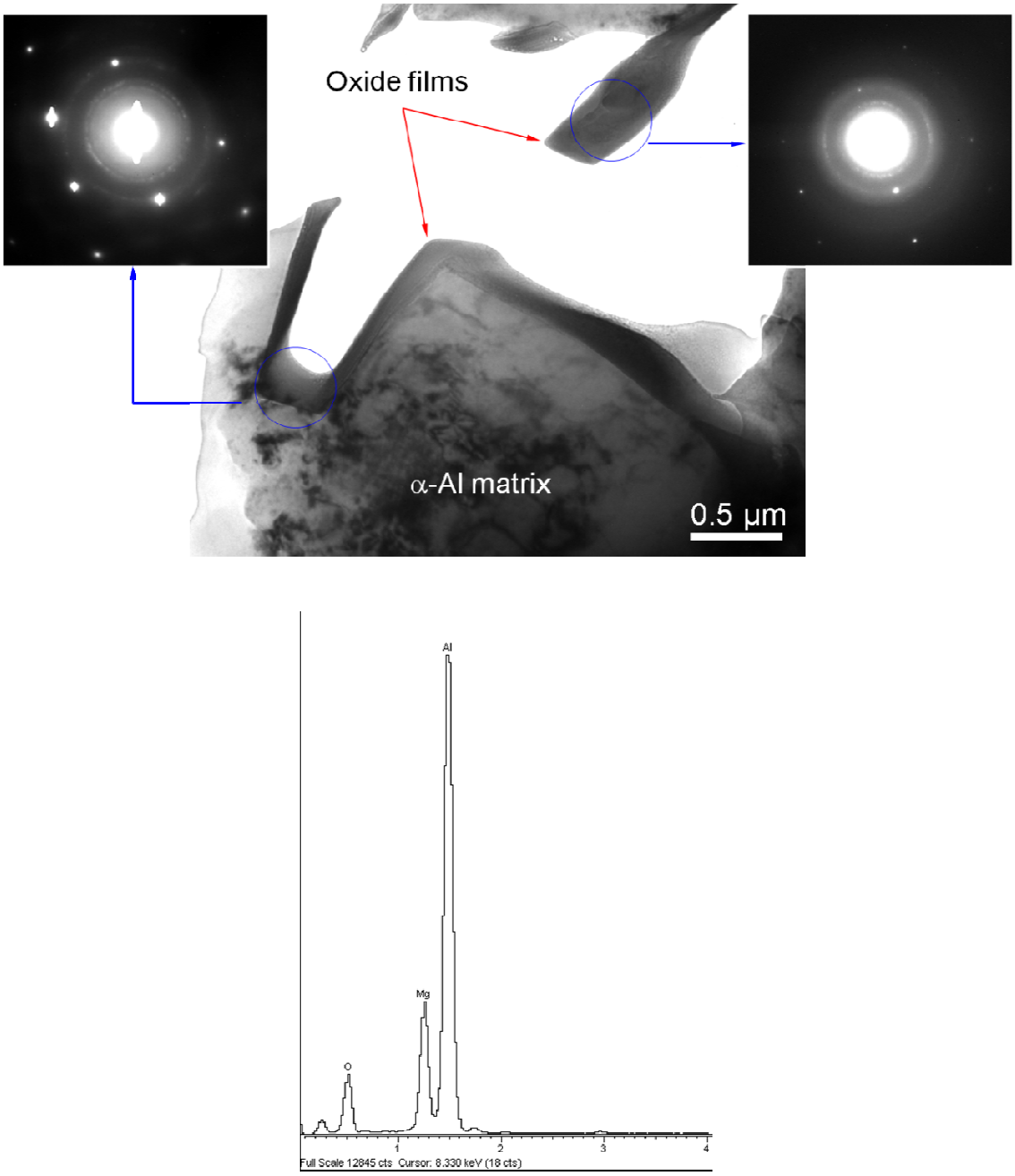

Figure 6.6 A typical *nano-crystalline $MgAl_2O_4$ film. (a) SADP indicating nano-crystalline oxide films (100-200nm thick); (b) TEM-EDX spectrum of the oxide film confirming it to be $MgAl_2O_4$.*

Figure 6.6 shows a typical TEM image of nanocrystalline oxide film with TEM-EDX spectrum confirming it to be $MgAl_2O_4$.

Figure 6.7 shows the morphology of MgO oxides formed in the Al-5Mg alloy isothermally held at 700°C for 4 h without shearing. It can be seen that an initially formed MgO exists in the form of very thin oxide film (marked by solid arrows in **Figure 6.7a**). **Figure 6.7b** shows the morphology of thick MgO films.

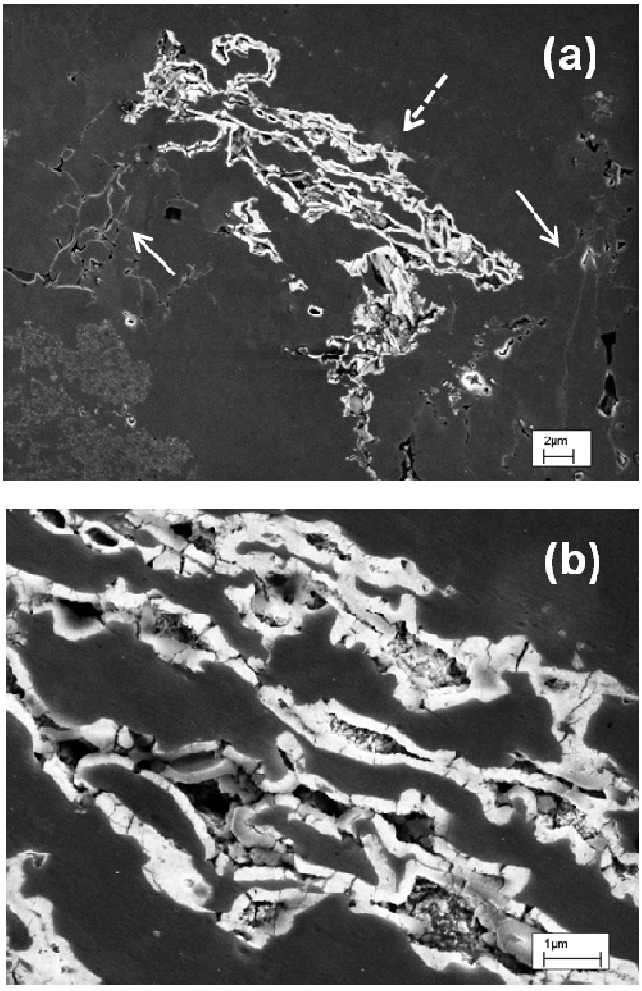

Figure 6.7 *MgO films with various thickness in the Al-5Mg alloy, non-sheared and pressure filtered sample: (a) MgO film indicated by solid arrows supposed to be relatively young; thick MgO film indicated by a dashed arrow supposed to be relatively old; (b)Enlarged view of the thick MgO in (a).*

With an extension of the oxidation time, the oxide film thickens and then breaks into small segments as shown in **Figure 6.8**. **Figure 6.8a** shows the locally thickening of MgO film. **Figure 6.8b** presents a thick MgO film (located at the lower part of this image).

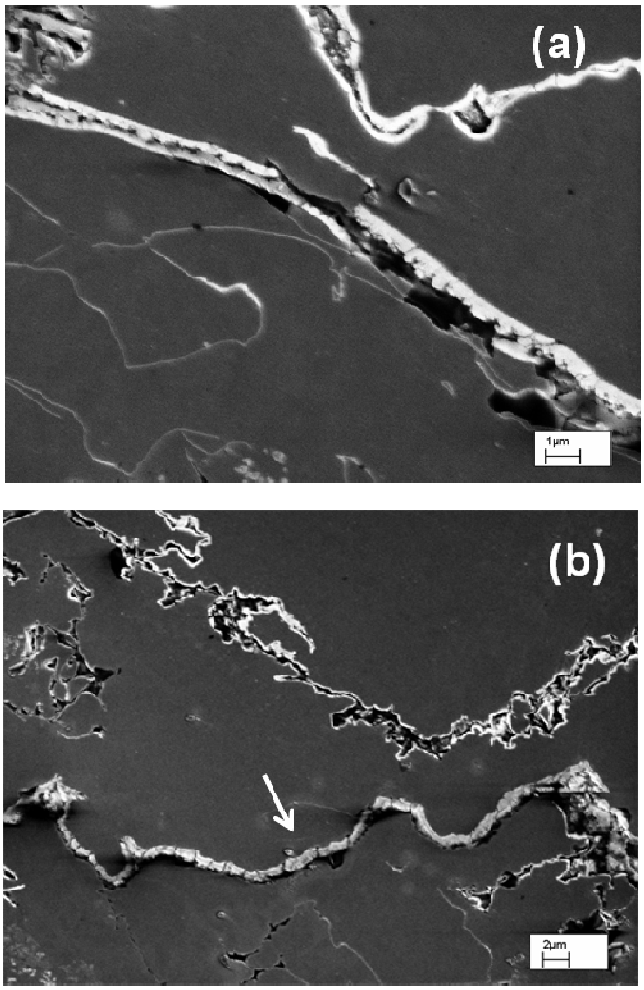

Figure 6.8 *Evolution of MgO in the Al-5Mg alloy, pressure filtered sample without shearing (a) high magnification image showing the locally thickening of MgO film; (b) a thick MgO film located at the lower part of the image (arrowed).*

Individual $MgAl_2O_4$ particles can also be observed in Al-5Mg (**Figure 6.9**). However, in the same alloy sheared at 700°C, only individual $MgAl_2O_4$ particles were observed (**Figure 6.10**) rather than the coexistence of MgO films and $MgAl_2O_4$ particles in the non-sheared sample. This transformation of MgO→$MgAl_2O_4$ with the introduction of intensive shearing will be discussed in the following sections.

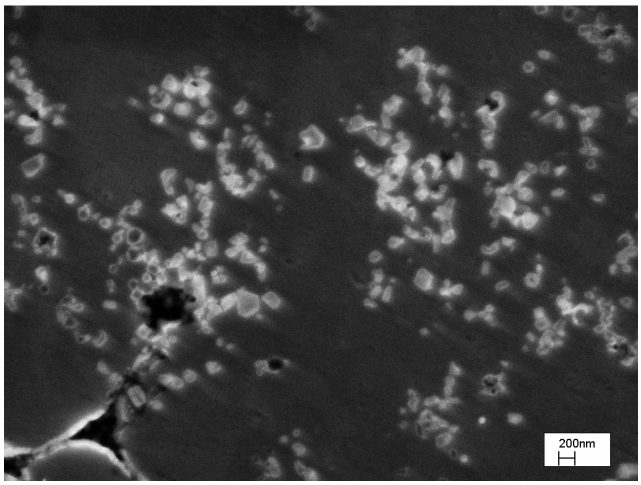

Figure 6.9 *$MgAl_2O_4$ formed in the sample of Al-5Mg alloy isothermally held at 700°C for 4 h, non-sheared and pressure filtered.*

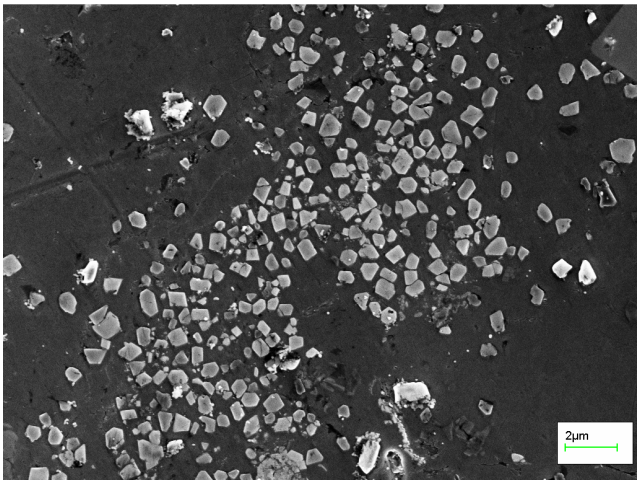

Figure 6.10 *Dispersed $MgAl_2O_4$ formed in the sample of Al-5Mg alloy sheared at 700°C and then pressure filtered.*

6.3 Discussion

6.3.1 Analysis of grain refinement from growth restriction factor theory

In the current study, the grain size decreased with an increase of the magnesium content in Al-Mg alloys as shown in **Figure 6.3** (solid line). With intensive shearing, the grain size

decreased more significantly as shown in **Figure 6.3** (dashed line), in particular for the case with low levels of magnesium concentration.

Easton and StJohn propose the solute paradigm to understand the grain refinement mechanisms incorporating the effect of both the addition of a grain refiner, including the potency and number density of a grain refiner, and cooling rate on the grain size (Easton and StJohn, 1999, 2001 and 2008). A growth restriction factor Q, was originally derived to be inversely proportional to the growth rate of the solidifying phase and has been used to characterize the solute effect (Maxwell and Hellawell, 1975; Easton and StJohn, 1999). **Table 6.1** gives the parameters used for the calculation of growth restriction factor Q.

$$Q = m_l C_0 (k - 1) \qquad (6.1)$$

Where m_l is the liquidus slope, k is the equilibrium partition coefficient, and C_0 is the solute content.

Table 6.1 *Parameters used for calculation of growth restriction factor Q by solutes in Al-Mg alloys (Easton and StJohn, 2005; Kearns and Cooper, 1997).*

Element	m, K/wt.%	k	$m(k-1)$,K/wt.%
Mg	-6.2	0.51	3.0
Ti	33.3	7.8	220
Ni	-3.3	0.007	3.3
Si	-6.6	0.11	5.9
Fe	-3.0	0.02	2.9
Mn	-1.6	0.94	0.1
Cu	-3.4	0.17	2.8
Cr	3.5	2.0	3.5
Zn	-1.2	0.20	0.96

It was found that grain size is related to solute content by a semi empirical relationship

$$d = a + b/Q \qquad (6.2)$$

Where d is the grain size and a and b are constants. It is also assumed that the same density of a particular type of nucleant particles is added to alloys with a range of Q values and under constant casting conditions. The gradient b is proportional to the nucleant potency and the intercept a is related to the maximum number of particles that are active nucleation sites of grains (StJohn *et al.*, 2007). A smaller value of b represents the lower undercooling required for nucleation, however, an increase in the active nucleation sites will decrease the intercept, a.

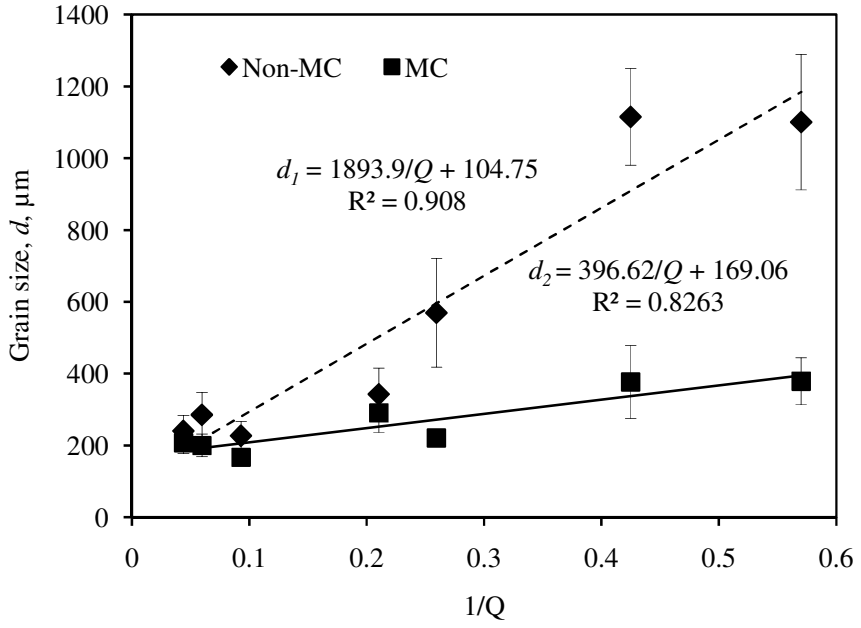

Figure 6.11 *Grain size against growth restriction factor Q in sheared and non-sheared TP-1 specimens of Al-Mg binary alloys, with that of CP Al included for comparison.*

In order to understand the mechanisms underlying the grain refinement with different magnesium concentration and intensive shearing, grain size against the reciprocal of growth restriction factor Q in sheared and non-sheared TP-1 specimens of Al-Mg binary alloys is

plotted in **Figure 6.11**, with data from CP Al included for comparison. The achievement of further grain refinement with intensive shearing shown in **Figure 6.11** cannot be understood directly in terms of the growth restriction factor *Q*. The lower value of *b* in sheared samples suggests a more powerful nucleant requiring smaller undercooling. In the current study, as no deliberate grain refiner additions were made, we need to understand which type of particle that was acting as heterogeneous nucleation sites. Considering the high affinity of magnesium for oxygen in aluminium alloys, the oxides possibly formed have been investigated and correlated to the grain refining effect achieved by intensive shearing.

6.3.2 The potency of oxides as nucleation sites for the α-Al phase

The interfacial free energy at the nucleating interface is the controlling factor in heterogeneous nucleation behaviour. However, a simple description of the interfacial energy is not possible since the total interfacial free energy of the system is composed of several contributory factors. Some of these factors reviewed by Bramfitt are as follows: the chemical nature of the substrate, the topographic features of the substrate surface, the electrostatic potential between the substrate and the nucleated solid, and the lattice strain or disregistry between the two phases at the interface (Bramfitt, 1970). In general, there is no doubt that a good crystallographic match between the crystal structures can be important (Bramfitt, 1970; Cao and Campbell, 2003; Campbell, 2003). In order to understand the role of oxides in the enhanced heterogeneous nucleation behaviour, the potency of different magnesium-containing oxides acting as nucleation sites of the α-Al phase, is analysed as follows in line with understanding their characteristics as heterogeneous nucleation sites.

Estimation of crystallographic match between oxides and the α-Al phase

Table 6.2 summarises the lattice misfit f_0 between some oxides and the α-Al phase at 660^{o}C along the close packed direction on the close packed planes. It is evident that the lattice misfit

between the possibly occurring oxides in Al-Mg alloys and the α-Al phase is relatively small, including for both MgO and $MgAl_2O_4$. In the current study, it can be expected that these oxides are all potential nucleation sites for the α-Al phase from the crystallographic match point-of-view. So their various performances as active nucleation sites may be influenced by the availability of sufficient number density or their spatial distribution characteristics. These will be discussed in the following sections.

Table 6.2 *Interatomic spacing misfit f_0 between some oxides and α-Al at 660°C.*

Interface	Crystal structure & lattice parameters, nm	OR: $(hkl)[hkl]_N$// $(uvw)[uvw]_S$	d[hkl], nm	d[uvw], nm	f_0 (%)
$MgAl_2O_4$/Al	N:fcc, a=0.81263, S: fcc, a=0.41212	(111)[110]// (111)[110]	0.57462	2×0.29141	1.41
MgO/Al	A: fcc, a=0.42477, B: fcc, a=0.41212	(111)[110]// (111)[110]	0.30036	0.29141	-3.07

Crystallographic orientation relationship between oxides and the α-Al phase

To make clear the potency of $MgAl_2O_4$ particles as nucleation sites of the α-Al phase in Al-Mg alloys, the crystallographic orientation relationship has been investigated by TEM. **Figure 6.12** shows the evidence of a cube-on-cube orientation relationship between $MgAl_2O_4$ and the α-Al matrix. The identified orientation relationship is:

$$(111)[110]\ MgAl_2O_4 \,//\, (111)\ [110]\ Al$$

This can be understood due to their similar crystal structures and the very small lattice mismatch estimated from the crystalline parameters of $MgAl_2O_4$ and the α-Al, as indicated in **Table 6.2.**

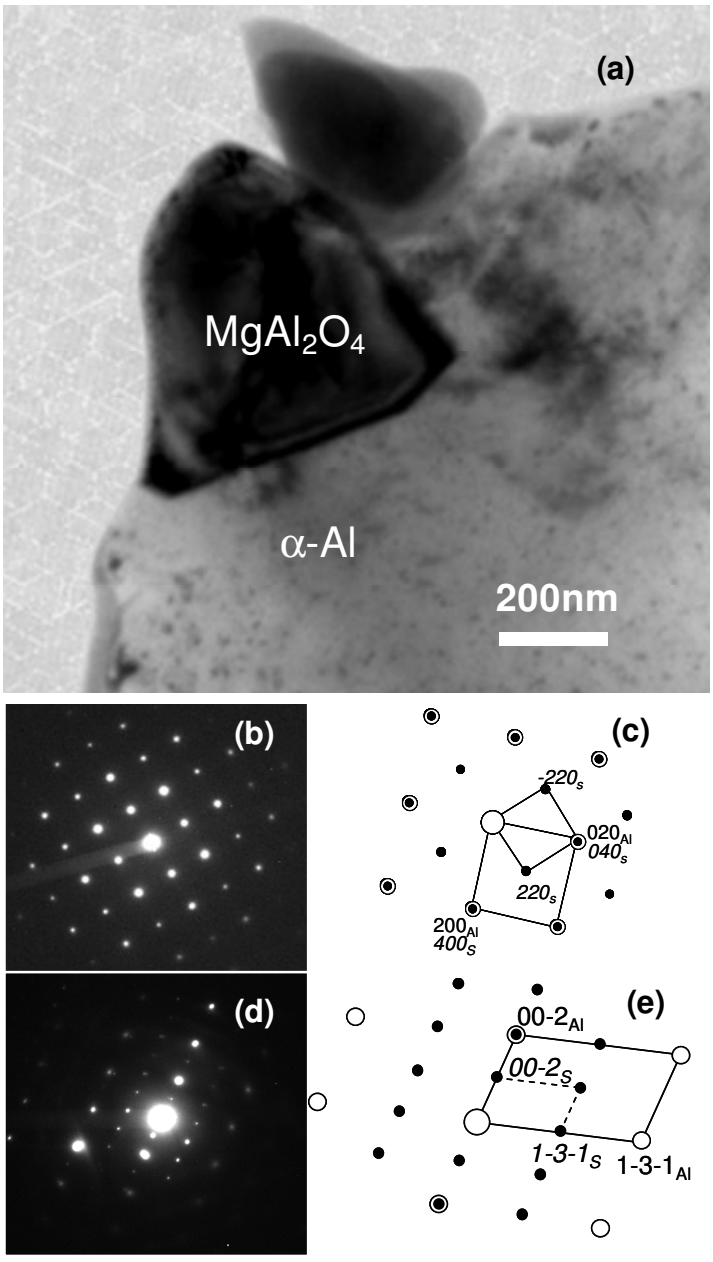

Figure 6.12 *Cube-on-cube crystallographic orientation relationship between $MgAl_2O_4$ and α-Al matrix: (a) TEM image and corresponding diffraction patterns along [001] zone axis in (b) and (c) and [310] zone axis in (d) and (e), confirming a cube-on-cube orientation relationship.*

Availability of close packed crystallographic plane {111} as nucleation sites of α-Al

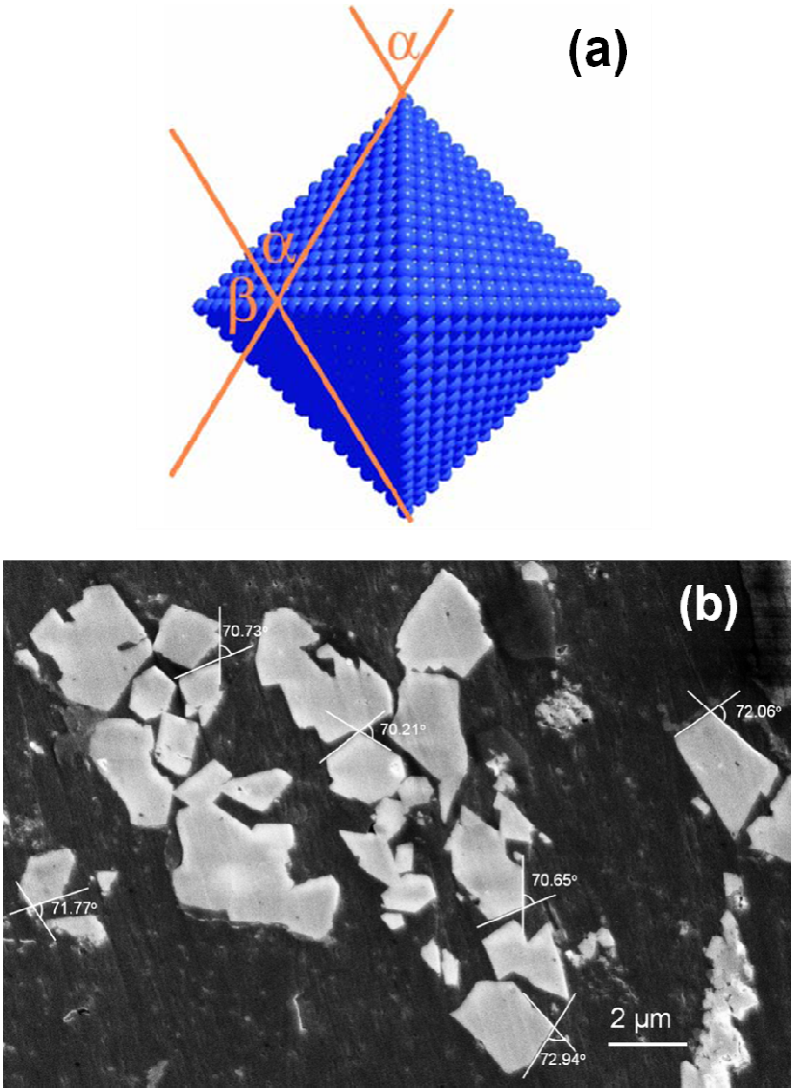

Figure 6.13 (a) *Arrangement of atoms in an ideal octahedron with fcc crystal structure. External facets represent four different planes of the group {111}. Two such facets can be parallel or cross themselves at the angle α = 70.5° or β =109.5° (Polak, 2007); (b) A typical SEM image of $MgAl_2O_4$ in Al-0.7Mg alloy showing the exposed surface of spinel particles being {111} planes, by identifying the characteristic angles between faceted planes which are very close to the calculated plane angles of the {111} crystal plane of fcc family, namely 70.5 and 109.5°.*

Extensive SEM observations were carried out to identify the crystallographic feature of the exposed surface of $MgAl_2O_4$ in Al-0.7Mg alloy. **Figure 6.13b** gives a typical image of

$MgAl_2O_4$ particles in Al-0.7Mg alloy. The characteristic angles between faceted planes are very close to the calculated angles between the {111} crystal plane of fcc family, namely 70.5 or 109.5^o (Hammond, 2009; Polak, 2007).

6.3.3 Oxidation kinetics in molten Al-Mg alloys with varying magnesium content

Under normal melting conditions, the oxidation of pure aluminium at the usual melting temperature such as ~100^{o}C above its melting point is a sluggish process, in particular, in the absence of any turbulence on the melt surface. In contrast, Al-Mg alloy melts under the same conditions can oxidize much more rapidly because of the formation of MgO and $MgAl_2O_4$ (Thiele, 1962; Cochran *et al.*, 1977).

Haginoya and Fukusako studied the oxidation behaviour of molten Al-Mg (2-12%) alloys from 650^{o}C to 900^{o}C for 3 h in dry air (Haginoya and Fukusako, 1983). It was identified by X-ray diffraction analysis that MgO was produced in an early stage of oxidation, and its amount increased temporarily and then decreased gradually, while the amount of $MgAl_2O_4$ increased gradually with time. The oxidation reactions can be described by two consecutive equations, $Mg + 1/2O_2 \rightarrow MgO$ and followed by $MgO + 2Al + 3/2O_2 \rightarrow MgAl_2O_4$ (ΔG_{700^oC}=-78.7kJ). This is consistent with the fact that $MgAl_2O_4$ is thermodynamically more stable than MgO (**Table 2.3)** (Scamans and Butler, 1975; Haginoya and Fukusako, 1983).

In the current study, with an increase of the magnesium content in Al-Mg binary alloys, oxidation kinetics can be accelerated progressively, as suggested by the oxidation dynamics results reported by Contreras et al., where oxidation occurred at 900^{o}C in Al-Mg alloys with a magnesium concentration in the range of 1-20wt.% (**Figure 2.9**) (Contreras *et al.*, 2004). In the Al-5Mg alloy, due to the relatively high magnesium content, MgO formed first, as predicted from thermodynamic stability calculation carried out by Surla et al. (**Figure 2.7**) (Surla *et al.*, 2001). On prolonged oxidation or with an increase of the magnesium content in

Al-Mg alloys, more MgO will be transformed to $MgAl_2O_4$. This has been evidenced by the SEM observation of the coexistence of MgO and $MgAl_2O_4$ in the non-sheared and pressure filtered Al-5Mg alloy (**Figures 6.7** through **6.9**). So the higher the magnesium content in Al-Mg alloys, the more $MgAl_2O_4$ can be expected in molten Al-Mg alloys.

6.3.4 Oxidation kinetics in molten Al-Mg alloys under intensive melt shearing

As discussed above, in Al-Mg alloys with high magnesium content, MgO forms first but transforms to $MgAl_2O_4$ with an extension of the oxidation duration. With intensive melt shearing, an accelerated transformation of $MgO \rightarrow MgAl_2O_4$ is evidenced by the extensive observations in the sheared and pressure filtered sample of the Al-5Mg alloy, where $MgAl_2O_4$ is the only oxides observed (**Figure 6.10**) rather than the coexistence of MgO and $MgAl_2O_4$ in its non-sheared counterpart (**Figures 6.7** through **6.9**). This transformation from MgO to $MgAl_2O_4$ can be understood from the viewpoint of a kinetic influence on the formation of oxides in aluminium alloys.

Previously, it was claimed that the transformation of amorphous to crystalline alumina is a nucleation and growth process at the melt/oxide interface (Impey *et al.*, 1988 and 1991; Wefers and Misra, 1987). During intensive melt shearing, the melt experiences cyclic stretching, folding and reorienting processes (**Figure 2.15**) (Ji *et al.*, 2001). Due to the brittle nature of oxides film, the oxide films are easily cracked and broken into smaller fragments. On the other hand, with intensive shearing, the diffusivity of species, such as magnesium, aluminium and oxygen in liquid aluminium alloys would be markedly accelerated (McCarty and Horsthemke, 1988). Through all the above-mentioned mechanisms, the transformation from MgO to $MgAl_2O_4$ would be enhanced significantly, which is thermodynamically favourable (Haginoya and Fukusako, 1983). As a consequence, more MgO will be transformed to $MgAl_2O_4$ via the following reaction

$$MgO + 2Al + 3/2O_2 \rightarrow MgAl_2O_4 \qquad (6.3)$$

6.3.5 Surfactant effect of solute magnesium and good wetting between oxides and α-Al

The achievement of a good wetting between oxides and liquid Al alloys is critical to the enhanced heterogeneous nucleation on oxide particles. The solute magnesium in liquid Al alloys is a powerful surfactant in Al alloys (Korol'kov, 1960; Delannay *et al.*, 1987). The magnesium moves to the free surface and can be readily oxidized to form MgO or $MgAl_2O_4$. In such a case, magnesium can reduce the surface tension and the viscosity of Al alloys (Contreras *et al.*, 2004). On the other hand, if an oxygen-containing surface comes into contact with magnesium, such as oxide particles presented by a gas bridge model (**Figure 2.14**), there is a likely chance of oxygen absorbed on the surface of the oxides becoming scavenged (Pai *et al.*,1995). Both these mechanisms would contribute to the improved wetting between oxide particles (such as $MgAl_2O_4$) and liquid Al-Mg alloy.

6.3.6 Feasibility of the achievement of dispersion of oxides in Al-Mg alloys

In Al-Mg alloys, a protective continuous oxide film cannot be formed and exudation of liquid aluminium would occur (Impey *et al.*, 1988). As a result, these oxide particles of $MgAl_2O_4$ or MgO are embedded in liquid Al matrix and held together by a capillary pressure. The capillary pressure P_c can be estimated by the Laplace-Young equation as (Trumble, 1998)

$$P_c = \frac{2\gamma_{LV}\cos\theta}{r} \qquad (6.4)$$

where γ_{LV} is the surface tension of liquid alloy, θ is the contact angle, and r is the radius of distance between $MgAl_2O_4$ particles in the current study. Elements that have a high affinity for oxygen lower the surface tension of liquid metals with oxides (Delannay *et al.*, 1987). It is known that the surface tension of molten aluminium drops significantly with the addition of solute element Mg (Korol'kov, 1960; Delannay *et al.*, 1987). At a concentration of 0.5wt.% Mg, the surface tension of pure aluminium at its melting point drops from 0.92 to 0.72 N/m (Korol'kov, 1960). Experimentally, Anson et al. have reported the reduced surface tension by

magnesium alloying addition in Al cast alloys (Anson *et al.*, 1999). As a consequence, it would be reasonable to expect a decreased capillary pressure in Al-Mg alloys compared with CP Al melt; especially in an Al-Mg alloy with higher magnesium content, where naturally dispersed $MgAl_2O_4$ particles can be expected. Therefore, it is more easily to achieve well dispersed oxide particles in Al-Mg alloys with high shear technology.

6.3.7 Oxide distribution characteristics in alloy melts with intensive melt shearing

Oxide distribution characteristics in alloy melts include aspects of both size and spatial distribution. With intensive melt shearing, oxides are dispersed throughout the entire volume of the alloy melt. Once the oxide particles are dispersed, after shearing, it will take a long time before any observable agglomerates of oxides form in the melt although the dispersed oxide particles have a tendency to agglomerate in order to minimize their interfacial energy. This agglomeration process is driven by the Brownian motion which is usually several orders of magnitude slower than that of de-agglomeration (Fan *et al.*, 2009).

6.3.8 The efficiency of oxides as nucleation sites of the α-Al phase

As discussed above, all the possibly formed oxides in Al-Mg binary alloys have a good crystallographic match with the α-Al phase and hence they all could be potent heterogeneous nucleation sites of the α-Al during solidification. However, nucleation efficiency also plays a key role in the resultant grain refining effect. Nucleation efficiency refers to the effectiveness of a given type of solid particle (e.g., TiB_2) with specific physical characteristics and solidification conditions, such as the number density, size, and size distribution of the nucleating substrates (Fan, 2010). For a given nucleating system, nucleation potency is fixed but nucleation efficiency can be changed by modifying the physical characteristics of the nucleating particles and/ or changing the solidification conditions such as the cooling rate (Fan, 2010). Only if the number density of potent nucleation sites with an appropriate particle size distribution is large enough, can a significant grain refinement be achieved in line with

the free growth model developed by Greer and his co-workers (Greer *et al.*, 2000; Quested and Greer, 2004; Men *et al.*, 2010).

In an Al-Mg alloy with low levels of magnesium content (<1.0wt. %), $MgAl_2O_4$ forms with relatively low oxidation rate and exists in the form of both oxide films and individual particles (**Figures 6.5 and 6.6**). As a result, under a condition without shearing, even if there is high potency as a nucleation site of α-Al phase, due to the insufficient number density of $MgAl_2O_4$ particles, the grain refining effect is very limited, as shown in **Figures 6.1b** through **6.1d**, and **Figure 6.3** for the alloys with a low level of magnesium contents (<1.0wt.%). However, for the Al-Mg alloys with a high level of magnesium, with an increase of the magnesium concentration, the oxidation rate can be accelerated significantly (**Figure 2.9**) (Contreras *et al.*, 2004) and the number density of naturally dispersed $MgAl_2O_4$ particles available in an Al-Mg alloy melt is expected to be increased. This extrapolation of the oxidation dynamics from the results by Contreras et al. is expected to be reasonable because their experiments were carried out at 900^{o}C which was still far below the boiling point of magnesium 1090^{o}C (Gaskell, 1996), while the alloys in the current study were melted at 750^{o}C below the temperature explored in theirs. On the other hand, due to the high magnesium content, (e.g. >1.0wt.%), the effect of growth restriction factor Q may contribute to certain extent to increasing of the active nuclei density. As a consequence, the nucleation rate would be increased sharply and hence the grain size is decreased markedly with an increase of the magnesium concentration in Al-Mg alloys even without shearing, as shown in **Figures 6.2a** to **6.2c** and **Figure 6.3** for the samples with a high magnesium concentration (>1.0wt.%).

With intensive shearing, for the Al-Mg alloys with a low magnesium concentration, due to the strong dispersion function of intensive melt shearing, a sufficient number density of

dispersed $MgAl_2O_4$ particles can be obtained. As a result, significant grain refinement can be achieved by intensive melt shearing as displayed in **Figures 6.1f** through **6.1h** and **6.3**, for the samples with a low level of magnesium (<1.0wt.%). For the Al-Mg alloys with high magnesium content, the grain refining effect by intensive shearing is relatively marginal although the dispersed $MgAl_2O_4$ can also be achieved (**Figure 6.10**). This is due to the originally finer grain size due to the contributions from both naturally dispersed $MgAl_2O_4$ particles and a high value of Q.

6.4 Conclusions of Chapter 6

(1) In Al-Mg alloys with low levels of magnesium, e.g. in Al-0.7Mg alloy, oxides are $MgAl_2O_4$ in the form of films or clusters; for the alloys with high levels of magnesium, naturally dispersed $MgAl_2O_4$ particles are formed even without shearing.

(2) With intensive melt shearing, films and clusters of $MgAl_2O_4$ were dispersed throughout the melts of Al-Mg alloys.

(3) Cube-on-cube orientation relationship is established between $MgAl_2O_4$ and α-Al matrix: (111) [110] $MgAl_2O_4$ // (111) [110] Al.

(4) Intensive melt shearing enhances the heterogeneous nucleation events on $MgAl_2O_4$ oxides by improved nucleation efficiency. This is especially effective for Al-Mg alloys containing low levels of magnesium (<1.0 wt.%), where the number density of individual dispersed $MgAl_2O_4$ particles naturally formed is limited in terms of being able to be active nucleation sites.

(5) $MgAl_2O_4$ is thermodynamically more stable than MgO in Al-Mg alloys. This is why intensive shearing can promote the formation of $MgAl_2O_4$ rather than MgO in Al-Mg alloys containing high levels of magnesium.

Chapter 7

Grain refinement in a commercial purity Al by intensive shearing

7.1 Introduction

In Chapter 6, grain refining effect of intensive melt shearing in Al-Mg alloys has been established. The grain refinement is due to the improved nucleation efficiency of $MgAl_2O_4$ particles as the active nucleation sites of α-Al phase by intensive melt shearing. In Al alloys, γ-Al_2O_3 and α-Al_2O_3 are also very common oxides naturally occurring depending on melting temperature and other conditions. Is it possible to use these oxides to manipulate the grain structures of Al alloys without deliberate additions of grain refiners?

In this chapter, the grain refining effect on commercial purity aluminium (CP Al) has been explored. CP Al (99.86 Wt. %Al, refer to **Table 3.4** for a detailed composition) was subjected to intensive melt shearing. Oxides formed under particular conditions were collected and analysed to identify the oxide type and its crystallographic characteristics. The crystallographic match between oxides and the α-Al phase is analysed to understand the enhanced heterogeneous nucleation behaviour.

7.2 Results

7.2.1 Effect of superheating temperature on the grain size in CP Al

It has been established that many transition aluminas exist in liquid aluminium with an increase of melting temperature. Raising the temperature above a critical level induces a gradual transformation of γ-Al_2O_3 to α-Al_2O_3. In order to investigate the effect of the oxides naturally occurring in liquid aluminium on the grain size of CP Al, different melting temperatures were adopted and the grain structure and grain size of TP-1 sample were evaluated. In consideration of the fact that the reverse transformation from α- to γ-Al_2O_3 does not occur on cooling (Yan *et al.*, 2010), the influence of different thermal histories of the alloy melt, i.e. both increasing and decreasing melt temperature, on the microstructures of CP Al were investigated.

The macrographs of TP-1 samples cast with increasing melt temperature from 680 to 920^{o}C and decreasing melt temperature from 920 to 680^{o}C, are shown in **Figure 7.1**. It can be seen clearly that the samples cast at lower superheating temperatures below 800^{o}C display two kinds of grain structures, i.e. columnar grains at the edge of the sample and equiaxed grains at the centre of the cross section, while for the samples cast at a higher superheating temperature above 840^{o}C, only equiaxed grains can be observed. This is easily understood in terms of decreased chilling capability (in other words, decreased thermal undercooling with increasing superheat) due to the higher heat capacity in the melt with increasing melt superheating temperature. So only the grains located at the central part of these samples, which are considered to correlate the nucleation behaviour with superheating temperature, are taken into account in the data analysis of grain size. This treatment is also applicable to the case of the TP-1 samples with intensive melt shearing. When the superheat was below 140^{o}C (melting and casting temperature lower than 800^{o}C), the grain size increased monotonically with an increase of the superheating temperature;

when the superheat exceeded 180°C (melting and casting temperature higher than 840°C), the grain size of CP Al decreased slightly from 840 up to 920°C. This suggests a transition of nucleation mechanism.

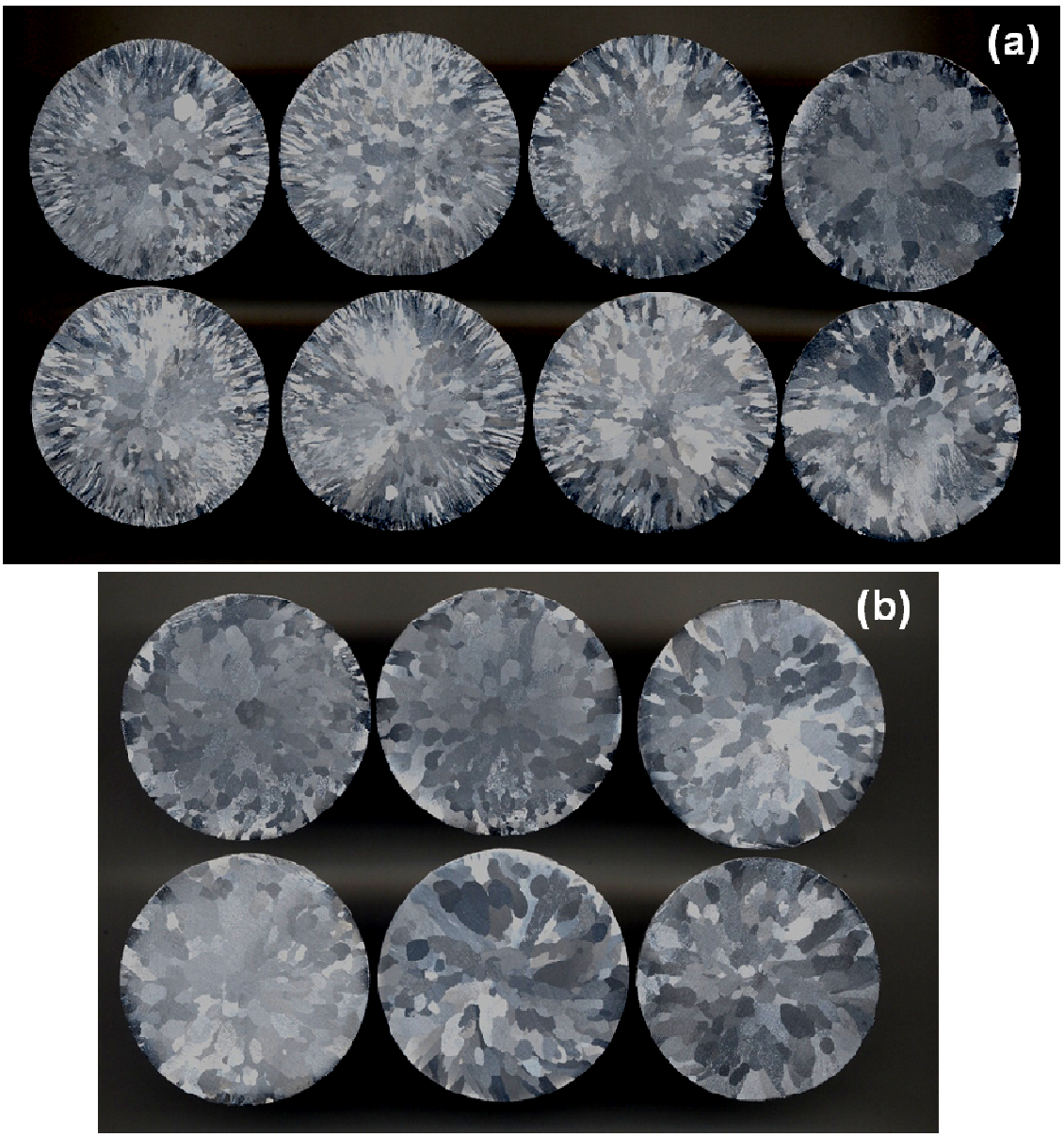

Figure 7.1 *Macrostructures of whole cross section in TP-1 samples of CP Al with varying superheat and different thermal histories: (a) Left to right: 680, 720, 760 and 800°C; (b) Left to right: 840, 880 and 920°C (Upper row: with increase of melting temperature and lower row: with decrease of melting temperature).*

The quantified grain size of CP Al is plotted against superheating temperature in **Figure 7.2**, for both increasing and decreasing temperature samples. It can be seen that the trend of grain size variation with superheating temperature can be categorised into two groups. From 680 to 840°C, the grain size increased monotonically with an increase of the superheating temperature, and then the grain size decreased slightly up to a superheating temperature of 920°C. In both cases, either increasing or decreasing temperatures, this trend is the same, although the samples prepared during decreasing temperatures displayed a slightly finer grain size compared with those prepared with increasing temperatures, when the grain size is compared at the corresponding superheating temperature.

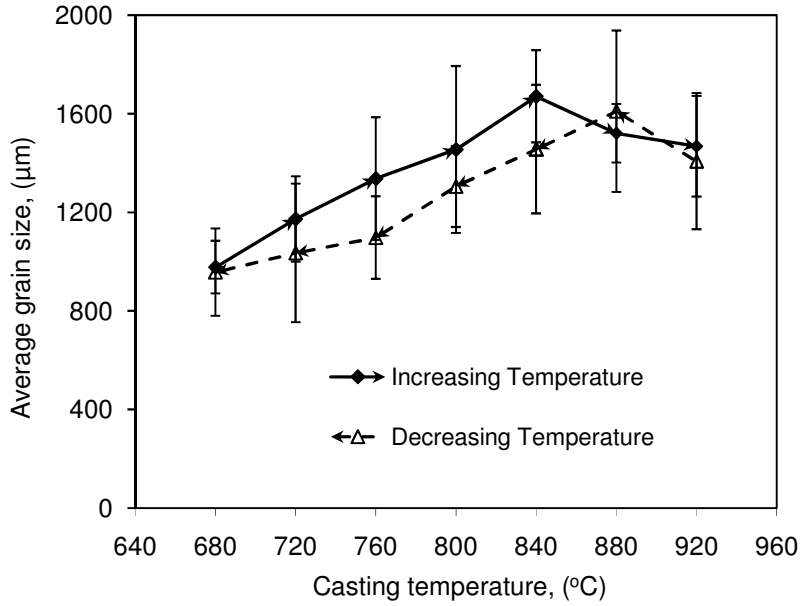

Figure 7.2 *Grain sizes as a function of superheating temperature with different thermal histories in TP-1 samples of CP Al.*

The microstructures of TP-1 samples cast with increasing melting temperature are presented in **Figures 7.3 (a-d)** and **7.4 (a-c)**, showing that the grain size increases monotonically with an increase of superheating temperature from 680 to 840°C.

7.2.2 Effect of intensive melt shearing on the grain size in CP Al

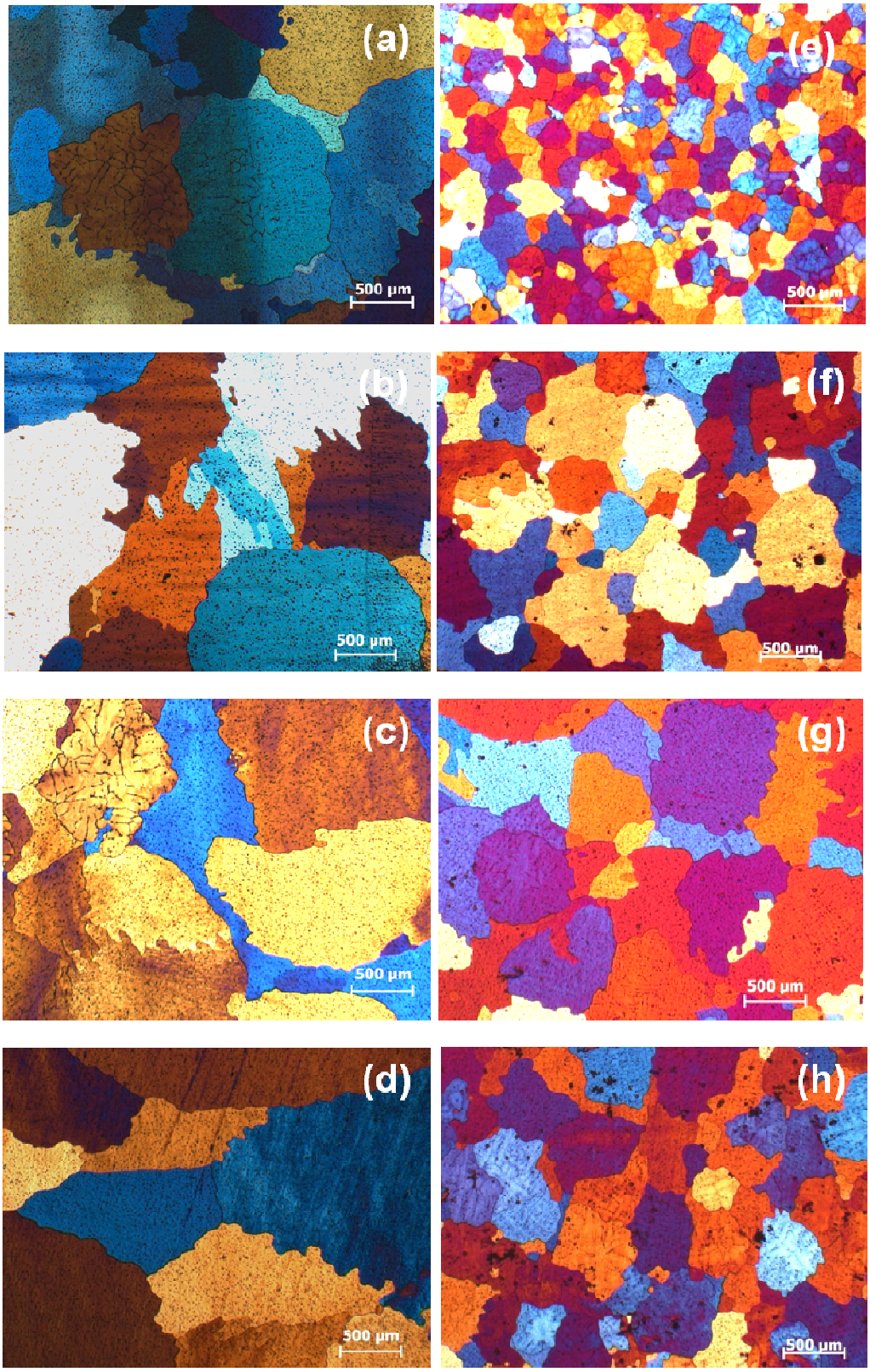

Figure 7.3 *Grain refining effect by intensive shearing in a lower shearing temperature, from 680 to 740°C. Micrographs of non-sheared TP-1 samples, cast at: (a) 680; (b) 700; (c) 720 and (d) 740 °C; Micrographs of sheared TP-1 samples, sheared and cast at: (e) 680; (f) 700; (g) 720 and (h)740°C.*

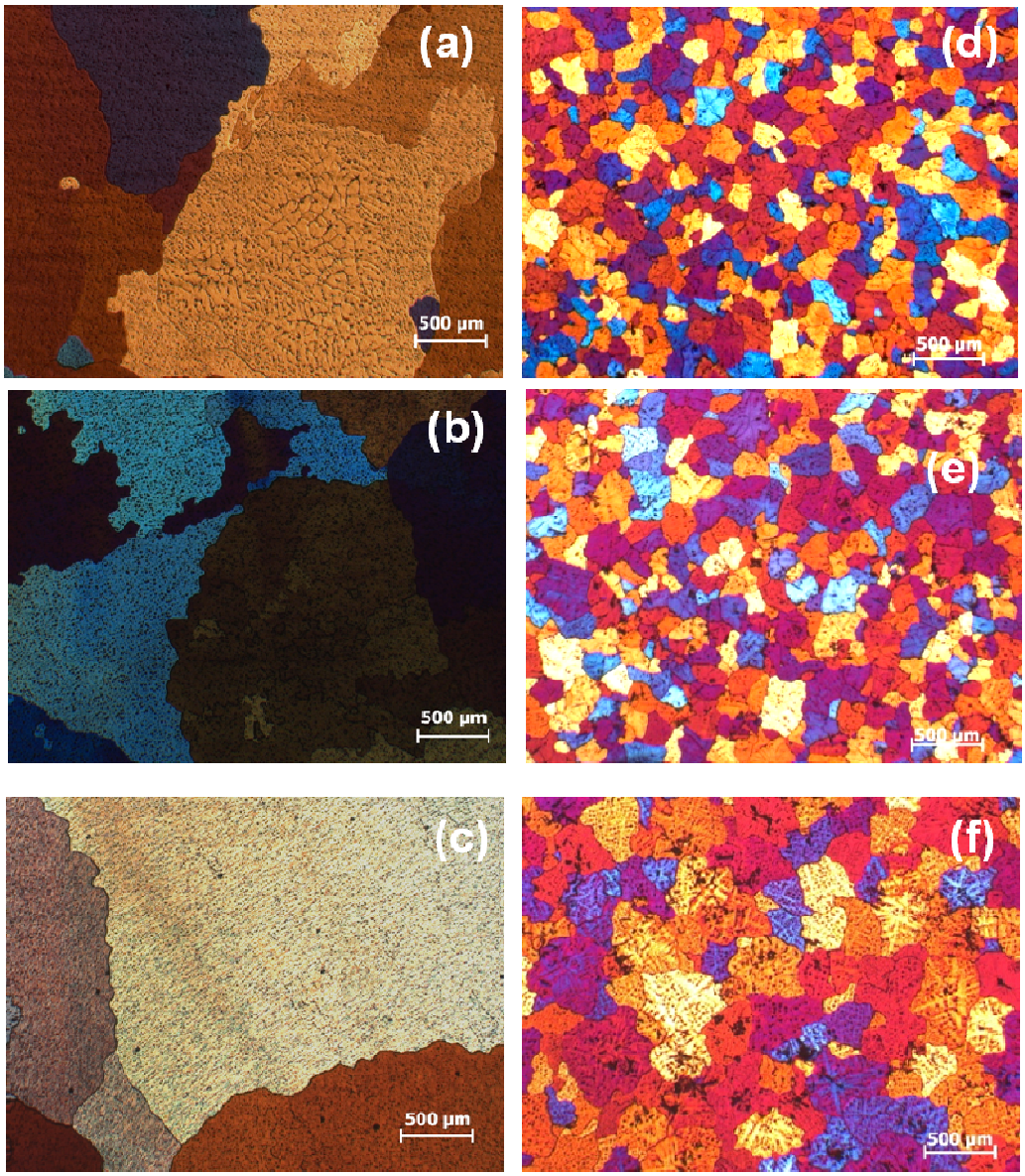

Figure 7.4 *More significant grain refining effect by intensive shearing in a higher shearing temperature, from 760 to 840°C. Micrographs of non-sheared TP-1 samples, cast at: (a) 760; (b) 800 and (c) 840 °C; Micrographs of sheared TP-1 samples, sheared and cast at: (d) 760; (e) 800 and (f) 840°C.*

In order to investigate the evolution of oxides in CP Al with different melting temperature under intensive shearing and the effect on the resulting grain size, shearing temperatures ranging from 680 to 840°C were adopted and then cast into TP-1 samples. **Figures 7.3** and

7.4 reveal the grain refining effect by intensive shearing in different regimes of temperature.

In the shearing temperatures range from 680 to 740°C, grain refinement can be achieved by shearing, as shown in **Figure 7.3**. Interestingly, more significant grain refining effect can be achieved in a higher shearing temperature from 760 to 840°C, as presented in **Figure 7.4.**

The grain sizes of CP Al against shearing temperatures are plotted in **Figure 7.5**, alongside the best fitted line.

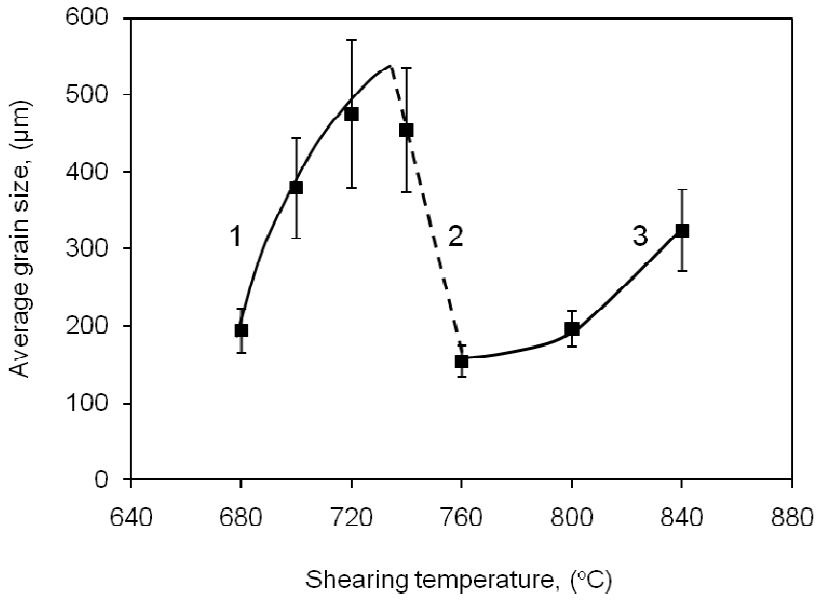

Figure 7.5 *Grain size as a function of shearing temperature in TP-1 samples of CP Al. The three lines represent the best fit to the experimental data.*

It is seen that three different lines can be used to describe the variation of grain size with an increase of the shearing temperature in the range of 680-840°C. When the melt was sheared at a temperature between 680 and 720°C, the grain size increased with an increase

of the shearing temperature (Line 1). At a shearing temperature of 740^{o}C, the grain size was finer compared with the sample sheared at 720^{o}C; moreover, the grain size was decreased further and the finest grain size was obtained at a shearing temperature of 760^{o}C, suggesting a turning point occurred at 740±20^{o}C (Line 2). As a shearing temperature exceeded 760 ^{o}C, the grain size increased slowly up to 840^{o}C (Line 3). These three distinct plots of the grain size against shearing temperature suggest a different sensitivity of grain size to an increase in the superheat temperature under intensive shearing; hence implying that there may be a difference in nucleation mechanisms. The lower gradient in the higher shearing temperature regime (Line 3, 760~840^{o}C) may imply a more potent nucleation site when compared to the higher gradient in the lower shearing temperature regime (Line 1, 680~720^{o}C).

7.2.3 Columnar to equiaxed transition achieved by intensive shearing

The role of a grain refining additive is, in essence, to promote the columnar to equiaxed transition (CET). The influence of intensive shearing on the achievement of CET was investigated for the samples cast at two temperatures, i.e. 680 and 760^{o}C. The macrographs of the longitudinal sections of the TP-1 samples cast at 680 and 760^{o}C are shown in **Figure 7.6**. The non-sheared samples cast at either 680 or 760^{o}C, exhibit columnar grain structures (**Figures 7.6a** and **7.6c**); in contrast, the sheared samples with the same cast temperatures, show an equiaxed grain structure (**Figures 7.6b** and **7.6d**). Furthermore, the sample sheared at 760^{o}C, displays much finer grains compared to the sample sheared at 680^{o}C (**Figures 7.6b** and **7.6d**). This observation is consistent with the quantitative results of the grain sizes presented in **Figure 7.5.**

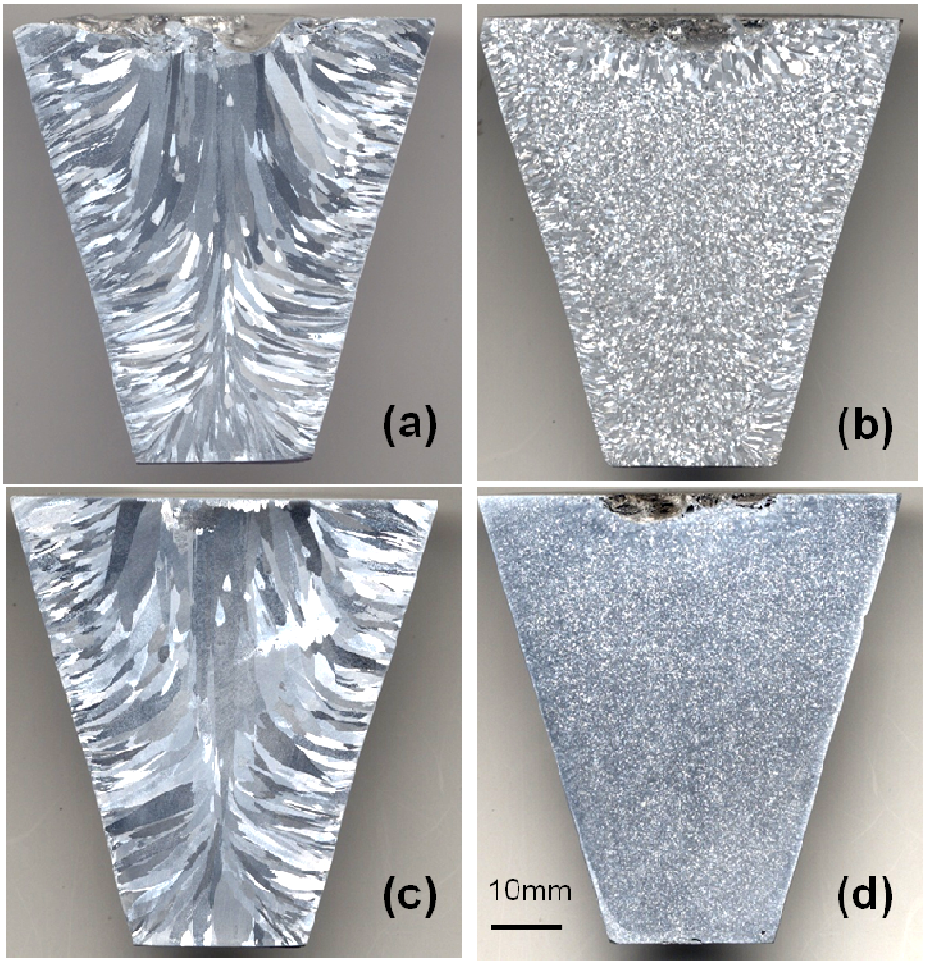

Figure 7.6 *Macrographs of the longitudinal sections of TP-1 samples of CP Al, showing the columnar to equiaxed transition by intensive melt shearing: (a) columnar grains in the sample cast at 680 °C without shearing; (b) Equiaxed grains in the sample sheared at 680 °C; (c) Columnar grains in the sample cast at 760°C without shearing and (d) much finer equiaxed grains in the sample sheared at 760 °C.*

7.2.4 SEM characterisation of oxides collected from CP Al melt

Due to the high affinity of aluminium for oxygen, oxide films are readily formed on the surface of liquid aluminium when it is exposed to an atmosphere containing oxygen (Impey *et al.*, 1988). In the current study, as a starting point, we collected the oxide films formed on the melt surface of CP Al at two melting temperatures, 700 and 920°C.

Scanning electron microscopy (SEM) micrographs of the oxides formed at 700 and 920°C

in CP Al melts without shearing are shown in **Figure 7.7** and **Figure 7.8**, respectively. It can be seen at 700°C, the dominant oxide formed in the CP Al melt is thin oxide films around 50-100 nm (**Figure 7.7a**). Close observations reveal that the oxide films formed at 700°C consists of platelet particles (**Figure 7.7b**).

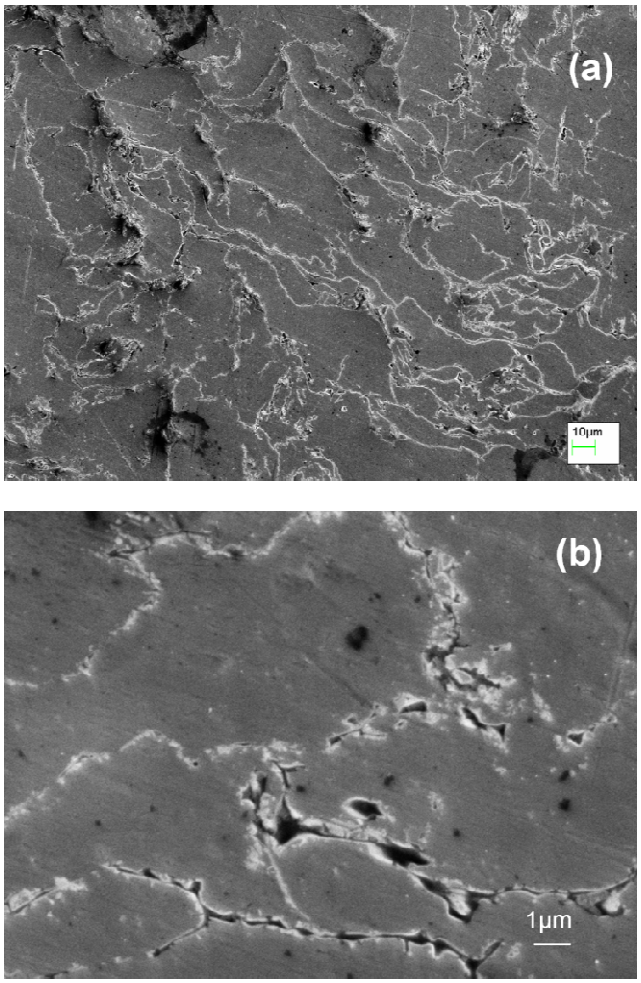

Figure 7.7 *SEM micrographs of oxide films in CP Al melts at 700°C (skimmed and collected): (a) low magnification image showing thin films; and (b) high magnification image showing the oxide films consisting of platelet particles.*

However, the oxides formed at 920°C are in the form of clusters consisting of individual faceted particles, as shown in **Figure 7.8**. This kind of structure of oxides suggests that it is more easily dispersed by intensive shearing.

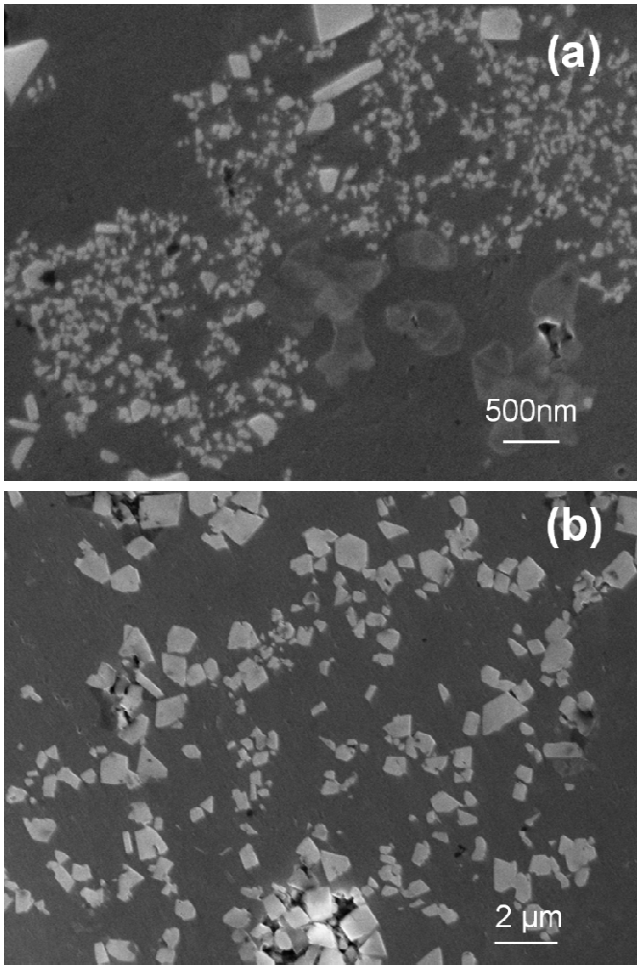

Figure 7.8 *SEM micrographs of oxides formed in CP Al melt at 920 ^{o}C, collected by the pressure filtration technique. (a) Smaller oxide particles; (b) Larger oxide particles, showing individual faceted oxide particle.*

7.2.5 Identification of oxides formed on CP Al melt surface

To identify the crystal structure of the oxides formed in the CP Al melt, X-ray diffraction (XRD) analysis was performed on the oxide samples collected from CP Al melt at 700 and 920^{o}C. **Figure 7.9a** shows the XRD pattern of the oxide sample collected from the CP Al melt at 700^{o}C (**Figure 7.7**). The peaks from γ-Al_2O_3 are evident but the peaks are not so sharp as indicated by the number "3" in **Figure 7.9a**, due to the fact that the particle size of γ-Al_2O_3 is very small. The peaks from α-Al are also evident including both from K_α and K_β due to the high volume fraction of the α-Al phase in the oxide sample. **Figure 7.9b** shows

the XRD pattern of the oxides collected from the CP Al melt at 920°C (**Figure 7.8**). The peaks from α-Al_2O_3 are apparent, as indicated by the number "3" in **Figure 7.9b**.

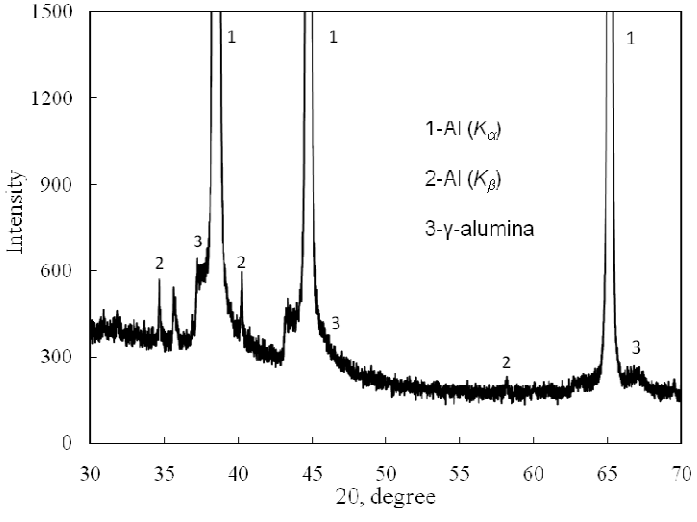

(a)

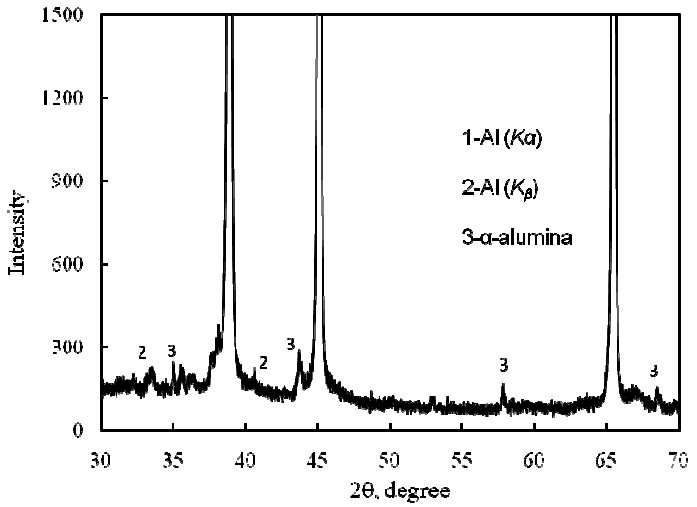

(b)

Figure 7.9 *XRD patterns of oxides formed in CP Al melt collected in skimmed samples at (a) 700°C and (b) 920°C.*

7.2.6 Dispersed oxide particles by intensive melt shearing

To correlate the oxides with the significantly refined grains by intensive shearing, the variation of oxides with intensive shearing was investigated. **Figure 7.10** shows the dispersed γ-Al_2O_3 oxides formed in the CP Al melt sheared at 700°C, which was

concentrated by the pressure filtration technique. With intensive shearing, they display dispersed platelet like particles, as shown in **Figure 7.10b**.

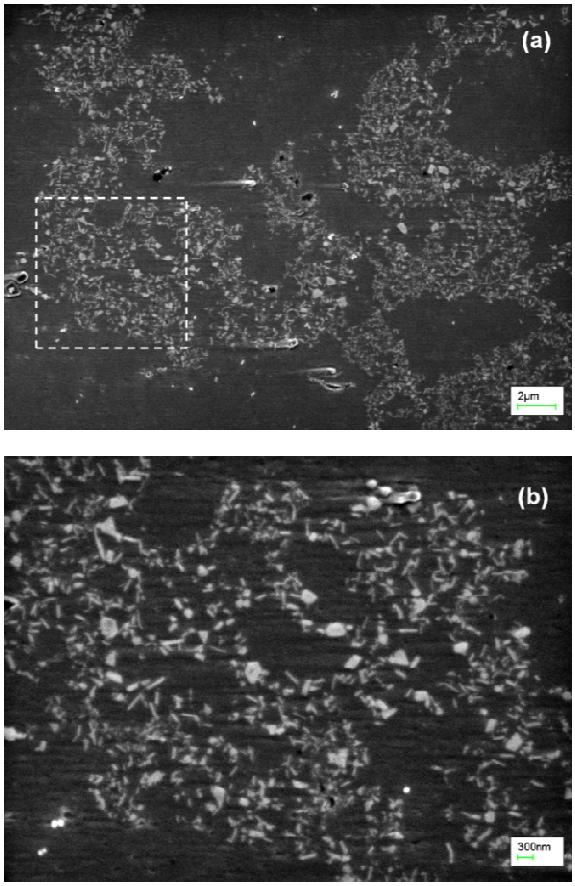

Figure 7.10 *SEM micrographs showing the dispersed platelet γ-Al_2O_3 in aluminium matrix in the CP Al sheared at 700°C and then pressure filtered. (a) Low magnification image of dispersed oxide particles; (b) Enlarged view of the squared area in (a) highlighting their platelet morphology.*

7.2.7 TEM and HRTEM characterisation of γ-Al_2O_3 formed in CP Al melt

To further understand the crystallographic characteristics of the oxides in α-Al matrix, TEM and HRTEM were carried out for the oxide formed in the CP Al melt sheared and pressure filtered at 700°C. The TEM image of dispersed γ-Al_2O_3 and its EDX spectrum are shown in **Figure 7.11**. The TEM image in **Figure 7.11a** gives the size of γ-Al_2O_3 platelet

to be about 50nm in thickness and 300~400nm in length. The TEM-EDX spectrum confirms it being a kind of Al_2O_3 (**Figure 7.11b**).

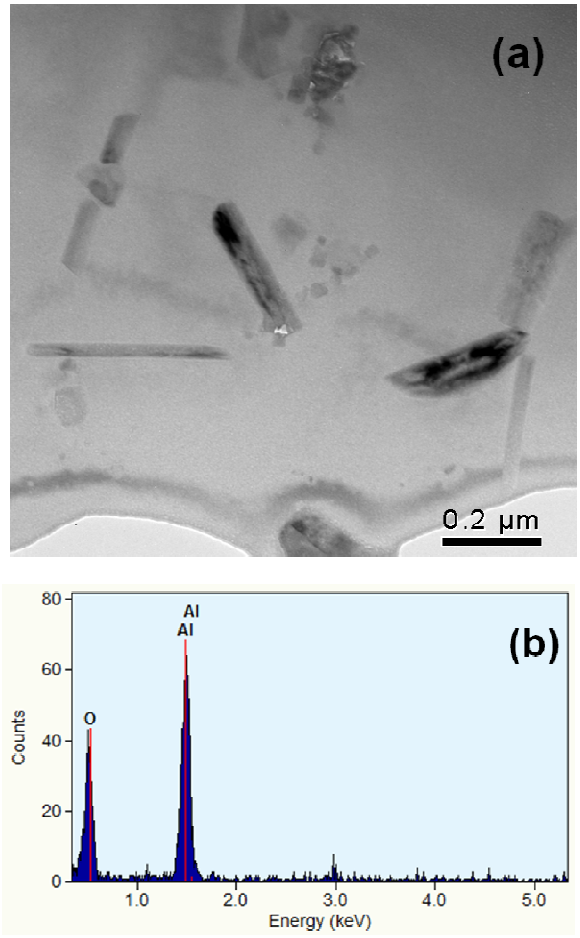

Figure 7.11 *(a) TEM micrograph of dispersed γ-Al_2O_3 platelets in CP Al melt sheared at 700°C and concentrated by pressure filtration; and (b) TEM-EDX spectrum of a γ-Al_2O_3 platelet.*

Figure 7.12 shows the TEM and HRTEM images of γ-Al_2O_3 particles in the sample of CP Al sheared at 700°C and then pressure filtered. The TEM image in **Figure 7.12a** shows features inside a γ-Al_2O_3 platelet. The selected area diffraction pattern (SAD) confirmed it to be γ-Al_2O_3, where the fundamental spots in the SAD pattern correspond to those for γ-Al_2O_3 in the [011] orientation (**Figure 7.12b**). The HRTEM image in **Figure 7.12c** reveals

the fine structure shown in **Figure 7.12a** is related to the twinning with a twinning plane {111}. This heavily twinned morphology is similar to that described in Yang et al's results on the investigation of γ-Al_2O_3, where γ-Al_2O_3 is formed by thermal oxidation on the surface of NiAl (Yang *et al.*, 1998). In their work, it was proposed that the platelet morphology of γ-Al_2O_3 is related to the twinning plane corresponding to (111) γ-Al_2O_3. The high number density of (111) γ-Al_2O_3 twins observed suggests that these twins play an important role in the oxide scale growth. A possible growth mechanism for the oxide platelets has been proposed where the (111) γ-Al_2O_3 twin boundaries provide a fast diffusion path for the Al cations (Yang *et al.*, 1998). In addition, **Figure 7.12c** reveals that the exposed surface of γ-Al_2O_3 platelets is the {111} crystallographic plane, in parallel to the twinning plane. This exposed {111} crystallographic plane of γ-Al_2O_3 platelets is crucial for the γ-Al_2O_3 platelet particles to be a heterogeneous nucleation site of α-Al phase during solidification.

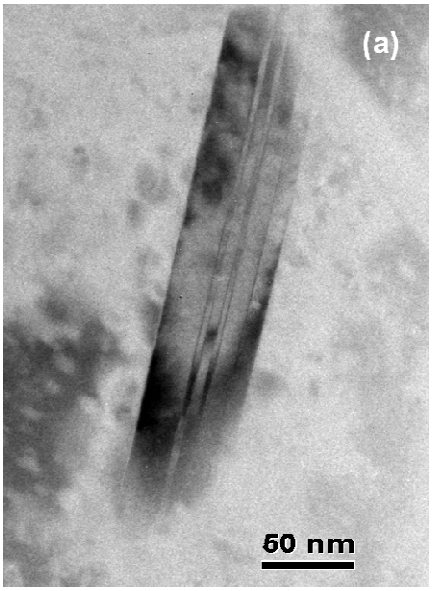

Figure 7.12 *(a) A typical TEM image showing a twinned structure inside a γ-Al_2O_3 platelet, formed in CP Al melt at 700°C; (b) SAD along [011] of γ-Al_2O_3; and (c) HRTEM image of a γ-Al_2O_3 platelet showing its exposed surface parallel to twinning plane (11-1)* ***(continued on the next page).***

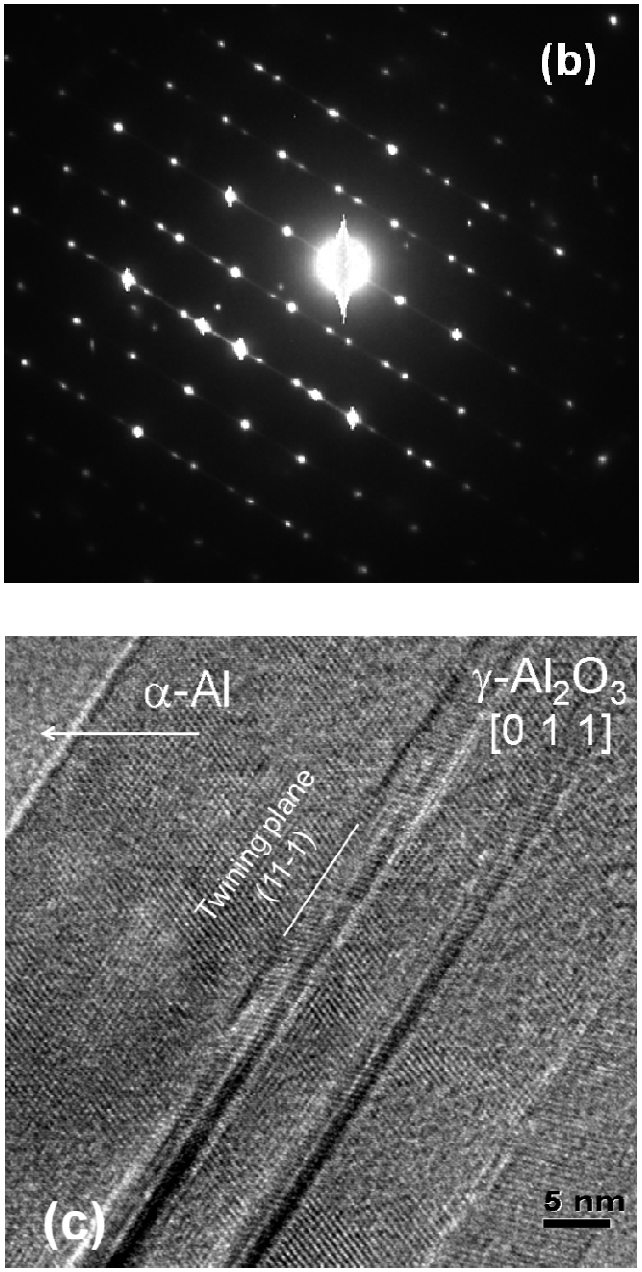

Figure 7.12 ***(continued)*** *(a) A typical TEM micrograph shows a twinned structure inside a γ-Al_2O_3 platelet, formed in CP Al at 700°C; (b) SAD along [011] of γ-Al_2O_3; and (c) HRTEM image of a γ-Al_2O_3 platelet showing its exposed surface parallel to twinning plane (11-1).*

7.3 Discussion

7.3.1 Analysis of the number density of active nucleation sites

Throughout the current work, the grain size is quoted as the mean linear intercept $\bar{l}$. In order to provide an insight into the underlying nucleation mechanisms with intensive

shearing, the number of grains per unit volume of sample N_V, grain density, has been calculated and analysed. The relationship between N_V and $\bar{l}$ is not straightforward and depends on the grain size distribution. An approximate relationship is derived, assuming an equiaxed grain structure with a grain size distribution typical of a metal, i.e., log-normal distribution. According to the derivation by Greer et al., grain density N_V can be related to mean linear intercept $\bar{l}$ by the following expression (Greer *et al.*, 2000):

$$N_V = \frac{0.5}{\bar{l}^3} \qquad (7.1)$$

Based on this relationship between N_V and $\bar{l}$, and the grain size data (**Figures 7.2** and **7.5**), grain densities as a function of superheating temperature are shown in **Figure 7.13.**

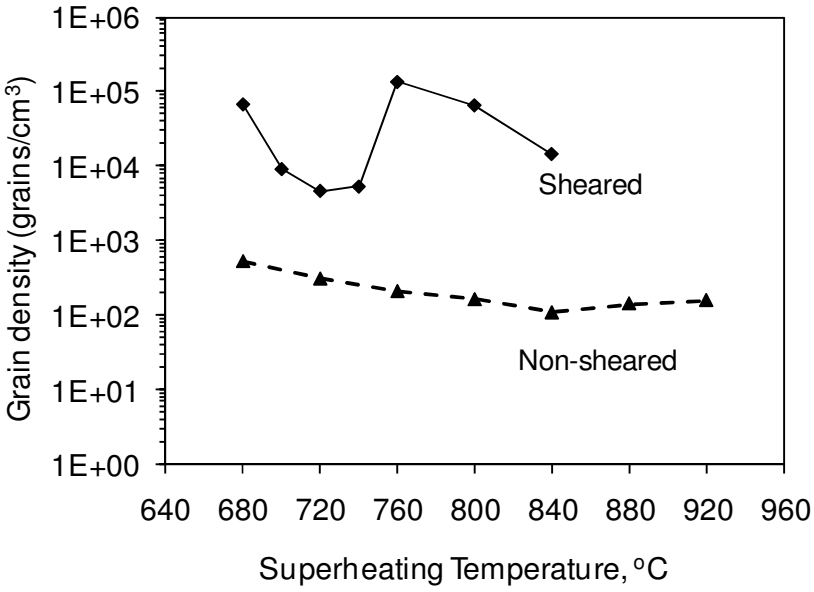

Figure 7.13 *The grain density against superheating temperature, with and without a shearing process calculated from the grain size data displayed in Figures. 7.2 and 7.5. The grain density is given in logarithmic scale.*

From **Figure 7.13**, it is evident that the grain densities of all sheared samples are at least a factor of 10 higher than their counterparts without shearing at identical superheat temperatures. This, in general, explains the grain refining effect of intensive shearing via an increased number density of nucleation sites (**Figures 7.3** and **7.4**). Now we come to see the individual plots of grain density evolution with melt superheating temperature. For the samples without shearing, it can be seen that the grain density decreased monotonically with an increase in the superheating temperature ranging from 680 to 840^{o}C, and then slightly increases in the range of temperature from 840 to 920^{o}C (dashed line in **Figure 7.13**). For the sheared samples, in the low superheating temperature regime (≤720^{o}C), the grain density decreased relatively rapidly with an increase of the shearing temperature; however, at a shearing temperature between 720 and 760^{o}C, namely, 740±20^{o}C, a turning point of grain density occurred, from which the grain density increased to 5343/ cm^{3} at 740^{o}C, to 136900/ cm^{3} at 760^{o}C, by a factor of 25 higher when compared to a value of 4665/cm^{3} of the sample sheared at 720^{o}C. As shearing temperature exceeded 760^{o}C, the grain density decreased relatively slowly with a further increase of the shearing temperature up to 840^{o}C, and the grain density still remained at a high level (solid line in **Figure 7.13**). For instance, the grain density at 840^{o}C is 14700/cm^{3}, which is still much higher than that of 4665/cm^{3} of the sample sheared at 720^{o}C. These much higher values of grain density account for the significant grain refining effect of intensive melt shearing revealed in **Figure 7.2** and **Figure 7.5**. This turning point of grain density occurred at a temperature 740±20^{o}C, suggesting that there might be a transition happening in the CP Al melt around this temperature. This transition should be heavily influenced by intensive melt shearing since there is not turning point occurring in the grain density (grain size) of the non-sheared sample around this temperature (**Figure 7.13**). In the case of non-sheared samples, a turning point is also noted at 840^{o}C (dashed line in **Figure 7.13**), although it is

not so significant as that in sheared samples. However, there should be no phases existing in the molten CP Al around this temperature except alumina, which is inevitably occurring.

7.3.2 Oxidation dynamics on the surface of liquid aluminium

Under normal melting conditions, the oxidation of pure aluminium in a usual melting superheating temperature, such as ~100 ^{o}C above its melting point, is a sluggish process because of the formation of a protective amorphous alumina film in close contact with liquid aluminium, where preferred diffusion paths such as grain boundaries are absent (Cao and Campbell, 2005).

The occurrence of breakaway oxidation, which means a catastrophic increase in oxidation rate, is critical to the oxidation dynamics as a whole in molten aluminium alloys. Impey et al. investigated the breakaway oxidation of commercial purity aluminum (Al-0.15Fe-0.08Si, wt.%) in dry air at 750^{o}C, where breakaway oxidation was observed after 5-20 h (Impey *et al.*, 1988). The time to breakaway appears to be a function of temperature, water vapour pressure, minor alloying additions and the presence of a disturbance on the surface of molten aluminium. Naturally, the occurrence of breakaway oxidation is related to the changes in the oxide structure and morphology. The transformation from γ- to α-Al_2O_3 is accompanied by a 24% decrease in the volume of the oxide and the tensile stresses which result fracture the oxide, resulting in a non-protective oxide. Localised failure of the protective oxide film can result in exudations forming on the melt surface. When this occurs, breakaway oxidation kinetics are observed (Impey *et al.*, 1988). A similar mechanism is also the reason why stirring the melt surface can accelerate the oxidation kinetics. With intensive melt shearing, the localised failure of the protective oxide film is expected to be more pronounced, as a consequence, accelerated oxidation take places, which occurs in the vicinity of the interface between the liquid aluminium and air. This will be discussed in detail in Section 7.3.4.

7.3.3 Identification of the transformation temperature from γ- to α-Al_2O_3

It is generally accepted that the transformation from a transition alumina to α-Al_2O_3 is a nucleation and growth process and the growth of α-Al_2O_3 appears to be very rapid. This means the formation of α-Al_2O_3 is a nucleation controlled process (Yang *et al.*, 1998; Chou and Nieh, 1991). It was reported that mechanical treatments of γ-alumina markedly increase the density of nuclei and hence the transformation rate from γ- to α-Al_2O_3. In a previous study, the detection of α-Al_2O_3 in molten CP Al at a temperature of 750^{o}C has been reported (Impey *et al.*, 1988). This result suggests that the equilibrium transformation temperature of γ- to α-Al_2O_3 could be around 750^{o}C. However, due to the sluggish nature of the γ- to α-Al_2O_3 transformation, the transformation of γ- to α- Al_2O_3 has long been debated in the scientific community.

By introduction of intensive melt shearing, the transformation from γ- to α-Al_2O_3 can be understood in terms of enhanced nucleation and accelerated diffusion via the twin screw mechanism and hence an accelerated transformation rate. It is expected that the existing γ-Al_2O_3 in liquid Al can be transformed to α-Al_2O_3 when the melt is subjected to intensive shearing at or above the equilibrium transition temperature from γ- to α-Al_2O_3. This can be understood from the following aspects. First, the transformation from amorphous to crystalline alumina takes place by nucleation and growth mainly at the melt/oxide interface (Impey *et al.*, 1988 and 1991; Wefers and Misra, 1987). During intensive shearing, many more portions of oxide film would be exposed to the interface between air and liquid aluminium due to the twin screw mechanism. Second, when subjected to intensive shearing, the liquid metal experiences cyclic stretching, folding and reorienting processes (Ji *et al.*, 2001). Due to the brittle nature of oxide films, the oxide films are easily cracked and broken into smaller segments, which has been observed and evidenced in the oxide sample in the CP Al melt sheared at 700^{o}C, as shown in **Figures 7.10b** and **7.11a**. Hence,

oxidation could be accelerated. More importantly, with intensive shearing, the diffusivity of species in liquid aluminium alloys can be accelerated markedly. This has been discussed in Chapter 5. As a consequence, the transformation from γ- to α-Al_2O_3 can be accelerated markedly. In other words, the transformation temperature from γ- to α-Al_2O_3 under intensive shearing is expected to shift towards the equilibrium transformation temperature. In the present study, based on an understanding of the higher potency of α-Al_2O_3 compared to γ-Al_2O_3, acting as heterogeneous nucleation sites of the α-Al phase, as will be discussed in the following section, the abrupt decreased grain size in sheared TP-1 samples when the shearing temperature was changed from 720 to 760°C (**Figure 7.5**), suggests the equilibrium transformation temperature from γ- to α-Al_2O_3 should be 740±20°C.

7.3.4 The potency of γ- and α-Al_2O_3 as nucleation sites of α-Al phase

As stated in Section 6.3.2 of Chapter 6, the interfacial free energy at the nucleating interface is the controlling factor in heterogeneous nucleation behaviour and influenced by several contributory factors (Bramfitt, 1970; Campbell, 2003). In order to understand the role of oxide particles in the enhanced heterogeneous nucleation, to a first approximation, the potency of γ- and α-Al_2O_3 formed in a CP Al melt is analysed as follows in terms of the lattice misfit at the interface between oxide particles and the α-Al phase.

Crystallographic match between oxide particles and α-Al phase

Jeurgens et al. investigated the orientation relationship between γ-Al_2O_3 and α-Al, where the γ-Al_2O_3 was formed by thermal oxidation on the surface of aluminium (Jeurgens *et al.*, 2002). The orientation relationship between the crystalline oxide γ-Al_2O_3 and the Al substrate is: (111) Al // (111) γ-Al_2O_3 and [110]Al // [110] γ-Al_2O_3. The calculated lattice misfit at 660°C is 3.38%.

The lattice misfit between α-Al_2O_3 and α-Al along the different directions on the closest crystal planes has been calculated and compared. The lowest misfit was obtained on the following orientation relationship: (0001) α-Al_2O_3 // (100) Al and [10-10]α-Al_2O_3 // [001]Al. This configuration matches the possible plane and direction of the α-Al with the close-packed plane and direction of the oxygen ion sublattice in the α-Al_2O_3. The calculated lowest lattice misfit at 660^{o}C is -0.48%. All the above results indicate the high potency of both γ- and α-Al_2O_3 as a nucleation site of the α-Al phase in terms of a crystallographic lattice match. However, α-Al_2O_3 should have higher potency than γ-Al_2O_3 as nucleation sites of α-Al due to the lower lattice misfit.

Availability of specific crystallographic plane of oxides as substrate for the α-Al phase nucleated

The availability of appropriate crystallographic planes is very important for an oxide particle to be an active nucleation site. In the present study, HRTEM observations have identified the exposed surface of γ-Al_2O_3 to be parallel to the twinning plane (11-1) (**Figure 7.12c**), indicating the availability of the closely packed plane of (111) of the γ-Al_2O_3 platelet in CP Al melt. The availability of the closely packed plane of (111) in γ-Al_2O_3 as exposed surface is closely related to the growth characteristics of γ-Al_2O_3.

7.3.5 Improved wetting between liquid aluminium and γ-/α-Al_2O_3 by intensive shearing

Numerous studies have shown that the contact angle of aluminium on alumina exceeded 90^o at temperatures below 950 to 1000^{o}C. This is due to the protective oxide film which forms on the molten aluminium (Weirauch and Krafick, 1990). In effect, this should also be influenced by the gaseous phase absorbed at the surface of oxides, as presented in a gas bridge model (**Figure 2.14)** (Ramani *et al.*,1991; Atamanenko *et al.*, 2010). Both the

protective oxide films on the surface of liquid Al and gaseous phases absorbed on the surface of oxides can act as a barrier to the formation of a true Al-oxide substrate interface and hence influence the achievement of a good wetting between liquid aluminium and γ-/α-Al_2O_3.

With intensive shearing, the wetting between oxides and liquid aluminium can be improved significantly. This can be ascribed to the dispersing of oxide films under intensive melt shearing and the related degassing effect (Zuo *et al.*, 2011), where the contributions to the decreased porosity content from decreased hydrogen content were identified and from dispersed oxides and hereby improved wetting ability were proposed. Here, the mechanisms underlying improved wetting behaviour between oxides and liquid Al by intensive melt shearing are analysed as follows. With intensive shearing, the liquid aluminum experiences cyclic stretching, folding and reorienting processes (**Figure 2.15**) (Ji *et al.*, 2001). The oxide films or clusters are dispersed into individual oxide particles, resulting in an increased contact area between oxides and liquid aluminium. Meanwhile, de-attachment of gaseous phases from oxide particles is expected to happen by a mechanism, which is similar to the cavitation effect happening in an ultrasonic melt treatment. Subsequently, due to the buoyant forces, gas bubbles float to the surface of liquid aluminium. As a result, good wetting between the dispersed oxide particles and liquid Al can be achieved. The γ-Al_2O_3 particles well embedded in α-Al matrix are an indication of the achievement of good wetting between γ-Al_2O_3 particles and α-Al matrix after intensive melt shearing (**Figure 7.10b**).

7.3.6 Improved efficiency of oxide particles as active nucleation sites of α-Al by intensive shearing

Given the equilibrium transition temperature from γ- to α-Al_2O_3 is 740±20^{o}C, the number of α-Al_2O_3 particles increases with an increase of the superheating temperature. Due to the

feature of α-Al_2O_3 which is loosely agglomerated by capillary pressure, as indicated in **Figure 7.8**, it is likely to be a nucleation site for α-Al upon the onset of solidification. As a result, the grain refinement induced by an increased nucleation rate on α-Al_2O_3 can compensate the grain coarsening by an increased superheating in the melt. This is why the grain size slightly decreased when the superheating temperature exceeded 840^{o}C in the cases without shearing, as shown in **Figures. 7.1** and **7.2**. On the other hand, without shearing, although the number of α-Al_2O_3 particles increases with an increase of the superheating temperature, only a very limited number of α-Al_2O_3 particles, which are in good contact and well wetted with liquid aluminium, can act as heterogeneous nucleation sites of α-Al during solidification. This explains why there is not huge difference in grain size for the samples experiencing different thermal histories as shown in **Figure 7.2**.

Based on the free growth model developed by Greer and co-workers, to be an effective heterogeneous nucleation site, potent nucleation agents should have sufficient number density and appropriate size distribution (Greer *et al.*, 2000; Quested and Greer, 2004; Fan *et al.*, 2009). With intensive melt shearing, for the samples sheared at a temperature below 740±20^{o}C, the oxide particles were γ-Al_2O_3 platelets; for the samples sheared at a temperature above 740±20^{o}C, the resultant oxides were α-Al_2O_3 particles. As a result, dispersed oxide particles with a sufficient number density throughout the entire aluminium melt can be achieved. These dispersed oxide particles, either γ-Al_2O_3 or α-Al_2O_3, can act as active nucleation sites of α-Al. In the current study, the grain refinement by intensive shearing within a wide range of superheat temperature is due to the improved heterogeneous nucleation efficiency (**Figure 7.5**).

7.3.7 Comparisons of the potency between γ- and α-Al_2O_3 particles as active nucleation sites of the α-Al phase

With intensive melt shearing, sufficient number density of oxide particles was available, whether the oxide particles are γ- or α-Al_2O_3. This is why the grain refinement can be achieved by intensive melt shearing, as shown in **Figures 7.3** and **7.4**. However, when the melt was sheared at 740^{o}C or above, the more significant grain refinement achieved cannot be explained in terms of the difference in the quantity of nucleant particles available. With shearing at 740±20^{o}C or above, the oxides formed in CP Al melt are α-Al_2O_3. Due to the lower lattice misfit between α-Al_2O_3 and α-Al, α-Al_2O_3 has higher potency than γ-Al_2O_3 as nucleation sites of α-Al. This means that nucleation can be triggered at a lower undercooling for α-Al_2O_3 to nucleate α-Al compared to γ-Al_2O_3. As a consequence, more active nucleation sites are available with identical thermal undercooling imposed by the particular solidification conditions and in turn, the finer the resultant grain size. This is why the much higher grain density and correspondingly, the more significant grain refinement can be achieved in the sheared samples when the shearing temperature exceeded 740±20^{o}C, where the transformation from γ- to α-Al_2O_3 occurred as discussed above. Under this circumstance, the difference in thermal undercooling, due to the increased melt superheat with an increase in the shearing temperature, had marginal effect on the resultant grain size, as evidenced in the sheared samples shown in **Figures 7.3** through **7.5**.

7.3.8 Columnar to equiaxed transition

Due to the enhanced heterogeneous nucleation by intensive melt shearing, a columnar to equiaxed transition can be achieved, as shown in **Figure 7.6**. It can be seen clearly that without melt shearing, the solidification started from the bottom of the TP-1 mould, as shown in **Figures 7.6a** and **7.6c**. With intensive shearing, the chilled grains zone in the TP-

1 samples were significantly reduced and replaced by finer equiaxed grains throughout the entire volume of the TP-1 samples, as shown in **Figures 7.6b** and **7.6d**. The enhanced heterogeneous nucleation is ascribed to the significantly increased number density of individual particles of γ- (**Figure 7.6b**) or α-Al_2O_3 (**Figure 7.6d**). In the case of the TP-1 sample sheared at 760°C (**Figure 7.6d**), where the dominant oxide is α-Al_2O_3 as discussed above, which has a higher potency than γ-Al_2O_3 as the nucleation site of α-Al, as a result, the grain size is much finer in **Figure 7.6d** than that in **Figure 7.6b**.

7.3.9 Mechanism of enhanced heterogeneous nucleation on oxides in Al alloys

Now we come to summarise the enhanced heterogeneous nucleation by intensive melt shearing in Al alloys. For different alloy systems, due to the different types of oxides formed and their different microstructural characteristics including crystallographic lattice match with the nucleated phases, surface crystallographic characteristics including the availability of the particular crystallographic plane, and chemical features such as the polarization related gaseous phase absorption, the availability and potency of the specific oxides as a nucleation site of the nucleated phase is different. In the present study, $MgAl_2O_4$ relative to MgO, and α-Al_2O_3 relative to γ-Al_2O_3, have higher potency as a heterogeneous nucleation site of α-Al phase in Al alloys. The mechanisms of enhanced heterogeneous nucleation on oxides in Al alloys by intensive shearing are proposed in a flow chart presented in **Figure 7.14**.

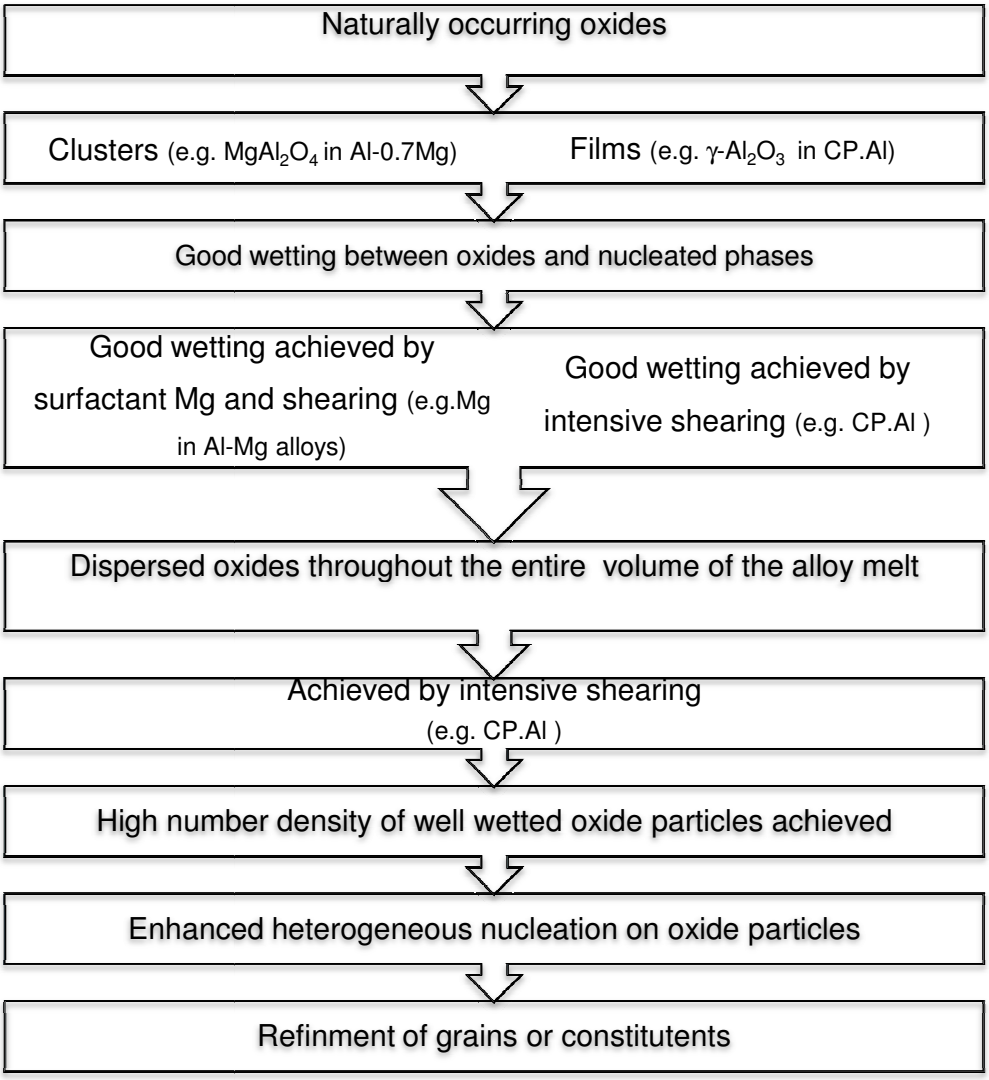

Figure 7.14 *The mechanism of enhanced heterogeneous nucleation on oxides in Al alloys by shearing.*

7.4 Conclusions of Chapter 7

(1) In CP Al, γ- and α-Al_2O_3 are two major oxide forms present at a lower temperature (<840^{o}C) or a higher temperature (>840^{o}C) under normal melting conditions.

(2) The equilibrium transformation temperature from γ- to α-Al_2O_3 has been identified as 740±20^{o}C in the current study.

(3) Significant grain refinement can be achieved in CP Al by intensive melt shearing. This can be attributed to an enhanced heterogeneous nucleation on dispersed oxide particles via an increased number density of oxide particles.

(4) α-Al_2O_3 has higher potency as a nucleation site for the α-Al phase relative to γ-Al_2O_3 during the solidification of CP Al. The difference between γ- and α-Al_2O_3 in terms of the potency as nucleation sites of α-Al phase can be related to their different crystallographic match with α-Al phase.

Chapter 8

Conclusions

1. Oxides formed in liquid Al alloys can be γ-Al_2O_3, α-Al_2O_3, $MgAl_2O_4$, MgO or $ZnAl_2O_4$, etc, depending on the alloy compositions and the melting conditions.
2. Oxides formed in liquid Al alloys are in the form of films or clusters consisting of oxide particles. These oxide particles are held together by capillary pressure with liquid Al matrix, which is governed by Laplace-Young equation.
3. Intensive melt shearing disperse oxide films or clusters into dispersed oxide particles throughout the entire volume of liquid Al alloys.
4. Intensive melt shearing enhances the heterogeneous nucleation on dispersed oxide particles and therefore refine the grains of α-Al phase. In the current study, grain refining effect of intensive shearing has been demonstrated in CP Al, Al-Mg binary alloys and a model wrought Al alloy.
5. The equilibrium transformation temperature from γ- to α-Al_2O_3 has been identified as $740\pm20^{o}C$ in the current study, which was indicated by the sharply decreased grain size of CP Al at this temperature with an increase in the melt shearing temperature.
6. α-Al_2O_3 has higher potency as nucleation sites of α-Al phase compared to γ-Al_2O_3 during the solidification of CP Al. This is due to a smaller lattice misfit between α-Al_2O_3 and α-Al phase than that between γ-Al_2O_3 and α-Al phase.

7. $MgAl_2O_4$ has higher potency than MgO as nucleation sites of α-Al phase in aluminium alloys due to a smaller lattice misfit between $MgAl_2O_4$ and α-Al phase than that between MgO and α-Al phase.
8. Intensive melt shearing enhances heterogeneous nucleation by increasing the number density of oxide particles as active nucleation sites of α-Al.
9. Intensive melt shearing promotes the formation of α-AlFe(Mn)Si phase by providing near equilibrium kinetic condition and enhances the nucleation of α-AlFe(Mn)Si phase on dispersed $MgAl_2O_4$ particles in LM24.
10. $MgAl_2O_4$ is thermodynamically more stable than MgO in Al-Mg alloys. This is why intensive shearing can promote the formation of $MgAl_2O_4$ rather than MgO in Al-Mg alloys with high levels of magnesium.

Chapter 9

Suggestions for further work

In this thesis, the effect of enhanced heterogeneous nucleation on oxides naturally occurring in liquid Al alloys by intensive melt shearing using the MCAST has been experimentally demonstrated in a series of Al alloys, including three commercial Al alloys and one model Al-Mg binary alloy. The acquired experimental results indicate some key points to obtain grain refining effect by harnessing the in-situ formed oxides in liquid Al alloys, such as good crystallographic match between oxides and nucleated phases, spatially uniform distribution throughout the entire volume of alloy melts, appropriate size distribution, and so on. However, more and in-depth understanding of the underlying mechanism is needed before the widespread use of this technology.

1. High resolution TEM analysis of the interface between oxides, either γ-Al_2O_3 or α-Al_2O_3, and Al matrix

Due to the very small size of γ-Al_2O_3 in sheared samples, the crystallographic orientation relationship between oxides and Al matrix cannot be identified using conventional transmission electron microscopy. In this regard, further high resolution TEM (HRTEM) investigation should be performed.

2. The possibility to achieve grain refining effect by other high shear techniques

Based on our results in this thesis, oxides in Al alloys exhibit films or clusters, where nano- or submicron sized oxides particles are held together by capillary pressure. For different oxides in Al alloys, due to their different crystallographic structures and surface features, the magnitude of capillary pressure may be different. For instance, for $MgAl_2O_4$ or α-Al_2O_3 containing Al alloys, where oxides are mainly in the form of clusters of particles, therefore, grain-refining effect may be achieved by other high-shear technique. This investigation will broaden the application of high shear technology.

3. Investigation of the feasibility of externally added oxides particles as grain refiners of Al alloys

It has been identified that both γ-Al_2O_3 and α-Al_2O_3 naturally formed in Al alloy melts are highly potent nucleation agents for α-Al. However, the efficiency of grain refining effect is heavily dependent on the particle sizes and wetting behaviour between oxides and liquid aluminium. In this regard, comparative investigation of the addition of externally added oxide particles on the grain refinement in combination with different shearing techniques should be carried out, where the effect of oxide particle size and wetting behaviour could be isolated.

4. Trace alloying elements addition on the grain refinement of α-Al on oxide particles

In our study, evidence has been obtained indicating the segregation behaviour to the interface between oxides and Al matrix. It is therefore expected that the crystallographic match or wetting behaviour between oxides and α-Al/liquid Al can be modified and hence influence the resulting grain refining effect.

5. Investigation of the modification of Fe-containing intermetallics by intensive melt shearing combined with low cooling rate casting process

In this study, the selection of primary α-AlFeSi intermetallic phase promoted by intensive shearing has been identified in a typical die casting Al alloy. However, due to the shear force at the gate imposed by a high pressure die caster itself, the effect by intensive shearing cannot be isolated in MC-HPDC. If combined with low cooling rate casting process, especially where there is no shear force during casting process such as sand casting, the advantage of intensive shearing on the modification of Fe-containing intermetallics would be more significant.

6. More understanding of the near equilibrium kinetic condition established by intensive melt shearing

In the current study, some experimental evidences have indicated that near equilibrium kinetic condition can be established by intensive melt shearing, including the formation of equilibrium α-AlFe(Mn)Si intermetallics and the identification of the transformation temperature from γ- to α-Al_2O_3 under intensive shearing. In future, some more experiments should be carried out using other alloy systems.

References

A

Agema, K. S., and Fray, D. J. (1989) Preliminary investigations on the deformation behaviour of an oxide scale on molten aluminium. Department of Material Science and Metallurgy, University of Cambridge.

Anson, J. P., Drew, R. A., and Gruzleski, J. E. (1999) The surface tension of molten Aluminium and Al-Si-Mg Alloy under vacuum and hydrogen atmospheres. *Metall. Mater. Trans. B*, 30, 1027-1032.

Arnberg, L., Backerud, L., and Klang, H. (1982) Grain refinement of aluminium - 2. intermetallic particles in Al-Ti-B type master alloys for grain refinement of aluminium. *Met.Technol.*, 7-13.

Ashtari, P., Tezuka, H., and Sato, T. (2005) Modification of Fe-containing intermetallic compounds by K addition to Fe-rich AA319 aluminium alloys. *Scripta Mater.*, 53,937-942.

Atamanenko, T. V., Eskin, D. G., Zhang, L., and Katgerman, L. (2010) Criteria of grain refinement induced by ultrasonic melt treatment of aluminium alloys containing Zr and Ti. Metall. *Mater. Trans. A*, 41A, 2056-2066.

Awano, Y., and Shimizu, Y. (1990) Non-equilibrium crystallization of AlFeSi compound in melt-superheated Al-Si alloy casting. *AFS Trans*, 98, 889-895.

B

Backerud, L. (1971) *Jernkot. Ann*, 155, 422-424.

Backerud, L., Chai, G., and Tamminen, J. (1990) *Solidification Characteristics of Aluminium Alloys*, Vol.2, Foundry Alloys. Skanaluminium, Des Plaines: AFS.

Bagwell, R. B., and Messing, G. L. (1999) Effect of seeding and water vapour on the nucleation and growth of alpha-alumina from gamma-alumina. *J. Am. Ceram. Soc.*, 82, 825-832.

Balitchev, E., Jantzen, T., Hurtado, I., and Neuschutz, D. (2003) Thermodynamic assessment of the quaternary system Al-Fe-Mn-Si in the Al-rich corner. *CALPHAD*, 27, 275-278.

Banerji, A., and Reif, W. (1985) Grain refinement of aluminium by TiC. *Metall. Trans. A*, 16A, 2065-2068.

Banerji, A., and Reif, W. (1986) Development of AI-Ti-C grain refiners containing TiC. *Metall. Trans. A*, 17A, 2127-2136.

Bergsmark, E., Simensen, C. J., and Kofstad, P. (1989) The oxidation of molten aluminum. *Mater. Sci. Eng. A*, A120, 91-95.

Black, P. J. (1955) XLIX. Brillouin Zones of some intermetallic compounds. *Philos. Mag*., 46, 401-409.

Bramfitt, B. L. (1970) The effect of carbide and nitride additions on the heterogeneous nucleation behaviour of liquid iron. *Metall. Trans.*, 1, 1987-1995.

C

Cabrera, N., and Mott, N. (1948) Theory of the oxidation of metals. *Rep. Prog. Phys.*, 12, 163-184.

Campbell, J. (1981) Effects of vibration during solidification. *Inter. Mater. Rev.*, 26, 71-108.

Campbell, J. (2003) The new metallurgy of cast metals: Castings. Oxford: Butterworth Heinemann.

Cao, X. (2005) Pressure filtration tests of liquid Al-Si cast alloys, I. Flow behaviour. *Mater. Sci. Eng. A*, A403, 101-111.

Cao, X., and Campbel, J. (2006) Morphology of beta-Al_5FeSi phase in Al-Si cast alloys. *Mater. Trans.*, 47, 1301-1312.

Cao, X., and Campbell, J. (2003) Effect of melt superheating on convection-free precipitation and sedimentation of primary alpha-Fe phase in liquid Al-11.5Si-0.4Mg alloy. *International journal of cast metals research*, 15, 595-608.

Cao, X., and Campbell, J. (2000) Effect of precipitation of primary intermetallic compounds on the mechanical properties of cast Al 11.5Si 0.4Mg alloy. *AFS Trans.*, 108, 391–399.

Cao, X., and Campbell, J. (2003) The nucleation of Fe-rich phases on oxide films in Al-11.5Si-0.4Mg cast alloys. *Metall. Mater. Trans. A*, 34A, 1409-1420.

Cao, X., and Campbell, J. (2004a) Effect of Sr on primary α-Fe phase in liquid Al-11.5Si-0.4Mg cast alloy. *Mater. Sci. Tech.*, 20,514-520.

Cao, X., & Campbell, J. (2004b) The solidification characteristics of Fe-rich intermetallics in Al-11.5Si-0.4Mg cast alloys. *Metall. Mater. Trans. A*, 35A, 1425-1435.

Cao, X., and Campbell, J. (2005) Oxide inclusion defects in Al-Si-Mg cast alloys. *Canadian Metallurgical Quarterly*, 44, 435-448.

Chaijaruwanich, A., Lee, P. D., Dashwood, R. J., Youssef, Y. M., and Nagaumi, H. (2007) Evolution of pore morphology and distribution during the homogenization of direct chill cast Al-Mg alloys. *Acta Mater.*, 55,285-293.

Chen, P. C., Shih, T. S., and Chen, J. S. (2010) Thermally formed oxide films on Al–6Zn–XMg (X = 0 and 2 mass%) alloys heated in different gases . *J. Therm. Anal. Calorim.*, 99, 229-235.

Chou, T. C., and Nieh, T. G. (1991) Nucleation and concurrent anomalous growth of alpha-aAl2O3 during gamma to alpha phase transformation. *J. Am. Ceram. Soc.*, 74, 2270-2279.

Cibula, A. (1949-1950) The mechanism of grain refinement of sand casting in aluminium alloys. *J. Inst. Met.*, 76,321-360.

Cochran, C. N., Belitskus, D. L., and Kinosz, D. L. (1977) Oxidation of aluminium-magnesium melts in air, oxygen, flux gas, and carbon dioxide. *Metall. Trans. B*, 8B, 323-332.

Contreras, A., Bedolla, E., & Perez, R. (2004) Interfacial phenomena in wettability of TiC by Al-Mg alloys. *Acta Mater.*, 52, 985-994.

Cooper, M. (1967) The crystal structure of the ternary alloy α(AIFeSi). Acta Cryst., 23,1106-1107.

Cornish, A. (1975) The influence of boron on the mechanism of grain refinement in dilute aluminium -titanium alloys. *Metal Sci.*, 9, 477-484.

D

Das, A., and Fan, Z. (2004) A Monte Carlo simulation of solidification structure formation under melt shearing. *Mater. Sci. Eng. A*, A365, 330-335.

Das, A., Ji, S., and Fan, Z. (2002) Morphological development of solidification structures under forced fluid flow: a Monte-Carlo simulation. *Acta Mater.*, 50, 4571-4585.

Dash, M., and Makhlouf, M. (2001) Effect of key alloying elements on the feeding characteristics of aluminum–silicon casting alloys. *J. Light Metals*, 1, 251-265.

Davies, I. G., Dennis, J. M., and Hellawell, A. (1970) The nucleation of aluminium grains in alloys of aluminum with titanium and boron. *Metall. Trans.*, 1, 275-280.

Davis, J. R. (1993) Molten aluminium processing and casting. In *ASM speciality handbook* (pp. 199-230).

Day, A. P., and Quested, T. E. (1999) A comparison of grain imaging and measurement using horizontal orientation and colour orientation contrast imaging, electron backscatter pattern and optical methods. *J. Microscopy*, 195,186-196.

Delannay, F., Froyen, L., and Deruyttere, A. (1987) The wetting of solids by molten metals and its relation to the preparation of metal-matrix composites. *J. Mater. Sci.*, 22, 1-16.

Dinnis, C. M., Taylor, J. A., and Dahle, A. K. (2005) As-cast morphology of iron-intermetallics in Al-Si foundry alloys. *Scripta Mater.*, 53, 955-958.

Dynys, F. W., and Halloran, J. W. (1982) Alpha alumina formation in alum-derived gamma alumina. *J. Am. Ceram. Soc.*, 65, 442-448.

E

Easton, M., and StJohn, D. (2001) A model of grain refinement incorporating alloy constitution and potency of heterogeneous nucleant particles. *Acta mater.*, 49, 1867-1878.

Easton, M., and StJohn, D. (2005) An analysis of the relationship between grain size, solute content, and the potency and number density of nucleant particles. *Metall. Mater. Trans. A*, 36, 1911-1920.

Easton, M., and StJohn, D. (1999a) Grain refinement of aluminium alloys: Part I. The nucleant and solute paradigms-A review of the literature. *Metall. Mater. Trans. A*, 1613-1623.

Easton, M., and StJohn, D. (1999b) Grain refinement of aluminium alloys: Part II. Confirmation of, and mechnism for, the solute paradigm. *Metall. Mater. Trans. A*, 30A, 1625-1633.

Easton, M., and StJohn, D. (2008) Improved prediction of the grain size of aluminium alloys that includes the effect of cooling rate. *Mater. Sci. Eng. A*, 486, 8-13.

Eivani, A. R., Ahmed, H., Zhou, J., and Duszczyk, J. (2009) Evolution of grain boundary phases during the homogenization of AA7020 aluminium alloy. *Metall. Mater. Trans. A*, 40A, 717-728.

Enright, P. G., Hughes, I. R., Pickering, J., Simard, A., and Proulx, J. (2003) Characterisation of molten metal quality using the pressure filtration. Retrieved 01 25, 2011, from www05.abb.com: http://www05.abb.com/global/scot/scot205.nsf/veritydisplay/d6d22d7550b631dd8525761800538bc0/$File/Characterisation%20of%20Molten%20Quality.pdf

Eskin, D. G. (2008) *Physical Metallurgy of Direct Chill Casting of Aluminium Alloys*. Boca Raton, London, New York: CRC Press, Taylor & Francis Group.

F

Fan, Z. (2010) An epitaxial model for heterogeneous nucleation on potent substrates. *Acta mater.* , submitted.

Fan, Z., and Liu, G. (2005a) Solidification behaviour of AZ91D alloy under intensive forced convection in the RDC process. *Acta Mater.*, 53, 4345-4357.

Fan, Z., and Liu, G. (2005b) Solidification behaviour under intensive forced convection. *Mater. Sci. Eng. A*, 413-414, 229-235.

Fan, Z., Wang, Y., Xia, M., & Arumuganathar, S. (2009) Enhanced heterogeneous nucleation in AZ91D alloy by intensive melt shearing. *Acta Mater.*, 57, 4891-4901.

Fang, X., Shao, G., Liu, Y. Q., and Fan, Z. (2007) Effects of intensive forced melt convection on the mechanical properties of Fe containing Al–Si based alloys. *Mater. Sci. Eng. A*, 445-446, 65-72.

Flemings, M. C. (1991) Behaviour of metal alloys in the semi-solid state . *Metall. Trans. A*, 22A, 957-981.

Flemings, M. C. (1974) *Solidification processing*. New York: McGraw-Hill.

Fortier, M., Parson, N. C., and Chen, X. G. (2008) Solidification processing of high strength wrought: Formation of primary $ZrAl_3$ intermetallic particles in AA7046A alloy. *Aluminium Alloys, Their Physical and Mechanical Properties*, ICAA 11 (pp. 348-354). KGaA: Wiley-VCH GmbH & Co.

G

Gandin, C. A., and Rappaz, M. (1994) A coupled finite element-cellular automaton model for the prediction of dendritic grain structures in solidification process. *Acta Metall. Mater.*, 42, 2233-2246.

Gao, N., Wang, S. C., Ubhi, H. S., and Starink, M. J. (2005) A comparison of grain size determination by light microscopy and EBSD analysis. *J. Mater. Sci.*, 40, 4971-4974.

Gaskell, D. R. (1996) Metallurgical Thermodynamics. In Cahn, R. W., and Haasen, P. *Physical Metallurgy* (p. 431). Elsevier Science BV.

Gaumann, M., Trivedi, R., and Kurz, W. (1997) Nucleation ahead of the advancing interface in directional solidification. *Mater. Sci. Eng. A*, 226-228A, 763-769.

Glaisher, W. H. (1951) Metallurgia, 43, 127-131.

Glicksman, M. E., and Childs, W. J. (1962) Nucleation catalysis in supercooled liquid tin. *Acta Metall.*, 10, 925-933.

Green, N. R., and Campbell, J. (1993) Statistical distributions of fracture strengths of cast Al-7Si-Mg alloy. *Mater. Sci. Eng. A*, A137, 261-266.

Green, N. R., and Campbell, J. (1994) The influence of oxide film filling defects on the strength of Al-Si7-Mg. *AFS Trans*, 102, 341-347.

Greer, A. L. (2003) Chapter 13, Control of grain size in solidification. In B. Cantor, and K. O'Reilly, *Solidification and casting* (p. 214). Bristol and Philadelphia: Institute of physics publishing.

Greer, A. L., and Quested, T. E. (2006) Heterogeneous grain initiation in solidification. *Philosophical Magazine*, 86, 3665-3680.

Greer, A. L., Bunn, A. M., Tronche, A., Evans, P. V., and Bristow, D. J. (2000) Modelling of inoculation of metallic melts application to grain refinement of aluminium by Al-Ti-B. *Acta Mater.*, 48, 2823-2835.

Griffiths, W. D. (1997) The effect of electromagnetic stirring on macrostructure and macrosegregation in the aluminium alloy 7150. *Mater. Sci. Eng. A*, 222, 140-148.

Gunther, R., Hartig, C., & Bormann, R. (2006) Grain refinement of AZ31 by $(SiC)_P$: Theoretical calculation and experiment. *Acta Mater.*, 54, 5591-5597.

Gustafsson, G., Thorvaldsson, T., & Dunlop, G. L. (1986) The influence of Fe and Cr on the microstructure of cast Al-Si-Mg alloys. *Metall. Trans. A*, 17A, 45-52.

H

Ha, W., and Kim, Y. J. (2006) Effects of cover gases on melt protection of Mg alloys. *Journal of Alloys and Compounds*, 422, 208-213.

Haginoya, I., and Fukusako, T. (1983) Oxidation of Molten Al-Mg alloys. *Trans. Japan Ins. Metals*, 24, 613-619.

Hammond, C. (2009) *The basics of crystallography and diffraction*. New York: Oxford University Press.

Hitchcock, M., Wang, Y., and Fan, Z. (2007) Secondary solidification behaviour of the Al-Si-Mg alloy prepared by the rheo-diecasting process. *Acta Mater.*, 55,1589-1598.

Humenik, J. M., and Kingery, W. D. (1954) Metal-Ceramic Interactions: III. Surface tension and wettability of metal-ceramic systems. *J. Am. Ceram. Soc.*, 37, 18-23.

Humphreys, F. J. (1999) Quantitative metallurgraphy by electron backscattered diffraction. *Journal of Microscopy*, 195, 170-185.

Hunt, J. D. (1984) Steady state columnar and equiaxed growth of dendrites and eutectic. *Mater. Sci. Eng.*, 65, 75-83.

I

Impey, S. A., Stephenson, D. J., and Nicholls, J. R. (1991) A study of the effect of magnesium additions on the oxide growth morphologies on liquid aluminium alloys. *Proceedings of the first international conference on the microscopy of oxidation*. University of Cambridge.

Impey, S. A., Stephenson, D. J., and Nicholls, J. R. (1988) Mechanism of scale growth on liquid aluminium. *Mater. Sci. Tech.*, 4, 1126-1132.

Iwahori, H., Takamiya, H., Yonekura, K., Yamamoto, Y., & Nakamura, M. (1988) Influence of iron and manganese on feedability of AC2B alloy (in Japanese). *Casting*, 60, 590-595.

J

Jackson, K. A., Beatty, K. M., and Gudgel, K. A. (2004) An analytical model for non-equilibrium segregation during crystallization. *J. Crys. Grow.*, 271, 481-494.

JCPDS. (2005) Card No. 01-071-4015. International centre for diffraction data.

Jeurgens, L. P., Sloof, W. G., Tichelaar, F. D., and Mittemeijer, E. J. (2002) Structure and morphology of aluminium-oxide films formed by thermal oxidation of aluminium. *Thin Solid Films*, 418, 89-101.

Ji, S., and Fan, Z. (2002) Solidification behaviour of Sn-15 Wt Pct Pb alloy under a high shear rate and high intensity of turbulence during semisolid processing. *Metall. Mater. Trans. A*, 33A, 3511-3520.

Ji, S., Fan, Z., and Bevis, M. J. (2001) Semi-solid processing of engineering alloys by a twin screw rheomoulding process. *Mater. Sci. Eng. A*, A299, 210-217.

Johnsson, M., and Bäckerud, L. (1996) The influence of composition on equiaxed crystal growth mechanisms and grain size in Al alloys. *Zeitschrift fuer Metallkunde*, 87, 216-220.

Jones, G. P. (1985) *International seminar on refining and alloying of liquid Al and ferro-alloys* (pp. 213-228). Trondheim, Norway: Dusseldorf: Aluminium-Verlag.

Jones, G. P. (1988) Grain refinement of castings using inoculants for nucleation above liquidus. *Solidification Processing 1987* (pp. 496-497). London: The Institute of Metals.

Jones, G. P., and Pearson, J. (1976) Factors affecting the grain-refinement of aluminium using titanium and boron additives. *Metall. Trans. B*, 223-234.

K

Kearns, M. A., and Cooper, P. S. (1997) Effects of solutes on grain refinement of selected wrought aluminium alloys. *Mater. Sci. Tech.*, 13,650-654.

Khalifa, W., Samuel, F. H., Gruzleski, J. E., Doty, H. W., and Valtierra, S. (2005) Nucleation of Fe-intermetallic phases in the Al-Si-Fe alloys. *Metall. Mater. Trans. A*, 36A, 1017-1032.

Khalifa, W., Samuel, F., and Gruzleski. (2004) Nucleation of solid aluminium on inclusion particles injected into Al-Si-Fe alloys. *Metall. Mater. Trans.*, 35A, 3233-3250.

Korol'kov, A. M. (1960) In *Casting Properties of Metals and Alloys* (p. 37). New York: Consultants Bureau.

Kotadia, H. R., Babu, N. H., Zhang, H., and Fan, Z. (2010) Microstructural refinement of Al–10.2%Si alloy by intensive shearing. *Mater. Lett.*, 64, 671-673.

Kral, M. V., McIntyre, H. R., and Smillie, M. J. (2004) Identification of intermetallic phases in a eutectic Al–Si casting alloy using electron backscatter diffraction pattern analysis. *Scripta Mater.*, 51, 215-219.

Kral, M., Nakashima, P. N., and Mitchell, D. R. (2006) Electron microscope studies of Al-Fe-Si intermetallics in an Al-11 pct Si alloy. *Metall. Mater. Trans. A*, 37A, 1987-1997.

Kumagai, M., Messing, G. L. (1985) Controlled transformation and sintering of a boehmite Sol-Gel by alpha alumina seeding. *J. Am. Ceram. Soc.*, 68, 500-505.

L

Levin, I., and Brandon, D. (1998) Metastable alumina polymorphs: crystal structures and transition sequences. *J. Am. Ceram. Soc.*, 81, 1995-2012.

Li, H. T., Xia, M., Jarry, P., Scamans, G. M., and Fan, Z. (2011) Grain refinement in a AlZnMgCuTi alloy by intensive melt shearing: A multi-step nucleation mechanism. *J. Crys. Growth*, 314, 285-292.

LIoyd, D. J. (1994) Particle reinforced aluminium and magnesium matrix composites. *Inter. Mater. Rev.*, 39, 1-23.

Livey, D. T., Murray, P. (1956) *Proceedings of 2nd Plansee seminar* (p. 375). Rentte//Tyrol: Metallwerk Plansee.

M

Marcantonio, J. A., and Mondolfo, L. F. (1971) Grain refinement in aluminium alloyed with titanium and boron. *Metall. Trans. A*, 2A, 465-471.

Maxwell, I., and Hellawell, A. (1975) A simple model for grain refinement during solidification. *Acta metall.*, 23, 229-237.

Maxwell, I., and Hellawell, A. (1975) An analysis of the peritectic reaction with particular reference to Al-Ti alloys. *Acta Metall.*, 23, 901-909.

Mbuya, T. O., Odera, B. O., and Nganga, S. P. (2003) Influence of iron on castability and properties of aluminium silicon alloys: literature review. *Inter. J. Cast Met. Res*, 16, 451-465.

McCartney, D. G. (1989) Grain refining of aluminium and its alloys using inoculants. *Inter. Mater. Rev.*, 34, 247-260.

McCarty, P., and Horsthemke, W. (1988) Effective diffusion coefficient for steady two-dimensional convective flow. *Physical Review A*, 37, 2112-2117.

McLeod, A. D., and Gabryel, C. M. (1992) Kinetics of the growth of spinel, $MgAl_2O_4$, on alumina particulate in aluminium alloys containing magnesium. *Metall. Trans. A*, 23A, 1279-1283.

Men, H., and Fan, Z. (2010) Transition of amorphous to crystalline oxide film in initial oxide overgrowth on liquid metals. *Mater. Sci. Tech.*, in press.

Men, H., Jiang, B., & Fan, Z. (2010) Mechanisms of grain refinement by intensive shearing of AZ91 alloy melt. *Acta Mater.*, 58, 6526-6534.

Metals Handbook. (1990) ASM International Handbook Committee.

Miller, D. N., Lu, L., and Dahle, A. K. (2006) The role of oxides in the formation of primary iron intermetallics in an Al-11.6Si-0.37Mg alloy. *Metall. Mater. Trans. B*, 37B, 873-878.

Mohanty, P. S., and Gruzleski, J. E. (1996) Grain refinement mechanisms of hypoeutectic A-Si alloys. *Acta Mater.*, 44, 3749-3760.

Mohanty, P. S., and Gruzleski, J. E. (1995) Mechanism of grain refinement in aluminium. *Acta Metall. Mater.*, 43, 2001-2012.

Mohanty, P. S., Guthrie, R. I., and Gruzleski, J. E. (1995) Studies on the fading behaviour of Al-Ti-B master alloys and grain refinement mechanism using LiMCA. *Light Metals 1995* (pp. 859-868). The minerals, Metals & Materials Society.

Moore, J. F., Attenkofer, K., Calaway, W. F., Hryn, J. N., King, B. V., and Krumdick, G. K. Retrieved June 10th, 2010, from www.aps.anl.gov/apsar2002/MOORE1.PDF

Murali, S., Raman, K. S., and Murthy, K. S. (1995) The formation of β-FeSiA15 and Be-Fe phases in A1-7Si-0.3Mg alloy containing Be. *Mater. Sci. Eng. A*, 190, 165-172.

Murray, J. L. (1982) *Bull. Alloy Phase Diagrams*, 60-74.

Murray, M. T., and Griffiths, J. R. (1996) The design of feed systems for thin-walled zinc high-oressure die castings. *Metall. Mater. Trans. B*, 27B, 115-118.

Murthy, V. S., and Rao, B. S. (1995) Microstructural development in the directed melt-oxidized (DIMOX). Al-Mg-Si alloys. *J. Mater. Sci.*, 30, 3091-3097.

Murty, B. S., Kori, S. A., and Chakraborty, M. (2002) Grain refinement of aluminium and its alloys by heterogenerous nucleation and alloying. *Inetr. Mater. Rev.*, 47, 3-29.

N

Nadella, R., Eskin, D. G., Du, Q., and Katgerman, L. (2008) Macrosegregation in direct-chill casting of aluminium alloys. *Progress in Materials Science*, 53, 421-480.

Naidich, J. V. (1981) Wettability of solids by liquid metals. *Prog. Surf. Membr. Sci.*, 14, 353-484.

Narayanan, L. A., Samuel, F. H., and Gruzleski, J. E. (1994) Crystallisation behavior of iron-containing intermetallic compounds in 319 aluminium alloy. *Metall. Mater. Trans. A*, 25A, 1761-1773.

Norman, A. F., Prangnell, P. B., and McEwen, R. S. (1998) The solidification behaviour of dilute aluminium-scandium alloys. *Acta Mater.*, 46, 5715-5732.

O

Ozdemir, O., Gruzleski, J. E., and Drew, R. A. (2009) Effect of low-levels of strontium on the oxidation behaviour of selected molten aluminium-magnesium alloys. *Oxidation of Metals*, 72, 241-257.

P

Pai, B. C., Ramani, G., Pillai, R. M., and Satyanarayana, K. G. (1995) Role of magnesium in cast aluminium alloy matrix composites. *J. Mater. Sci.*, 30, 1903-1911.

Phragmen, G. (1950) On the phases occupying in alloys of aluminium with copper, magnesium, manganese, iron, and silicon. *J. Inst. Metals*, 77, 489-552.

Pilling, N. B., and Bedworth, R. E. (1923) The Oxidation of Metals at High Temperatures. *J. Inst. Met.*, 29, 529-591.

Polak, W. (2007) Preference for fcc atom stacking observed during growth of defect-free LJ3281 clusters. *Cryst. Res. Technol.*, 42, 1207-1216.

Q

Qin, R. S., and Fan, Z. (2000) Theoretical study on the evolution of grain morphology under high shear rate. *Proceedings of the 6th International Conference on Semi-Solid Processing of Alloys and Composites*, (pp. 819-824). Turin, Italy.

Quested, T. E. (2004) *Solidification of Inoculated Aluminium Alloys*. PhD thesis. UK: Department of Materials Science and Metallurgy, Cambridge University.

Quested, T. E. (2004) Understanding mechanisms of grain refinement of aluminium alloys by inoculation. *Mater. Sci. Tech.*, 20, 1357-1369.

Quested, T. E., and Greer, A. L. (2004) The effect of the size distribution of inoculant particles on as-cast grain size in aluminium alloys. *Acta Mater.*, 52, 3859-3868.

R

Radjai, A., and Miwa, K. (2000) Effects of the intensity and frequency of electromagnetic vibrations on the microstructural refinement of hypoeutectic Al-Si alloys. *Metall. Mater. Trans. A*, 31A, 755-762.

Raiszadeh, R., and Griffiths, W. D. (2006) A method to study the history of a double oxide film defect in liquid aluminium alloys. *Metall. Mater. Trans. B*, 37B, 865-871.

Ramani, G., Pillai, R. M., Pai, C., and Ramamohan, T. R. (1991) Factors affecting the stability of non-wetting dispersoid suspensions in metallic melts. *Composites*, 22, 143-150.

Roy, N., Samuel, A. M., and Samuel, F. H. (1996) Porosity formation in AI-9 Wt Pct Si-3 Wt Pct Cu alloy systems: Metallographic observations. *Metall. Mater. Trans. A*, 27A, 415-429.

S

Samuel, A. M., and Samuel, F. H. (1996) Observations on the formation of β-AlFeSi phase in 319 type AI-Si alloys. *J. Mater. Sci.*, 31, 5529-5539.

Sannes, S., and Westengen, H. (1998) The influence of process conditions on the microstructure and mechanical properties of magnesium die castings. *Magnesium alloys and their applications* (pp. 223-228). Frankfurt, Germany: Werkstoff-InformationsgesellschaftmbH.

Scamans, G. M., and Butler, E. P. (1975) In situ observations of crystalline oxide formation during aluminium and aluminium alloy oxidation. *Metall. Trans. A*, 6A, 2055-2063.

Schumacher, P., and Greer, A. L. (1994b) Enhanced heterogeneous nucleation of α-Al in amorphous aluminium alloys. *Mater. Sci. Eng. A*, A181-182, 1335-1339.

Schumacher, P., and Greer, A. L. (1994a) Heterogeneously nucleated α-Al in amorphous aluminium alloys. *Mater. Sci. Eng. A*, A178, 309-313.

Schumacher, P., and Greer, A. L. (1997) On the reproducibility of heterogeneous nucleation in amorphous Al85Ni10Ce5 alloys. *Mater. Sci. Eng. A*, A226-228, 794-798.

Schumacher, P., Greer, A. L., Worth, J., Evans, P. V., Kearns, M. A., Fisher, P., et al. (1998) New studies of nucleation mechanisms in aluminium alloys: implications for grain refinement practice. *Mater. Sci. Tech.*, 14,394-404.

Seifeddine, S. (2007) The influence of iron on the microstructure and mechanical properties of cast Al-Si alloys, Vilmer project- 5.2 casting . Jönköping University, Sweden.

Shabestari, S. G., and Gruzleski, J. E. (1995) Gravity segregation of complex intermetallic compounds in liquid aluminium-silicon alloys. *Metall. Mater. Trans. A*, 26, 999-1006.

Shelleman, R. A., and Messing, G. L. (1988) Liquid-phase-assisted transformation of seeded gamma-alumina. *J. Am. Ceram. Soc.*, 71, 317-322.

Shen, P., Zhang, D., Qiao, L. L., Shi, L. X., and Jiang, Q. C. (2010) Wetting of polycrystalline alpha Al2O3 by molten Mg in Ar atmosphese. *Metall. Mater. Trans. A*, 41A, 1621-1626.

Sigworth, G. K. (1986) Author's reply to Discussion of "The grain refining of aluminium and phase relationships in the Al-Ti-B system". *Metall. Trans. A*, 17A, 349-351.

Sigworth, G. K. (1996) Communication on mechanism of grain refinement in aluminum. *Scripta Mater.*, 34, 919-922.

Sigworth, G. K. (1984) The grain refining of aluminium and phase relationships in the aluminum-titanium-boron system. *Metall. Trans. A*, 15A, 277-282.

Sigworth, G. K., Shivkumar, S., and Apelian, D. (1989) The influence of molten metal processing on mechanical properties of cast Al-Si-Mg alloys. *AFS Trans.*, 97, 811-824.

Spear, R. E., and Gardner, G. R. (1963) Dendrite cell size. *AFS Trans.*, 71, 209-215.

Spittle, J. A. (2006) Columnar to equiaxed grain transition in as solidified alloys. *Inter. Mater. Rev.*, 51, 247-269.

Spittle, J. A., and Sadli, S. (1995) Effect of alloy variables on grain refinement of binary Al alloys with Al-Ti-B. *Mater. Sci. Tech.*, 11, 533-537.

Sreekumar, V. M., Pillai, R. M., Pai, B. C., and Chakraborty, M. (2008) Microstructural development in Al/$MgAl_2O_4$ in situ metal matrix composite using value-added silica sources. *Sci. Tech. Adv. Mater.*, p. 015004.

StJohn, D. H., and Hogan, L. M. (1982) Thermal analysis of peritectic alloys. *J. Mater. Sci.*, 17, 2413-2418.

StJohn, D. H., Cao, P., Qian, M., and Easton, M. A. (2007) A new analytical approach to reveal the mechanisms of grain refinement. *Adv. Eng. Mater.*, 9, 739-746.

Surendran, K. P., Santha, N., Mohanan, P., and Sebastian, M. T. (2004) Temperature stable low loss ceramic dielectrics in (1-x)$ZnAl_2O_4$-xTiO2 system for microwave substrate applications. *Eur. Phys. J. B*, 41, 301-306.

Surla, K., Valdivieso, P., Soustelle, M., and Prin, M. (2001) Kinetic study of the oxidation by oxygen of liquid Al-Mg 5%alloys. *Solid State Ionics*, 143, 355-365.

T

Taylor, J. A. (2004) The effect of iron in Al-Si casting alloys. Casting Concepts, *35th Australian Foundry Institute National Conference* (pp. 148-157). Adelaide, South Australia: Australian Foundry Institute (AFI).

Taylor, J. A., Schaffer, G. B., and StJohn, D. H. (1999a) The role of iron in the formation of porosity in Al-Si-Cu–based casting Alloys: Part I. Initial experimental observations. *Metall. Mater. Trans. A*, 30A, 1643-1650.

Taylor, J. A., Schaffer, G. B., and StJohn, D. H. (1999b) The role of Iron in the formation of porosity in Al-Si-Cu–based casting alloys: Part II. A phase-diagram approach. *Metall. Mater. Trans. A*, 30A, 1651-1655.

Taylor, J. A., Schaffer, G. B., and StJohn, D. H. (1999c) The role of iron in the formation of porosity in Al-Si-Cu–based casting alloys: Part III. A microstructural model. *Metall. Mater. Trans. A*, 30A, 1657-1662.

Thiele, W. V. (1962) Aluminium, 38, 780-786.

Tibballs, J. E., Horst, J. A., and Simensen, C. J. (2001) Precipitation of alpha-Al(Fe,Mn)Si from the melt. *J. Mater. Sci.*, 36, 937-941.

Timelli, G., and Bonollo, F. (2010) The influence of Cr content on the microstructure and mechanical properties of AlSi9Cu3Fe die-casting alloys. *Mater. Sci. Eng. A*, A528, 273-282.

TP-1. (1987) *Standard Test Procedure for Aluminium Alloy Grain Refiners*. Washington, DC: The Aluminium Association.

Trumble, K. P. (1998) Spontaneous infiltration of non-cylindrical porosity: Close-packed spheres. *Acta Mater.*, 46, 2363-2367.

V

Vandyoussefi, M., and Greer, A. L. (2002) Application of cellular automaton-finite element model to the grain refinement of directionally solidified Al-4.15wt.% Mg alloys. *Acta Mater*, 50, 1693-1705.

Villars, P., and Calvert, L. D. (1991) *Pearson's Handbook of Crystallographic Data for Intermetallic Phases*. ASM INTERNATIONAL.

Vorren, O., Evensen, J. E., & Pedersen, T. B. (1984) Microstructure and mechanical properties of AlSi (Mg) casting alloy. *AFS Trans.*, S, 459-466.

W

Wang, J., He, S., Sun, B., Li, K., Shu, D., and Zhou, Y. (2002) Effects of melt thermal treatment on hypoeutectic Al-Si alloys. *Mater. Sci. Eng. A*, A338, 101-107.

Wang, L., Makhlouf, M., and Apelian, D. (1995) Aluminium die casting alloys: alloy composition, microstructure, and properties-performance relationships. *Inter. Mater. Rev.*, 40, 221-238.

Wang, P. X. (2000) *The effects of Be and solution temperature on the mechanical properties of A319.0 alloys*. Taiwan: PhD thesis, National Central University.

Wang, Q. G., Caceres, C. H., and Griffiths, J. R. (1998) The cracking of Fe-rich and eutectic Si particles in an Al-7Si-0.7Mg casting alloy. *AFS Trans.*, 106,131-136.

Wang, Y., and Xiong, Y. (2000) Effects of beryllium in Al–Si–Mg–Ti cast alloy. *Mater. Sci. Eng. A*, 280, 124-127.

Wefers, K., and Misra, C. (1987) *Oxides and hydroxides of aluminium*. Alcoa, USA: Alcoa Laboratories.

Weirauch, D. A., and Krafick, W. J. (1990) The effect of carbon on wetting of aluminium oxide by aluminium. *Metall. Trans. A*, 21, 1745-1751.

Weyl, W. A. (1953) In R. Gomer, and C. S. Smith, *Structure and properties of solid surface* (p. 147). University of Chicago Press.

X

Xia, M., Wang, Y., Li, H., Arumuganathar, S., Zuo, Y., Scamans, G. M., et al. (2009) Refinement of Solidification Microstructure by MCAST Process. *Proceedings of Magnesium Technology* (pp. 135-140). TMS.

Xu, C., and Gao, W. (2000) Pilling-Bedworth ratio for oxidation of alloys. *Mat. Res. Innovat.*, 3, 231-235.

Y

Yan, P. F., Du, K., and Sui, M. L. (2010) α- to γ-Al_2O_3 martensitic transformation induced by pulsed laser irradiation. *Acta Mater.*, 58, 3867-3876.

Yang, J. C., Schumann, E., and Ruhle, M. (1998) Transient oxidation of NiAl. *Acta Mater.*, 46, 2195-2201.

Z

Zhang, D. L., and Cantor, B. (1992) The effect of dopants on the heterogeneous nucleation of solidification of Cd and Pb particles embedded in an Al matrix. *Acta Metall. Mater.*, 40, 2951-2960.

Zheng, J. G., Vincent, R., and Steeds, J. W. (2000) Crystal structure of an orthorhombic phase in β-(Al-Fe-Si) precipitates determined by convergent-beam electron diffraction. *Philos. Mag. A*, 80A, 493-500.

Zhou, R. S., and Snyder, L. S. (1991) Structures and transformation mechanisms of the eta, gamma and theta transition aluminas. *Acta. Cryst.*, B47, 617-630.

Zuo, Y., Li, H., Xia, M., Jiang, B., Scamans, G. M., and Fan, Z. (2011) Refining grain structure and porosity of an aluminium alloy with intensive melt shearing. *Scripta Mater.*, 64, 209-212.